TUDelft

Delft University of Technology

The Bits of Nature

Bioinspired bitmap composites

Cruz Saldivar, M.

Important note
To cite this publication, please use the final published version (if applicable).
Please check the document version above.

The Bits of Nature:

Bioinspired Bitmap Composites

The Bits of Nature:

Bioinspired bitmap composites

Proefschrift

ter verkrijging van de graad van doctor

aan de Technische Universiteit Delft,

opgezag van de Rector Magnificus, Prof.dr.ir. T.H.J.J. van der Hagen,

voorzitter van het College voor Promoties,

in het openbaar te verdedigen op maandag, 19 juni 2023 om 17:30 uur.

door

Mauricio CRUZ SALDIVAR

Master of Science in Biomedical Engineering,

Technische Universiteit Delft, the Netherlands,

geboren te Mexico Stad, Mexico.

Dit proefschrift is goedgekeurd door de promotor: Prof.dr. A.A. Zadpoor en copromotor:
Dr. M.J. Mirzaali Mazandarani.

Samenstelling promotiecommissie bestaat uit:

Rector magnificus,	Voorzitter
Prof.dr. A.A. Zadpoor,	Technische Universiteit Delft, promotor
Dr.ir. M.J. Mirzaali,	Technische Universiteit Delft, copromotor

Onafhankelijke leden:

Prof.dr. G.J.V.M. van Osch,	Erasmus MC, the Netherlands
Prof.dr.ir. K.M.B. Jansen,	Technische Universiteit Delft
Prof.dr.ir. J.L. Herder,	Technische Universiteit Delft
Prof.dr.ir. H.E.J.G. Schlangen,	Technische Universiteit Delft

Summary

In the vast domain of biomedical engineering, the challenge of developing synthetic materials that can replace damaged tissues has proved a daunting task. Millions of years of adaptation have provided natural tissues with multiple strategies that yield highly efficient mechanical properties that are not found in human-made materials. The first of these strategies relates to the material composition of living tissues. Natural materials tune their functionality thanks to the presence of multiple constituting phases with highly different properties (*e.g.,* soft collagen and the hard mineral phase in the bone). The second strategy is manifested in the arrangement of these phases, where these constituents take a wealth of intricate geometries to strengthen and toughen their structures. For example, the hierarchical arrangement of different constituents at multiple length scales enables them to work in synergy to distribute the deformation energy within tissues, thereby delaying their critical failure. Yet another strategy is the use of functional gradients, where the volume fraction of one material changes across a relatively short interface, thereby attenuating the stress concentrations caused by the mismatch between the mechanical properties of the different constituents.

In recent years, replicating these exceedingly complex yet harmonious natural design paradigms has been a significant drive in the scientific community. Mainly achieved using multi-material additive manufacturing techniques, architected materials have been developed that implement some of the design strategies found in natural materials to achieve seemingly contradictory design objectives, such as simultaneously high strength and toughness. However, limitations in computational resources and standard processing methods hinder the complexity and multi-scale rationality of the design features that one can introduce within a construct. Bitmap multi-material 3D-printing techniques, however, offer the possibility to experiment with different design strategies at the level of individual microscale voxel, leading to the emergence of 'voxel-by-voxel' approaches. In such approaches, the constituting material of each voxel can be individually selected, yielding

unprecedented freedom to generate microarchitectures that seamlessly mimic the morphologies observed in natural tissues.

In pursuit of highly efficient and tunable *bioinspired bitmap composites,* this thesis aims to study how the incorporation of the aforementioned natural design paradigms using voxel-by-voxel additive manufacturing techniques enhances the performance of such types of designer materials. In Part I of this thesis, the mechanical interactions between soft and hard voxels are extensively studied to determine multiple material-property relationships and devise computational tools that enable the optimization of bitmap constructs. Various experimental methodologies (*i.e.,* nanoindentation and quasi-static tension) at multiple length scales (*i.e.,* micro and mesoscales) enabled us to map the elastic design space of voxelized materials, where co-continuous nonlinear models are used for the direct design of biomimetic devices (Chapter 2). The effective mechanical properties of these structures were accurately tuned, while the designs that included functionally graded interfaces presented highly efficient post-yield behavior. A similar approach was implemented for mapping the elastoplastic behavior of randomly distributed voxels (Chapter 3). By using experimental test data to train constitutive models for large deformations, we developed a coarse-graining approach that provided highly efficient computational simulations that proved ideal for the analysis and inverse design of biomimetic constructs. The outcomes and tools developed in this part can facilitate the seamless integration of bioinspired design paradigms into voxel-based materials.

Part II of this thesis deals with functional gradients and multi-hierarchical organization to generate design strategies that enhance the performance of bitmap composites in general and soft-hard interfaces in particular. Computational and experimental studies of architected materials with functional gradients demonstrated that ideal soft-hard interfaces constrain and attenuate strain concentrations through concave features, smooth surface area patterns, and compliant elastic modulus transition functions (Chapter 4). Interpenetrating geometries that incorporate these guidelines were shown to perform close to the theoretical limits of the soft material. A similar systematic approach was presented for studying the different toughening contributions achieved by hierarchically organizing multiple levels of brick-and-mortar structures and functional gradients (Chapter 5). In these analyses that were performed on fracture specimens, we showed how the increased ductility of gradients and

strengthening effect provided by brick-and-mortar structures work in synergy to yield highly efficient synthetic composites. Furthermore, two hierarchical organization levels of voxel features were incorporated into the design of metamaterial lattices using tissue adaptation algorithms (Chapter 6). These allowed for the redistribution of the strain energy density profile of the lattices at the unit cell level, leading to stress-worthy metamaterials. Moreover, the implemented design strategy enabled us to adjust the anisotropic behavior of the resulting materials and extend the envelope of their elastic properties.

This thesis contributes new computational and experimental techniques, design strategies, and comprehensive data to facilitate the development of biomimetic bitmap composites of hard and soft phases for various (biomedical) applications.

Samenvatting

In het uitgestrekte domein van de biomedische techniek is de uitdaging om synthetische materialen te ontwikkelen die beschadigde weefsels kunnen vervangen een ontmoedigende taak gebleken. Miljoenen jaren aan aanpassing hebben natuurlijke weefsels voorzien van meerdere strategieën die zeer efficiënte mechanische eigenschappen opleveren die niet worden gevonden in door de mens gemaakte materialen. De eerste van deze strategieën heeft betrekking op de materiaalsamenstelling van levende weefsels. Natuurlijke materialen stemmen hun functionaliteit af dankzij de aanwezigheid van meerdere samenstellende fasen met sterk verschillende eigenschappen (bijv. zacht collageen en de harde mineraalfase in het bot). De tweede strategie manifesteert zich in de rangschikking van deze fasen, waarbij deze bestanddelen een rijke verscheidenheid aan ingewikkelde geometrieën aannemen om hun structuren te versterken en te verharden. Bijvoorbeeld, de hiërarchische rangschikking van verschillende bestanddelen op meerdere lengteschalen maakt het mogelijk dat ze in synergie werken om de vervormingsenergie binnen weefsels te verdelen, waardoor het falen van weefsels wordt uitgesteld. Nog een andere strategie is het gebruik van functionele gradiënten, waarbij de volumefractie van een materiaal verandert over een relatief korte interface, waardoor de spanningsconcentraties worden verminderd die worden veroorzaakt door het verschil in mechanische eigenschappen van de verschillende bestanddelen.

In de afgelopen jaren is het repliceren van deze buitengewoon complexe, maar harmonieuze, natuurlijke ontwerpparadigma's een belangrijke drijfveer geweest in de wetenschappelijke gemeenschap. Voornamelijk bereikt met behulp van additieve productietechnieken met meerdere materialen, zijn ontworpen materialen ontwikkeld die enkele van de ontwerpprincipes die in natuurlijke materialen worden gevonden implementeren om schijnbaar tegenstrijdige ontwerpdoelstellingen te bereiken, zoals gelijktijdig hoge sterkte en taaiheid. Beperkingen in computermiddelen en standaardverwerkingsmethoden hinderen echter de complexiteit en de multischalige methodologie van de ontwerpkenmerken die men kan introduceren in een constructie. Bitmap additieve productietechnieken voor meerdere materialen bieden echter de

mogelijkheid om te experimenteren met verschillende ontwerpprincipes op het niveau van individuele microscopische voxels, wat leidt tot het ontstaan van 'voxel-by-voxel'-benaderingen. Bij dergelijke benaderingen kan het opmakende materiaal van elke voxel afzonderlijk worden geselecteerd, wat ongekende vrijheid oplevert om microstructuren te genereren die naadloos de morfologieën nabootsen die worden waargenomen in natuurlijke weefsels.

Met als doel zeer efficiënte en afstembare bio-geïnspireerde bitmap-composieten te ontwikkelen, onderzoekt deze scriptie hoe de incorporatie van bovengenoemde natuurlijke ontwerpmethoden met behulp van voxel-by-voxel additieve productietechnieken de prestaties van dit soort ontwerpmaterialen kan verbeteren. In Deel I van deze scriptie worden de mechanische interacties tussen zachte en harde voxels uitgebreid bestudeerd om meerdere materiaaleigenschappenrelaties vast te stellen en rekenkundige hulpmiddelen te ontwikkelen die de optimalisatie van bitmapconstructies mogelijk maken. Verschillende experimentele methodologieën (zoals nano-indentatie en quasi-statische spanning) op meerdere lengteschalen (micro- en mesoschalen) stellen ons in staat om het elastische ontwerpgebied van voxelmateriaal in kaart te brengen, waarbij co-continue niet-lineaire modellen worden gebruikt voor de directe ontwikkeling van biomimetische apparaten (Hoofdstuk 2). De effectieve mechanische eigenschappen van deze structuren zijn nauwkeurig afgestemd, terwijl de ontwerpen die functioneel gegradeerde interfaces omvatten, een zeer efficiënt gedrag na vloeigrens vertonen. Een vergelijkbare aanpak werd toegepast om het elastoplastische gedrag van willekeurig verdeelde voxels in kaart te brengen (Hoofdstuk 3). Door experimentele testgegevens te gebruiken om constitutieve modellen voor grote vervormingen te trainen, hebben we een grofkorrelige aanpak ontwikkeld die zeer efficiënte rekenkundige simulaties bood die ideaal waren voor de analyse en het omgekeerd ontwerpen van biomimetische constructies. De resultaten en hulpmiddelen die in dit deel zijn ontwikkeld, kunnen de naadloze integratie van bio-geïnspireerde ontwerpmethoden in op voxel gebaseerde materialen vergemakkelijken.

Deel II van deze thesis behandelt functionele gradiënten en multi-hiërarchische organisatie om ontwerpprincipes te genereren die de prestaties van bitmapcomposieten in het algemeen en zachte-harde interfaces in het bijzonder verbeteren. Rekenkundige en experimentele studies van ontworpen materialen met functionele gradiënten hebben

aangetoond dat ideale zachte-harde interfaces de concentratie van spanningen beperken en verminderen door middel van holle kenmerken, gladde oppervlaktepatronen en soepele elastische modulusovergangsfuncties (Hoofdstuk 4). Interpenetrerende geometrieën die deze richtlijnen bevatten, bleken dicht bij de theoretische limieten van het zachte materiaal te presteren. Een soortgelijke systematische aanpak werd gepresenteerd voor het bestuderen van de verschillende versterkingen die worden bereikt door meerdere niveaus van steen-en-mortelstructuren en functionele gradiënten hiërarchisch te organiseren (Hoofdstuk 5). In deze analyses die werden uitgevoerd op breukmonsters, hebben we aangetoond hoe de verhoogde ductiliteit van gradiënten en het versterkende effect van steen-en-mortelstructuren samenwerken om zeer efficiënte synthetische composieten op te leveren. Bovendien werden twee hiërarchische organisatieniveaus van voxel-eigenschappen opgenomen in het ontwerp van metamateriaalroosters met behulp van weefseladaptatie-algoritmen (Hoofdstuk 6). Deze maakten de herverdeling mogelijk van de spanning-energiedichtheid van de rasters op het niveau van de eenheidscel, wat leidde tot spanningswaardige metamaterialen. Bovendien maakte de geïmplementeerde ontwerpstrategie het mogelijk om het anisotrope gedrag van de resulterende materialen aan te passen en het bereik van hun elastische eigenschappen te vergroten.

Deze thesis draagt nieuwe rekenkundige en experimentele technieken, ontwerpprincipes en uitgebreide gegevens bij om de ontwikkeling van biomimetische bitmapcomposieten van harde en zachte fasen voor verschillende (biomedische) toepassingen te vergemakkelijken..

Contents

1

Introduction

"A sun of rubber was convulsed and set;
And blood-black nothingness began to spin
A system of cells interlinked within
Cells interlinked within cells interlinked
Within one stem. And dreadfully distinct
Against the dark, a tall white fountain played."

— Vladimir Nabokov, Pale Fire

1.1 Background

One of the current goals of biomedical engineering is to develop materials that can replace the function of once-healthy tissues [1–3]. Despite remarkable progress, this remains a formidable task. That is partially due to the fact that the structural tissues of the human body, such as the bones, articular cartilage, ligaments, and tendon, have remarkably efficient mechanical properties. For example, they are lightweight, heterogeneous, highly anisotropic, and particularly tough and strong [4–6]. In comparison, engineering materials often face the conundrum of having to sacrifice one set of these properties for the sake of achieving another [7]. Indeed, more than 4 million years of adaptation to perilous environments and limited resources still outpaces the achievements of humankind across its seven material ages [8,9].

1.2 Natural materials

For many years, the quest for highly efficient synthetic materials has driven scientists to explore the secrets of the remarkable properties of natural materials [10–12]. The performance of such materials originates from multiple 'fitness' strategies. First, natural materials are composites made from a combination of a 'soft' phase and a 'hard' material phase that are mixed at different ratios to fulfill multiple functionalities [13]. Second, the two material phases are arranged hierarchically across multiple length scales [13–15] to reconcile contradictory design requirements, such as achieving both a high strength and a high stiffness [16]. Third, functional gradients in which the ratios and/or types of the constituting phases are changed enable efficient and durable interfacing of materials with dissimilar properties [17].

The bone, which is a magnificent composite of a soft organic matrix (made mostly from collagen type I) and a hard mineral phase (hydroxyapatite), serves as a prime example of the marvels of heterogeneous hierarchical systems [18]. Akin to the seven pillars of life [19], these two materials combine in the so-called 'seven hierarchies of bone', forming multiple substructures. These include mineralized collagen fibrils and their arrays at the microscale, fiber patterns and osteons at the mesoscale (*i.e.,* hundreds of microns), and compact bone at the macroscale [20,21]. Each of these structures fulfills a different toughening role. For example, fibrillar features provide the composite with tensile strength through molecular uncoiling and fibrillar sliding, fiber arrays dissipate energy through the introduction of

microcracks and ligament bridging, and osteon features twist and deflect major cracks through sacrificial bond failure [18]. The harmonious arrangement of these structural features results in multiple coexisting toughening mechanisms, showcasing the brilliance of the nature's design.

The tendon, connecting bones to muscles, is another example of a hierarchical structure [22,23]. This soft composite works primarily under tension and is primarily made from collagen type I within a matrix of proteoglycans [24,25]. The collagen molecules bundle in microfibrils at the nanoscale, which then connect with proteoglycans to form fibrils and fascicles at the microscale. These fascicles, in turn, merge to form the final tendon at the mesoscale (Figure 1.1A) [10,24]. Tendon owes its energy absorption ability to the load transfer capacity of each long fiber, while the short collagen fibrils mainly determine its tensile strength. All in all, the remarkable synergy between the complex arrangements of these two dissimilar materials at various length scales affords natural materials with their superior mechanical properties.

Functional gradients are found at the juncture between two materials of vastly dissimilar mechanical properties and play a crucial role in the resilience of natural tissues [17,26]. In the case of the human body, such regions as the dentinoenamel junction (*i.e.,* where stiff enamel connects to tough dentin) and the tendon enthesis (*i.e.,* where the hard bone connects to the soft tendon) are among the most studied functional gradients in the literature [27–31]. Even though functional gradients primarily consist of the gradual transition between two phases along a relatively short distance, they are also accompanied by other features, such as morphological interdigitations and changes in anisotropy [32,33]. Combining such multiple features reduces the stresses caused by property mismatch and prevents energy from propagating cracks.

From these examples, it is clear that replicating the extraordinary mechanical behavior of natural tissues requires the incorporation of these natural design principles into synthetic materials. This bioinspiration has been a main drive within the scientific community to design materials that resemble natural tissues as closely as possible. However, this process requires a manufacturing technique that allows for the replication of such complex features at multiple length scales.

1.3 Bioinspired bitmap composites

Multi-material additive manufacturing (AM) is particularly suitable for the fabrication of synthetic materials that embody the design principles found in natural materials [34–36]. Multiple AM technologies, such as material extrusion, stereolithography, and fused deposition modeling, can be used to deposit multiple material phases with different mechanical properties (*e.g.,* a soft and a hard phase) to create heterogeneous architectures. Designed rationally or aided by theoretical or computational models, these bioinspired architected materials can exhibit remarkable properties that are generally considered mutually exclusive (*e.g.,* toughness and strength) and have been shown to be tunable [37–40]. However, classic design processing methods based on surface approximations (*e.g.,* standard tessellation language (STL) files) and insufficient computational resources restrict the number of achievable features within a design. These challenges hinder the incorporation of multiple natural design paradigms into the design of architected biomimetic materials.

An approach that circumvents the aforementioned drawbacks is bitmap material jetting [43]. This "voxel-by-voxel" technique allows for controlling the deposition of individual droplets of multiple UV-curable photopolymers at the microscale (*i.e.,* tens of microns). Instead of the commonly used STL files, each design is defined by multiple stacks of binary images, where the (positive) values of each bit determine the presence of a material (Figure 1.1B). This technique, therefore, offers unprecedented freedom to generate microarchitectures that seamlessly mimic the morphologies observed in mineral-collagen tissues [44] (Figure 1.1C). Studies involving these **bioinspired bitmap composites**, however, are barely past the conceptual design stage. The hard and soft voxel interactions have not been adequately characterized, and optimizations for yielding a specific effective mechanical behavior are still missing. Furthermore, systematic studies on the contributions, synergy, and optimization of structures that include multiple design paradigms as well as design tools and standards for effectively generating efficient soft-hard interfaces are lacking. Tackling these challenges is fundamental to improving the efficiency and performance of synthetic materials for their eventual biomedical applications.
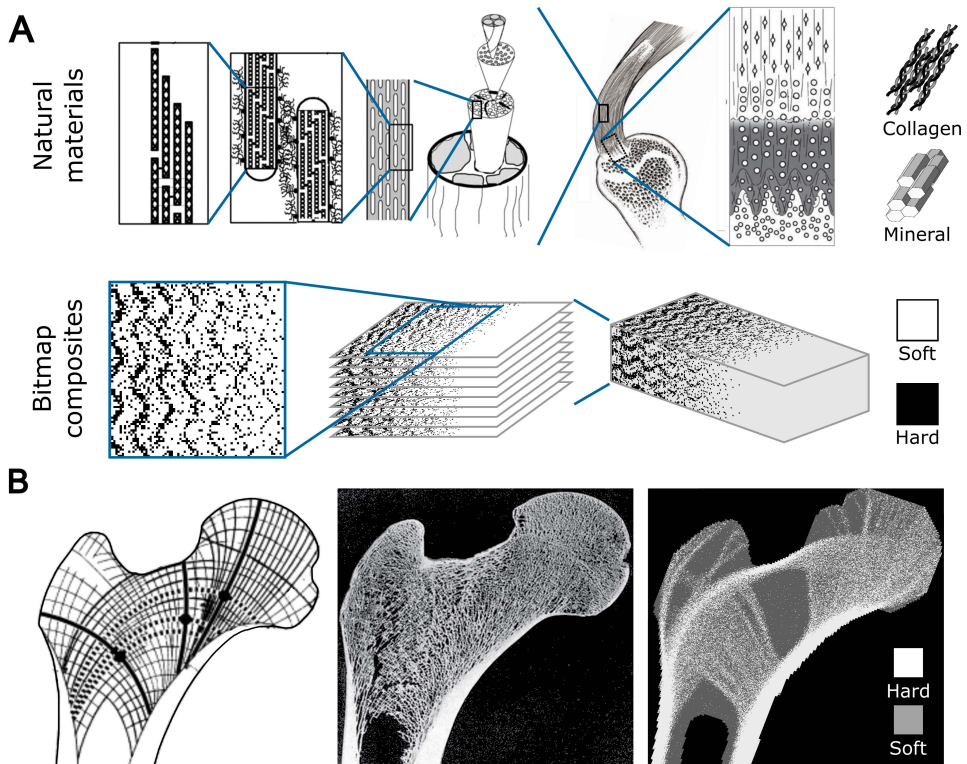
Figure 1.1: A) The tendon and enthesis structures serve as brilliant demonstrations of the nature's efficient use of materials incorporating both multiscale hierarchical organization and functional gradients to give rise to materials with remarkable mechanical performance (images obtained with permission from [22,33]). B) Bitmap composites can replicate these intricate design principles, utilizing stacks of binary images to define their microarchitecture. C) The head of a femoral bone serves as a prime example of the nearly limitless design capabilities provided by this 3D-printing method, closely resembling natural tissues in form and function (images obtained with permission from [41,42]).

1.4 Main goal and thesis outline

Driven by the necessity to generate highly efficient and tunable materials for biomedical applications, the aim of this thesis is:

To study the effects of multiple bioinspired design principles and their synergy in the development of high-performing bioinspired bitmap composites.

The approach towards achieving this goal is to incorporate multiple morphological and mechanistic bioinspired design principles within the scope of voxel-based multi-material additive manufacturing to design highly efficient and tunable architected materials. Three main sub-objectives are, thus, defined as:

1. Introduction

1. To study the mechanical interactions between soft and hard voxels to characterize and model their behavior.
2. To develop strategies to devise efficient functionally graded soft-hard interfaces.
3. To develop composites that profit from the synergy of multiscale hierarchical organization.

The first part of this thesis, which involves **Chapters 2 and 3**, delves deep into the analysis and study of the mechanical interactions between soft and hard voxels and introduces tools and methodologies to analyze and optimize voxelized materials. In **Chapter 2**, we generate soft-hard interfaces that span a wide range of possible voxelized composites and evaluate their mechanical performance with experiments at the microscale and mesoscale. The generated data is used to establish nonlinear models that determine the elastic behavior of soft-hard composites and generate accurate computational models. These models are then applied for the optimization of biomimetic constructs. In **Chapter 3**, we propose using foam-based large-deformation constitutive models for the coarse-graining of large voxel systems. We show how this approach adequately captures the mechanical behavior of the composites and reduces the computational time required to perform nonlinear simulations. Coarse graining is then implemented for the analysis and inverse design of highly complex microarchitectures.

Within **Chapters 4 to 6**, the second part of this thesis focuses on incorporating the aforementioned functional gradient and multi-hierarchical organization paradigms as well as the generation of design strategies to optimize biomimetic constructs. **Chapter 4** focuses on unraveling the principles that determine the performance of soft-hard interfaces by analyzing different functional gradient architectures with experimental and computational tools. **Chapter 5** analyzes the impact and interplay of multiple toughening mechanisms organized under a multiscale hierarchical organization. Finally, in **Chapter 6**, tissue adaptation algorithms are employed to introduce hierarchical features into metamaterial lattices, thereby enhancing their elastic properties and improving the energy distribution within such structures.

Chapter 7 summarizes and discusses the findings of this work and suggests an extended list of future research directions and applications for bitmap biomimetic composites.

References

[1]   P.J. Yang, J.S. Temenoff, Engineering orthopedic tissue interfaces, Tissue Eng. - Part B Rev. 15 (2009) 127–141. https://doi.org/10.1089/TEN.TEB.2008.0371/ASSET/IMAGES/LARGE/FIG-1.JPEG.

[2]   R. Dimitriou, E. Jones, D. McGonagle, P. V. Giannoudis, Bone regeneration: Current concepts and future directions, BMC Med. 9 (2011) 1–10. https://doi.org/10.1186/1741-7015-9-66/FIGURES/1.

[3]   D.C. Tapscott, C. Wottowa, Orthopedic Implant Materials, StatPearls Publishing, 2020. http://www.ncbi.nlm.nih.gov/pubmed/32809340 (accessed April 16, 2021).

[4]   U.G.K. Wegst, M.F. Ashby, The mechanical efficiency of natural materials, Philos. Mag. 84 (2004) 2167–2186. https://doi.org/10.1080/14786430410001680935.

[5]   T.M. Keaveny, E.F. Morgan, G.L. Niebur, O.C. Yeh, Biomechanics of Trabecular Bone, Annu. Rev. Biomed. Eng. 3 (2001) 307–333. https://doi.org/10.1146/annurev.bioeng.3.1.307.

[6]   S. Weiner, H.D. Wagner, THE MATERIAL BONE: Structure-Mechanical Function Relations, Https://Doi.Org/10.1146/Annurev.Matsci.28.1.271. 28 (2003) 271–298. https://doi.org/10.1146/ANNUREV.MATSCI.28.1.271.

[7]   R.O. Ritchie, The conflicts between strength and toughness, Nat. Mater. 10 (2011) 817–822. https://doi.org/10.1038/nmat3115.

[8]   T.D. White, G. WoldeGabriel, B. Asfaw, S. Ambrose, Y. Beyene, R.L. Bernor, J.R. Boisserie, B. Currie, H. Gilbert, Y. Haile-Selassie, W.K. Hart, L.J. Hlusko, F.C. Howell, R.T. Kono, T. Lehmann, A. Louchart, C.O. Lovejoy, P.R. Renne, H. Saegusa, E.S. Vrba, H. Wesselman, G. Suwa, Asa Issie, Aramis and the origin of Australopithecus, Nat. 2006 4407086. 440 (2006) 883–889. https://doi.org/10.1038/nature04629.

[9]   N. Smith, The Seven Ages of Materials, Eng. Technol. 14 (2019) 22–25. https://doi.org/10.1049/ET.2019.0900.

[10]   S.E. Naleway, M.M. Porter, J. McKittrick, M.A. Meyers, Structural Design Elements in Biological Materials: Application to Bioinspiration, Adv. Mater. 27 (2015) 5455–5476. https://doi.org/10.1002/adma.201502403.

[11]   C. Ortiz, M.C. Boyce, Materials science: Bioinspired structural materials, Science (80-.). 319 (2008) 1053–1054. https://doi.org/10.1126/science.1154295.

[12]   D. Bhate, C.A. Penick, L.A. Ferry, C. Lee, Classification and selection of cellular materials in mechanical design: Engineering and biomimetic approaches, Designs. 3 (2019) 1–31. https://doi.org/10.3390/designs3010019.

[13]   P. Fratzl, M.M.G. Guille, Hierarchy in Natural Materials, Hierarchically Struct. Porous Mater. From Nanosci. to Catal. Sep. Opt. Energy, Life Sci. (2011) 29–39. https://doi.org/10.1002/9783527639588.CH2.

[14]   D. Sen, M.J. Buehler, Structural hierarchies define toughness and defect-tolerance despite simple and mechanically inferior brittle building blocks, Sci. Rep. 1 (2011) 1–9. https://doi.org/10.1038/srep00035.

[15]   S. Weiner, L. Addadi, Design strategies in mineralized biological materials, J. Mater. Chem. 7 (1997) 689–702. https://doi.org/10.1039/a604512j.

1. Introduction

[16]   A.R. Studart, A.R. Studart, Towards High-Performance Bioinspired Composites, Adv. Mater. 24 (2012) 5024–5044. https://doi.org/10.1002/ADMA.201201471.

[17]   A.R. Studart, R. Libanori, R.M. Erb, Functional Gradients in Biological Composites, in: Bio-Bioinspired Nanomater., Wiley-VCH Verlag GmbH & Co. KGaA, Weinheim, Germany, 2014: pp. 335–368. https://doi.org/10.1002/9783527675821.ch13.

[18]   M.E. Launey, M.J. Buehler, R.O. Ritchie, On the Mechanistic Origins of Toughness in Bone, Http://Dx.Doi.Org/10.1146/Annurev-Matsci-070909-104427.   40   (2010)   25–53. https://doi.org/10.1146/ANNUREV-MATSCI-070909-104427.

[19]   D.E. Koshland, The Seven Pillars of Life, Science (80-.). 295 (2002) 2215–2216. https://doi.org/10.1126/SCIENCE.1068489.

[20]   R.O. Ritchie, Toughening materials: enhancing resistance to fracture, Philos. Trans. R. Soc. A. 379 (2021). https://doi.org/10.1098/RSTA.2020.0437.

[21]   U.G.K.K. Wegst, H. Bai, E. Saiz, A.P. Tomsia, R.O. Ritchie, Bioinspired structural materials, 14 (n.d.) 23–36. https://doi.org/10.1038/nmat4089.

[22]   P. Fratzl, Cellulose and collagen: from fibres to tissues, Curr. Opin. Colloid Interface Sci. 8 (2003) 32–39. https://doi.org/10.1016/S1359-0294(03)00011-6.

[23]   G.A. Holzapfel, R.W. Ogden, Mechanics of Biological Tissue, Springer Berlin Heidelberg, 2006. https://doi.org/10.1007/3-540-31184-X.

[24]   M.A. Meyers, P.Y. Chen, A.Y.M. Lin, Y. Seki, Biological materials: Structure and mechanical properties, Prog. Mater. Sci. 53 (2008) 1–206. https://doi.org/10.1016/j.pmatsci.2007.05.002.

[25]   X. Hu, P. Cebe, A.S. Weiss, F. Omenetto, D.L. Kaplan, Protein-based composite materials, Mater. Today. 15 (2012) 208–215. https://doi.org/10.1016/S1369-7021(12)70091-3.

[26]   A. Seidi, M. Ramalingam, I. Elloumi-Hannachi, S. Ostrovidov, A. Khademhosseini, Gradient biomaterials for soft-to-hard interface tissue engineering, Acta Biomater. 7 (2011) 1441–1451. https://doi.org/10.1016/j.actbio.2011.01.011.

[27]   H. Chai, J.J.-W. Lee, P.J. Constantino, P.W. Lucas, B.R. Lawn, Remarkable resilience of teeth, Proc. Natl. Acad. Sci. 106 (2009) 7289–7293. https://doi.org/10.1073/PNAS.0902466106.

[28]   S.P. Ho, S.J. Marshall, M.I. Ryder, G.W. Marshall, The tooth attachment mechanism defined by structure, chemical composition and mechanical properties of collagen fibers in the periodontium, Biomaterials. 28 (2007) 5238–5245. https://doi.org/10.1016/J.BIOMATERIALS.2007.08.031.

[29]   A.C. Deymier, Y. An, J.J. Boyle, A.G. Schwartz, V. Birman, G.M. Genin, S. Thomopoulos, A.H. Barber, Micro-mechanical properties of the tendon-to-bone attachment, Acta Biomater. 56 (2017) 25–35. https://doi.org/10.1016/J.ACTBIO.2017.01.037.

[30]   L. Rossetti, L.A. Kuntz, E. Kunold, J. Schock, K.W. Müller, H. Grabmayr, J. Stolberg-Stolberg, F. Pfeiffer, S.A. Sieber, R. Burgkart, A.R. Bausch, The microstructure and micromechanics of the tendon–bone insertion, Nat. Mater. 2017 166. 16 (2017) 664–670. https://doi.org/10.1038/nmat4863.

[31]   Y.X. Liu, S. Thomopoulos, V. Birman, J.S. Li, G.M. Genin, Bi-material attachment through a compliant interfacial system at the tendon-to-bone insertion site, Mech. Mater. 44 (2012) 83–92. https://doi.org/10.1016/J.MECHMAT.2011.08.005.

[32]   C. Pitta Kruize, S. Panahkhahi, N.E. Putra, P. Diaz-Payno, G. Van Osch, A.A. Zadpoor, M.J. Mirzaali, Biomimetic Approaches for the Design and Fabrication of Bone-to-Soft Tissue Interfaces,

ACS Biomater. Sci. Eng. (2021). https://doi.org/10.1021/ACSBIOMATERIALS.1C00620.

[33]   G. GM, T. S, The tendon-to-bone attachment: Unification through disarray, Nat. Mater. 16 (2017) 607–608. https://doi.org/10.1038/NMAT4906.

[34]   Y. Yang, X. Song, X. Li, Z. Chen, C. Zhou, Q. Zhou, Y. Chen, Y. Yang, X. Li, Y. Chen, X. Song, Z. Chen, Q. Zhou, C. Zhou, Recent Progress in Biomimetic Additive Manufacturing Technology: From Materials to Functional Structures, Adv. Mater. 30 (2018) 1706539. https://doi.org/10.1002/ADMA.201706539.

[35]   F. Libonati, M.J. Buehler, Advanced Structural Materials by Bioinspiration , Adv. Eng. Mater. 19 (2017) 1600787. https://doi.org/10.1002/adem.201600787.

[36]   A.R. Studart, Biological and Bioinspired Composites with Spatially Tunable Heterogeneous Architectures, Adv. Funct. Mater. 23 (2013) 4423–4436. https://doi.org/10.1002/adfm.201300340.

[37]   M.J. Mirzaali, V. Moosabeiki, S.M. Rajaai, J. Zhou, A.A. Zadpoor, Additive Manufacturing of Biomaterials—Design Principles and Their Implementation, Mater. 2022, Vol. 15, Page 5457. 15 (2022) 5457. https://doi.org/10.3390/MA15155457.

[38]   Z. Jin, Z. Zhang, K. Demir, G.X. Gu, Machine Learning for Advanced Additive Manufacturing, Matter. 3 (2020) 1541–1556. https://doi.org/10.1016/j.matt.2020.08.023.

[39]   D. Kokkinis, F. Bouville, A.R. Studart, 3D Printing of Materials with Tunable Failure via Bioinspired Mechanical Gradients, Adv. Mater. 30 (2018) 1705808. https://doi.org/10.1002/ADMA.201705808.

[40]   F. Libonati, V. Cipriano, L. Vergani, M.J. Buehler, Computational Framework to Predict Failure and Performance of Bone-Inspired Materials, ACS Biomater. Sci. Eng. 3 (2017) 3236–3243. https://doi.org/10.1021/ACSBIOMATERIALS.7B00606/SUPPL_FILE/AB7B00606_SI_001.PDF.

[41]   J. Wolff, Ueber die innere Architectur der Knochen und ihre Bedeutung für die Frage vom Knochenwachsthum, Arch. Für Pathol. Anat. Und Physiol. Und Für Klin. Med. 50 (1870) 389–450. https://doi.org/10.1007/BF01944490/METRICS.

[42]   H.F.R.S. Gray, Antomy of the human body, twentieth, Lippincott-Raven Publishers, Philadelphia and New York, 1918.

[43]   E.L. Doubrovski, E.Y. Tsai, D. Dikovsky, J.M.P. Geraedts, H. Herr, N. Oxman, Voxel-based fabrication through material property mapping: A design method for bitmap printing, CAD Comput. Aided Des. 60 (2015) 3–13. https://doi.org/10.1016/j.cad.2014.05.010.

[44]   Mirzaali, Nava, Gunashekar, Nouri-Goushki, Doubrovski, Zadpoor, Fracture Behavior of Bio-Inspired Functionally Graded Soft–Hard Composites Made by Multi-Material 3D Printing: The Case of Colinear Cracks, Materials (Basel). 12 (2019) 2735. https://doi.org/10.3390/ma12172735.

PART I

On the Interactions Between Soft and Hard Voxels

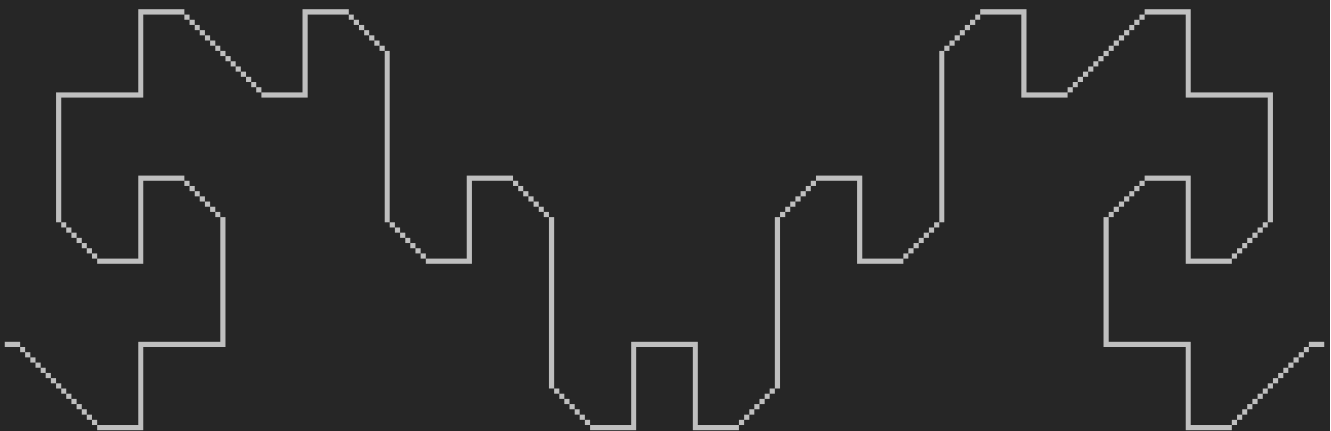*"Everything that lives is unique. It is unimaginable that two people, or two briar-roses, should be identical. If you attempt to erase the peculiarities and individuality of life, then life itself must suffocate."*

-Vasily Grossman, Life and Fate.

2

Rational positioning of 3D printed micro-bricks to realize high-fidelity, multi-functional soft-hard interfaces

2. Rational positioning of 3D printed micro-bricks to realize high-fidelity, multi-functional soft-hard interfaces

Abstract

Living organisms have developed design principles, such as functional gradients (FGs), to interface hard materials with soft ones (e.g., bone and tendon). Mimicking such design principles can address the challenges faced when developing engineered constructs with soft-hard interfaces. To date, implementing these FG design principles has been primarily performed by varying the ratio of the hard phase to that of the soft phase. Such design approaches, however, lead to inaccurate mechanical properties within the transition zone. That is due to the highly nonlinear relationship between the material distribution at the microscale and the macroscale mechanical properties. Here, we 3D print micro-bricks from either a soft or a hard phase and study the nonlinear relationship between their arrangements within the transition zone and the resulting macroscale properties. We carry out experiments at the micro- and macroscales as well as finite element simulations at both scales. Based on the obtained results, we develop a co-continuous power-law model relating the arrangement of the micro-bricks to the local mechanical properties of the micro-brick composites. We then use this model to rationally design FGs at the individual micro-brick level and create two types of biomimetic soft-hard constructs, including a specimen modeling bone-ligament junctions in the knee and another modeling the nucleus pulposus-annulus fibrosus interface in intervertebral discs. We show that the implemented FGs drastically enhance the stiffness, strength, and toughness of both types of specimens as compared to non-graded designs. Furthermore, we hypothesize that our soft-hard FGs regulate the behavior of murine preosteoblasts and primary human bone marrow-derived mesenchymal stromal cells (hBMSCc). We culture those cells to confirm the effects of soft-hard interfaces on cell morphology as well as on regulating the expression of focal adhesion kinase, subcellular localization, and YAP nuclear translocation of hBMSCs. Taken together, our results pave the way for the rational design of soft-hard interfaces at the micro-brick level and (biomedical) applications of such designs.

2.1. Introduction

Natural materials have developed smart design principles over millennia of evolution to interface materials with highly dissimilar mechanical properties (*e.g.*, a hard material like bone and a soft material like cartilage or tendon) [1,2]. These structural interfaces, commonly

known as functional gradients (FGs), exhibit specific mechanical property transition functions (*e.g.*, linear, power, exponential) [3,4] and are present in a vast array of biological systems, including the squid beak [5], dentinoenamel junction [6,7], bone-soft tissue insertion [8–10], and byssal thread [11]. The development of advanced materials with enhanced, mutually exclusive mechanical properties (*e.g.*, strength and toughness) are often inspired by such biomimetic design principles [12] to address challenges associated with the arising stress concentrations and the mismatch between the load-carrying capacities of both materials [13–16].

Recent progress in polymer-based multi-material additive manufacturing (AM, known as 3D printing) [17,18] has enabled the realization of FGs through several processes, such as material extrusion [19–23] and material jetting [24–26]. Among those techniques, voxel-based material jetting provides unparalleled freedom to design complex structures, thanks to its hallmark drop-on-demand capability [27,28]. Voxel-based design of soft-hard interfaces is then akin to the positioning of soft and hard micro-bricks with side lengths of, say, 40 μm next to each other to create a specific transition zone between 100% hard and 100% soft micro-bricks. Different variations of this technique have already been used to generate hierarchical and graded constructs with improved strength and toughness [29–31]. At the macroscale, however, we usually do not care about the exact organization of micro-bricks but would, instead, like to realize transition zones with specific variations in the mechanical properties. The studies performed to date have mainly analyzed such transition zones in terms of the ratio of the number of hard micro-bricks to that of soft micro-bricks without considering all the possible permutations of hard and soft micro-bricks [32–34]. Moreover, the relationship between the numbers of hard and soft micro-bricks and the realized macroscale properties is often assumed to be linear, neglecting its highly nonlinear nature. It has already been shown that such assumptions can lead to inaccurate estimations of effective mechanical behavior [35–37].

Here, we aim to establish nonlinear models that relate the positioning of micro-bricks to the actual values of the elastic modulus within the transition zone of FG soft-hard interfaces. We then use these models to create FG soft-hard interfaces with multiple types of functionalities. Our methodology combines experimental tools to characterize FGs through nanoindentation experiments at the microscale, quasi-static tensile tests analyzed with digital

image correlation (DIC) at the macroscale, with detailed finite element models at both scales. We showcase the applications of such FG soft-hard interfaces by: 1. rationally designing the soft-hard interfaces of two types of 3D printed biomimetic constructs, and 2. demonstrating that such transition zone can be used to regulate cell behavior. The biomimetic constructs include a bone-ligament junction of the knee and the nucleus pulposus-annulus fibrosus interface of an intervertebral disk. As for the second application, property-based FGs are shown to direct the migration (*i.e.*, durotaxis) and potential differentiation of living cells [38–42]. Here, we demonstrate that our micro-brick positioning approach can be used to regulate the behavior of murine preosteoblasts and human bone marrow-derived mesenchymal stromal cells (hBMSCs). Toward this aim, we analyzed the morphological differences, FAK expression, subcellular localization, and YAP nuclear translocation of primary hBMSCs across graded and non-graded specimens.

2.2 Results and discussion

2.2.1 Material characterization and modeling

Using voxel-based AM technology, we 3D printed two types of prismatic-shaped specimens with a linear gradient of hard material volume fraction (ρ) projected into their volume (Figure 2.1A-C). We used VeroCyan™ (Stratasys® Ltd., USA) UV-curable photopolymer as the hard phase for both specimens. For the soft material, however, we assigned Agilus30™ Clear (Stratasys® Ltd., USA) to the first specimen type and MED625FLX™ (Stratasys® Ltd., USA) to the second specimen type. We tested these specimens using a nanoindentation (NI) protocol [32,43] which allowed us to interrogate multiple locations within the FG transition zones, revealing the entire elastic behavior achievable by these composites (Figure 2.1B-E). Furthermore, the mechanical properties of several representative volumetric elements (RVEs) extracted from these specimens were simulated using the finite element method (FEM), which indicated a good agreement between the simulations and experimental results (Figure 2.1D-E).
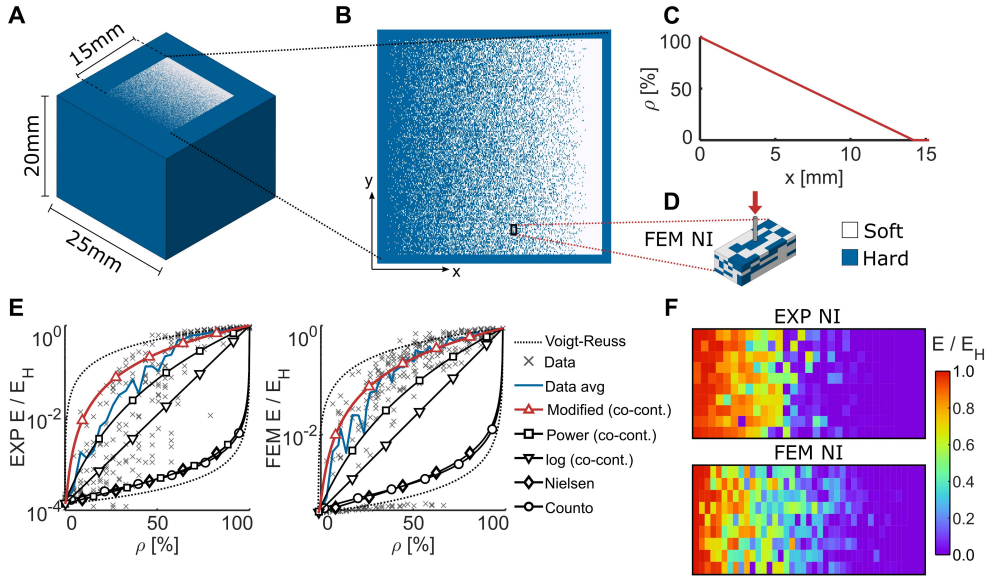
Figure 2.1. A) The design of the 3D printed specimen used for testing the properties of voxel-based composites via nanoindentation. B) A representative binary image of the nanoindentation specimens with a gradient of material properties projected onto their geometry. C) The ρ function applied to the specimen for measuring the properties of these composites across their entire property space. D) A representative volumetric element of a subsection of the nanoindentation specimens used to create FEM models of nanoindentation. E) The normalized elastic modulus *vs.* ρ and the corresponding average response (in blue) measured (EXP) through nanoindentation and predicted by computational models (FEM). These values and their associated trend lines are compared with several existing models for these composites. The modified co-continuous model was found to be the most accurate. F) The heatmap plots of the elastic moduli measured with nanoindentation and the corresponding FEM predictions across the FG specimens with a linear variation of ρ.

On average, the elastic modulus of the hard material, E_H, was 1994.7 ($\pm$74.89) MPa. The elastic moduli of the soft materials, E_S, were 0.507 ($\pm$ 0.171) MPa and 5.4282 ($\pm$ 2.72) MPa for Agilus and MED625FLX, respectively. For the linear gradient of ρ, both the experiments and simulations showed high variations in the local elastic response (Figure 2.1E and Figure S2.1A-B of the supporting information). The heterogeneous nature of the composites at the micro-brick (*i.e.*, voxel) scale caused these variations, which is the length scale probed during the NI tests (Figure 2.1F). Regardless of the local variations, the average response of both types of specimens showed a nonlinear transition of elastic modulus across the gradient, which contrasted with the linear transition in ρ. Moreover, the observed behaviors of both

types of specimens and their corresponding FEM estimations were remarkably similar (Figure S2.1C of the supporting information). These two observations confirmed the validity of the obtained data and allowed us to use them as input for the mechanical characterization of such 3D printed micro-brick arrangements.

Most of the predictions made by the classic models of particle-reinforced composites did not match the elastic response observed during our experiments and simulations. These models included those proposed by Nielsen [44], Counto [45], and the simplified power and logarithmic co-continuous models proposed by Davies [46] (Section S2.1 of the supporting information). Among these models, the simplified power-based co-continuous model was the most accurate. This observation is in line with the findings of a recent study performed on non-voxelated specimens with homogeneous distributions of ρ [43]. The residual plots of this model, however, highly increased for most ρ values (Figure S2.1 D-F of the supporting information). These high errors indicate that this version of the co-continuous model is insufficient for capturing the elastic behavior of the voxel-based composites studied here. We, therefore, generalized the power law-based co-continuous model as:

$$E^{1/\alpha} = E_H^{1/\alpha}\rho + E_S^{1/\alpha}(1 - \rho) \tag{1}$$

where E is the elastic modulus of the composite material. Similarly, α is a power law coefficient that determines the nonlinear behavior of the composite and depends on the geometrical arrangement of the micro-bricks, the ratio of the elastic modulus of both phases (E_H/E_S), and the particle joint probability function of the micro-brick arrangements [39]. After fitting this parameter with a bi-square nonlinear regression algorithm, we obtained $\alpha = 1.95$ (95% confidence interval, C.I. = 1.82 - 2.1) and $\alpha = 1.86$ (95% C.I. = 1.75 - 1.97) for the experiments on AgilusClear and MED625FLX, respectively. Similarly, we obtained $\alpha = 1.93$ (95% C.I. = 1.83 - 2.04) for the FEM simulations. The residual of different models strongly depended on ρ. For $\rho < 25\%$, higher residuals were observed, highlighting the complexity of capturing the behavior of composites when their mechanical behavior is dominated by the soft phase. Nevertheless, the nonlinear model proposed here achieved lower residual values across the entire design space of the micro-brick arrangements (Figure S2.1 D-E of the supporting information) as compared to the simplified power and logarithmic co-continuous models. We, therefore, proceeded to the evaluation of the

modified co-continuous model by designing FGs using the direct design of local elastic properties instead of designing the ratio of hard micro-bricks to that of soft micro-bricks.

2.2.2 Property-by-design of FGs

Generating three FGs with three different transition functions enabled us to evaluate the precision of the model (Equation 1). These FGs had linear ($E_{lin}(x)$), step-wise ($E_{ste}(x)$), and sigmoidal ($E_{sig}(x)$) functions (Figure 2.2), which were 3D printed using VeroCyan and AgilusClear. To generate their equivalent $\rho(x)$ functions, we used the inverse of Equation (1), which has the following form:

$$\rho(x) = \frac{E(x)^{1/\alpha} - E_S^{1/\alpha}}{E_H^{1/\alpha} - E_S^{1/\alpha}} \qquad (2)$$

where $E(x)$ is the desired FG function. For simplicity, we chose $\alpha = 2.0$ to design these FGs because this value was within the 95% C.I. of the nonlinear fitting results obtained for both experiments and simulations.

Similar to FGs with a linear ρ, we observed high variations in both experimentally obtained and FEM-predicted values of the local elastic moduli (Figure 2.2 A-C). The average behavior of the FGs was, however, highly correlated with the target elastic modulus functions (*i.e.*, R^2 > 92%), particularly for the sigmoid gradients (*i.e.*, R^2 > 98%, Figure 2.2C). Despite the higher number of estimation points for the simulations (*i.e.*, 1405 simulation points per FG and 320 experimental points per FG), the average response and standard deviation of both types of characterization techniques were similar. Although many factors can complicate the NI testing of polymeric materials (*e.g.*, adhesion and viscoelasticity), the strong similarity between NI and FEM suggests that the heterogeneous nature of the micro-brick composites is the main cause for the high standard deviations observed here. The mean trendlines of the elastic modulus of all the measurement groups resembled their corresponding designs except for the step-wise FG group, which despite having a high coefficient of determination (R^2 = 92.67%), substantially deviated from its design function. The deviations observed in the step-wise FG group can be explained by the fact that the size of each step in that group was smaller than the observed variations in the local elastic response.

2. Rational positioning of 3D printed micro-bricks to realize high-fidelity, multi-functional soft-hard interfaces
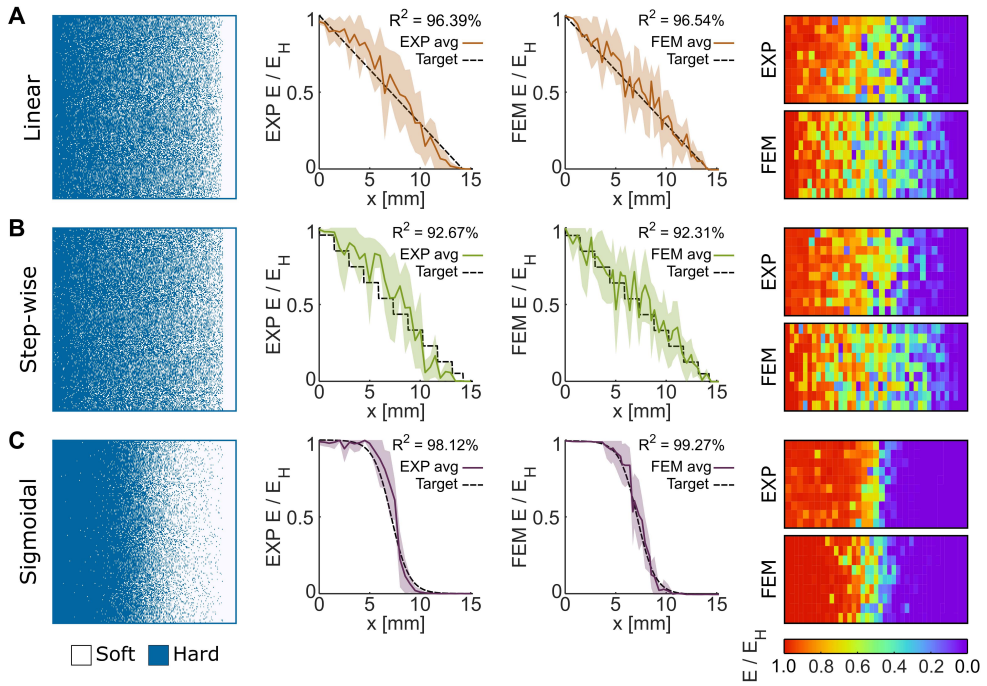
Figure 2.2. The measured and FEM-predicted nanoindentation results for various FG designs according to the modified co-continuous model. These tests were performed for the FGs with linear (A), step-wise (B), and sigmoidal (C) variations in the elastic modulus.

The NI experiments and their corresponding FEM simulations probed the properties of individual voxels and their close neighbors at the micrometer length scales. To assess how the microscale measurements relate to those performed at larger scales, we performed quasi-static tensile tests that measured the mechanical response of the specimens across the entire FG. We used digital image correlation (DIC) during those tests to measure the full-field strain distributions. We modeled the FGs as systems of linear springs subjected to tensile loading. To obtain the mesoscale spatial variation of the elastic modulus from the experimentally measured strains, we assumed that the local elastic modulus value along the x-coordinate, $E(x)$, is equivalent to the slope between the normal stress applied to the system ($\sigma = \frac{F}{A_o}$, $A_o = 32.512$ mm) and the average longitudinal (engineering) strains ($\epsilon_{p,avg}(x)$) of each cross-sectional layer of the FG ($E(x) = \sigma/\epsilon_{p,avg}(x)$).
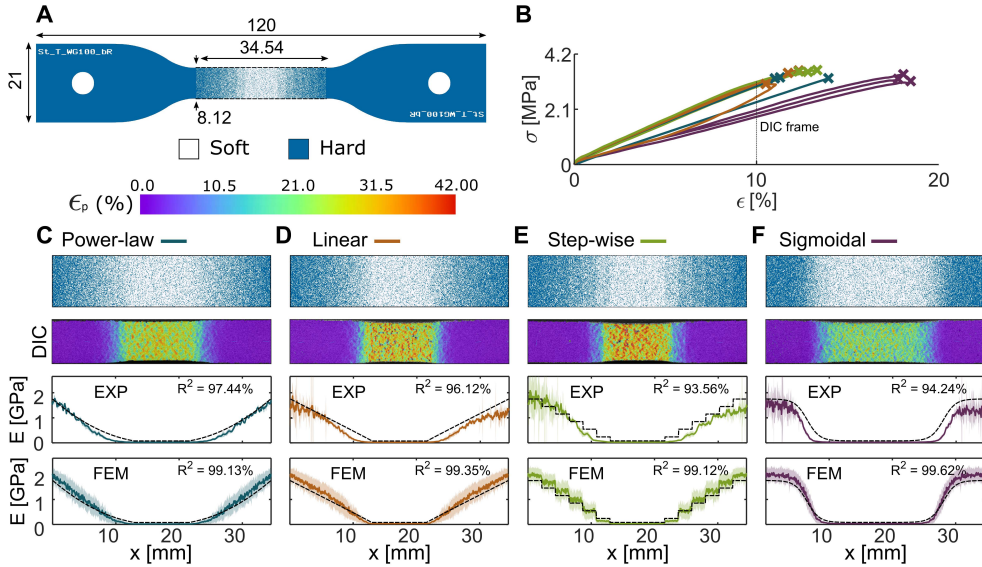
Figure 2.3. Additional FGs with different elastic modulus transition shapes, which were designed with the modified co-continuous model after idealizing the tensile test specimens under uniaxial deformations as systems of linear springs. A) A representative binary image of the tensile test specimens (out-of-plane thickness = 4 mm). The gauge region was designed with four symmetric FGs. We performed DIC measurements and FEM estimations to obtain the local deformations along the gradients. B) The stress-strain curves of the experiments. The FGs included those with power-law (C), linear (D), step-wise (E), and sigmoidal (F) changes in the elastic modulus.

The stresses measured for four groups of the tensile test specimens (*i.e.,* power-law, linear, step-wise, and sigmoidal) monotonically increased with the applied strain (Figure 2.3B). The sigmoidal design exhibited the most compliant response. The local distributions of the elastic modulus were determined by the underlying design functions ($R^2 > 93\%$) (Figure 2.3C-F). Similarly, the effective elastic moduli, $\hat{E}$, which is the equivalent modulus of the entire interface calculated from each $E(x)$ value along the gradient, strongly correlated with the elastic moduli measured from the general stress-strain curves, E_G ($R^2 = 95.76\%$, Table S2.1 of the supporting information). Despite their considerable standard deviations, the average elastic modulus across the linear, power, and sigmoid gradients followed their target elastic modulus functions, validating the possibility of generating accurate FGs. The mean $E(x)$ of the step-wise FG specimens, however, deviated from their corresponding design function. In fact, only the most compliant steps of these gradients were discernible. Two

21

factors might have caused the absence of stiffer steps. First, the 6 times larger facet size of the DIC recordings as compared to the micro-brick size has likely led to the averaging of strains in the regions where sharp step transitions were present, blurring the measured step feature. Second, partial resin mixing at the interface between the micro-bricks may have resulted in a gradual transition of the elastic properties across the steps, similar to what other studies have suggested [37,43,47,48]. In contrast, none of these effects were present when simplifying the outcome from the FEM estimations into systems of linear springs. The obtained mechanical properties of the simulations showed the highest coefficients of determination in this study (R^2 > 99 %), and the shapes of the gradients followed the expected gradient shapes. These results confirm that the deviations in the experimental measurements were due to the imaging resolution and potential material mixing effects. Therefore, these quasi-static tensile test experiments confirm that the presented model allows for the adjustment of the actual macroscale properties of voxel-based 3D printed FGs.

2.2.3. Tough biomimetic structures

We used the modified co-continuous model proposed and corroborated in the previous sections to explore the applications of FGs in the design of clinically relevant biomimetic structures. First, we considered the challenging problem of interfacing soft and hard tissues, such as ligaments and bones, tendons and bones, and cartilage and bone. Toward this end, we designed two different systems of knee ligaments and performed quasi-static tension experiments and FEM simulations (Figure 2.4A). In the first group, we incorporated a sigmoidal FG into the design of each ligament-bone connection (Figure 2.4B and Figure S2.3B of the supporting information). In the second group, however, we simply connected the soft and hard phases, effectively implementing a step function. The second group served as the control group (Figure 2.4C). The choice of sigmoidal functions was motivated by the results obtained in the above-presented tensile experiments and the fact that the strain distributions of these transition functions indicated a smooth transition between the hard and soft phases.
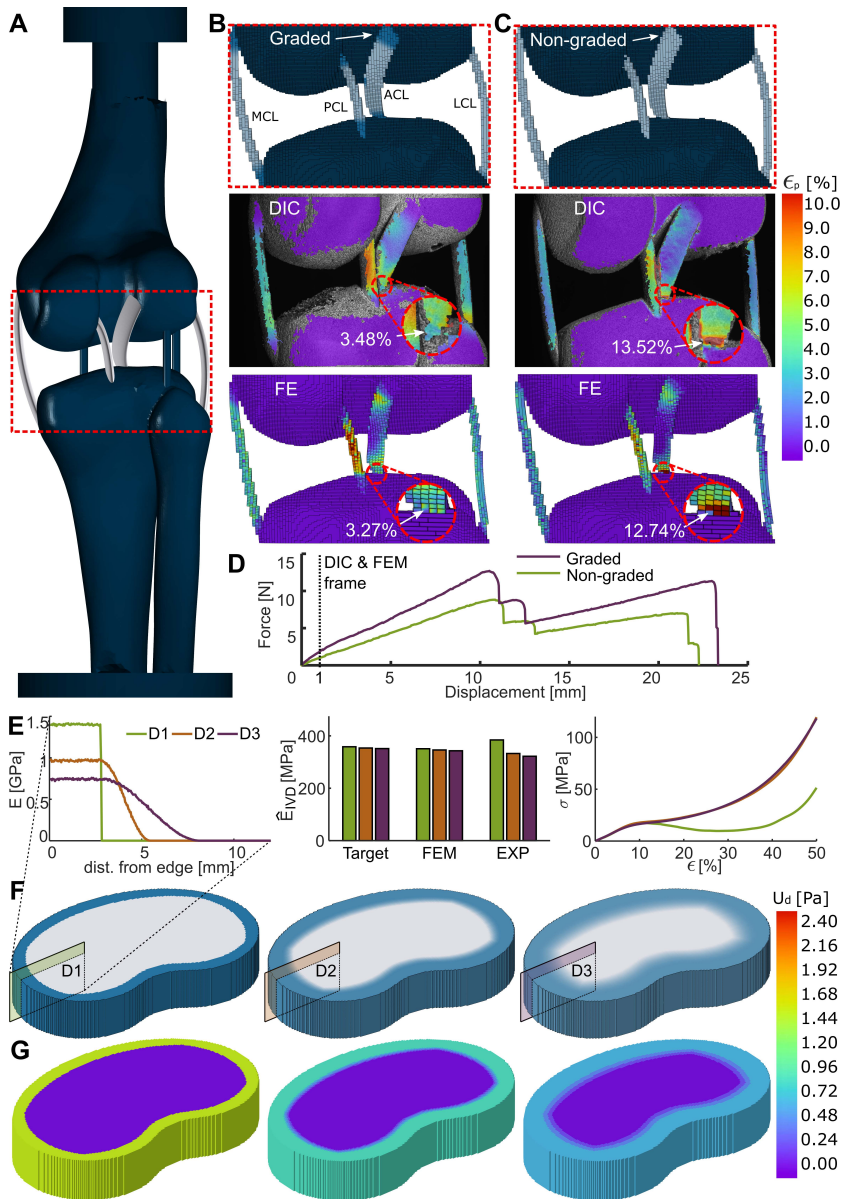
Figure 2.4. A case study where we implemented several strategies of functional grading to design biomimetic devices with enhanced strength and toughness. A) The design of a knee ligament system. B) graded and C) non-graded versions of this knee system were defined to study the failure mechanisms of the biomimetic bone-ligament connections through DIC measurements and FEM simulations. D) The force-displacement curves of both graded and non-graded designs. E) The different sinusoidal transition functions defined for each IVD design together with the resulting mechanical properties and stress-strain curves. F) The representative renders of each design after projecting the elastic modulus FGs onto each lamella of the IVD. G) The elastic strain energy density distributions resulting from the FEM simulations performed for all designs. The specimens were subjected to quasi-static compression.

2. Rational positioning of 3D printed micro-bricks to realize high-fidelity, multi-functional soft-hard interfaces

The non-graded (*i.e.*, control) design exhibited substantial strain concentrations at their soft-hard ligament interface, particularly within the ACL region (Figure 2.4C). This early onset of strain concentrations resulted in non-critical cracks for low displacements (Figure S2.3B of the supporting information). Furthermore, the FEM predictions revealed that shear deformations at the ligament-bone interface cause the inadequate performance of the non-graded design (Figure S2.3C of the supporting information). In contrast, the graded design showed lower strain values at the ligament-bone interfaces, indicating an improved distribution of stresses that led to a higher ultimate load before failure (Figure 2.4B). Moreover, the FEM simulations showed no substantial shear deformations in the graded system. These positive effects caused by the presence of FGs were reflected in the force-displacements curves of these experiments (Figure 2.4D). The graded structure was 1.3 times stiffer (*i.e.*, K_g = 1.09 N/mm *vs.* K_{ng} = 0.84 N/mm), 1.44 times stronger (*i.e.*, $F_{max,g}$ = 12.7 N *vs.* $F_{max,ng}$ = 8.82 N), and 1.55 times tougher (*i.e.*, U_g = 180.66 mJ *vs.* U_{ng} = 116.77 mJ) than the non-graded design. It can, therefore, be concluded that decreased stress concentrations at soft-hard interfaces and reduced shear deformations improve the overall mechanical performance of the biomimetic FG design as compared to a non-graded design.

The second biomimetic, clinically relevant construct was an intervertebral disc (IVD) with rationally designed elastic properties (Figure 2.4E). Although similar bioinspired structures have been introduced in the literature [20], the gradient strategy applied in that study consisted of a step-wise FG to transfer the failure mode from the nucleus pulposus (NP) to the edge of the annulus fibrosus (AF). Their applied design methodology, however, resulted in a lower toughness as compared to that of non-graded designs. To overcome this issue, we assumed that the vertical deformations of an IVD under compression occur at the same rate across its surface and that the construct fails once the lamella with the lowest ultimate strain fracture. For soft-hard micro-brick composites arranged in parallel as NP and AF, this failure will typically occur in the region with the highest number of stiff micro-bricks (*i.e.*, highest ρ value). We hypothesized that implementing an FG transition zone will reduce the interface stresses between the NP and AF. Moreover, we adjusted the maximum ρ value within the AF to be high enough to enable the construct to withstand physiological loads while remaining as low as possible to maximize its potential to store strain energy. Based on

these strategies, we defined different transition functions within IVDs to increase their overall toughness while maintaining the same effective elastic response.

To demonstrate the design freedom provided by the micro-bricks, we designed three types of specimens with three different gradient functions across the lamellae of the IVDs using sinusoidal elastic modulus functions. All the constructs were designed to have effective elastic moduli of around 350 MPa, which we calculated using Equation 1 under the assumption that IVDs behave like systems of parallel springs. Only the last two types of IVDs included an FG transition zone (Figure 2.4E). After manufacturing these specimens and testing them under quasi-static compression, we compared their actual elastic moduli, which were E_{D1} = 384.3 MPa, E_{D2} = 332.6 MPa, and E_{D3} = 322.1 MPa for the first to the final design, respectively. Since the elastic properties estimated with the FEM simulations were highly similar for all the designs (*i.e.*, $E_{D1,FEM}$ = 367.5 MPa, $E_{D2,FEM}$ = 357.1 MPa, and $E_{D3,FEM}$ = 359.3 MPa), we attributed the variations in the measurements to the overestimations that the corrected model yields for lower ρ values. Integrating a model correction based on the residual values of the co-continuous model may improve the precision of the designs and is suggested to be performed in future studies. Implementing a machine learning modeling approach may further minimize these errors. However, such a methodology would generally require a large number of experiments and simulations [49] and could betray the purpose of offering a simple and practical model.

The toughness values measured for both graded designs (*i.e.*, D2 and D3) were $\approx$ 2.4 times higher than that of the non-graded design (U_{D1} = 7.79 MPa, U_{D2} = 18.86 MPa, and U_{D3} = 19.05 MPa). The lower toughness of the non-graded design was caused by the sudden separation of the AF from the NP due to their stiffness mismatch (Figure S2.3D of the supporting information), leading to a critical stress drop at $\approx$ 27% strain. In contrast, the graded designs cracked around the annulus fibrosus but did not show critical separation between their phases, which resulted in their continuous hardening. These outcomes support the suitability of the approach chosen for implementing FG in the design of IVDs to improve their toughness. Moreover, these experiments further corroborated the property-by-design approach proposed in the current study that allows for the free adjustment and improvement of the mechanical properties of biomimetic structures for different applications.

2.2.4. Regulating cell behavior

We then moved to a smaller length scale and assessed the possibility of using soft-hard transition functions to regulate the behavior of living cells. More specifically, we hypothesized that we could use the local variations in the elastic modulus of the substrates created through the rational arrangement of micro-bricks to regulate the morphology and function of cells. The use of UV-curable photopolymers in combination with voxel-based additive manufacturing techniques in the biomedical field has been so far limited because the biocompatibility of commercially available UV-curable photopolymers has only been assessed for a few cell types [50,51]. One factor limiting the extensive use of these materials is the adverse effects their leachates have on cells [52,53]. Therefore, prior to the direct seeding of cells on these materials, we assessed the cytotoxicity of materials by exposing hBMSCs and cells from a murine preosteoblast cell line (MC3T3-E1) to the material leachates (Section S2.4ii of the supporting information). We did not observe a substantial number of dead cells in any of the conditions considered here. The live/dead images, however, showed limited proliferation of both MC3T3-E1 and BMSC (Figure S2.4B-C of the supporting information). The leachates from the soft material (*i.e.*, MED625FLX) inhibited proliferation more than those from the hard material (*i.e.*, VeroClear) (Figure S2.4D-E of the supporting information). For the direct cell cultures, a series of surface treatments consisting of grinding, protein coatings, and the combination thereof were first tested to improve the adhesion of the cells to the 3D printed soft-hard substrates (Sections S4iii, S1.5, and Figure S2.5 of the supporting information). We found that a combination of grinding (SiC abrasive paper, grain size = 5 μm) followed by fetal bovine serum (FBS) protein coating was the most efficient way to improve the cell adherence to the substrates for both hBMSC and MC3T3-E1 cells (Figure S2.5D-E of the supporting information).
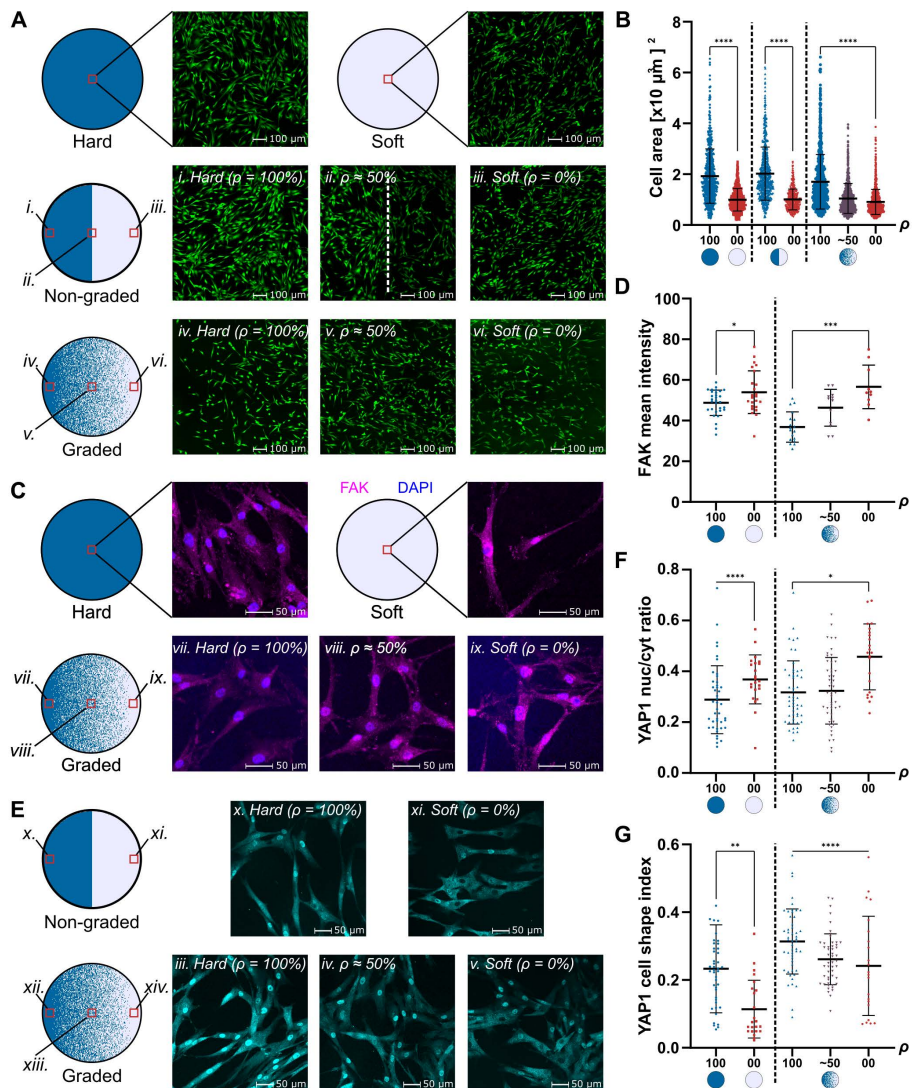
Figure 2.5. A) The live/dead images corresponding to the monolithically hard and soft, non-graded, and graded specimens. B) A scatter plot indicating the surface area of individual cells at the specified locations across the specimens. An intermediate average surface area value was present at the center of the graded specimens. C) The FAK immunofluorescence staining of the cells seeded on the monolithic and graded specimens. D) A scatter plot depicting the mean FAK intensity signal. An intermediate level (greater than the one for the hard material and less that of the soft material) was present at the center of the graded specimens. E) Representative images of YAP1 (cyan, visualized via immunofluorescent staining) of the cells adhering to the non-graded and graded specimens. F) and G) Quantification of the YAP1 nuclear/cytoplasmatic ratio and cell shape index of the cells adhering to the specimens. The data presented in each scatter plot indicates the value per single cell. Unpaired t-tests with the Welch's correction were performed to compare the ranks of the extremely hard and soft results. The significance of each comparison is marked with *, **, ***, or ****, which correspond to $p < 0.05$, 0.01, 0.001, and 0.0001, respectively.

2. Rational positioning of 3D printed micro-bricks to realize high-fidelity, multi-functional soft-hard interfaces

We first investigated the effects of the hard, soft, graded, and non-graded specimens on the morphology of hBMSC (*i.e.*, the area covered by each cell) after one day of direct culture (Figure 2.5A-B). The cell area on the non-graded soft-hard specimens and at the extremes of the graded specimens was similar to that of their respective monolithic materials, with a clear interface observed between the hard and soft phases on the non-graded specimens (Figure 2.5B). The mean cell area at the center of the FG specimens was an intermediate value between the values observed for the hard and soft phases, while the values corresponding to the soft and hard extremes were similar to those observed for the non-graded specimens. This finding should be interpreted taking into account the fact that the chemical leachate compositions of the graded and non-graded specimens were the same, meaning that the factor affecting the cell behavior is likely to be local.

To understand whether the adhesion to the different substrates would result in differential mechano-response, we evaluated the expression of focal adhesion kinase (FAK) by the hBMSC seeded on the graded and monolithic specimens through immunofluorescence staining (Figure 2.5C). FAK is part of integrin-mediated signal transduction and participates in the formation of focal adhesions between the cells and the substrate [54–57]. The FAK signal was more homogeneously distributed within the cells seeded on the hard material, implying a more uniform formation of focal adhesions within the hard substrate than in the soft one. As for the soft phase, the FAK signal was more intense and was concentrated around the cell nuclei (Figure S2.6 of the supporting information). Once again, the use of a graded substrate led to an intermediate level of FAK expression at the center of the specimens (Figure 2.5D). The mean intensity of FAK on the graded specimens increased gradually from the hard extreme to the soft one. Even though the regulation of FAK expression at the protein level cannot be easily attributed to single mechanical cues of the substrate, these results provide some insight into the potential effects of such soft-hard interfaces and the role of FG. More decisive conclusions, however, can only be drawn with a more thorough investigation in future studies.

Another fundamental factor in mechanosensing and mechanotransduction pathways is the Yes-associated Protein/transcriptional co-activator (YAP1/TAZ) factor [58]. Cell adhesion to substrates results in the assembly of actin fibers, which then transfer the cytoskeletal tension to the nuclei, opening mechanosensitive channels [59]. This process, in

turn, allows YAP translocation to the nucleus with enhanced nuclear translocation of YAP corresponding to increased tensile forces. We, therefore, evaluated the presence of this factor and assessed if changes in the mechanical properties of the specimens regulate the nuclear translocation of the hBMSC that were seeded on different types of specimens. The cells seeded on the non-graded specimens showed a different response to the hard and soft materials (Figure 2.5E). The cells seeded on the regions made of the hard phase had higher YAP1 nuclear to cytoplasmatic ratios than those seeded on the soft phase (Figure 2.5F). On the graded specimens, the nuclear to cytoplasmatic ratio increased with the presence of the hard phase, although variations existed between cells. The observation that nuclear to cytoplasmatic signal ratio is higher for stiffer materials than for more compliant ones has been reported in the literature [60], which corroborates our results. Furthermore, the YAP staining signal in the regions with mostly hard material was significantly different from those of mostly soft material for both the non-graded and the graded specimens ($p < 0.05$). Similarly, the cell shape index was, on average, lower for the cells seeded on the soft material than those seeded on the hard material for both graded and non-graded specimens (Figure 2.5G). This observation indicates that the cells residing on the soft material have a more circular shape than those on the hard material. Previous studies have shown that cells exposed to substrates with different stiffnesses tend to migrate toward regions with higher stiffness [61]. It could, therefore, be the case that the cells adhering to the central region of the graded specimens preferentially attach or locally migrate to the stiffer substrate, resulting in the mechanoresponse not being fully correlated with the local ratios of both phases. Nevertheless, the differences between the hard and soft phases in terms of YAP translocation to the nucleus of the cells suggest differential activation of mechanosensitive pathways, which have been shown to play a key role in controlling cell behavior, including growth, proliferation, and differentiation [54,58,62].

2.3. Conclusions

We developed a modified version of classic co-continuous models originally derived for particle-reinforced composites. These models are aimed at establishing a direct relationship between the arrangement of micro-bricks and the macroscale elastic behavior of multi-material 3D printed specimens with voxel-level FGs between their soft and hard phases. Using these models, FGs can be designed at the micro-brick level given the target function

describing the variation of the elastic properties between the hard and soft materials. Our experiments and computational models indicated a high degree of correlation between the model-based designs and the actual elastic properties ($R^2 > 90\%$) of such FGs as characterized by both nanoindentation and quasi-static tension tests. We then applied the developed model to design complex biomimetic systems (*i.e.*, knee ligaments and IVDs) with pre-programmed variations of elastic properties between their soft and hard phases. The biomimetic specimens incorporating FGs were at least 130% stronger and 140% tougher than their non-graded counterparts, indicating improved load transfer at their soft-hard interfaces. At the cell scale, our experiments supported the hypothesis that cell behavior can be guided by the selective deposition of hard and soft phases within a transition region. Our results, therefore, pave the way for the application of graded soft-hard interfaces fabricated by voxel-level 3D printing to various areas within biomedicine (*e.g.*, regenerative medicine and implantable medical devices). Future studies should focus on the characterization of the anisotropic response of soft-hard micro-brick arrangements by canvassing the space of all possible permutations of soft and hard micro-bricks. Moreover, more extensive studies should be performed to better understand how the arrangement of micro-bricks influences the mechanoresponse of cells. Finally, there is a need for more cytocompatible UV-curable photopolymers than can be used with the existing printers to create arbitrarily complex soft-hard interfaces at the voxel level.

2.4. Materials and methods

2.4.1. 3D printing

We fabricated all the specimens through multi-material poly-jet 3D printing (ObjetJ735 Connex3, Stratasys® Ltd., USA). The resolution of the printer (*i.e.*, 600×300 dpi in layers of 27 μm) enables a minimum micro-brick size of 42×84×27 μm³. The material deposition was controlled using a stack of binary images, which provided a voxel-by-voxel description of the deposition coordinates of both phases. The white bits within each of these stacks represented the location where the 3D printer created each type of micro-brick. We prepared the binary images with MATLAB (R2018b, Mathworks, USA) and processed the prints with GrabCAD Print (Stratasys® Ltd., USA). For most of the mechanical experiments, the hard and soft phases were made from the UV-curable photopolymers VeroCyan™ (RGD841, Stratasys® Ltd., USA) and Agilus30™ Clear (FLX935, Stratasys® Ltd., USA), respectively. The biocompatible

MED625FLX™ (Stratasys® Ltd., USA) was used as the soft phase in a single nanoindentation specimen with a linear ρ gradient and for all the biological experiments. Further details regarding the fabrication process are presented below.

2.4.2. Nanoindentation

Specimen design

To create the FGs, we discretized their $\rho(x)$ functions across the printing direction (*x*-direction, Figure 2.1A) at the maximum voxel resolution (*i.e.*, 42 μm/voxel). For each of the 355 points of the $\rho(x)$ function, we calculated the total number of hard micro-bricks (n_H) required to achieve their respective $\rho(x)$ value (*i.e.*, $n_H(x) = \rho(x) \times n_{layer}$, $n_{layer} = 177 \times 740$ voxels²) and randomly distributed them over the micro-bricks with the same x coordinate. We projected the resulting design at the center of cubic geometries (25×25×20 mm³) with the hard phase bounding the FGs. Additionally, the final 1 mm of every design was assigned with ρ = 0 %, which served as a reference for the nanoindentation procedure. The shape of the initial FG was a linear function of ρ ($\rho_{lin}(x) = -x/L_G + 100$), which was printed twice: once with Agilus Clear as the soft phase and the other with MED625FLX as the soft phase. These specimens were used for material characterization. Later, we defined three specimens with different elastic modulus functions. Their shapes were linear ($E_{lin}(x) = -(E_H - E_S)x/L_G + E_H$), step-wise (*i.e.*, $E_{step}(x)$, similar to $E_{lin}(x)$ but discretized in nine steps), and sigmoidal ($E_{sig}(x) = (E_H - E_S)/(1 + \exp(d(x - L_G/2))) + E_S$, $d = 8/9$ mm⁻¹), all with a gradient length of L_G = 14.8 mm. These latter specimens were used for validation. We used a water jet system (Genie 600, Gemini Cleaning Systems, UK) at 12 bar to remove the support material from the specimens.

Nanoindentation experiments

We used a TI 950 Triboindenter (Bruker, US) with a diamond conospherical probe with a tip radius of 20 μm to perform the nanoindentation experiments. We followed a previously-described polishing and nanoindentation protocol [32,43]. The nanoindentations were performed in a grid of 33 points along the *x*-direction and 10 points along the *y*-direction, yielding 330 experimental data points per FG. For each FG, the initial position of the nano-indenter was placed at the edge between the regions with only soft and only hard micro-bricks. The distance between successive test points was 500 μm in both directions. Whenever

the pull-off forces were >5% of the maximum load, we obtained the reduced elastic modulus (E_r) of each point using the JKR model [63]. For cases where the pull-off forces were <5% of the maximum load, we used the Oliver-Pharr model [64]. Finally, we calculated the associated elastic moduli (*i.e.*, $E(x) \approx E_r(1 - v(x)^2)$) by assuming the Poisson's ratio along the gradient ($v(x)$) to be described by the rule of mixtures between the hard and soft phases (*i.e.*, $v(x) = v_H \rho(x) + (1 - \rho(x))v_S$, $v_H = 0.4$, $v_S = 0.495$). For the linear ρ FG results, we compared the resulting elastic modulus functions against predictions made by several existing models for particle reinforced composites, including those proposed by Nielsen [44], Counto [45], and both simplified co-continuous models proposed by Davies (*i.e.*, power and logarithmic models) [46]. The comparison with these equations, which are described in detail in Section S2.1 of the supporting information, allowed us to obtain the most accurate model that fits our data. For obtaining the α value of the modified co-continuous model (Equation (1)), we performed a bisquare non-linear regression between all the available elastic moduli of the linear ρ function and their corresponding values of the hard micro-bricks volume fraction. For the linear, step-wise, and sigmoid $E(x)$ functions, we calculated the coefficients of determination (ordinary R^2 values) between the measured data and the designed functions to validate the accuracy of the selected characterization model.

FEM simulations of the nanoindentation experiments

We used a commercial software suite (Abaqus Standard v.6.14, Dassault Systèmes Simulia, France) to perform the FEM simulations of the nanoindentation experiments. Each model was built using a grid of representative volumetric elements (RVEs) taken from 39 positions along the *x*-direction and 9 positions along the *y*-direction (Figure 2.1B). After a mesh convergence study (Section S2.1.2 and Figure S2.2A of the supporting information), each RVE included a matrix of 6×6×6 micro-bricks. Each micro-brick was discretized using a cluster of 6×6×6 linear hexahedral elements (C3D8H). We simplified the indenter probe as a cylindrical rigid body defined as a rigid analytic shell with a radius (R_p) of 6.25 μm. We performed four simulations per RVE to account for the nano-indenter position during the tests. In these simulations, the indenter was randomly positioned above the centermost half of the mesh. This process resulted in 1404 simulations per FG. We defined the elastic properties of every hard (*i.e.*, $E_H = 2000$ MPa, $v_H = 0.4$) and soft (*i.e.*, $E_S = 0.87$ MPa, $v_S = 0.495$) element based on the NI experimental results. The Poisson's ratio of both

materials and the elastic modulus of the soft phase were obtained from the quasi-static tensile tests performed on monolithic materials (Figure S2.2B-C of the supporting information). We constrained all the degrees of freedom of the bottom and lateral regions of every mesh. For the probe, we prescribed an indentation depth (h) of 1 μm and recorded its respective reaction forces (RF) for each simulation. We calculated the reduced elastic modulus ($E_r = \sqrt{\pi}\, RF/(2\, h\, \sqrt{A_p}\,), A_p = \pi\, R_p^2$) and used the Poisson's ratios of the RVEs (*i.e.*, $v = v_H \rho(x) + v_S(1 - \rho(x))$) to estimate the elastic modulus ($E = E_r\,(1 - v(x)^2)$) for every simulation.

2.4.2. Tensile tests

Tensile mechanical tests

First, we prepared monolithic specimens made of only hard and only soft micro-bricks according to the description of type IV specimens in ASTM D638-14 standard [65]. These specimens allowed us to characterize the elastic properties of these materials when loaded in the printing direction. Furthermore, we designed four elastic moduli FGs to validate the accuracy of the corrected characterization models under quasi-static tensile conditions. The shapes of the FGs were a power-law (*i.e.*, $E_{pow}(x) = (E_{max} - E_{min})((L_G - x)/L_G)^2 + E_{min}$), linear (*i.e.*, $E_{lin}(x) = -(E_{max} - E_{min})/L_G + E_{max}$), step (*i.e.*, $E_{step}(x)$, similar to $E_{lin}(x)$ but discretized using 9 equally spaced steps), and sigmoid ($E_{sig}(x) = (E_{max} - E_{min})/(1 + \exp(d(x - L_G/2))) + E_{min}, d = 8/9$ mm^{-1}), all with $L_G = 12.2$ mm. We symmetrically projected these FGs onto the gauge region of the specimens, with their centermost 8.13 mm defined by E_{min} (Figure 2.3A). We defined E_{max} = 1750 MPa and E_{min} = 75 MPa for all these FGs. The $\rho(x)$ functions were obtained using Equation (2) with $\alpha = 2$, $E_S = 0.87$ MPa, and $E_H = 2650$ MPa (E_H and E_S were obtained from tensile tests performed on monolithic specimens). We manufactured each design threefold and removed the support material using a water jet system (Genie 600, Gemini Cleaning Systems, UK) at 12 bar. We tested the specimens using an LR5K mechanical testing machine (LLOYD, USA) with a 5 kN load cell at a rate of 2 mm×min^{-1}. We recorded the local deformations of the specimens during the tests using a DIC system (Q-400 2x 12 MPixel, LIMESS GmbH, Krefeld, Germany) that captured the surface of the specimens with a frequency of 1 Hz. These measurements required applying a black dot speckle pattern over a white paint background on each specimen. We calculated the first principal (true) strain distributions with the Instra

2. Rational positioning of 3D printed micro-bricks to realize high-fidelity, multi-functional soft-hard interfaces

4D v4.6 (Danted Dynamics A/S, Skovunde, Denmark) software and the DIC measurements. Furthermore, we generated the general stress-strain curves across time (t) using the engineering stress $(\sigma(t) = f(t)/A_0, A_0 = 32.512 \text{ mm}^2)$ and engineering strain vectors, $\epsilon(t)$, measured using a digital extensometer within Instra 4D. From these curves, we measured the general elastic modulus of each tensile test specimen, E_G, from the slope of a fitted polynomial of order one. To calculate the elastic modulus along the x-direction, $E(x)$, we fitted polynomials using the average longitudinal (engineering) strains ($\epsilon_{avg}(x,t)$) of each x-position and the engineering stress vectors. All the slopes were obtained between stresses of 0.2 and 15 MPa. We then averaged the $E(x)$ results for three repetitions of each FG and calculated the corresponding coefficients of determinations (ordinary R^2 values) between the experimental results and the FG designs. We further validated this method of measuring $E(x)$ by calculating the effective elastic modulus $\hat{E}$ of each test using the equivalent equation for the systems of linear springs ($\hat{E} = W_G \left(\int_0^{W_G} dx/E(x) \right)^{-1}$, where W_G is the total length of the DIC recording region) and by comparing them to the elastic moduli measured from the general stress-strain curves (E_G).

FEM simulations of the tensile tests on FG specimens

We modeled one-half of the gauge section of the tensile test specimens with a cross-section of 24×24 micro-bricks and discretized them with linear hexahedral elements (C3D8H). The resulting meshes consisted of 235008 elements. Given these considerations, we prescribed symmetric boundary conditions at the symmetric end (*i.e.,* at the center plane of the soft region) of the design and at two of its lateral surfaces. We also prescribed a uniaxial displacement of 0.26 mm at the hard end of the mesh (equivalent to 1.5% uniaxial strain) while restraining its remaining degrees of freedom. The elastic properties were defined using the tensile test data obtained using the monolithic specimens (*i.e.,* $E_H = 2650 \text{ MPa}, \nu = 0.4$ for the hard phase and $E_S = 0.87 \text{ MPa}, \nu_S = 0.495$ for the soft phase). After processing the simulations, we extracted the reaction forces at the hard end of the FG and the main principal strains at the centroid of every element of the mesh. We performed the same procedure described for the experimental tensile tests to obtain the estimated $E(x)$ functions of every FG and to calculate their coefficients of determination (ordinary R^2- values) *vs.* the designed functions.

2.4.3. Design, testing, and FEM simulation of knee ligament systems

The geometry of the knee-ligament system was adapted from an open-source CAD database [66]. It consisted of a femur, a tibia, and a fibula (153 mm long) with the respective anterior cruciate (ACL, 15 mm long), posterior cruciate (PCL, 20 mm long), lateral collateral (LCL, 30 mm long), and medial collateral (MCL, 35 mm long) ligaments (Figure 2.5A). From this assembly, we generated two designs. The first one had FGs between the bone-ligament interfaces. The second design, which worked as our control, was not graded and had abrupt material transitions. The material assignment of both structures was generated with MATLAB (R218b, Mathworks, USA). The FGs of the first design had a sigmoid transition function with $L_G = 1.5$ mm. To attach the structures to the tensile testing machine, we integrated three cylinders between the femur and tibia regions, which we cut before testing. After removing the support material with a water jet (Genie 600, Gemini Cleaning Systems, UK) at 12 bar, we applied a black dot speckle pattern to a white paint background to measure the system's deformations with the DIC system. We tested the assemblies under the same conditions as the tensile tests. Furthermore, we built FEM models of both test configurations after reducing their voxel resolution to greyscale RVEs covering 6×6×6 of the original voxels. We discretized each RVE as a single element (C3D8) and assigned its mechanical properties based on its average ρ after using Equation (1). We constrained all the degrees of freedom at the bottom surface of the tibial bone. Similarly, we constrained all the degrees of freedom at the top surface of the femur mesh except for the vertical displacement, which was defined as 1 mm. We compared the resulting strain fields of these simulations with the results of the DIC measurements.

2.4.4. Design, testing, and FEM simulation of graded IVDs

We based the dimensions of the IVDs on the L4L5 disc [67] and generated the design with SolidWorks 2021 SP2.0 (Dassault Systèmes, France). The major axis was 49.7 mm, with a minor axis of 31.83 mm and a height of 8.42 mm. After voxelizing the design using MATLAB R2018, we generated three different IVD systems. These IVDs had different sinusoidal FG functions that connected the AF and NP regions (Section S2.3 of the supporting information). To discretize these functions, we partitioned the IVDs into concentric lamellae and assigned their respective ρ value. The three designs were calculated to have an equivalent elastic modulus of 350 MPa after considering the IVDs as systems of

parallel springs (Figure 2.4E). After printing these designs and removing the support material with a water jet (Genie 600, Gemini Cleaning Systems, UK) at 12 bar, we tested them under uniaxial compression with a mechanical testing machine (Load cell = 100 kN, Zwick Z100, Germany) and using a stroke rate of 2 mm×min^{-1}. The stresses and strains were calculated from the loadcell readings and the corresponding crosshead displacements. To obtain more accurate elastic modulus (E_{IVD}) values, we printed additional specimens of each design and tested them with the same LR5K testing machine (5 kN load cell). The local deformations were measured using the above-described DIC system. Based on these results, we defined a digital extensometer around the centermost part of the IVDs to calculate the average vertical strains of each specimen. Then, we obtained E_{IVD} from the slope of the linear region of the stress-strain recordings (*i.e.*, between the stress values $\sigma = 3$ MPa and 4 MPa). We compared these measurements with the values predicted by the FE models of these designs, which were built using the same discretization conditions as for the knee ligament constructs. However, each RVE had 3×3×3 voxels, and the simulations were performed under a uniaxial compression equivalent to 5% strain.

2.4.5. Cell culture experiments

3D printed specimens

We designed and 3D printed four types of disk-shaped specimens (*i.e.*, with a diameter of 9.75 mm and an out-of-plane thickness of 2 mm) to perform the cell culture experiments. Two of these were made of purely hard (*i.e.*, VeroClear™, Stratasys® Ltd., USA) and purely soft (*i.e.*, MED625FLX™, Stratasys® Ltd., USA) materials. The other two were designed as non-graded and graded multi-material configurations. The non-graded design had a sharp interface at the center of the disk, with one side of the specimen made only of the hard micro-bricks and the other printed from the soft micro-bricks. The graded design had a linear ρ FG analogous to the FG of the initial nanoindentation characterizations.

Specimen preparation for direct cell seeding

After 3D printing the specimens, the support material was removed from the printed specimens using a water jet (Genie 600, Gemini Cleaning Systems, UK) at 12 bar. Further removal of support material residuals was done by submerging the specimens in isopropanol under sonication (5510, Branson, UK) for 30 min. Thereafter, the specimens were surface

treated by grinding and subsequent FBS coatings, as described in Section S2.5 of the supporting information.

Cell viability and FAK analyses

Human BMSC (Lonza, 19TL155677) were thawed and plated at 6000 cells/cm^2 in an expansion culture medium containing a basal alpha minimum essential medium (alpha-MEM,22571), 10% (v/v) fetal bovine serum (FBS, Hyclone), 100 U/mL penicillin, 100 μg/mL streptomycin, and 10 mM 4-(2-hydroxyethyl)-1-piperazineethanesulfonic acid (HEPES), supplemented with 1 ng/mL of fibroblast growth factor 2 (all from Thermo Fisher Scientific). The culture medium was renewed every two days. Upon reaching 80% confluency, the cells were detached from plastic using 0.05% trypsin-EDTA solution (Thermo Fisher Scientific, USA). At passage three, 104 BMSC suspended in 300 μL (33000 cells/mL) were seeded directly onto the specimens and were kept at 37 °C in a 5% CO_2 incubator for 2 h. Then, the medium was changed to remove the unadhered cells. The specimens were kept in culture for 48 h, with medium renewal after 24 h, and were then harvested for cell viability and FAK analysis.

Cell viability was analyzed using live/dead assays (LIVE/DEAD® Viability/Cytotoxicity Kit, Thermo Fisher, USA). After removing the culture medium and washing the cells two times with Phosphate-Buffered Saline (PBS, ThermoFisher), we stained the live and dead cells using 2 mM ethidium homodimer-1 and 5 mM calcein-AM for 15 min at room temperature. Then, the solution was removed, and the cells were washed twice with PBS. Finally, the cells were imaged with a ZOE fluorescent cell imager (Bio-Rad, The Netherlands).

For the FAK immunofluorescence staining, BMSC were fixed for 10 min with 2% paraformaldehyde and washed twice with PBS. The cells were permeabilized with 0.5% Triton X-100 for 5 min, followed by 1-hour blocking of non-specific binding sites with PBS with 5%v/v bovine serum albumin (BSA) (Sigma Aldrich) at room temperature. The cells were then incubated with FAK primary mouse monoclonal antibody (1:200, AHO1272, Thermo Fisher Scientific) dissolved in PBS with 1% BSA for 1 hour at room temperature. The specimens were subsequently washed three times with PBS and were incubated with a secondary fluorescent goat anti-mouse AlexaFluor647-conjugate (A21235, ThermoFisher Scientific) at a dilution of 1:1000 in the blocking solution of PBS containing 1% BSA together with 300 nM DAPI nuclei staining. After 1 hour of incubation at room temperature, the

specimens were washed with PBS and were stored at 4 °C until the images were taken using a confocal microscope (Leica- SP8, Leica, Germany) using a 20× air-dry objective.

YAP analysis

Human bone marrow-derived mesenchymal stromal cells (BMSC) isolated from the surplus bone chips from the iliac crest of a donor (age = 9 years, male) undergoing alveolar bone graft surgery were obtained with the approval of the Medical Ethics Committee of Erasmus MC (MEC-2014-16). The cells were isolated through plastic adherence and were expanded in α-MEM, supplemented with 10% v/v FBS, 1.5 µg/ml fungizone, 50 µg/ml Gentamicin (all Thermo Fisher Scientific, Welthon, MA, USA), 25 µg/ml L-ascorbic acid 2-phosphate (Sigma Aldrich, St. Luis, MO, USA), and 1 ng/ml fibroblast growth factor 2 (Instruchemie, Delfzjil, Netherlands) in a humidified atmosphere at 37 °C with 5% of CO_2 up to passage 4. 104 BMSC suspended in 300 µL (33000 cells/mL) were seeded directly onto the specimens and were kept at 37 °C in a 5% CO_2 incubator. The samples were kept in culture for 48 h in a culture medium containing alpha -MEM supplemented with 10% v/v of FBS 1.5 µg/ml fungizone, 50 µg/ml Gentamicin, and 25 µg/ml L-ascorbic acid 2-phosphate.

For the YAP immunofluorescence staining, the cells were fixated using 4% paraformaldehyde (Boomlap, Meppel, Netherlands) for 10 min, were washed twice with PBS, and were kept in PBS at 4 °C until further processing. To stain the cells, they were permeabilized with 0.5% Triton X-100 for 5 min, followed by blocking the non-specific binding sites with PBS supplemented with 1%v/v bovine serum albumin (BSA) (Sigma Aldrich, St. Luis, MO, USA). The cells were then incubated with primary antibody rabbit anti-YAP1 (1: 500, AB52771, Abcam, Cambridge, UK) dissolved in PBS with 1% BSA for 1 hour. A rabbit Igg isotype (X0903, Agilent Technologies, Santa Clara, CA, USA) was used as the negative control. The specimens were washed three times with PBS and were incubated with secondary fluorescent antibody goat anti-rabbit (1:1000, AB150077, ABCAM, Cambridge, UK) dissolved in PBS with 1% BSA for 1 h at room temperature. The nuclei staining was done using Hoechst dye 33542 (1:2000, Thermo Fisher Scientific, Welthon, MA, USA) for 5 min, followed by two washing steps with PBS 1% with BSA. Finally, the specimens were kept in PBS and were stored in the dark at 4 °C until imaging. Images were taken with a confocal microscope (Leica- SP8, Leica, Germany) using a 20× air-dry objective.

Image analysis

All the images were processed using Fiji (version 1.53q, a distribution of ImageJ2, USA). The quantification of the mean FAK and YAP signal intensity, as well as the cell surface area and shape index, were performed using an in-house macro for the Fiji software. To analyze the surface area of the cells based on the live/dead images, the borders of the cells were automatically selected based on thresholding. The same process was applied manually for the FAK and YAP signal intensity analyses because the background signal was too high. The cell shape index (CSI) was calculated from the cytoplasm results of every manually selected cell from the YAP analysis. This index was defined as $CSI = \frac{4\pi A}{P^2}$, where A and P represent the area and perimeter of the cell, respectively. A CSI value of 1 indicates that the cell is entirely circular, while zero indicates a straight line. The scatter plots of the cell area were created based on 400-500 selected cells for each experimental condition. For the FAK and YAP plots, at least 10 cells were selected to perform the analysis, mainly among the isolated cells that were not overlapping or connected to other cells.

Statistical analyses of images

Statistical analyses were performed for the cell surface area, FAK mean signal intensity, and YAP1 nuclei to cytoplasmic ratio using Prism (version 9.4.1, GraphPad Software, USA). Scatter plots were obtained from each corresponding evaluation, where the respective mean and standard deviations were included. For every analysis, we performed unpaired *t*-tests without assuming equal standard deviations (*i.e.*, Welch's correction) to compare the ranks of the results corresponding to the hard and soft materials. We indicated the significance of each comparison with *, **, ***, or ****, which correspond to $p < 0.05$, 0.01, 0.001, and 0.0001.

2. Rational positioning of 3D printed micro-bricks to realize high-fidelity, multi-functional soft-hard interfaces

References

[1]   S.E. Naleway, M.M. Porter, J. McKittrick, M.A. Meyers, Structural Design Elements in Biological Materials: Application to Bioinspiration, Adv. Mater. 27 (2015) 5455–5476. https://doi.org/10.1002/adma.201502403.

[2]   Z. Liu, M.A. Meyers, Z. Zhang, R.O. Ritchie, Functional gradients and heterogeneities in biological materials: Design principles, functions, and bioinspired applications, Elsevier Ltd, 2017. https://doi.org/10.1016/j.pmatsci.2017.04.013.

[3]   A.E. Giannakopoulos, S. Suresh, Indentation of solids with gradients in elastic properties: Part I. Point force, Int. J. Solids Struct. 34 (1997) 2357–2392. https://doi.org/10.1016/S0020-7683(96)00171-0.

[4]   S. Suresh, Graded materials for resistance to contact deformation and damage, Science (80-.). 292 (2001) 2447–2451. https://doi.org/10.1126/SCIENCE.1059716/ASSET/04A3403E-4A23-4FDA-9FB3-407247772966/ASSETS/GRAPHIC/SE2519535004.JPEG.

[5]   A. Miserez, T. Schneberk, C. Sun, F.W. Zok, J.H. Waite, The Transition from Stiff to Compliant Materials in Squid Beaks, Science (80-.). 319 (2008) 1816–1819. https://doi.org/10.1126/SCIENCE.1154117.

[6]   G.W. Marshall, M. Balooch, R.R. Gallagher, S.A. Gansky, S.J. Marshall, Mechanical properties of the dentinoenamel junction: AFM studies of nanohardness, elastic modulus, and fracture, (2000). https://doi.org/10.1002/1097-4636.

[7]   S.P. Ho, S.J. Marshall, M.I. Ryder, G.W. Marshall, The tooth attachment mechanism defined by structure, chemical composition and mechanical properties of collagen fibers in the periodontium, Biomaterials. 28 (2007) 5238–5245. https://doi.org/10.1016/J.BIOMATERIALS.2007.08.031.

[8]   L. Rossetti, L.A. Kuntz, E. Kunold, J. Schock, K.W. Müller, H. Grabmayr, J. Stolberg-Stolberg, F. Pfeiffer, S.A. Sieber, R. Burgkart, A.R. Bausch, The microstructure and micromechanics of the tendon–bone insertion, Nat. Mater. 2017 166. 16 (2017) 664–670. https://doi.org/10.1038/nmat4863.

[9]   A. Tits, D. Ruffoni, Joining soft tissues to bone: Insights from modeling and simulations, Bone Reports. 14 (2021) 100742. https://doi.org/10.1016/j.bonr.2020.100742.

[10]   C. Pitta Kruize, S. Panahkhahi, N.E. Putra, P. Diaz-Payno, G. Van Osch, A.A. Zadpoor, M.J. Mirzaali, Biomimetic Approaches for the Design and Fabrication of Bone-to-Soft Tissue Interfaces, ACS Biomater. Sci. Eng. (2021). https://doi.org/10.1021/ACSBIOMATERIALS.1C00620.

[11]   J.H. Waite, H.C. Lichtenegger, G.D. Stucky, P. Hansma, Exploring Molecular and Mechanical Gradients in Structural Bioscaffolds†, Biochemistry. 43 (2004) 7653–7662. https://doi.org/10.1021/BI049380H.

[12]   A.R. Studart, Biological and Bioinspired Composites with Spatially Tunable Heterogeneous Architectures, Adv. Funct. Mater. 23 (2013) 4423–4436. https://doi.org/10.1002/adfm.201300340.

[13]   R.D. Adams, J. Coppendale, N.A. Peppiatt, Stress analysis of axisymmetric butt joints loaded in torsion and tension:, Http://Dx.Doi.Org/10.1243/03093247V131001. 13 (1978) 1–10. https://doi.org/10.1243/03093247V131001.

[14]   R. Balokhonov, V. Romanova, ON THE PROBLEM OF STRAIN LOCALIZATION AND FRACTURE SITE PREDICTION IN MATERIALS WITH IRREGULAR GEOMETRY OF

INTERFACES, Facta Univ. Ser. Mech. Eng. 17 (2019) 169–180. https://doi.org/10.22190/FUME190312023B.

[15]   M.N. Saleh, M. Saeedifar, D. Zarouchas, S.T. De Freitas, Stress analysis of double-lap bi-material joints bonded with thick adhesive, Int. J. Adhes. Adhes. 97 (2020) 102480. https://doi.org/10.1016/J.IJADHADH.2019.102480.

[16]   R. Lopes Fernandes, S. Teixeira de Freitas, M.K. Budzik, J.A. Poulis, R. Benedictus, Role of adherend material on the fracture of bi-material composite bonded joints, Compos. Struct. 252 (2020) 112643. https://doi.org/10.1016/J.COMPSTRUCT.2020.112643.

[17]   E. Pei, I.R. Kabir, D. Godec, J. Gonzalez-Gutierrez, A. Nordin, Functionally graded additive manufacturing, Addit. Manuf. with Funct. Nanomater. (2021) 35–54. https://doi.org/10.1016/B978-0-12-823152-4.00006-5.

[18]   W. Gao, Y. Zhang, D. Ramanujan, K. Ramani, Y. Chen, C.B. Williams, C.C.L. Wang, Y.C. Shin, S. Zhang, P.D. Zavattieri, The status, challenges, and future of additive manufacturing in engineering, CAD Comput. Aided Des. 69 (2015) 65–89. https://doi.org/10.1016/j.cad.2015.04.001.

[19]   S.E. Bakarich, R. Gorkin, R. Gately, S. Naficy, M. in het Panhuis, G.M. Spinks, 3D printing of tough hydrogel composites with spatially varying materials properties, Addit. Manuf. 14 (2017) 24–30. https://doi.org/10.1016/j.addma.2016.12.003.

[20]   D. Kokkinis, F. Bouville, A.R. Studart, 3D Printing of Materials with Tunable Failure via Bioinspired Mechanical Gradients, Adv. Mater. 30 (2018) 1705808. https://doi.org/10.1002/ADMA.201705808.

[21]   L. Ren, Z. Song, H. Liu, Q. Han, C. Zhao, B. Derby, Q. Liu, L. Ren, 3D printing of materials with spatially non-linearly varying properties, Mater. Des. 156 (2018) 470–479. https://doi.org/10.1016/J.MATDES.2018.07.012.

[22]   D.T. Nguyen, T.D. Yee, N.A. Dudukovic, K. Sasan, A.W. Jaycox, A.M. Golobic, E.B. Duoss, R. Dylla-Spears, D.T. Nguyen, T.D. Yee, N.A. Dudukovic, K. Sasan, A.W. Jaycox, A.M. Golobic, E.B. Duoss, R. Dylla-Spears, 3D Printing of Compositional Gradients Using the Microfluidic Circuit Analogy, Adv. Mater. Technol. 4 (2019) 1900784. https://doi.org/10.1002/ADMT.201900784.

[23]   S. Hasanov, A. Gupta, A. Nasirov, I. Fidan, Mechanical characterization of functionally graded materials produced by the fused filament fabrication process, J. Manuf. Process. 58 (2020) 923–935. https://doi.org/10.1016/J.JMAPRO.2020.09.011.

[24]   E. Salcedo, D. Baek, A. Berndt, J.E. Ryu, Simulation and validation of three dimension functionally graded materials by material jetting, Addit. Manuf. 22 (2018) 351–359. https://doi.org/10.1016/J.ADDMA.2018.05.027.

[25]   M.A. Skylar-Scott, J. Mueller, C.W. Visser, J.A. Lewis, Voxelated soft matter via multimaterial multinozzle 3D printing, Nature. 575 (2019) 330–335. https://doi.org/10.1038/s41586-019-1736-8.

[26]   S. Kumar, S. Tan, L. Zheng, D.M. Kochmann, Inverse-designed spinodoid metamaterials, Npj Comput. Mater. 6 (2020) 1–10. https://doi.org/10.1038/s41524-020-0341-6.

[27]   E.L. Doubrovski, E.Y. Tsai, D. Dikovsky, J.M.P. Geraedts, H. Herr, N. Oxman, Voxel-based fabrication through material property mapping: A design method for bitmap printing, CAD Comput. Aided Des. 60 (2015) 3–13. https://doi.org/10.1016/j.cad.2014.05.010.

2. Rational positioning of 3D printed micro-bricks to realize high-fidelity, multi-functional soft-hard interfaces

[28]   C. Bader, D. Kolb, J.C. Weaver, S. Sharma, A. Hosny, J. Costa, N. Oxman, Making data matter: Voxel printing for the digital fabrication of data across scales and domains, Sci. Adv. 4 (2018). https://doi.org/10.1126/sciadv.aas8652.

[29]   G.X. Gu, L. Dimas, Z. Qin, M.J. Buehler, Optimization of Composite Fracture Properties: Method, Validation, and Applications, J. Appl. Mech. Trans. ASME. 83 (2016). https://doi.org/10.1115/1.4033381.

[30]   D.W. Abueidda, M. Almasri, R. Ammourah, U. Ravaioli, I.M. Jasiuk, N.A. Sobh, Prediction and optimization of mechanical properties of composites using convolutional neural networks, Compos. Struct. 227 (2019) 111264. https://doi.org/10.1016/j.compstruct.2019.111264.

[31]   M.J. Mirzaali, M. Cruz Saldívar, A. Herranz de la Nava, D. Gunashekar, M. Nouri-Goushki, E.L. Doubrovski, A.A. Zadpoor, Multi-Material 3D Printing of Functionally Graded Hierarchical Soft–Hard Composites, Adv. Eng. Mater. 22 (2020) 1901142. https://doi.org/10.1002/adem.201901142.

[32]   M.J. Mirzaali, A. Herranz de la Nava, D. Gunashekar, M. Nouri-Goushki, R.P.E. Veeger, Q. Grossman, L. Angeloni, M.K. Ghatkesar, L.E. Fratila-Apachitei, D. Ruffoni, E.L. Doubrovski, A.A. Zadpoor, Mechanics of bioinspired functionally graded soft-hard composites made by multi-material 3D printing, Compos. Struct. 237 (2020) 111867. https://doi.org/10.1016/J.COMPSTRUCT.2020.111867.

[33]   M.C. Saldivar, E.T.W. Shen, E.L. Doubrovski, M.J. Mirzaali, A.A. Zadpoor, Bioinspired rational design of multi-material 3D printed soft-hard interfaces, (2022). https://doi.org/10.48550/arxiv.2206.13615.

[34]   M.C. Saldívar, E.L. Doubrovski, M.J. Mirzaali, A.A. Zadpoor, Nonlinear coarse-graining models for 3D printed multi-material biomimetic composites, Addit. Manuf. 58 (2022) 103062. https://doi.org/10.1016/J.ADDMA.2022.103062.

[35]   N.A. Meisel, D.A. Dillard, C.B. Williams, Impact of material concentration and distribution on composite parts manufactured via multi-material jetting, Rapid Prototyp. J. 24 (2018) 872–879. https://doi.org/10.1108/RPJ-01-2017-0005/FULL/PDF.

[36]   A. Aghaei, N. Bochud, G. Rosi, Q. Grossman, D. Ruffoni, S. Naili, Ultrasound characterization of bioinspired functionally graded soft-to-hard composites: Experiment and modeling, J. Acoust. Soc. Am. 151 (2022) 1490. https://doi.org/10.1121/10.0009630.

[37]   L. De Noni, L. Zorzetto, F. Briatico-Vangosa, M. Rink, D. Ruffoni, L. Andena, Modelling the interphase of 3D printed photo-cured polymers, Compos. Part B Eng. 234 (2022) 109737. https://doi.org/10.1016/J.COMPOSITESB.2022.109737.

[38]   A. Shellard, R. Mayor, Durotaxis: The Hard Path from In Vitro to In Vivo, Dev. Cell. 56 (2021) 227–239. https://doi.org/10.1016/J.DEVCEL.2020.11.019.

[39]   A. Isomursu, K.-Y. Park, J. Hou, B. Cheng, M. Mathieu, G.A. Shamsan, B. Fuller, J. Kasim, M.M. Mahmoodi, T.J. Lu, G.M. Genin, F. Xu, M. Lin, M.D. Distefano, J. Ivaska, D.J. Odde, Directed cell migration towards softer environments, Nat. Mater. 2022. (2022) 1–10. https://doi.org/10.1038/s41563-022-01294-2.

[40]   T. Kawano, S. Kidoaki, Elasticity boundary conditions required for cell mechanotaxis on microelastically-patterned gels, Biomaterials. 32 (2011) 2725–2733. https://doi.org/10.1016/J.BIOMATERIALS.2011.01.009.

[41]   G. Charras, E. Sahai, Physical influences of the extracellular environment on cell migration, Nat. Rev. Mol. Cell Biol. 2014 1512. 15 (2014) 813–824. https://doi.org/10.1038/nrm3897.

[42]   P.U. Shirke, H. Goswami, V. Kumar, D. Shah, S. Beri, S. Das, J. Bellare, S. Mayor, K. V. Venkatesh, J.R. Seth, A. Majumder, "Viscotaxis"- directed migration of mesenchymal stem cells in response to loss modulus gradient, Acta Biomater. (2021). https://doi.org/10.1016/J.ACTBIO.2021.08.039.

[43]   L. Zorzetto, L. Andena, F. Briatico-Vangosa, L. De Noni, J.M. Thomassin, C. Jérôme, Q. Grossman, A. Mertens, R. Weinkamer, M. Rink, D. Ruffoni, Properties and role of interfaces in multimaterial 3D printed composites, Sci. Reports 2020 101. 10 (2020) 1–17. https://doi.org/10.1038/s41598-020-79230-0.

[44]   L.E. Nielsen, L.A. Wre, " Ce, E. Nielsen, Generalized Equation for the Elastic Moduli of Composite Materials, J. Appl. Phys. 41 (1970) 4626. https://doi.org/10.1063/1.1658506.

[45]   U.J. Counto, The effect of the elastic modulus of the aggregate on the elastic modulus, creep and creep recovery of concrete, Http://Dx.Doi.Org/10.1680/Macr.1964.16.48.129. 16 (1964) 129–138. https://doi.org/10.1680/MACR.1964.16.48.129.

[46]   W.E.A. Davies, The theory of elastic composite materials, J. Phys. D. Appl. Phys. 4 (1971) 1325. https://doi.org/10.1088/0022-3727/4/9/313.

[47]   F. Liu, T. Li, X. Jiang, Z. Jia, Z. Xu, L. Wang, The effect of material mixing on interfacial stiffness and strength of multi-material additive manufacturing, Addit. Manuf. 36 (2020) 101502. https://doi.org/10.1016/J.ADDMA.2020.101502.

[48]   D.W. Abueidda, M. Bakir, R.K. Abu Al-Rub, J.S. Bergström, N.A. Sobh, I. Jasiuk, Mechanical properties of 3D printed polymeric cellular materials with triply periodic minimal surface architectures, Mater. Des. 122 (2017) 255–267. https://doi.org/10.1016/j.matdes.2017.03.018.

[49]   Z. Jin, Z. Zhang, K. Demir, G.X. Gu, Machine Learning for Advanced Additive Manufacturing, Matter. 3 (2020) 1541–1556. https://doi.org/10.1016/j.matt.2020.08.023.

[50]   Y.W. Chen, H.Y. Fang, M.Y. Shie, Y.F. Shen, The mussel-inspired assisted apatite mineralized on PolyJet material for artificial bone scaffold, Int. J. Bioprinting. 5 (2019) 83–88. https://doi.org/10.18063/IJB.V5I2.197.

[51]   E.R. Currens, M.R. Armbruster, A.D. Castiaux, J.L. Edwards, R.S. Martin, Evaluation and optimization of PolyJet 3D-printed materials for cell culture studies, Anal. Bioanal. Chem. 414 (2022). https://doi.org/10.1007/S00216-022-03991-Y/FIGURES/5.

[52]   R.P. Rimington, A.J. Capel, D.J. Player, R.J. Bibb, S.D.R. Christie, M.P. Lewis, Feasibility and Biocompatibility of 3D-Printed Photopolymerized and Laser Sintered Polymers for Neuronal, Myogenic, and Hepatic Cell Types, Macromol. Biosci. 18 (2018) 1800113. https://doi.org/10.1002/MABI.201800113.

[53]   C.G.Y. Ngan, C.D. O'Connell, R. Blanchard, M. Boyd-Moss, R.J. Williams, J. Bourke, A. Quigley, P. McKelvie, R.M.I. Kapsa, P.F.M. Choong, Optimising the biocompatibility of 3D printed photopolymer constructs in vitro and in vivo, Biomed. Mater. 14 (2019) 035007. https://doi.org/10.1088/1748-605X/AB09C4.

[54]   R.G. Wells, The role of matrix stiffness in regulating cell behavior, Hepatology. 47 (2008) 1394–1400. https://doi.org/10.1002/HEP.22193.

[55]   T. Wang, S.S. Nanda, G.C. Papaefthymiou, D.K. Yi, Mechanophysical Cues in Extracellular Matrix Regulation of Cell Behavior, ChemBioChem. 21 (2020) 1254–1264. https://doi.org/10.1002/CBIC.201900686.

[56]   E. Urciuoli, B. Peruzzi, Involvement of the FAK Network in Pathologies Related to Altered Mechanotransduction, Int. J. Mol. Sci. 21 (2020) 1–12. https://doi.org/10.3390/IJMS21249426.

[57]   J. Cornillon, L. Campos, D. Guyotat, J. Cornillon, L. Campos, D. Guyotat, Focal adhesion kinase (FAK), une protéine aux fonctions multiples, Médecine/Sciences. 19 (2003) 743–752. https://doi.org/10.1051/MEDSCI/20031967743.

[58]   S. Dupont, L. Morsut, M. Aragona, E. Enzo, S. Giulitti, M. Cordenonsi, F. Zanconato, J. Le Digabel, M. Forcato, S. Bicciato, N. Elvassore, S. Piccolo, Role of YAP/TAZ in mechanotransduction, Nature. 474 (2011) 179–184. https://doi.org/10.1038/NATURE10137.

[59]   G. Brusatin, T. Panciera, A. Gandin, A. Citron, S. Piccolo, Biomaterials and engineered microenvironments to control YAP/TAZ-dependent cell behaviour, Nat. Mater. 17 (2018) 1063–1075. https://doi.org/10.1038/S41563-018-0180-8.

[60]   S.R. Caliari, S.L. Vega, M. Kwon, E.M. Soulas, J.A. Burdick, Dimensionality and spreading influence MSC YAP/TAZ signaling in hydrogel environments, Biomaterials. 103 (2016) 314–323. https://doi.org/10.1016/J.BIOMATERIALS.2016.06.061.

[61]   C.M. Lo, H.B. Wang, M. Dembo, Y.L. Wang, Cell Movement Is Guided by the Rigidity of the Substrate, Biophys. J. 79 (2000) 144–152. https://doi.org/10.1016/S0006-3495(00)76279-5.

[62]   A.J. Engler, S. Sen, H.L. Sweeney, D.E. Discher, Matrix Elasticity Directs Stem Cell Lineage Specification, Cell. 126 (2006) 677–689. https://doi.org/10.1016/J.CELL.2006.06.044.

[63]   J.C. Kohn, D.M. Ebenstein, Eliminating adhesion errors in nanoindentation of compliant polymers and hydrogels, J. Mech. Behav. Biomed. Mater. 20 (2013) 316–326. https://doi.org/10.1016/J.JMBBM.2013.02.002.

[64]   W.C. Oliver, G.M. Pharr, An improved technique for determining hardness and elastic modulus using load and displacement sensing indentation experiments, J. Mater. Res. 7 (1992) 1564–1583. https://doi.org/10.1557/JMR.1992.1564.

[65]   ASTM D638, ASTM D638 - 14 Standard Test Method for Tensile Properties of Plastics, ASTM Stand. (2004). https://www.astm.org/Standards/D638 (accessed September 28, 2021).

[66]   Knee joint, (2020). https://www.thingiverse.com/thing:4283166/attribution_card (accessed April 8, 2021).

[67]   S.H. Zhou, I.D. McCarthy, A.H. McGregor, R.R.H. Coombs, S.P.F. Hughes, Geometrical dimensions of the lower lumbar vertebrae – analysis of data from digitised CT images, Eur. Spine J. 2000 93. 9 (2000) 242–248. https://doi.org/10.1007/S005860000140.

2.5 Supporting information

S2.1. Characterization of voxel-based particle-reinforced composites

We evaluated the ability of several models available in the literature to predict the elastic modulus of micro-brick composites. These models included those proposed by Nielsen [1], Counto [2], and two simplified co-continuous models proposed by Davies (*i.e.,* power-based and logarithmic-based) [3] and are formulated as follows:

Nielsen [1]
$$E = \frac{1 + A\,B\,\rho}{1 - \psi\,B\,\rho}$$

$$For: A = k_e - 1; \quad B = \frac{\frac{E_H}{E_S} - 1}{\frac{E_H}{E_S} + A}; \quad k\_e = 2.5 \tag{S1}$$

Counto [2]
$$E = \left(\frac{1 - \sqrt{\rho}}{E_S} + \frac{1}{\frac{E_S(1 - \sqrt{\rho})}{\sqrt{\rho}} + E_H} \right)^{-1} \tag{S2}$$

Davies (ln) [3]
$$E = \exp(\rho \ln(E_H) + (1 - \rho)\ln(E_S)) \tag{S3}$$

Davies (power) [3]
$$E = \left(\rho E_H^{1/5} + (1 - \rho)E_S^{1/5} \right)^5 \tag{S4}$$

where A, B, and k_e are model parameters, ρ is the volume ratio of the hard material, and E_H, E_S, and E are the elastic moduli of the hard, soft, and composite material, respectively. Additionally, we evaluated a modified version of Equation (S3), where we replaced the fixed exponential with a parameter α, taking the form:

Co-continuous
(modified)
$$E = \left(\rho E_H^{1/\alpha} + (1 - \rho)E_S^{1/\alpha} \right)^{\alpha} \tag{S5}$$

We determined this α parameter through curve fitting using a bisquare non-linear regression algorithm. We evaluated these five models against the NI experimental data (*i.e.,* for AgilusClear and MedFLX625 as soft material) and the estimated FEM nanoindentation data. These evaluations were performed by obtaining the residual plots for the three best-performing models (Figures S1.1 D-F).

2. Rational positioning of 3D printed micro-bricks to realize high-fidelity, multi-functional soft-hard interfaces

S2.2. Mesh convergence test

We carried out a mesh convergence study prior to the FEM simulations of the NI experiments. More specifically, we evaluated how many micro-bricks per representative volumetric element (RVE) and how many elements per micro-brick were required to accurately model the mechanical behavior of our micro-brick composites. We, therefore, simulated RVEs under the same conditions as described in the main text, where only hard material properties were assumed (E_H = 2000 MPa). The selected RVE matrix sizes were 2×2×2, 4×4×4, and 6×6×6 micro-bricks per RVE. Furthermore, we subdivided each micro-brick into arrays of 1×1×1, 2×2×2, 4×4×4, or 6×6×6 C3D8H elements (*i.e.,* equivalent to 1, 8, 64, 216 total elements per micro-brick). Combining these two parameters resulted in 12 discretizations, each of which we simulated 4 times after varying the initial position of the indenter randomly within the top side of the RVE. According to this study (Figure S2.2A), the error of our simulations was the smallest (*i.e.,* 2.46%) when each RVE consisted of 6×6×6 micro-bricks and each micro-brick was represented by 6×6×6 (*i.e.,* 216) elements.

S2.3. Elastic modulus functions for the intervertebral disc designs

We partitioned the voxelated 3D image of the IVD into 182 concentric lamellae (n_l = 182). This partitioning allowed us to define the elastic modulus functions (E_l) in terms of each lamella (*l*) with three distinct regions (*i.e.,* the annulus fibrosus AF, the FG region, and the nucleus pulposus NP) using the following expression:

$$E_l = \begin{cases} E_{AF} & ; & l < l_{AF} \\ \dfrac{E_{AF} - E_{NP}}{2}\left(1 + \cos\left(\dfrac{l - l_{AF}}{l_{FG}}\pi\right)\right) & ; & l_{AF} \leq l < l_{AF} + l_{FG} \\ E_{NP} & ; & l_{AF} + l_{FG} \leq l \end{cases} \tag{S6}$$

where E_{AF} and E_{NP} are the elastic moduli of the AF and NP, respectively. l_{AF} and l_{FG} are the numbers of the lamellae that define AF and FG regions, respectively. Since the objective was to tune the elastic properties of the IVDs by assuming they behave like systems of parallel springs, we estimated the elastic response of the IVD ($\hat{E}_{IVD}$) as:

$$\hat{E}_{IVD} = \frac{1}{A_{IVD}}\sum_{l=1}^{N_l} A_l E_l \tag{S7}$$

where A_l and A_{IVD} are the surface areas of each lamella and the IVD, respectively. We designed three different IVDs with this approach (*i.e.,* with l_G = 1, 32, and 64 lamellae) and

tuned the E_{AF} value of Equation (3) to obtain an E_{IVD} of 350 MPa with an E_{NP} of 0.87 MPa and an l_{AF} of 33 lamellae. After this parametrization process, we calculated the equivalent ρ_l for each E_l using Equation (2) and assuming E_S = 0.87 MPa and E_H = 2000 MPa.

S2.4. Biocompatibility analysis of voxel-based materials

i. Materials and Methods:

MC3T3-E1 cell preculture: MC3T3-E1 cells (Sigma Aldrich, Germany) were plated at 4000 cells/cm^2 in alpha minimum essential medium (alpha-MEM) supplemented with 10% (v/v) fetal bovine serum (FBS) and 1% (v/v) penicillin-streptomycin. The medium was refreshed every two days. Upon reaching 80% confluency, the cells were detached and used for indirect or direct seeding. To analyze the cytotoxicity of the material leachates, we cultured both BMSC and MC3T3-E1 cells in the extracts of both hard and soft materials. These were prepared by the immersion of the printed, cleaned, and sterilized specimens in 48 well-plates with 1 mL of culture medium. After 24 h of conditioning at 37 °C, the medium from each well was collected, pooled together, and immediately used for cell culture. The medium was changed daily with the medium from the same batch of the conditioned medium that was stored at 4 °C until the test time.

DNA quantification assay: 10^4 cells were initially seeded in 24 well-plates cultured in the hard and soft material extracts (conditioned medium) to assess their effects on the proliferative potential of the cell. After three days of culture, the medium was removed, and the cells were washed and freeze-dried overnight. The cell number was then calculated using the CyQUANT˚ Cell Proliferation Assay Kit (Invitrogen) according to the provider's protocol. Briefly, the cell lysis buffer was diluted 20X in distilled water and was used to dilute CyQUANT˚ GR stock solution 400X. 200 μL of the final solution was added to each well, and fluorescence measurements were performed using a microplate reader with an excitation wavelength of 485 nm and emission detection at 530 nm. A reference standard curve was also created separately for both BMSC and MC3T3-E1 according to the providers' protocol for converting the fluorescence values into cell numbers.

Surface grinding and protein coating: For the preliminary direct seeding experiments, we tested four different protein coatings: fibronectin bovine plasma (Sigma-Aldrich, USA), collagen (CellAdhere™ Type I Collagen, STEMCELL, USA), medium 10% fetal bovine serum

2. Rational positioning of 3D printed micro-bricks to realize high-fidelity, multi-functional soft-hard interfaces

(FBS, Qualified, One shot, Gibco, Thermo Fisher Scientific, USA), and 100% (pure) FBS. The medium composition for each cell type is presented in the main text. Before coating, we placed the specimens in 48 well-plates (Greiner, Bio-One, The Netherlands). For the fibronectin group, we coated each specimen with 500 µL of the fibronectin solution (50 µg/mL in PBS). For the collagen group, we used 500 µL of collagen (STEMCELL, USA) (50 µg/mL in deionized water). For the other two groups, we added 500 µL of culture medium containing 10% FBS or pure FBS to each specimen. After keeping the specimens at room temperature for 2 h, we removed the excess solution from all the specimens.

SEM imaging: The cell-seeded specimens were fixated, followed by a dehydration step that consisted of a series of sub-steps: washing with MilliQ water for 10 min, 50% ethanol for 15 min, 70% ethanol for 20 min, and 96% ethanol for 20 min. Then, we soaked the specimens in hexamethyldisilazane (Sigma Aldrich, USA) for 15 min and left them to dry in the open air overnight. A scanning electron microscope (SEM, JEOL JSM-IT100, Japan) was used to acquire the images. The specimens were gold-sputtered prior to SEM analysis.

ii. Indirect seeding and leachate analysis:

We analyzed the cytotoxicity of the leachates obtained from the UV-curable materials. We performed this task by exposing the BMSC and the MC3T3-E1 cells to material-extracted substances for up to 3 days. On days 1 and 3, the metabolic activity of the cells, the number of the cells, and their viability were determined.

The live/dead results showed few dead cells in all the conditions (Figure S2.4B-C). The culturing of the MC3T3-E1 cells in the extracts from the hard material caused the cells to exhibit 78% of the metabolic activity of the control group on day 3 (Figure S2.4D). As for the soft material, the viability decreased to 16% on day 3 (Figure S2.4E). The DNA quantification results indicated that the leachates of the soft material decreased the proliferation potential of the MC3T3-E1 and BMSCs more significantly than the hard material ($p < 0.01$).

iii. Direct seeding and protocol development:

The BMSC and MC3T3 cells were seeded directly on the printed substrates (Figure S2.5). Only a few cells adhered to the surface of the untreated specimens after 24 h (Figure S2.5B). To enhance the number of adhered cells, we smoothened the surface topography of the printed substrates by grinding them with two different SiC abrasive papers (grain size of

10 and 5 um). In addition, we tested the effects of four different protein coatings (*i.e.,* fibronectin, collagen, culture medium containing 10% FBS, and pure FBS). Among the tested protein coatings, the medium containing 10% FBS increased the number of cells that adhered to the substrate, exceeding the performance of pure FBS. In fact, FBS coating enhanced the cell attachment for both cell types on both materials. For all conditions, fewer cells adhered to the soft material than to the hard one. Applying the grinding process was possible for all the substrate types, even when both phases were non-graded (Figure S2.5C). After grinding, the cell seeding results showed enhanced seeding efficiency and viability, with the best results obtained after grinding with a fine SiC paper with a grain size of 5 μm. This outcome was further improved when combining grinding with pure FBS coating (Figure S2.5D-F). Consequently, this surface optimization protocol allowed us to perform additional experiments to evaluate the cell behavior in specimens containing hard and soft materials in graded and non-graded configurations.

List of supporting tables

Table S2.1. A comparison of the effective elastic moduli found through tensile tests. All values are in MPa. The values calculated using the local response of the DIC images ($\hat{E}$) are compared with the measurements using a digital extensometer (E_G). The overall ordinary coefficient of determination was $R^2 = 95.76\%$

	Power-law			Linear			Step-wise			Sigmoidal		
$\hat{E}$	27.0	28.6	27.7	29.2	18.5	32.0	28.9	30.6	31.2	18.1	17.8	16.4
E_G	24.7	28.1	29.3	28.2	18.8	29.1	27.2	28.8	29.8	16.0	17.4	14.9

2. Rational positioning of 3D printed micro-bricks to realize high-fidelity, multi-functional soft-hard interfaces

List of supporting figures
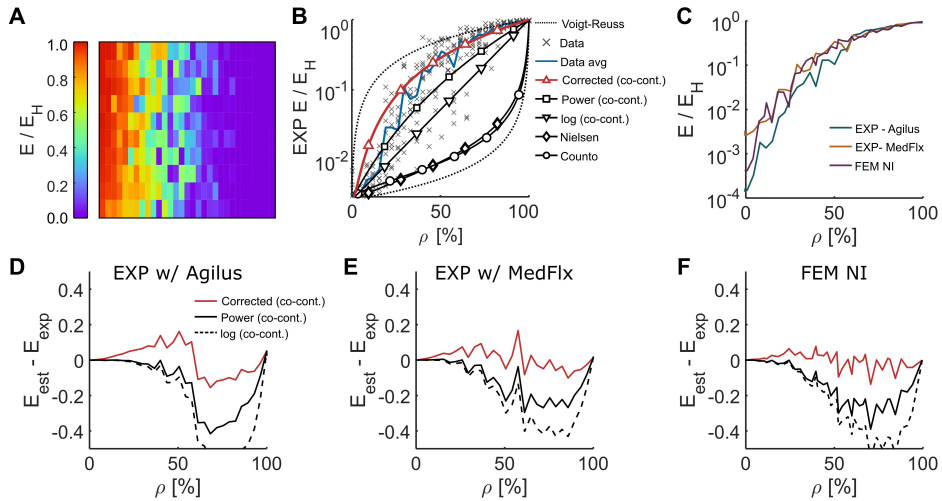
Figure S2.1. A) The distribution and B) average values of the elastic modulus as measured by NI for a soft phase made from MED625FLX™ (Stratasys® Ltd., USA). The models used for comparison are enlisted in the S1 section of this document. C) A comparison between the average response of the experimental datasets and FEM estimations. D-F) The residual plots (E_{est}-E_{exp}) of the three best-performing models (*i.e.,* Equations S3, S4, and S5) for the NI experiments performed with Agilus30 (D) and MED625FLX (E) as well as for the corresponding FEM estimations (F).
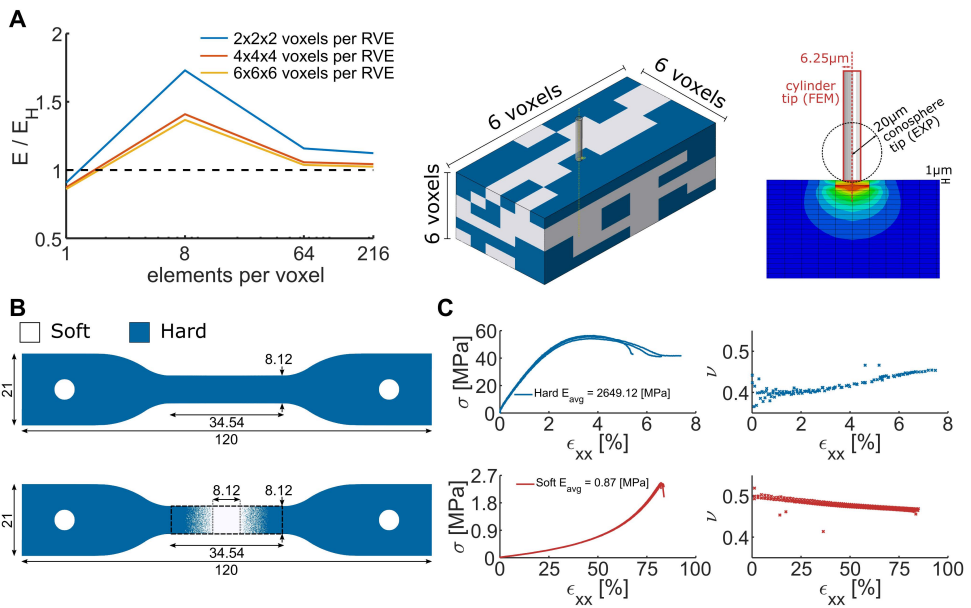
Figure S2.2. A) The results of the mesh convergence study. RVEs consisting of 6×6×6 micro-bricks and 216 linear hexahedral linear elements per micro-cube led to the smallest error when choosing a flat indenter with a radius of 5 μm and an indentation depth of 1 μm. B) the designs of the monolithic specimens used in quasi-static tensile testing (thickness = 4 mm). C) The results of the quasi-static tensile tests performed on the monolithic specimens. We obtained the average elastic modulus of both phases for the specimens printed in the loading direction. The Poisson's ratios of the materials were determined using the DIC system.

2. Rational positioning of 3D printed micro-bricks to realize high-fidelity, multi-functional soft-hard interfaces
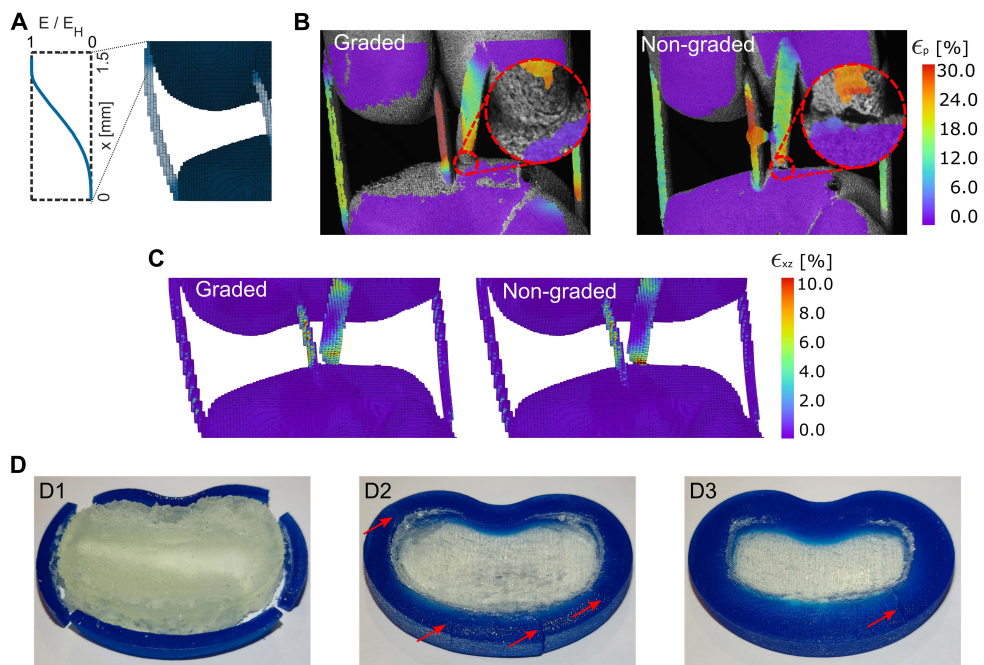

Figure S2.3. A) Representative example for discretizing an FG in the knee-ligament system. A sigmoidal gradient with a length of 1.5 mm was applied to every bone-ligament interface. B) The DIC images of the graded and non-graded knee ligament constructs after 5 mm of deformation. We observed the propagation of a non-critical crack in the non-graded specimen while the graded sample remained fully bonded. C) The distribution of the shear strain (ϵ_{xz}) within the graded and non-graded knee-ligament as predicted by the FEM models. These results show the relationship between the strain concentrations present in the non-graded specimens and shear deformations, which are highly reduced when an FG is applied. D) The failure modes of the three IVD designs after the quasi-static compression tests. The gradient-less (D1) design showed a total separation between both material phases, while the graded designs did not fail critically and merely presented non-critical cracks around the annulus fibrosus regions.
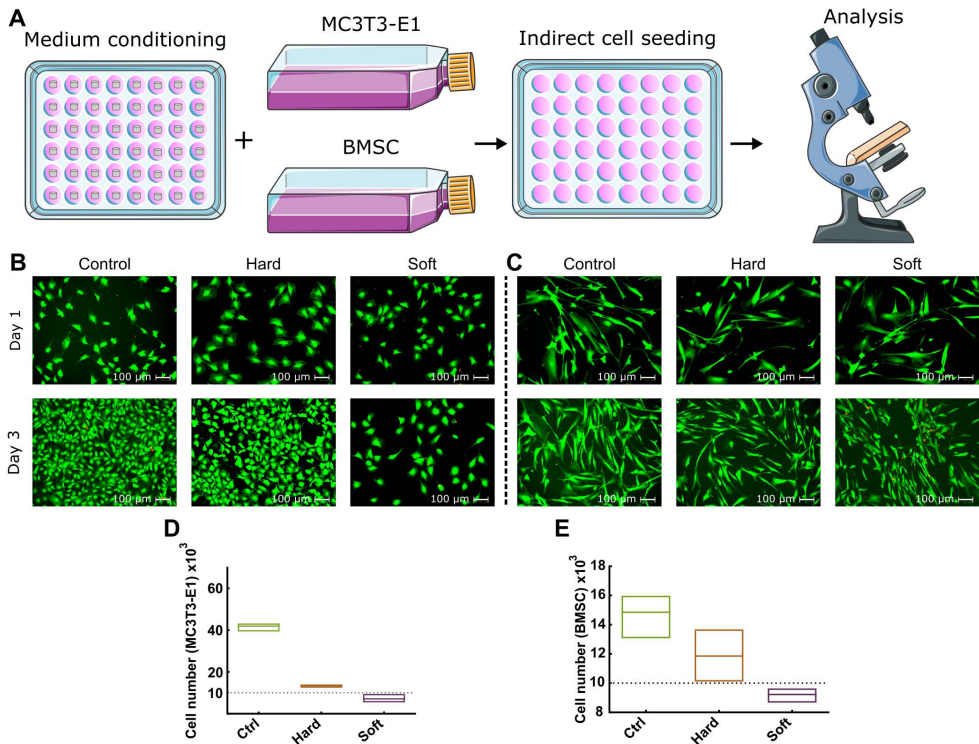
Figure S2.4. The results of indirect cell seeding in conditioned medium. A) A schematic drawing of the workflow used for indirect cell seeding. Each specimen was immersed in a culture medium for 24 h. The collected medium was used to culture the cells in standard well-plates. B-C) The live/dead images of MC3T3-E1 (B) and BMSC (C) after 1 and 3 days of culture in the extracts of the hard (VeroClear) and soft (MED625FLX) materials. Although few dead cells can be detected in all the conditions considered here, the cells cultured in the extracts of the soft material were smaller in number as compared to that of the hard material or that of the control group. D) and E) indicate the number of the MC3T3-E1 cells and BMSC cultured with the extracts.

2. Rational positioning of 3D printed micro-bricks to realize high-fidelity, multi-functional soft-hard interfaces
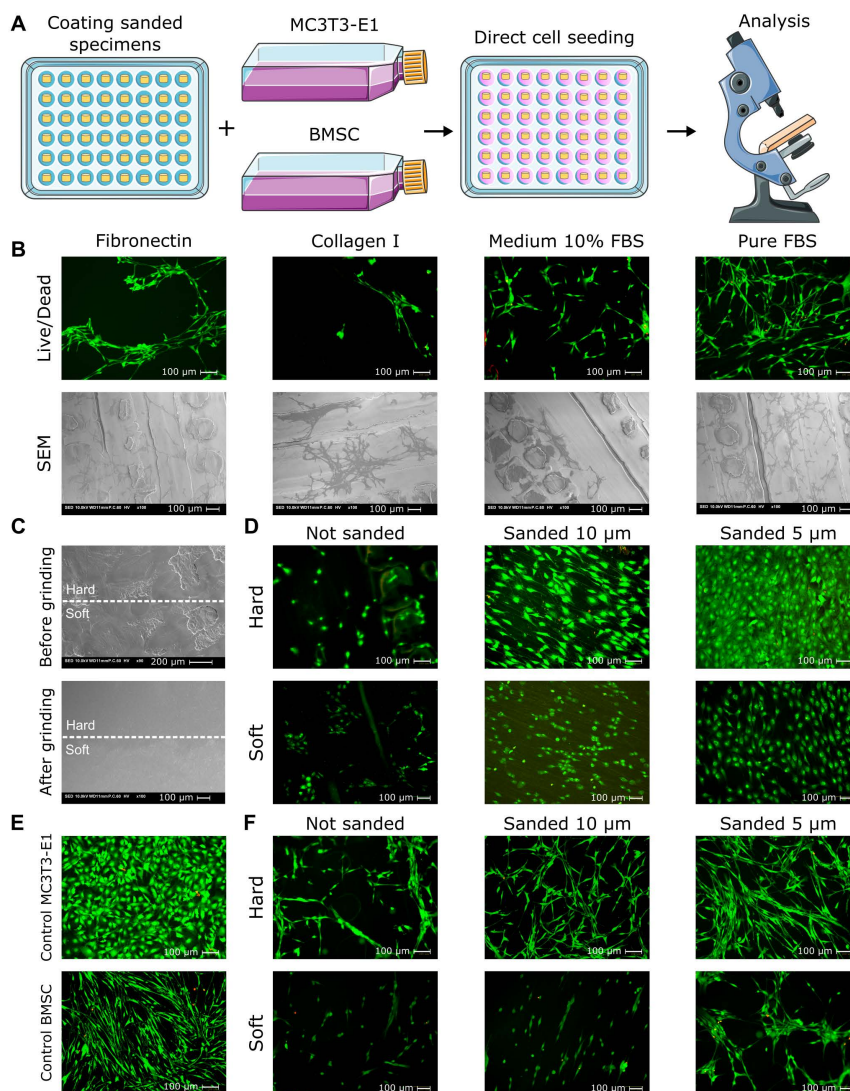
**Figure S2.5**. Direct cell seeding and the optimization of its protocol. A) A schematic drawing of the workflow for direct cell seeding. B) The live/dead images of the BMSC after 1 day of culture on the specimens with different types of protein coatings. C) The SEM images comparing the surface topography of a non-graded specimen before and after applying the grinding process using a 5 μm SiC paper. D) The direct seeding of the MC3T3-E1 cells cultured on the hard and soft specimens after their surfaces were grounded with SiC papers (5 and 10 μm) and coated with 100% (pure) FBS. The live/dead assay was performed after 24 h. E) The live/dead assays of the control groups (seeded on standard well-plates) for both cell types were performed after 24 h. F) The direct seeding of BMSC on the hard and soft specimens after grinding with 5 and 10 μm SiC papers and coating with 100% (pure) FBS. The live/dead assay was performed after 24 h.
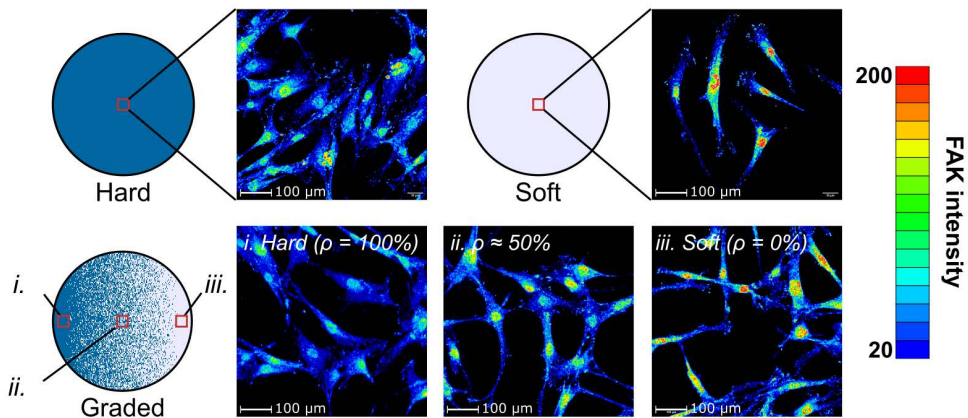
Figure S2.6. The heatmap of the FAK signal. The cells on the hard material (A) exhibited more uniform distributions of the signal, while the cells seeded on the soft material (B) showed a concentrated area around the nuclei where the FAK signal intensity was high. This trend was also observed for the cells cultured on the graded specimens. C) The signal intensity in the regions close to the nuclei increased with the volumetric percentage of the soft material.

Supporting references

[1]   L.E. Nielsen, L.A. Wre, " Ce, E. Nielsen, Generalized Equation for the Elastic Moduli of Composite Materials, J. Appl. Phys. 41 (1970) 4626. https://doi.org/10.1063/1.1658506.

[2]   U.J. Counto, The effect of the elastic modulus of the aggregate on the elastic modulus, creep and creep recovery of concrete, http://Dx.Doi.Org/10.1680/Macr.1964.16.48.129. 16 (1964) 129–138.

[3]   W.E.A. Davies, The theory of elastic composite materials, J. Phys. D. Appl. Phys. 4 (1971) 1325. https://doi.org/10.1088/0022-3727/4/9/313.

2. Rational positioning of 3D printed micro-bricks to realize high-fidelity, multi-functional soft-hard interfaces

3

# Nonlinear coarse-graining models for 3D printed multi-material biomimetic composites

3. Nonlinear coarse-graining models for 3D printed multi-material biomimetic composites

Abstract

Bio-inspired composites are a great promise for mimicking the extraordinary and highly efficient properties of natural materials. Recent developments in voxel-by-voxel 3D printing have enabled extreme levels of control over the material deposition, yielding complex micro-architected materials. However, design complexity, very large degrees of freedom, and limited computational resources make it a formidable challenge to find the optimal distribution of both hard and soft phases. To address this, a nonlinear coarse-graining approach is developed, where foam-based constitutive equations are used to predict the elastoplastic mechanical behavior of biomimetic composites. The proposed approach is validated by comparing coarse-grained finite element predictions against full-field strain distributions measured using digital image correlation. To evaluate the degree of coarse-graining on model accuracy, pre-notched specimens decorated with a binarized version of a renowned painting were modeled. Subsequently, coarse-graining is used to predict the fracture behavior of bio-inspired composites incorporating complex designs, such as functional gradients and hierarchical organizations. Finally, as a showcase of the proposed approach, the inverse coarse-graining is combined with a theoretical model of bone tissue adaptation to optimize the microarchitecture of a 3D-printed femur. The predicted properties were in exceptionally good agreement with the corresponding experimental results. Therefore, the coarse-graining method allows the design of advanced architected materials with tunable and predictable properties.

3.1. Introduction

Extending and optimizing the design space of synthetic engineering materials remains an open problem. Overcoming this challenge is possible thanks to the additive manufacturing (AM, also known as 3D printing) of architected materials because the spectrum of achievable material properties can be dramatically extended by using single or multiple material phases in a wide range of geometrical configurations.[1–4] The emergence of these materials has, however, created new challenges because finding the proper design features at the smaller scales (*i.e.,* micro/nano) to create the desired and optimal combination of properties at a larger scale (*i.e.,* meso) is not trivial.[5–8]

In the recent past, researchers have used different approaches to design microarchitectures that lead to extraordinary macroscale properties.[9,10,19–23,11–18] One such approach is biomimetic design, where the essential characteristics of natural materials (*e.g.,* length-scale multi-hierarchical organization and functional grading) are used to rationally design a new class of engineered materials known as biomimetic architected materials (bio-AM). When designed optimally, such bio-AM exhibit some desirable combinations of ordinarily mutually exclusive properties (*e.g.,* high-strength and high-toughness).[24,25,34–36,26–33] Despite these advantages, the highly complex microarchitectures of bio-AM make their fabrication and analysis a formidable challenge.

Recent developments in the (multi-material) AM techniques have created new opportunities for fabricating such materials.[37,38,47,48,39–46] More specifically, voxel-based 3D printing has the potential to revolutionize architected materials.[49] This AM technique allows for a reliable "voxel-by-voxel" deposition of hard and soft material phases at the microscale, making it possible to mimic the spatial distribution of organic and mineral phases in natural composites [50,51] and provides an unlimited level of design freedom to create advanced bio-AM.[52–57] However, this approach can lead to exceptionally detailed microarchitectures that are highly challenging to analyze using the finite element method, particularly when such nonlinear aspects as elastoplasticity and ductile damage are considered. The optimization of such designs is, therefore, only possible for small constructs because extensive simulations are typically needed to analyze every possible permutation of the hard and soft phases.[58–61]

A potentially useful approach to limit the computational cost associated with complex bitmap designs is to use coarse-graining.[5] This process has, for example, been used to represent monophasic porous materials (*e.g.,* bone, truss structures) by their grayscale equivalents, where the gray value represents the volume ratio of the solid phase. Although the classic implementations of this method do not necessarily result in manufacturable architectures, bitmap designs do not suffer from this issue. That is because the coarse-grained gray values of each representative volumetric element (RVE) directly translate to the volume fraction of the hard phase, ρ. The coarse-graining problem is, therefore, reduced to the problem of selecting the proper set of constitutive equations to serve as the gray value-property relationships of these composites while also adequately capturing their generalized

nonlinear behavior (e.g., elastoplasticity, continuum damage, and softening), which is fundamental for estimating the mechanical limits of architected materials.

Here, we developed a coarse-graining approach that allows for a highly efficient prediction of the nonlinear mechanical response of bio-AM. This methodology combined the design freedom of voxel-based AM with the simplicity of foam-based constitutive models to obtain the gray value-property estimation functions. This powerful approach circumvented the need for computationally expensive models and provided a highly efficient and cost-effective tool for the rational design of bio-AM. After performing only a few mechanical tests, we generated the data required to characterize the nonlinear constitutive equations and validated them via computational simulations. We then evaluated the effects of the coarse-graining degree by performing FEA on a highly-detailed portrait and gradually increasing the coarse-graining degree. Furthermore, we demonstrated the applications of this approach by extending it to the analysis of the ductile fracture behavior of bioinspired materials.[53,62] Finally, we utilized the inverse coarse-graining operation to obtain the microarchitecture of a remodeled femoral bone.

3.2. Results and discussion

The results of 21 quasi-static tensile tests with different values of ρ provided the data needed to characterize the gray value-property relationships for coarse-graining (Figure 3.1). Multi-material 3D printing based on the jetting of UV-curable polymers with voxel-level control over the type of the deposited material enables the generation of such tensile test specimens. To this end, stacks of binary images with randomly deposited white or black pixels represented the hard and soft phases, respectively (Figure 3.1A-B). Stacking these binary images made it possible to fabricate composites with reinforcement distributions in 3D (Figure 3.1C). This design freedom allowed including all the features required to 3D print the dogbone tensile tests specimens without additional post-processing (Figure 3.1D).
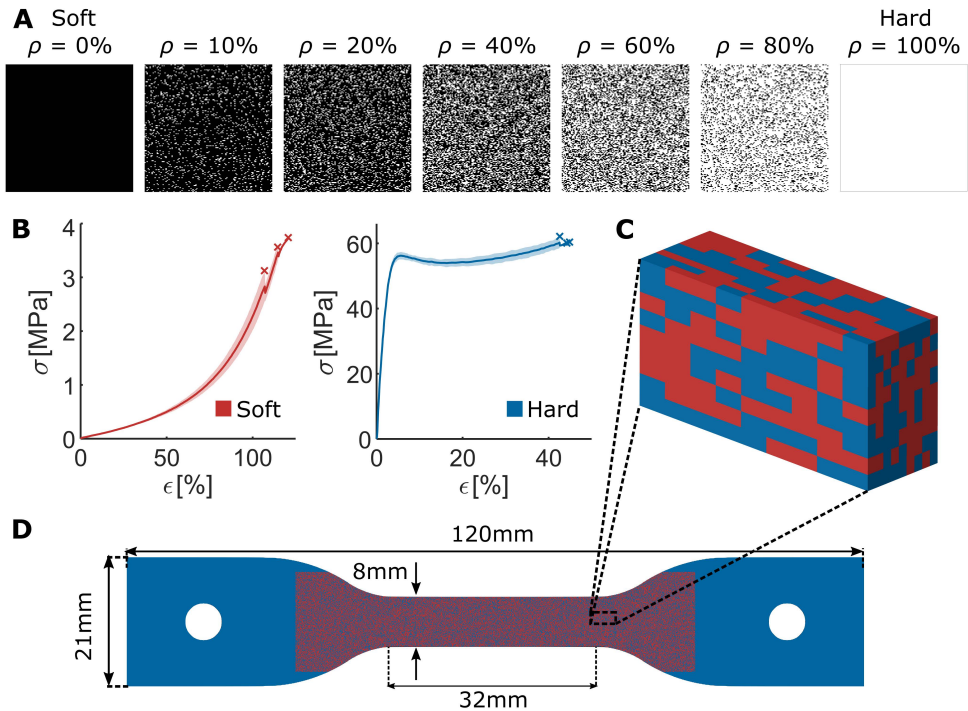
Figure 3.1. A) The representative binary images used to design and fabricate the tensile test specimens. These were 3D printed with a multi-material 3D printer and contained different values of the volume fraction of the hard phase (ρ). B) The stress-strain curves of monolithically soft and hard specimens. C) A representative volume element of a 3D printed specimen designed by voxel-based 3D printing. These composites contained randomly distributed hard and soft voxels. D) A standard tensile test specimen implementing the random design within its gauge length (out-of-plane thickness = 4 mm).

The behavior of the stress-strain curves resulting from the tensile tests ranged from hyperelastic (pure soft, $\rho = 0\%$) to elastoplastic (pure hard, $\rho = 100\%$) (Figure 3.2A). The ultimate von Mises strength achievable by these materials was 3.4748 ($\pm$ 0.3169) MPa and 60.967 ($\pm$ 1.0805) MPa for the soft and hard materials, respectively. Similarly, the elastic modulus of the specimens varied between 0.9716 ($\pm$ 0.0657) MPa and 2576.13 ($\pm$ 285.30) MPa (Table S3.1 of the supporting information) and increased nonlinearly in relation to ρ (Figure 3.2B). These observations confirm the composite design range achievable by these materials, covering three orders of magnitude.[54] Therefore, to properly coarse-grain these materials, it is important to select a constitutive model that allows for retaining the characteristic curves and the magnitude of the changes that these composites present. Foam-

3. Nonlinear coarse-graining models for 3D printed multi-material biomimetic composites

based constitutive models for large deformations satisfy these conditions.[63] They can represent both linear elastic and hyperelastic mechanical behaviors and can follow both hardening- or softening-like nonlinear regimes. The constitutive model used here defines the von Mises stress (σ) of a homogeneous material as: [63]

$$\sigma = A \frac{e^{\alpha \epsilon} - 1}{1 + e^{\beta \epsilon}} \tag{1}$$

In this equation, the constant A has stress units, while the constants α and β are dimensionless. Additionally, separating the contributions of the elastic (ϵ_{el}) and plastic (ϵ_{pl}) strains is possible with the expression:

$$\epsilon = \epsilon_{el} + \epsilon_{pl} = \frac{\sigma}{E} + \epsilon_{pl} \tag{2}$$

where the total von Mises strain (ϵ) varies between zero and the ultimate strain (ϵ_{ult}). Moreover, obtaining the elastic modulus (E) from equation 1 is possible after evaluating its derivative against the origin ($\frac{d\sigma(\epsilon=0)}{d\epsilon}$), resulting in the expression:

$$E = \frac{A\alpha}{2} \tag{3}$$

To generate the coarse-graining estimation functions, we characterized the parameters A, α, β, and ϵ_{ult} in terms of ρ. To achieve this goal, we first obtained the equivalent parameters from our tensile test stress-strain results (Figure 3.2C). To more accurately represent the complex nature of the resulting curves, we generalized the parameters A and α with two different power-law functions, with a transition region at $\rho = 40\%$ (Table 3.1). This simple parametrization led to an accurate numerical estimation of the elastic properties of voxel-based composites, which was substantially more accurate than the results obtained using the recently reported power-law and logarithmic co-continuous models of particle-based composites (Figure 3.2B). [48,64] Furthermore, we characterized the α/β ratio and ultimate strain ϵ_{ult} with exponential decay functions. These four simple parametrizations allowed us to accurately estimate the entire stress-strain behavior of any bio-AM for any ρ value (Figure 3.2A, black curves).
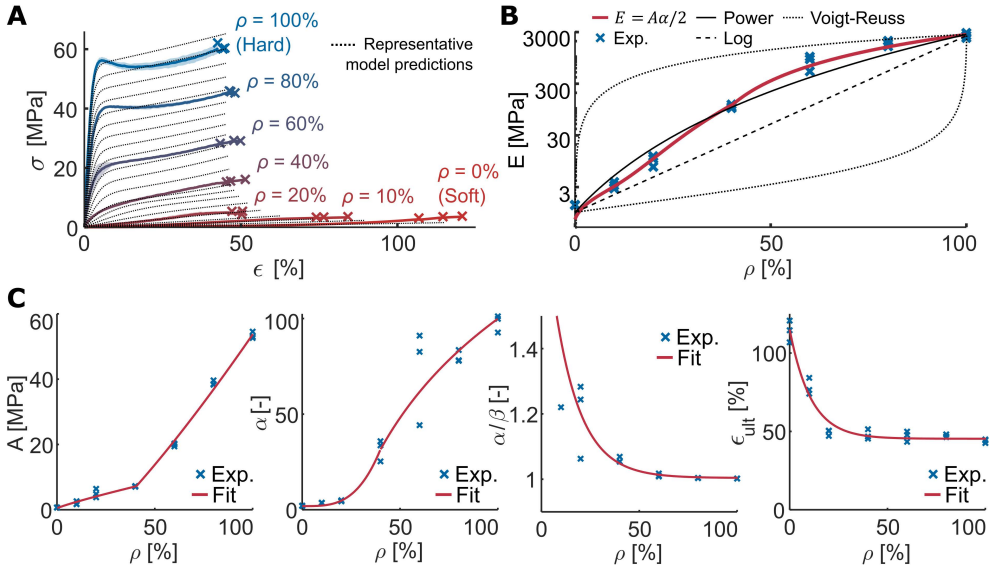
Figure 3.2. A) The average stress-strain curves of the tensile tests. The shaded area around the mean curves represents ±SD. The different line and color gradients refer to the specimens with different ρ values. The dotted black lines represent the predictions obtained using the coarse-graining functions, showcasing the possibility of simulating the complete design space of voxel-based composites. B) A comparison between the experimental values of the elastic modulus and the predictions of the coarse-graining equations as well as the existing co-continuous models (i.e., logarithmic and power-based) of particle-reinforced composites. C) The average values of the experimental (Exp.) vs. fitted parameters that define the constitutive model represented in equation 1 (i.e., A, α, and α/β) and ultimate strain before failure (ϵ_{ult}) used to coarse-grain the bitmap composites.

To validate the coarse-graining equations, we developed FEA simulations of the tensile experiments (Figure 3.3). We changed the original resolution of the designs from 768×96×150 binary voxels to 128×16×25 greyscale RVEs. In this process, the gray value of each RVE represents the average ρ value of the original voxels within it (Figure S3.1 of the supporting information). Then, we used the characterized coarse-graining functions to assign the respective mechanical properties to each RVE. As hexagonal elements were used to represent each RVE, the coarse-graining process reduced the element count by three orders of magnitude from 11.05×10^6 to 51.2×10^3, rendering the analyses computationally feasible.

3. Nonlinear coarse-graining models for 3D printed multi-material biomimetic composites

Table 3.1. The foam-based constitutive equation parameters used to coarse-grain bio-AM in terms of the local value of the volume fraction of the hard phase (ρ).

Parameter	$\rho \leq 40\%$	$\rho > 40\%$
A [MPa]	$A = 14.951\rho^{0.882} + 0.695$	$A = 67.980\rho^{1.272} - 14.015$
α [-]	$\alpha = 642.599\rho^{3.36} + 2.035$	$\alpha = 4778.62\rho^{0.0157} - 4678.65$
α/β [-]	$\alpha/\beta = 0.892e^{-7.52\rho} + 1.0037$	
ϵ_{ult} [mm mm^{-1}]	$\epsilon_{ult} = 0.698e^{-9.218\rho} + 0.452$	
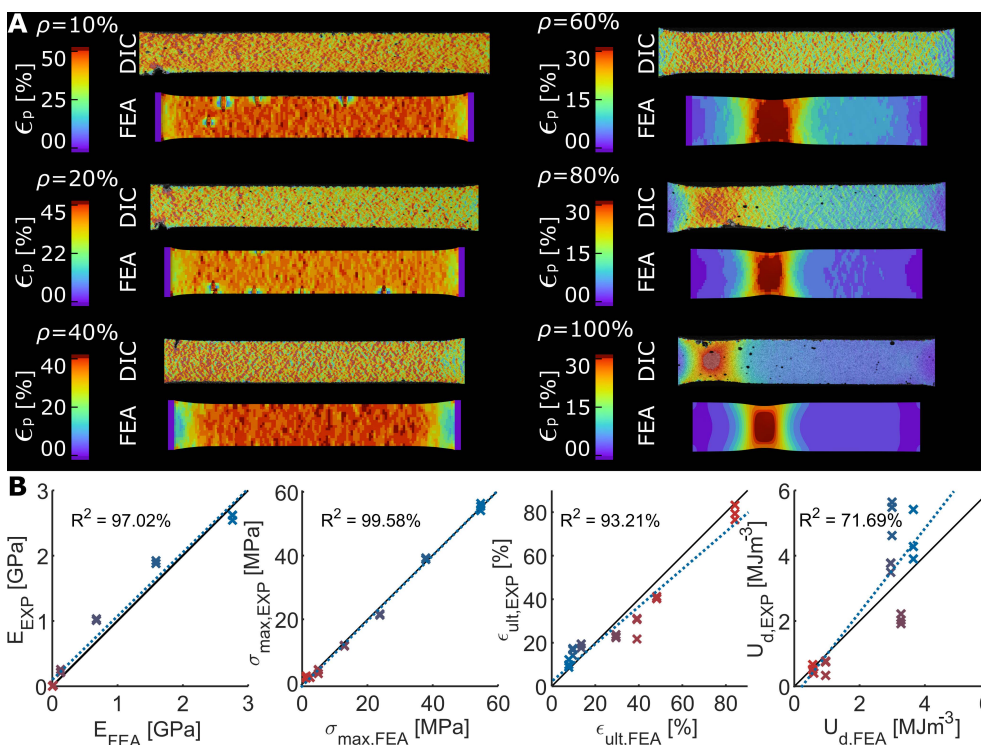
Figure 3.3. A) The distribution of the first principal true strain (ϵ_p) measured experimentally using DIC and calculated with coarse-grained FEA of the same specimens. All the images refer to the last time point before critical separation. B) The experimental (Exp.) vs. FEA results for the elastic modulus (E), ultimate tensile strength (σ_{max}), ultimate strain (ϵ_{ult}), and strain energy density (U_d) obtained from the quasi-static tensile tests for all the specimens, together with the corresponding coefficients of determination (ordinary unadjusted R^2 values).

Overall, the true principal logarithmic strain maps (ϵ_p) resulting from digital image correlation (DIC) measurements were remarkably akin to those predicted by FEA (Figure

3.3A, Figure S3.2B of the supporting information). Moreover, the behavior of the computational analyses adequately followed the transition from a highly elastic material with multiple cracks ($\rho = 10\% - 40\%$) to a more rigid material that presents necking ($\rho = 60\% - 100\%$). This high precision across the entire design space was also present in the comparisons between the properties estimated by the FEA and those obtained in the experiments (Figure 3.3B). In those, the elastic modulus and ultimate strength properties were very highly correlated (*i.e.*, $R^2 = 97.02\%$ for the elastic modulus and $R^2 = 99.58\%$ for the ultimate strength), with slight underpredictions of the elastic modulus for the intermediate values of ρ. Additionally, the stress-strain curves of the computational models followed the hardening- or softening-like behaviors of their respective tests (Figure S3.2C of the supporting information). However, FEA overpredicted the ϵ_{ult} and toughness (U_d) for the tests with $\rho < 50\%$ and underpredicted them for $\rho > 50\%$. These differences are likely caused by the processes involved in the DIC measurements and can be reduced by performing the DIC recordings at the micro-scale, leading to a higher precision than the macro-level recordings of this study. Regardless of these differences, the R^2 values characterizing the agreement between our numerical data and the experiments approached unity. The qualitative, characteristic features of the curves and the ductile failure mechanisms of the bitmap composites were also retained in the coarse-grained simulations. These observations confirm the accuracy and utility of the presented coarse-graining approach for capturing the nonlinear behavior of voxel-based 3D printed composites. Improving the performance of the coarse-graining parameters that detail the nonlinear behavior of these composites, however, could be explored in a future study. In it, a bottom-up multiscale scheme to predict the general behavior of different RVE designs via homogenization or topology optimization is suggested, similar to what other recent studies have proposed [65–69].

To further validate the application of our coarse-graining process, we evaluated how the degree of coarse-graining affects the overall FEA performance in a process similar to a mesh convergence study. To consider a structure with more refined local features, we used a part of the famous portrait *Girl with a pearl earring* by Johannes Vermeer (Delft, c. 1665) (Figure 3.4) to generate a 3D bitmap composite. We simulated the mechanical response of the portrait-decorated design in two different FEA analyses, each with a different initial binary

resolution. The first set of the simulations comprised a set of linear elastic simulations, where the original binary 3D image was represented by 288×288 voxels in the plane and six voxels in depth and was coarse-grained to different degrees (Figure 3.4A). The second set of simulations was performed until the yield point and had an original resolution of 126×126 voxels in the plane and 4 voxels in depth (Figure 3.4B). We then compared the outcomes of these simulations and the required computational resources to better understand the effects of the coarse-graining degree.
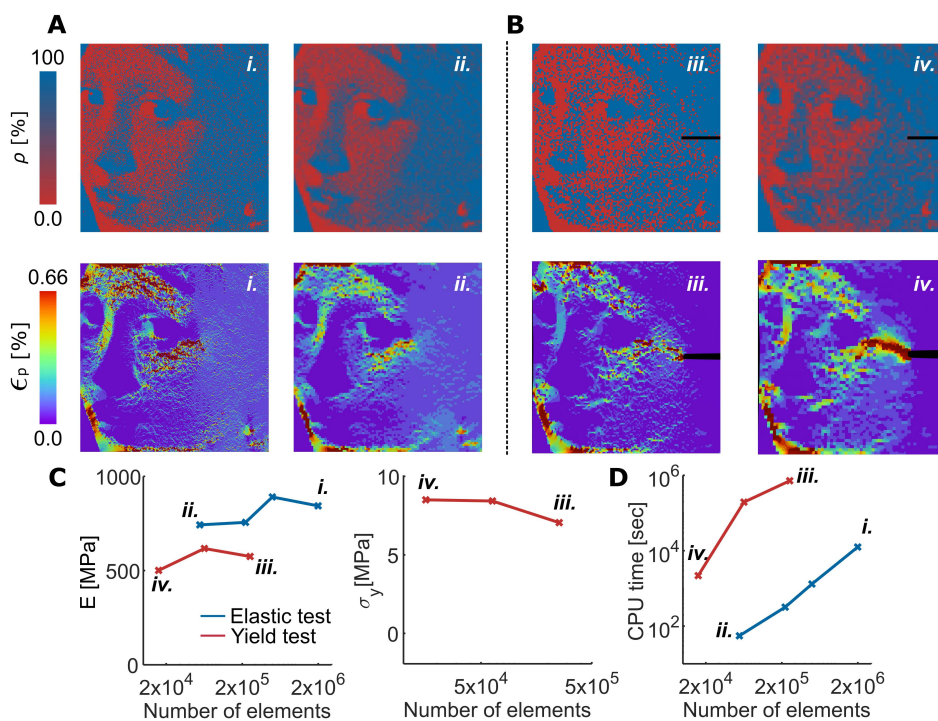
Figure 3.4. The effects of the degree of coarse-graining on the strain distributions and the effective mechanical properties of the specimens. These simulations were performed on a binarized copy of a part of the renowned painting *Girl with a pearl earring* (Johannes Vermeer, Delft, c. 1665), where coarse-graining was performed to different degrees. A) The distribution of the principal true strain calculated using linear elastic finite element models. The original model had a resolution of 288×288 binary bits and was coarse-grained from 1.99×10^6 (*i.*) to 5.52×10^4 (*ii.*) hexagonal FEA elements. B) The strain distribution predicted by the finite elements that simulated the loading of the specimens until yielding occurred at the crack tip. The original model had a resolution of 126×126 binary bits and was coarse-grained from 2.54×10^5 (*iii.*) to 1.58×10^4 (*iv.*) hexagonal FEA elements. C) The elastic modulus and yield strength of calculated using the finite element models. D) The computational time *vs.* the number of linear hexagonal elements used in these simulations.

The original binary images and the coarse-grained specimens shared the same regions of strain concentration (Figure 3.4A-B). The strains concentrated mainly at the forehead, chin, and cheek regions, which are the regions with abrupt transitions in the material type. However, the simulations at higher resolutions showed more heterogeneous strain patterns and had higher local strain values than the coarse-grained ones. Although these effects must be acknowledged and considered when coarse-graining designs with fine features (*e.g.,* under the presence of a crack front or when abrupt material transitions are present), the local strain distributions did not substantially affect the overall response of the architected materials (Figure 3.4C). When comparing the overall mechanical properties calculated using the different models, the prediction error for the elastic modulus was always <13%. At the same time, the yield strength did not deviate more than 17% from the estimates obtained using the original model. Although these deviations may be critical depending on the application type, one must consider the efficiency gained from the process. The required computational time dropped (Figure 3.4D) by three orders of magnitude such that the most coarse-grained models required only 0.45% (reduced from 12224 to 55.3 seconds) and 0.3% (reduced from 717976 to 2182 seconds) of the original time to compute the elastic modulus and yield stress, respectively. Such a huge drop in the required computational cost can change the fate of an intended simulation from "practically impossible" to "routinely possible", making it possible to take design steps (*e.g.,* optimization iterations) that are otherwise infeasible. The price paid in terms of the lost accuracy should, however, be carefully considered for each specific application.

To harness the advantages of the proposed coarse-graining approach for simulating large and complex bio-AM structures, we simulated the ductile mode I crack propagation of designs from two of our previous studies [53,62]. These were three different bioinspired designs and three crack designs with randomly distributed particles ($\rho =$ $[100\%, 75\%, 50\%]$) (Figure 3.5A, Figure S3.3B-C of the supporting information). The bioinspired designs included a functional gradient (FG) and two hierarchically organized (*i.e.,* with one and two hierarchy levels) brick and mortar designs with embedded FGs (BMG-1L and BMG-2L). Initially, these designs had a resolution of 1728×864×111voxels, which we coarse-grained to 864×432×1, thereby making 2D plane stress computational analyses feasible. These models allowed us to study the differences between the strain distributions

3. Nonlinear coarse-graining models for 3D printed multi-material biomimetic composites

and the macroscopic properties (*i.e.,* elastic modulus and ultimate strength) calculated using the coarse-grained FE models and the effective mechanical properties and full-field strain distributions measured experimentally for the original bio-AM designs.

The strain distributions of the coarse-grained models were similar to those measured using DIC (Figure 3.5B-E, Figure S3.3 of the supporting information). In the case of the particle-distributed designs ($\rho = 50\%, 75\%, 100\%$), both the DIC and FEA strains presented the butterfly-shaped crack tip regions usually observed in pre-notched mode I specimens. In contrast, the strains of the FG design followed a horizontal pattern ahead of the crack tip, concentrating in the region with the softer material. Furthermore, both the BMG-1L and BMG-2L designs presented the small horizontal and vertical strain concentration lines that are characteristics of the brick and mortar designs [53] and combined the previously described butterfly and horizontal strain distribution patterns. These observations further confirm that the proposed coarse-graining method can successfully capture the original features of complex bio-AM designs. Similar to the strain distributions, the effective behavior predicted with FEA followed the same trends observed in the experiments (Figure 3.5F). The predicted values were, however, somewhat lower than the measured ones. In the case of the elastic modulus, the underestimations were mostly present when the concentration of the hard phase around the crack tip was low (*e.g.,* the designs with $\rho = 50\%$, FG). Since the ductile fracture criterion used here is based on the ultimate strain (and not ultimate stress), an underestimation of the elastic modulus also led to an underestimation of the strength. Future studies should evaluate the use of other types of ductile fracture criteria. Despite these limitations, the ranking and the rough values of the estimated quantities matched the experimental results. These agreements confirm that the coarse-graining approach presented here can capture the effects of complex hierarchical design features reasonably well, making it suitable for the design of micro-architected bio-AM composites.
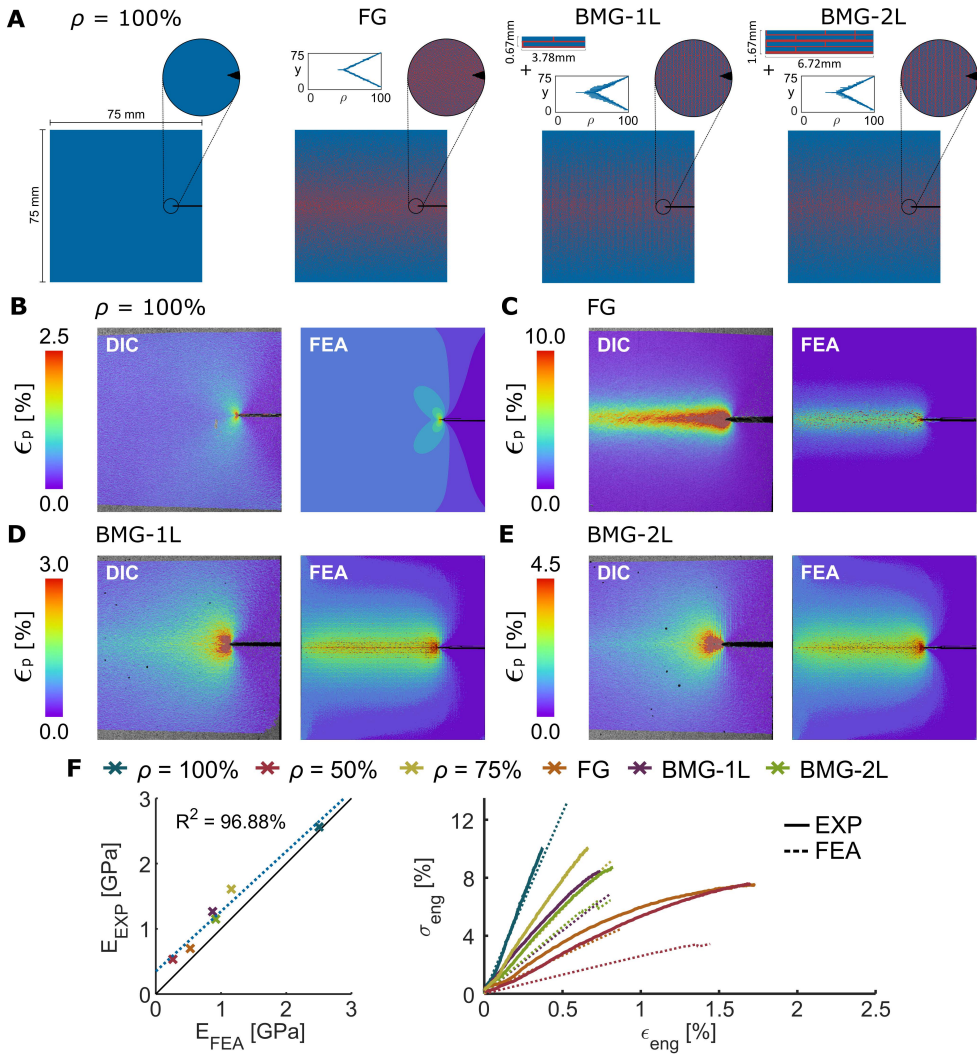
Figure 3.5. A) As a case study, we selected several bio-AM microstructures with complex features for modeling. These designs were compared with a pre-notched specimen with a ρ of 100%. A functionally graded (FG) specimen, as well as two FG designs embedded with brick and mortar designs with one (BMG-1L) and two (BMG-2L) levels of hierarchical organization were also included. The predicted values of the principal strain are compared with the DIC results for the B) $\rho = 100\%$, C) FG, D) BMG-1L, and E) BMG-2L specimens. F) A comparison between the measured (Exp) and predicted behaviors of the different designs.

3. Nonlinear coarse-graining models for 3D printed multi-material biomimetic composites
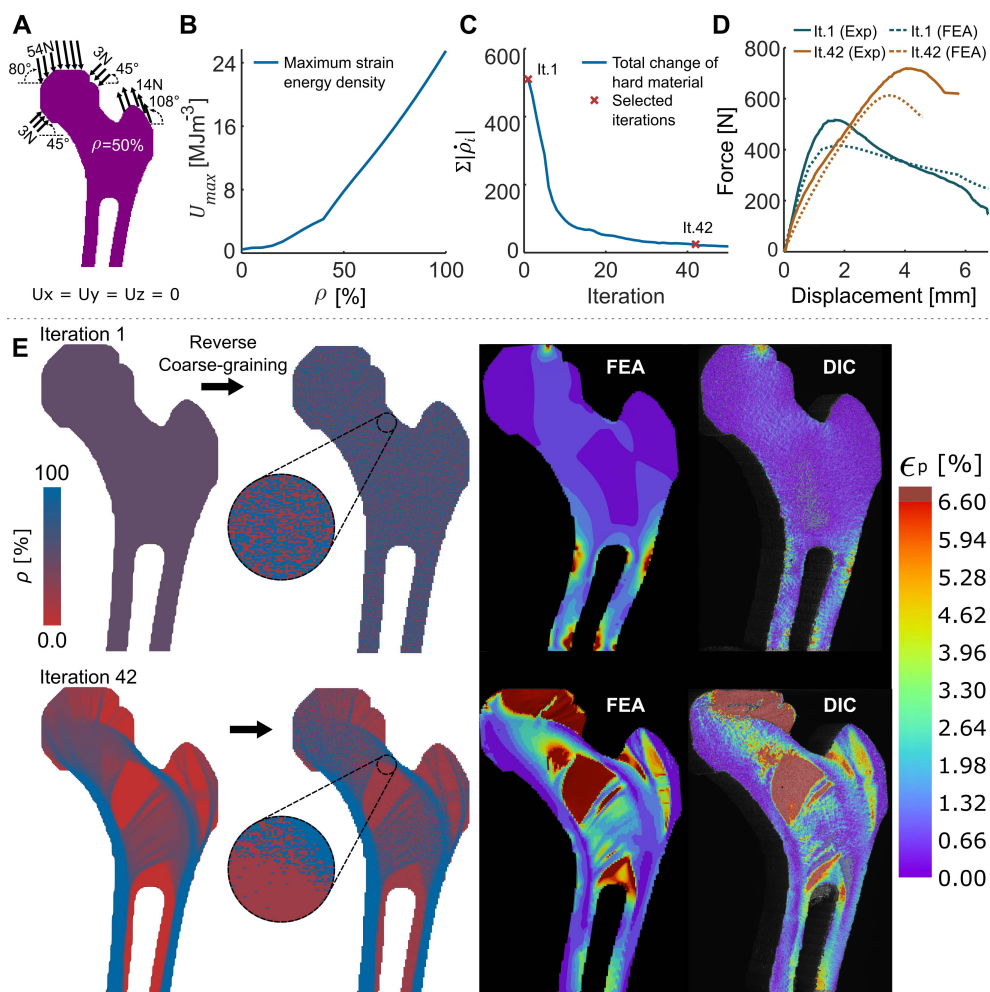
Figure 3.6. The optimization of the femoral microarchitecture using a theoretical model of the bone tissue adaptation process and implementing an inverse version of the proposed coarse-graining approach. A) The initial FEA remodeling setup and boundary conditions. B) The maximum value of the strain energy density (U_{max}) that an element can withstand as a function of ρ. C) The convergence curve of the remodeling process, where the total rate of change in the volume fraction of the hard phase ($\Sigma|\dot{\rho}_i|$) was calculated for every iteration. D) The force-displacement curves corresponding to the compression tests performed on the starting and final microarchitectures resulting from the optimization process (both measured and predicted values). E) A comparison between the designs and FEA strain field distributions of the grayscale models and those from the discretized bitmap structures obtained from the inverse-coarse graining process

The functionality and precision offered by the coarse-graining approach are not only limited to the simplification of large-scale and complex bitmap structures. Given the accuracy of the gray value-property relationships, we hypothesized that it should be possible to use their inverse operation to back-calculate the bio-AM microarchitectures of grayscale structures without changing the expected mechanical response. Therefore, we extended our analyses by using this inverse coarse-graining operation to discretize, manufacture, and test the voxel structures obtained from a bone remodeling process.[70] For that purpose, we considered a 2D proximal femur that initially contained a homogeneous distribution of 50% hard material (Figure 3.6A). We used FEA to numerically simulate the femur under force-controlled conditions. For optimization, we updated every element's ρ_i value by comparing its normalized strain energy density (normalized with respect to the maximum value of the same quantity, Figure 3.6B) (S_i) with the mean normalized strain energy density of the structure (S_{avg}) at the end of each iteration. After the convergence of the remodeling process (*i.e.,* after 42 iterations, Figure 3.6C), we 3D printed and tested the first and last iterations. To perform the inverse coarse-graining operation, we transformed every greyscale RVE into a random group of 3×3×3 binary voxels (*i.e.,* a change in the resolution from 206×118×1 to 618×354×3 voxels), where the number of the hard voxels depended on the ρ value of each RVE. We repeated this voxel assignment process 144 times to generate all the 432 different bitmap images required to manufacture these femora. Finally, we 3D printed these designs and tested them under uniaxial compression until failure.

The force-displacement plots proved that the remodeling process enhanced the total energy capacity of the designed bone (Figure 3.6D). This process estimated a maximum force improvement of 146% (from 418.43 N to 612.85 N) while reducing the entire stiffness of the system from 485.09 Nmm^{-1} to 205.67 Nmm^{-1} (42.4%). Similar improvements were also present in the experimental results, where the maximum force increased by 139.2% (from 516.67 N to 719.27 N), accompanied by a 42.76% reduction in the stiffness (from 518.25 Nmm^{-1} to 221.61 Nmm^{-1}). These results indicate that FEA underestimated the experimental outcome. The FE-predicted stiffness values were between 92.8% and 93.6% of the corresponding experimental values, and the FE-predicted maximum force ranged between 81.0% and 85.2% of the corresponding experimental values. Despite these differences, the percentages of the property changes between the last and first iterations were very close for

the FEA predictions and experimental measurements (*i.e.,* 146% *vs.* 139.2% for the maximum force and 42.4% *vs.* 42.76% for the stiffness). Moreover, the patterns of the changes in the strain distributions, which improved the overall properties of the designs, were virtually indistinguishable between the FEA results and the DIC measurements (Figure 3.6E). After concluding the optimization process, the designed femur exhibited high strain concentrations across the head, neck, and greater trochanter regions, suggesting an appropriate and efficient internal load distribution.[71] In contrast, the initial iteration only showed strain concentrations in the diaphyseal regions. These results highlight the potential of the proposed inverse coarse-graining approach as a tool to design, optimize, and discretize bio-AM, enabling the development of highly efficient and miniaturizable (medical) devices with advanced functionalities.

3.3. Conclusion

In summary, we showed that foam-based constitutive equations for large deformations effectively and accurately model the nonlinear mechanical behavior of bio-AM. This simple and elegant system of functions combined with voxel-by-voxel 3D printing techniques provides the user with a methodology to coarse-grain large systems of binary images and represent them at smaller greyscaled resolutions to perform nonlinear quasi-static numerical analyses and optimization processes. The coarse-graining and numerical modeling of the detailed bitmap designs substantially reduced the simulation time by three orders of magnitude while only causing reasonably small deviations from the true mechanical response. Thanks to this huge reduction in the simulation time, we could perform an analysis of large and complex bio-AM to study their local strain distributions and estimate their performance. Furthermore, the proposed coarse-graining approach enabled us to mimic the internal material distribution of a femoral bone that results from a remodeling algorithm, yielding a complex local strain distribution that enhanced the overall nonlinear response of the structure. The inverse coarse-graining process enabled discretizing these greyscaled structures into manufacturable equivalents while maintaining the outstanding mechanical response estimated by their computational counterparts. The proposed methodology, therefore, creates new opportunities for designing advanced materials given their desired properties in a reliable and straightforward manner. Many high-tech industries, such as soft robotics, aerospace, orthopedics, and tissue engineering, may benefit from such a simulation

approach that could enable them to incorporate more voxel-based approaches into the design of their architected materials.

3.4. Materials and methods

3D printing: We used a multi-material jetting 3D printer (ObjetJ735 Connex3, Stratasys® Ltd., USA) with UV-curable photopolymers to fabricate the specimens. The deposition of each polymer type (*e.g.*, hard *vs.* soft) could be controlled at the level of individual voxels. Stacks of binary images were, therefore, required as input. Each material phase required its own stack of images, wherein the white bits (*i.e.*, 1) represent the location where the 3D printer will deposit that material particle. The resolution of the machine was 600×300 dpi in layers of 27 µm, which yields voxels with the native dimensions of 42×84×27 µm³. We selected the rigid opaque VeroCyan™ (RGD841, Stratasys® Ltd., USA) and rubber-like Agilus30™ Clear (FLX935, Stratasys® Ltd., USA) photopolymers as the hard and soft phases, respectively. We processed the prints with GrabCAD Print (Stratasys® Ltd., USA). All the voxel-based designs and their respective stacks of binary images were prepared using in-house MATLAB R2018b (Mathworks, USA) codes (available from the authors upon request). We aligned the designs and bitmap images along the same axis as the printing direction, thereby minimizing the inclusion of printing-related anisotropy in our specimens.

Design and testing of the tensile test specimens: We defined the tensile test specimens with seven values of the volume fraction of the hard phase (*i.e.*, $\rho = 0, 10, 20, 40, 60, 80, 100\%$, Figure 3.1A). We then randomly distributed a large enough number of voxels to discretize the internal architecture of these designs. We projected these designs onto the standard tensile test specimen shape (type IV) described in ASTM D638-14 (thickness = 4 mm) (Figure 3.1D).[72] A particular approach was followed for the pure soft (*i.e.*, $\rho = 0\%$) specimens since we only applied the design at at the centermost 8 mm of the gauge length while connecting the edges with a monotonic gradient of ρ (Figure S3.2A of the supporting information). We assigned the hard phase to the gripping part of each specimen. Three specimens were then 3D printed from each of the abovementioned designs. We used a mechanical testing machine (LLOYD instrument LR5K, load cell = 5 kN) to deform the specimens at a rate of 2 mm min⁻¹ until failure. The measured time (t) and force (f) signals were recorded at a frequency of 100 Hz. To improve the accuracy of our measurements, we

3. Nonlinear coarse-graining models for 3D printed multi-material biomimetic composites

recorded the local displacement fields of every test by using a DIC system (Q-400 2x 12 MPixel, LIMESS GmbH, Krefeld, Germany) at a frequency of 1 Hz. Towards that aim, we applied a black dot speckle pattern over a white paint background on every specimen prior to testing. Then, we used a commercial program (Instra 4D v4.6, Danted Dynamics A/S, Skovunde, Denmark) to calculate the full-field strain maps (equivalent von Mises true strains and first principal true strains) of each tested specimen. To extract the numerical data and to characterize the behavior of the composites, we used a point digital extensometer at the failure location of each specimen to extract the corresponding vectors of true von Mises strains (ϵ). Similarly, to obtain data for the FEA validations of these tests, we used a line extensometer that spanned the entire gauge length of the specimen and extracted the respective true strain vectors. Then, we used MATLAB R2018b to calculate the true stresses ($\sigma = fA_o^{-1}\exp(\epsilon)$, $A_o = 32.512$ mm^2) and elastic modulus, E, of the specimens. To determine the elastic modulus, a line was fitted between 0% and 30% of the maximum recorded stress. The ultimate tensile strength, σ_{max}, was determined as the maximum recorded stress while the strain at failure, ϵ_{ult}, was defined as the last recorded strain. Finally, the strain energy density, U_d, was calculated as the area under the stress-strain curve of each specimen.

Characterization of Foam based constitutive models: The original foam-based constitutive model for large deformations chosen for this study has the form: [63]

$$\sigma = A\,\frac{\mathrm{e}^{\alpha\epsilon} - 1}{B + \mathrm{e}^{\beta\epsilon}} \tag{A}$$

In this function, A has the unit of stress and represents the asymptotic value of the stress that is reached when α and β are equal. α and β are the dimensionless constants that influence how fast the stress (σ) will reach the asymptotic value A. Their ratio (α/β) determines whether the curve is hardening-like or softening-like. B is a dimensionless parameter that generates a toe region in the curve. We defined this latter parameter as unity ($B=1$) for simplicity, yielding the function presented in equation 1. This equation represents the entire history of the von Mises stress for a composite and is directly related to the respective von Mises strains (ϵ) until the ultimate strain (ϵ_{ult}) is reached. To use this equation in FEA, one needs to separate the plastic strain (ϵ_{pl}) from the elastic (ϵ_{el}) strain. Assuming

that the elastic regime is linear elastic for all cases, it is possible to derive the following equations:

$$\epsilon = \epsilon_{el} + \epsilon_{pl} \tag{B}$$

$$\epsilon_{el} = \sigma/E \tag{C}$$

Equation 2 is easily obtained after combining these two expressions. Furthermore, since the elastic modulus (E) is the initial slope of the stress-strain curve, it can be obtained by differentiating equation 1 with respect to strain and evaluating the resulting function at the origin:

$$\frac{d\sigma}{d\epsilon} = A\frac{\alpha e^{\alpha\epsilon}\left(1 + e^{\beta\epsilon}\right) - \beta e^{\beta\epsilon}(e^{\alpha\epsilon} - 1)}{(1 + e^{\beta\epsilon})^2} \tag{D}$$

$$E = \frac{d\sigma(\epsilon = 0)}{d\epsilon} = A\frac{\alpha(1 + 1) - \beta(1 - 1)}{(1 + 1)^2} = \frac{A\alpha}{2} \tag{E}$$

To generate the input data to characterize the parameters of the constitutive model, we used nonlinear least squares to fit equation 1 to each of the stress-strain curves of the tensile test specimens. Then, we used the resulting values of the parameters A, α, β, ϵ_{ult}, and their respective ρ values to generate the desired gray value-property functions. We also used nonlinear least squares to fit the functions expressed in Table 3.1 to these parameters.

FEA of tensile test experiments: We used a commercially available nonlinear solver (*i.e.*, Abaqus Standard v.6.14, Dassault Systèmes Simulia, France) to create quasi-static finite element models of the gauge length of the tensile test specimens (the narrow region). The pre-processing of every simulation was performed with custom-made Python codes, which read the 3D bitmap structures of the designs and transformed them into equivalent finite element meshes. We used hexagonal hybrid elements with reduced integration (C3D8RH) for discretizing each RVE of the coarse-grained designs. We used the gray value-property relationships obtained in the previous step and the ρ value of each RVE to calculate their respective mechanical properties. Additionally, we assigned element deletion via ductile fracture, where the ultimate plastic displacement of every element was obtained from the ultimate strain function and equation 2. The specimens were loaded by prescribed uniaxial displacement as the boundary condition at the one end of the specimens and applying fixed

3. Nonlinear coarse-graining models for 3D printed multi-material biomimetic composites

displacement (encastre) boundary conditions on the cross-section of the other end. The outputs of the computational models were the forces and displacements of the structure, which we converted into true stresses and strains. The predicted mechanical properties corresponding to the measured values were then calculated using a procedure similar to the one used in the experimental data analysis. For validation, we made one-to-one comparisons between the FEA results and all the available experimental data and calculated the corresponding coefficients of determination (unadjusted R^2 values) using the *fitlm* MATLAB R2018 function to evaluate the accuracy of our models.

Design and FEA of portrait specimens: We discretized a grayscale copy of a part of the renowned painting *Girl with a pearl earring* into two different 3D binary images with different resolutions (*i.e.,* 288×288×6 and 126×126×4) (Figure 3.4). To binarize the image, we first reduced its resolution to the mentioned 2D resolutions and assigned the number of hard voxels randomly depending on the local ρ values. We then applied this process to each layer of every design (*i.e.,* 6 or 4 times) and stacked the results to generate the 3D binary images. To generate the FEA meshes, we coarse-grained these images at different resolutions. For the simulations focused on determining the elastic modulus (*i.e.,* the design with a native resolution of 288×288×6 voxels), we coarse-grained the portrait to the following resolutions: 144×144×6, 96×96×6, and 48×48×6 (greyscale RVEs in all cases). To calculate the yield stress (*i.e.,* the design with a native resolution of 126×126×4 voxels), coarse-graining resulted in the following resolutions: 72×72×4, and 36×36×4 (greyscale RVEs). We represented each RVE with four hexagonal hybrid elements with reduced integration (C3D8RH). These discretizations resulted in meshes with $1.99×10^6$, $4.97×10^5$, $2.21×10^5$, and $5.52×10^4$ elements for the simulations aimed at determining the elastic modulus and $2.54×10^5$, $6.35×10^4$, and $1.58×10^4$ for those performed to calculate the yield stress. The mechanical properties assigned to each RVE were determined using the above-derived gray value-property relationships. We then used these models for performing some simulations that resembled quasi-static tensile tests by applying a constant vertical displacement on the top end of the specimens while constraining all the displacements at the bottom end of the specimens. These boundary conditions were applied to two reference points at the top and bottom of the specimens, respectively, which were fully constrained using coupling interactions (Figure S3.3A of the supporting information). The displacement applied to the top reference point was equivalent

to 0.1% strain for the linear elastic simulations and 2% strain for the yield simulations. The simulation results were subsequently used to calculate the elastic modulus and maximum strength for all the analyses. The computational time required to run each simulation was also measured.

Design, testing, and FEA of bioinspired pre-notched specimens: We used six different bioinspired pre-notched specimen designs that had a total of 1728×864×111 binary voxels, which is equivalent to the following dimensions: 73.152×73.152×2.997 mm^3. These structures included a single-edged crack at the middle of their length that spanned 20% of their width. We used the hard phase to define the gripping part of each specimen according to their original studies.[53,54] We then 3D printed and tested these specimens using the same equipment and methodology as described above for the tensile test specimens. For post-processing, we created virtual strain gauges on the DIC results that encompassed the entire region of each design to extract the engineering strain vectors of every specimen. We used the force vectors obtained from the testing machine to calculate the respective engineering stress vectors ($\sigma = fA_o^{-1}, A_o = 219.23$ mm^2) and to calculate the elastic modulus and maximum strength for each specimen. After post-processing the experimental results, we modeled these tests using finite element models. To generate the geometries used in the models, we coarse-grained the specimens from 1728×864×111voxels to 864×432 RVEs and used the previously obtained gray value-property relationships to determine the mechanical properties that were subsequently assigned to the RVEs. We used quadrilateral plane stress elements with reduced integration (CPS4R) for meshing and enabled element deletion via ductile failure, where the ultimate plastic displacement of every element was obtained from the ultimate strain function and equation 2. As for the boundary conditions, we prescribed uniaxial displacement until separation at the top end of the specimens while constraining all the movements of the bottom surface. We made one-to-one comparisons between the predicted and measured mechanical properties while also comparing their corresponding stress-strain curves. We also calculated the coefficients of determination between the modeling and experimental results to assess the accuracy of the finite element predictions.

Design, remodeling, testing, and FEA validation of a femoral bone: The original femoral bone design consisted of a long femur bone STL obtained from a free CAD website,[73] which we converted into a 3D image using a program provided by Adam A.[74] The final 2D image

was a slice cut on the frontal plane of the proximal section of the femur. The resolution of the image was 206×118 voxels. For the remodeling process, the FEA simulations were performed using a 2D mesh of quadrilateral plane strain elements with reduced integration (CPE4R) and were loaded according to Figure 3.6A. The position and orientation of these loads are chosen such that they represent the equivalent compressive loads experienced by the femoral head and the tensile loads applied in the greater trochanter region [75–77]. The magnitudes of the loads were selected such that the maximum deformation within the femoral head region did not exceed 3% strain. Similarly, the initial value of ρ across the entire geometry was set to 50%. After every remodeling iteration, we updated the ρ_i value of every element (*i.e.,* subindex *i*) depending on their normalized strain energy density (S_i), inspired by the homeostasis-based approaches for modeling the bone tissue adaptation process.[78] We defined the normalized strain energy density with the following expression:

$$S_i = \frac{U_i}{U_{max}(\rho_i)} \tag{F}$$

In this expression, U_i is the strain energy density of each element while $U_{max}(\rho_i)$ is the maximum value of the strain energy density that the material can withstand (Figure 3.6B) and is obtained by integrating the stress-strain curve:

$$U_{max}(\rho_i) = \int_0^{\epsilon_{ult}} A \frac{e^{\alpha\epsilon} - 1}{1 + e^{\beta\epsilon}} d\epsilon \tag{G}$$

For every iteration, we updated the rate of the change in the volume fraction of the hard phase ($\dot{\rho}_i$) corresponding to each element using the following relationships:

$$S_{avg} = \sum_{i=1}^{N} \frac{S_i}{N} \tag{H}$$

$$\dot{\rho}_i = \left(\frac{S_i}{S_{avg}} - 1\right)\dot{\rho}_s \tag{I}$$

where S_{avg} is the average normalized strain energy density across the entire bone and $\dot{\rho}_s = 0.05$ is the slope of the rate of change function. Then, we incorporated a "lazy zone" in which no change in the hard volume fraction occurs and truncated the upper and lower boundaries of $\dot{\rho}_i$ possible in each iteration. These processes involve adding the following conditional expression:

$$\dot{\rho}_i = \begin{cases} 0 & |\dot{\rho}_i| < \dot{\rho}_{lazy} \\ \dot{\rho}_i & \dot{\rho}_{lazy} \leq |\dot{\rho}_i| \leq \dot{\rho}_{max} \\ \pm\dot{\rho}_{max} & |\dot{\rho}_i| > \dot{\rho}_{max} \end{cases} \tag{J}$$

$$\rho_i = \rho_i + \dot{\rho}_i \tag{K}$$

where $\dot{\rho}_{lazy} = 0.005$ is the limit value of $\dot{\rho}$ where no change of ρ occurs and $\dot{\rho}_{max} = 0.1$ is the maximum (or minimum) value of $\dot{\rho}$ enabled for each iteration. Finally, we updated the ρ_i values corresponding to each element using the following relationship:

$$\rho_i = \rho_i + \dot{\rho}_i \tag{L}$$

We continued this iterative remodeling process until the total change of hard material volume fraction ($\sum_{i=1}^{N} |\dot{\rho}_i|$) dropped to 5% when compared to the corresponding value of the initial iteration (Figure 3.6C). Consequently, a total of 42 remodeling iterations were required for convergence. Once the bone remodeling concluded, we performed the above-described inverse coarse-graining operation to obtain the 3D printable geometries of the specimens corresponding to the first and last iterations. We tested these designs under quasi-static compression under the same conditions and with the same equipment as the tensile tests and extracted the resulting forces and displacements. For a final validation of the coarse-graining equations, we performed additional FEA of these tests under the same compression loading conditions. For this purpose, we coarse-grained back the 618×354×432 voxels of these designs into an equivalent of 206×118×4 RVEs and discretized the resulting geometries using the C3D8RH elements. We used 432 voxels in the thickness direction to prevent off-plane deformations (e.g., buckling) during the quasi-static compression of the specimens. The four RVEs in the thickness direction were selected because no complex features were present along that direction, allowing for a computationally efficient simulation.

3. Nonlinear coarse-graining models for 3D printed multi-material biomimetic composites

References

[1]   J.R. Greer, V.S. Deshpande, Three-dimensional architected materials and structures: Design, fabrication, and mechanical behavior, MRS Bull. 44 (2019) 750–757. https://doi.org/10.1557/mrs.2019.232.

[2]   T.A. Schaedler, W.B. Carter, Architected Cellular Materials, Annu. Rev. Mater. Res. 46 (2016) 187–210. https://doi.org/10.1146/annurev-matsci-070115-031624.

[3]   N.A. Fleck, V.S. Deshpande, M.F. Ashby, Micro-architectured materials: past, present and future, Proc. R. Soc. A Math. Phys. Eng. Sci. 466 (2010) 2495–2516. https://doi.org/10.1098/RSPA.2010.0215.

[4]   M. Rafiee, R.D. Farahani, D. Therriault, Multi-Material 3D and 4D Printing: A Survey, Adv. Sci. 7 (2020) 1902307. https://doi.org/10.1002/ADVS.201902307.

[5]   W. Gao, Y. Zhang, D. Ramanujan, K. Ramani, Y. Chen, C.B. Williams, C.C.L. Wang, Y.C. Shin, S. Zhang, P.D. Zavattieri, The status, challenges, and future of additive manufacturing in engineering, CAD Comput. Aided Des. 69 (2015) 65–89. https://doi.org/10.1016/j.cad.2015.04.001.

[6]   D. Han, H. Lee, Recent advances in multi-material additive manufacturing: methods and applications, Curr. Opin. Chem. Eng. 28 (2020) 158–166. https://doi.org/10.1016/J.COCHE.2020.03.004.

[7]   J. Chen, X. Liu, Y. Tian, W. Zhu, C. Yan, Y. Shi, L.B. Kong, H.J. Qi, K. Zhou, 3D-Printed Anisotropic Polymer Materials for Functional Applications, Adv. Mater. (2021) 2102877. https://doi.org/10.1002/ADMA.202102877.

[8]   K.R. Ryan, M.P. Down, C.E. Banks, Future of additive manufacturing: Overview of 4D and 3D printed smart and advanced materials and their applications, Chem. Eng. J. 403 (2021) 126162. https://doi.org/10.1016/J.CEJ.2020.126162.

[9]   O. Sigmund, Tailoring materials with prescribed elastic properties, Mech. Mater. 20 (1995) 351–368. https://doi.org/10.1016/0167-6636(94)00069-7.

[10]   L. Valdevit, A.J. Jacobsen, J.R. Greer, W.B. Carter, Protocols for the Optimal Design of Multi-Functional Cellular Structures: From Hypersonics to Micro-Architected Materials, J. Am. Ceram. Soc. 94 (2011) s15–s34. https://doi.org/10.1111/J.1551-2916.2011.04599.X.

[11]   M. Osanov, J.K. Guest, Topology Optimization for Architected Materials Design, 2016. https://www.annualreviews.org/doi/abs/10.1146/annurev-matsci-070115-031826 (accessed May 25, 2021).

[12]   S. Shan, S.H. Kang, J.R. Raney, P. Wang, L. Fang, F. Candido, J.A. Lewis, K. Bertoldi, Multistable Architected Materials for Trapping Elastic Strain Energy, Adv. Mater. 27 (2015) 4296–4301. https://doi.org/10.1002/adma.201501708.

[13]   K. Bertoldi, Harnessing Instabilities to Design Tunable Architected Cellular Materials, Annu. Rev. Mater. Res. 47 (2017) 51–61. https://doi.org/10.1146/ANNUREV-MATSCI-070616-123908.

[14]   M. Maurizi, C. Gao, F. Berto, Interlocking mechanism design based on deep-learning methods, Appl. Eng. Sci. 7 (2021) 100056. https://doi.org/10.1016/J.APPLES.2021.100056.

[15]   G.D. Goh, S.L. Sing, W.Y. Yeong, A review on machine learning in 3D printing: applications, potential, and challenges, Artif. Intell. Rev. 54 (2020) 63–94. https://doi.org/10.1007/s10462-020-09876-9.

[16]   Z. Jin, Z. Zhang, K. Demir, G.X. Gu, Machine Learning for Advanced Additive Manufacturing, Matter. 3 (2020) 1541–1556. https://doi.org/10.1016/j.matt.2020.08.023.

[17]   J. Deering, K.I. Dowling, L.A. DiCecco, G.D. McLean, B. Yu, K. Grandfield, Selective Voronoi tessellation as a method to design anisotropic and biomimetic implants, J. Mech. Behav. Biomed. Mater. 116 (2021) 104361. https://doi.org/10.1016/j.jmbbm.2021.104361.

[18]   Y. Chiang, C.C. Tung, X. Di Lin, P.Y. Chen, C.S. Chen, S.W. Chang, Geometrically toughening mechanism of cellular composites inspired by Fibonacci lattice in Liquidambar formosana, Compos. Struct. 262 (2021) 113349. https://doi.org/10.1016/J.COMPSTRUCT.2020.113349.

[19]   M.T. Hsieh, B. Endo, Y. Zhang, J. Bauer, L. Valdevit, The mechanical response of cellular materials with spinodal topologies, J. Mech. Phys. Solids. 125 (2019) 401–419. https://doi.org/10.1016/j.jmps.2019.01.002.

[20]   Z. Jia, Y. Yu, L. Wang, Learning from nature: Use material architecture to break the performance tradeoffs, Mater. Des. 168 (2019) 107650. https://doi.org/10.1016/j.matdes.2019.107650.

[21]   W. Huang, D. Restrepo, J.Y. Jung, F.Y. Su, Z. Liu, R.O. Ritchie, J. McKittrick, P. Zavattieri, D. Kisailus, Multiscale Toughening Mechanisms in Biological Materials and Bioinspired Designs, Adv. Mater. 31 (2019) 1901561. https://doi.org/10.1002/ADMA.201901561.

[22]   Y. Li, Z. Feng, L. Hao, L. Huang, C. Xin, Y. Wang, E. Bilotti, K. Essa, H. Zhang, Z. Li, F. Yan, T. Peijs, A Review on Functionally Graded Materials and Structures via Additive Manufacturing: From Multi-Scale Design to Versatile Functional Properties, Adv. Mater. Technol. 5 (2020) 1900981. https://doi.org/10.1002/admt.201900981.

[23]   E. Pei, I.R. Kabir, D. Godec, J. Gonzalez-Gutierrez, A. Nordin, Functionally graded additive manufacturing, Addit. Manuf. with Funct. Nanomater. (2021) 35–54. https://doi.org/10.1016/B978-0-12-823152-4.00006-5.

[24]   S.E. Naleway, M.M. Porter, J. McKittrick, M.A. Meyers, Structural Design Elements in Biological Materials: Application to Bioinspiration, Adv. Mater. 27 (2015) 5455–5476. https://doi.org/10.1002/adma.201502403.

[25]   F. Libonati, M.J. Buehler, Advanced Structural Materials by Bioinspiration , Adv. Eng. Mater. 19 (2017) 1600787. https://doi.org/10.1002/adem.201600787.

[26]   J. Aizenberg, P. Fratzl, Biological and biomimetic materials, Adv. Mater. 21 (2009) 387–388. https://doi.org/10.1002/adma.200803699.

[27]   A. Vigliotti, D. Pasini, Mechanical properties of hierarchical lattices, Mech. Mater. 62 (2013) 32–43. https://doi.org/10.1016/J.MECHMAT.2013.03.003.

[28]   A.R. Studart, R. Libanori, R.M. Erb, Functional Gradients in Biological Composites, in: Bio-Bioinspired Nanomater., Wiley-VCH Verlag GmbH & Co. KGaA, Weinheim, Germany, 2014: pp. 335–368. https://doi.org/10.1002/9783527675821.ch13.

[29]   Z. Liu, M.A. Meyers, Z. Zhang, R.O. Ritchie, Functional gradients and heterogeneities in biological materials: Design principles, functions, and bioinspired applications, Elsevier Ltd, 2017. https://doi.org/10.1016/j.pmatsci.2017.04.013.

3. Nonlinear coarse-graining models for 3D printed multi-material biomimetic composites

[30]   R.O. Ritchie, Toughening materials: enhancing resistance to fracture, Philos. Trans. R. Soc. A. 379 (2021). https://doi.org/10.1098/RSTA.2020.0437.

[31]   C. Pitta Kruize, S. Panahkhahi, N.E. Putra, P. Diaz-Payno, G. Van Osch, A.A. Zadpoor, M.J. Mirzaali, Biomimetic Approaches for the Design and Fabrication of Bone-to-Soft Tissue Interfaces, ACS Biomater. Sci. Eng. (2021). https://doi.org/10.1021/ACSBIOMATERIALS.1C00620.

[32]   A. Tits, D. Ruffoni, Joining soft tissues to bone: Insights from modeling and simulations, Bone Reports. 14 (2021) 100742. https://doi.org/10.1016/j.bonr.2020.100742.

[33]   A. Tits, E. Plougonven, S. Blouin, M.A. Hartmann, J.F. Kaux, P. Drion, J. Fernandez, G.H. van Lenthe, D. Ruffoni, Local anisotropy in mineralized fibrocartilage and subchondral bone beneath the tendon-bone interface, Sci. Reports 2021 111. 11 (2021) 1–17. https://doi.org/10.1038/s41598-021-95917-4.

[34]   B.S. Lazarus, A. Velasco-Hogan, T. Gómez-del Río, M.A. Meyers, I. Jasiuk, A review of impact resistant biological and bioinspired materials and structures, J. Mater. Res. Technol. 9 (2020) 15705–15738. https://doi.org/10.1016/j.jmrt.2020.10.062.

[35]   G. Grezzana, H.-C. Loh, Z. Qin, M.J. Buehler, A. Masic, F. Libonati, Probing the Role of Bone Lamellar Patterns through Collagen Microarchitecture Mapping, Numerical Modeling, and 3D-Printing, Adv. Eng. Mater. 22 (2020) 2000387. https://doi.org/10.1002/adem.202000387.

[36]   N.S. Ha, G. Lu, A review of recent research on bio-inspired structures and materials for energy absorption applications, Compos. Part B Eng. 181 (2020). https://doi.org/10.1016/j.compositesb.2019.107496.

[37]   A. Velasco-Hogan, J. Xu, M.A. Meyers, Additive Manufacturing as a Method to Design and Optimize Bioinspired Structures, Adv. Mater. 30 (2018). https://doi.org/10.1002/adma.201800940.

[38]   G.X. Gu, I. Su, S. Sharma, J.L. Voros, Z. Qin, M.J. Buehler, Three-dimensional-printing of bio-inspired composites, J. Biomech. Eng. 138 (2016). https://doi.org/10.1115/1.4032423.

[39]   Z. Jia, L. Wang, 3D printing of biomimetic composites with improved fracture toughness, Acta Mater. 173 (2019) 61–73. https://doi.org/10.1016/j.actamat.2019.04.052.

[40]   F. Liu, T. Li, Z. Jia, L. Wang, Combination of stiffness, strength, and toughness in 3D printed interlocking nacre-like composites, Extrem. Mech. Lett. 35 (2020) 100621. https://doi.org/10.1016/j.eml.2019.100621.

[41]   D. Kokkinis, F. Bouville, A.R. Studart, 3D Printing of Materials with Tunable Failure via Bioinspired Mechanical Gradients, Adv. Mater. 30 (2018) 1705808. https://doi.org/10.1002/ADMA.201705808.

[42]   A. Aghaei, N. Bochud, G. Rosi, Q. Grossman, D. Ruffoni, S. Naili, Ultrasound characterization of bioinspired functionally graded soft-to-hard composites: Experiment and modeling, J. Acoust. Soc. Am. 151 (2022) 1490. https://doi.org/10.1121/10.0009630.

[43]   F. Liu, T. Li, X. Jiang, Z. Jia, Z. Xu, L. Wang, The effect of material mixing on interfacial stiffness and strength of multi-material additive manufacturing, Addit. Manuf. 36 (2020) 101502. https://doi.org/10.1016/J.ADDMA.2020.101502.

[44]   X. Kuang, J. Wu, K. Chen, Z. Zhao, Z. Ding, F. Hu, D. Fang, H.J. Qi, Grayscale digital light processing 3D printing for highly functionally graded materials, Sci. Adv. 5 (2019). https://doi.org/10.1126/SCIADV.AAV5790/SUPPL_FILE/AAV5790_SM.PDF.

[45]   D.T. Nguyen, T.D. Yee, N.A. Dudukovic, K. Sasan, A.W. Jaycox, A.M. Golobic, E.B. Duoss, R. Dylla-Spears, D.T. Nguyen, T.D. Yee, N.A. Dudukovic, K. Sasan, A.W. Jaycox, A.M. Golobic, E.B. Duoss, R. Dylla-Spears, 3D Printing of Compositional Gradients Using the Microfluidic Circuit Analogy, Adv. Mater. Technol. 4 (2019) 1900784. https://doi.org/10.1002/ADMT.201900784.

[46]   K. Ko, S. Jin, S.E. Lee, I. Lee, J.W. Hong, Bio-inspired bimaterial composites patterned using three-dimensional printing, Compos. Part B Eng. 165 (2019) 594–603. https://doi.org/10.1016/J.COMPOSITESB.2019.02.008.

[47]   T.S. Lumpe, J. Mueller, K. Shea, Tensile properties of multi-material interfaces in 3D printed parts, Mater. Des. 162 (2019) 1–9. https://doi.org/10.1016/J.MATDES.2018.11.024.

[48]   L. Zorzetto, L. Andena, F. Briatico-Vangosa, L. De Noni, J.M. Thomassin, C. Jérôme, Q. Grossman, A. Mertens, R. Weinkamer, M. Rink, D. Ruffoni, Properties and role of interfaces in multimaterial 3D printed composites, Sci. Reports 2020 101. 10 (2020) 1–17. https://doi.org/10.1038/s41598-020-79230-0.

[49]   M.A. Skylar-Scott, J. Mueller, C.W. Visser, J.A. Lewis, Voxelated soft matter via multimaterial multinozzle 3D printing, Nature. 575 (2019) 330–335. https://doi.org/10.1038/s41586-019-1736-8.

[50]   P. Fratzl, H.S. Gupta, E.P. Paschalis, P. Roschger, Structure and mechanical quality of the collagen-mineral nano-composite in bone, J. Mater. Chem. 14 (2004) 2115–2123. https://doi.org/10.1039/b402005g.

[51]   H.S. Gupta, J. Seto, W. Wagermaier, P. Zaslansky, P. Boesecke, P. Fratzl, Cooperative deformation of mineral and collagen in bone at the nanoscale, Proc. Natl. Acad. Sci. U. S. A. 103 (2006) 17741–17746. https://doi.org/10.1073/pnas.0604237103.

[52]   M.J. Mirzaali, V. Mussi, P. Vena, F. Libonati, L. Vergani, M. Strano, Mimicking the loading adaptation of bone microstructure with aluminum foams, Mater. Des. 126 (2017) 207–218. https://doi.org/10.1016/j.matdes.2017.04.039.

[53]   M.J. Mirzaali, M. Cruz Saldívar, A. Herranz de la Nava, D. Gunashekar, M. Nouri-Goushki, E.L. Doubrovski, A.A. Zadpoor, Multi-Material 3D Printing of Functionally Graded Hierarchical Soft–Hard Composites, Adv. Eng. Mater. 22 (2020) 1901142. https://doi.org/10.1002/adem.201901142.

[54]   Mirzaali, Nava, Gunashekar, Nouri-Goushki, Doubrovski, Zadpoor, Fracture Behavior of Bio-Inspired Functionally Graded Soft–Hard Composites Made by Multi-Material 3D Printing: The Case of Colinear Cracks, Materials (Basel). 12 (2019) 2735. https://doi.org/10.3390/ma12172735.

[55]   R. Mirzeifar, L.S. Dimas, Z. Qin, M.J. Buehler, Defect-Tolerant Bioinspired Hierarchical Composites: Simulation and Experiment, ACS Biomater. Sci. Eng. 1 (2015) 295–304. https://doi.org/10.1021/ab500120f.

[56]   F. Libonati, G.X. Gu, Z. Qin, L. Vergani, M.J. Buehler, Bone-Inspired Materials by Design: Toughness Amplification Observed Using 3D Printing and Testing , Adv. Eng. Mater. 18 (2016) 1354–1363. https://doi.org/10.1002/adem.201600143.

[57]   M.J. Mirzaali, A. Herranz de la Nava, D. Gunashekar, M. Nouri-Goushki, R.P.E. Veeger, Q. Grossman, L. Angeloni, M.K. Ghatkesar, L.E. Fratila-Apachitei, D. Ruffoni, E.L. Doubrovski, A.A. Zadpoor, Mechanics of bioinspired functionally graded soft-hard composites made by multi-material 3D printing, Compos. Struct. 237 (2020) 111867. https://doi.org/10.1016/J.COMPSTRUCT.2020.111867.

3. Nonlinear coarse-graining models for 3D printed multi-material biomimetic composites

[58]   G.X. Gu, L. Dimas, Z. Qin, M.J. Buehler, Optimization of Composite Fracture Properties: Method, Validation, and Applications, J. Appl. Mech. Trans. ASME. 83 (2016). https://doi.org/10.1115/1.4033381.

[59]   D.W. Abueidda, M. Almasri, R. Ammourah, U. Ravaioli, I.M. Jasiuk, N.A. Sobh, Prediction and optimization of mechanical properties of composites using convolutional neural networks, Compos. Struct. 227 (2019) 111264. https://doi.org/10.1016/j.compstruct.2019.111264.

[60]   C.T. Chen, G.X. Gu, Machine learning for composite materials, MRS Commun. 9 (2019) 556–566. https://doi.org/10.1557/mrc.2019.32.

[61]   K. Guo, Z. Yang, C.-H. Yu, M.J. Buehler, Artificial intelligence and machine learning in design of mechanical materials, Mater. Horizons. (2021). https://doi.org/10.1039/d0mh01451f.

[62]   M.J. Mirzaali, M.E. Edens, A.H. de la Nava, S. Janbaz, P. Vena, E.L. Doubrovski, A.A. Zadpoor, Length-scale dependency of biomimetic hard-soft composites, Sci. Rep. 8 (2018) 12052. https://doi.org/10.1038/s41598-018-30012-9.

[63]   Q. Liu, G. Subhash, A phenomenological constitutive model for foams under large deformations, Polym. Eng. Sci. 44 (2004) 463–473. https://doi.org/10.1002/PEN.20041.

[64]   W.E.A. Davies, The theory of elastic composite materials, J. Phys. D. Appl. Phys. 4 (1971) 1325. https://doi.org/10.1088/0022-3727/4/9/313.

[65]   **M.G.D. Geers, V.G. Kouznetsova, K. Matouš, J. Yvonnet, Homogenization Methods and Multiscale Modeling: Nonlinear Problems**, Encycl. Comput. Mech. Second Ed. (2017) 1–34. https://doi.org/10.1002/9781119176817.ECM2107.

[66]   M. Jamshidian, N. Boddeti, D.W. Rosen, O. Weeger, Multiscale modelling of soft lattice metamaterials: Micromechanical nonlinear buckling analysis, experimental verification, and macroscale constitutive behaviour, Int. J. Mech. Sci. 188 (2020) 105956. https://doi.org/10.1016/J.IJMECSCI.2020.105956.

[67]   F. Greco, L. Leonetti, A. Pranno, S. Rudykh, Mechanical behavior of bio-inspired nacre-like composites: A hybrid multiscale modeling approach, Compos. Struct. 233 (2020) 111625. https://doi.org/10.1016/J.COMPSTRUCT.2019.111625.

[68]   J. Fu, H. Li, L. Gao, M. Xiao, Design of shell-infill structures by a multiscale level set topology optimization method, Comput. Struct. 212 (2019) 162–172. https://doi.org/10.1016/J.COMPSTRUC.2018.10.006.

[69]   L. Cera, G.M. Gonzalez, Q. Liu, S. Choi, C.O. Chantre, J. Lee, R. Gabardi, M.C. Choi, K. Shin, K.K. Parker, A bioinspired and hierarchically structured shape-memory material, Nat. Mater. 2020 202. 20 (2020) 242–249. https://doi.org/10.1038/s41563-020-0789-2.

[70]   H. Weinans, R. Huiskes, H.J. Grootenboer, The behavior of adaptive bone-remodeling simulation models, J. Biomech. 25 (1992) 1425–1441. https://doi.org/10.1016/0021-9290(92)90056-7.

[71]   J. Park, A. Sutradhar, J.J. Shah, G.H. Paulino, Design of complex bone internal structure using topology optimization with perimeter control, Comput. Biol. Med. 94 (2018) 74–84. https://doi.org/10.1016/J.COMPBIOMED.2018.01.001.

[72]   ASTM D638, ASTM D638 - 14 Standard Test Method for Tensile Properties of Plastics, ASTM Stand. (2004). https://www.astm.org/Standards/D638 (accessed September 28, 2021).

[73]   Femur (bone) | 3D CAD Model Library | GrabCAD, (2019). https://grabcad.com/library/femur-bone-5 (accessed April 8, 2021).

[74]   A. Adam, Mesh voxelisation, MATLAB Cent. File Exch. (2013). https://nl.mathworks.com/matlabcentral/fileexchange/27390-mesh-voxelisation (accessed April 8, 2021).

[75]   K.I. Tsubota, T. Adachi, Y. Tomita, Functional adaptation of cancellous bone in human proximal femur predicted by trabecular surface remodeling simulation toward uniform stress state, J. Biomech. 35 (2002) 1541–1551. https://doi.org/10.1016/S0021-9290(02)00173-2.

[76]   H. Kainz, B.A. Killen, M. Wesseling, F. Perez-Boerema, L. Pitto, J.M.G. Aznar, S. Shefelbine, I. Jonkers, A multi-scale modelling framework combining musculoskeletal rigid-body simulations with adaptive finite element analyses, to evaluate the impact of femoral geometry on hip joint contact forces and femoral bone growth, PLoS One. 15 (2020) e0235966. https://doi.org/10.1371/JOURNAL.PONE.0235966.

[77]   B. Mathai, S. Dhara, S. Gupta, Bone remodelling in implanted proximal femur using topology optimization and parameterized cellular model, J. Mech. Behav. Biomed. Mater. 125 (2022) 104903. https://doi.org/10.1016/J.JMBBM.2021.104903.

[78]   R. Huiskes, R. Rulmerman, G.H. Van Lenthe, J.D. Janssen, Effects of mechanical forces on maintenance and adaptation of form in trabecular bone, Nat. 2000 4056787. 405 (2000) 704–706. https://doi.org/10.1038/35015116.

3.5 Supporting Information

List of tables

Table S3.1. The stress-strain parameters used to generate the gray value-property relationships.

Hard volume fraction ρ [%]	Elastic modulus E [MPa]	Ultimate strain ϵ_{ult} [%]	A [MPa]	α [-]	β [-]	α/β [-]
100	2551.4	44.87	53.0043	101.132	100.9521	1.00178
	2304.0	44.25	52.6095	92.6680	92.46914	1.00215
	2873.0	42.58	54.5556	99.8240	99.61041	1.00214
80	1900.5	46.75	39.6295	83.5239	83.26803	1.00307
	1505.0	46.32	38.5210	77.8658	77.55830	1.00396
	1679.7	48.1	38.2841	78.1795	77.88944	1.00372
60	859.0718	43.38	20.2856	91.0357	90.28438	1.00832
	1080.6	47.76	19.4017	82.5668	81.72414	1.01031
	364.3084	49.87	19.9986	44.2234	43.45982	1.01757
40	136.2017	51.4	7.2762	25.2922	23.66572	1.06873
	289.1867	45.38	7.0272	35.8492	34.01885	1.05380
	435.6102	46.71	7.2068	33.6541	31.94064	1.05364
20	13.4849	50.28	3.7988	4.63241	3.610059	1.28319
	14.9081	47.13	4.7896	4.95781	3.985408	1.24399
	14.1926	50.51	6.4106	4.38324	4.124398	1.06275
10	6.0528	74.08	2.6111	3.66420	3.002437	1.22041
	4.4305	84.18	1.6784	3.49397	2.238234	1.56103
	4.7784	76.47	1.7702	3.70300	2.449381	1.51181
0	0.9631	114.54	0.7124	1.99523	4.965e-08	4e07 [a]
	0.9106	120.69	0.7478	1.92538	2.100e-08	9e07 [a]
	1.0411	106.84	0.6247	2.18548	5.229e-08	4e07 [a]

[a] These data points were removed from the α/β parametrization since their inclusion made fitting impossible.

Table S3.2. Quasi-static tensile tests: experimental **vs.** FEA results.

Hard volume fraction ρ [%]	Experimental (Exp)				Finite Element Analysis (FEA)			
	Elastic modulus E [MPa]	Maximum strength σ_{max} [MPa]	Ultimate strain ϵ_{ult} [%]	Strain energy density U_d [MJm^{-3}]	Elastic modulus E [MPa]	Maximum strength σ_{max} [MPa]	Ultimate strain ϵ_{ult} [%]	Strain energy density U_d [MJm^{-3}]
100	2616.69	56.43	8.727	3.927	2759.48	55.07	7.979	3.669
	2543.07	54.17	9.948	4.308				
	2622.77	55.54	12.257	5.444				
80	1881.95	39.06	17.386	5.668	1587.62	38.25	9.27	3.016
	1879.41	39	16.72	5.51				
	1923.55	39.51	14.193	4.644				
60	1013.02	21.72	19.482	3.804	675.52	24.18	14.612	2.977
	1007.16	22.12	19.342	3.793				
	1033.9	22.09	17.621	3.52				
40	218.23	12.23	22.809	2.058	127.07	13.31	34.376	3.292
	257.85	12.4	23.751	2.243				
	209.13	12.12	22.306	1.946				
20	15.93	4.66	30.66	0.773	14.44	5.33	36.863	0.982
	15.39	4.86	31.174	0.799				
	12.09	3.59	21.72	0.36				
10	4.57	2.4	40.205	0.432	6.39	2.83	44.378	0.617
	4.48	2.36	40.553	0.437				
	4.06	2.42	41.297	0.433				
0	1.71	2.26	76.5	0.538	1.23	1.03	83.74	0.433
	1.81	2.84	83.247	0.69				
	1.58	2.2	79.371	0.547				

3. Nonlinear coarse-graining models for 3D printed multi-material biomimetic composites

Table S3.3. The effects of the degree of coarse-graining on the estimated properties and computational time.

Portrait 3D resolution [voxels]	Number of hexagonal elements	Elastic modulus E [MPa]	Yield strength σ_y [MPa]	CPU time [sec]
288×288×6	1.99×10^6	843.45	-	12224
	4.97×10^5	890.51	-	1307.5
	2.21×10^5	755.92	-	318.9
	5.52×10^4	742.44	-	55.3
126×126×4	2.54×10^5	574.92	7.05	717976
	6.35×10^4	617.19	8.43	194599
	1.58×10^4	500.89	8.50	2182

Table S3.4. The experimental and coarse-grained FEA results obtained for the **bioinspired pre-notched** specimens.

Design	Experimental		FEA	
	Elastic modulus E [MPa]	Yield strength σ_y [MPa]	Elastic modulus E [MPa]	Yield strength σ_y [MPa]
$\rho = 100\%$	2561.23	10.07	2503.25	13.14
$\rho = 75\%$	1608.49	10.06	1157.17	9.14
$\rho = 50\%$	533.13	7.58	261.49	3.43
FG	698.57	7.52	528.27	4.43
BMG-1L	1264.55	8.44	870.93	6.87
BMG-2L	1148.83	8.72	917.90	6.44

Table S3.5. The experimental and coarse-graind FEA results pertaining to the design of a 3D printed femur.

Design	Experimental		FEA	
	Stiffness [Nmm^{-1}]	Maximum force [N]	Stiffness [Nmm^{-1}]	Maximum force [N]
Initial design (iteration 1)	518.24	516.67	485.09	418.43
Final design (iteration 42)	221.61	719.67	205.67	612.85
Total change ratio (Final/Initial)	42.76%	146.46	42.40%	139.21%

List of supporting figures
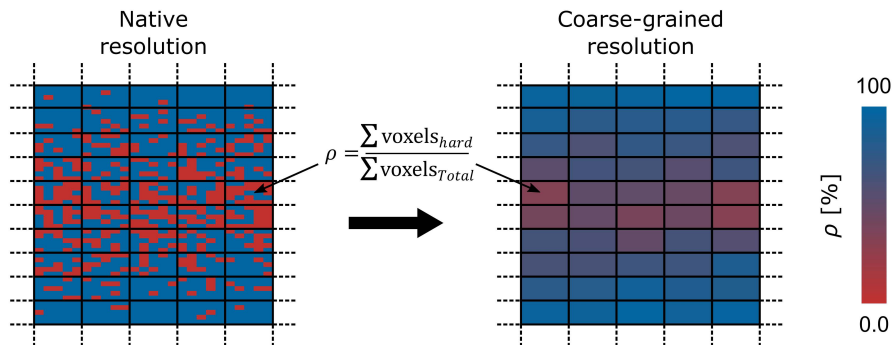
Figure S3.1. A schematic representation of the coarse-graining process where the average ρ value of every coarse-grained representative volumetric element was calculated and used to determine its coarse-grained mechanical properties based on the gray value-property relationships.

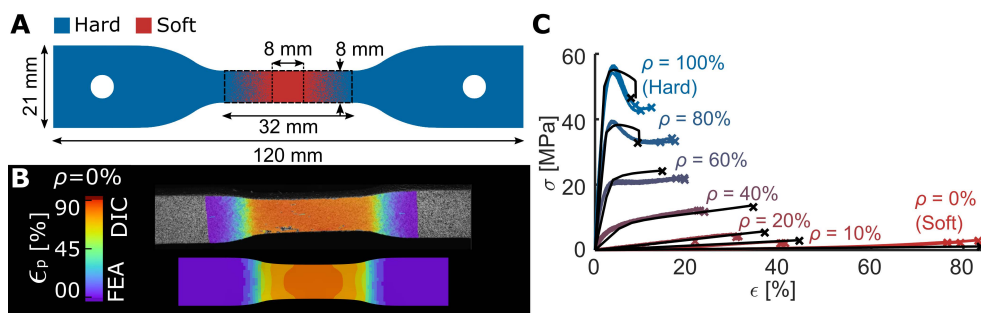# 3. Nonlinear coarse-graining models for 3D printed multi-material biomimetic composites

Figure S3.2. A) A standard tensile test specimen with ρ = 0% in the centermost (8mm) region of its gauge length, connected to the grippers via monotonic gradients of ρ. B) The distribution of the first principal true strain (ϵ_p) was measured experimentally using DIC and was estimated with coarse-grained FEA. C) The stress-strain curves of the tensile tests were measured with digital strain gauges across the entire design length of the specimen. Different line and color gradients refer to the specimens with different ρ values. The black lines show the FEA predictions.
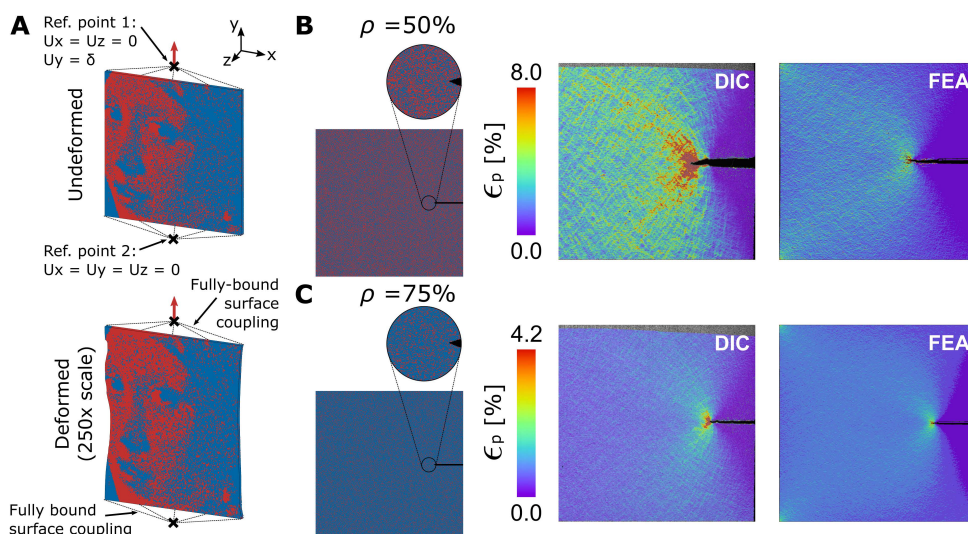

Figure S3.3. A) The boundary conditions applied to the portrait specimens, where two reference points were fully constrained to the top and bottom surfaces of the specimens, respectively. The vertical displacement, δ, applied to the top reference point was equivalent to 0.1% strain for the linear elastic simulations and 2% strain for the yield simulations. B-C) A case study in which the DIC and FEA results are compared with each other. The strain distributions pertain to the first principal true strains of pre-notched bio-AM specimens made with ρ = 50% (B) and ρ = 75% (C).

PART II

On the Behavior of Bioinspired Bitmap Composites

"The best things in life are beyond money; their price is agony and sweat and devotion, and the price demanded for the most precious of all things in life is life itself — Ultimate cost for perfect value."
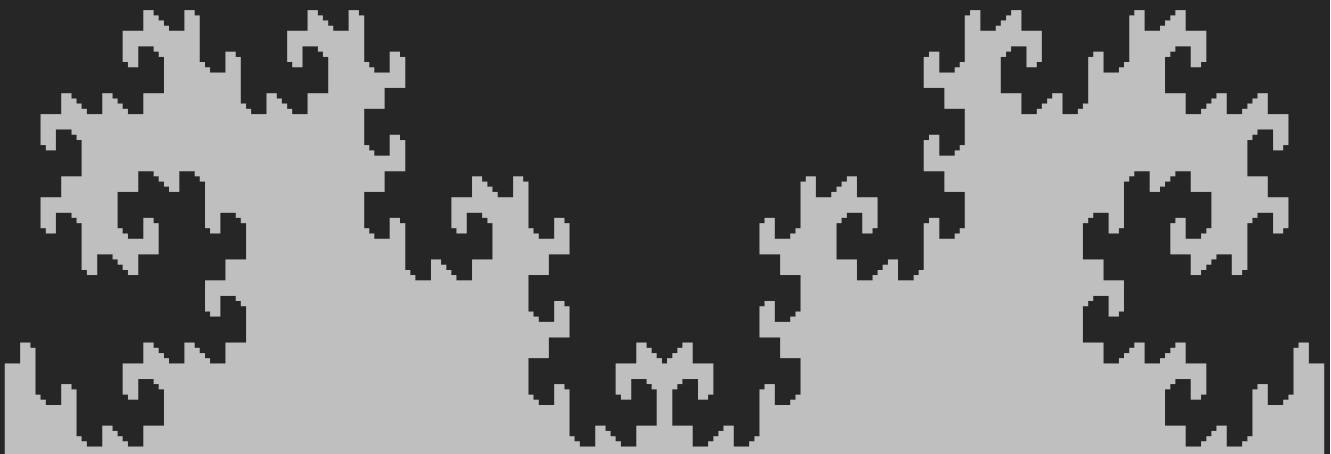
-**Robert A. Heinlein, Starship Troopers.**

4

Bioinspired rational design of bi-material 3D printed soft-hard interfaces

Abstract

Durable interfacing of hard and soft materials is a major design challenge caused by the ensuing stress concentrations. In nature, soft-hard interfaces exhibit remarkable mechanical performance, with failures rarely happening at the interface. Here, we mimic the strategies observed in nature to design efficient soft-hard interfaces. We based our geometrical designs on triply periodic minimal surfaces (i.e., Octo, Diamond, and Gyroid), collagen-like triple helices, and randomly distributed particles. A combination of computational simulations and experimental techniques, including uniaxial tensile and quad-lap shear tests, were used to characterize the mechanical performance of the interfaces. Our analyses suggest that smooth interdigitated connections, compliant gradient transitions, and either decreasing or constraining strain concentrations lead to simultaneously strong and tough interfaces. We generated additional interfaces where the abovementioned toughening mechanisms work synergistically to create soft-hard interfaces with strengths approaching the upper achievable limit and toughness values enhanced by 50%, as compared to the control group.

4.1. Introduction

Joining materials with dissimilar mechanical properties is inherently challenging due to the complexities present at the soft-hard interfaces [1–3]. These complexities include the different load-carrying capacities of both materials, interfacial damages caused by the failure of any adhesives present at the interface, and the stress concentrations caused by the sudden changes in the material properties [4–7]. Among those factors, the lattermost is particularly concerning because interfacial microarchitecture and geometry play key roles in the development of stress singularities [8]. In contrast, several millennia of evolution has endowed natural architected structures with remarkable mechanical properties that originate from their complex yet highly efficient arrangements of mechanically dissimilar phases [9–11]. Given the failure of engineered constructs in reproducing the high level of efficiency exhibited by natural materials, it is important to understand and mimic the naturally occurring design strategies.

A prime example of such high performing interface is the tendon enthesis, where the soft tendon connects to the much stiffer bony tissue along a relatively short transitional length [12], employing an efficient mixture of design features, such as morphological

interdigitations and anisotropic orientations [13–16]. Moreover, functional gradients (FGs) enable a smooth transition of material properties from bone to tendon, reducing interfacial stresses [17–21]. The synergy of these mechanisms makes the bone-tendon connection highly efficient [12].

To date, a major impediment to the application of such design features has been the lack of suitable manufacturing techniques. The emergence of multi-material additive manufacturing (=3D printing) techniques has addressed this limitation and has enabled us to closely emulate the abovementioned natural design paradigms. These techniques allow for the design of structures with interpenetrating soft and hard material phases, yielding composites with optimized properties [22–26]. In particular, controlling the type of the deposited material at the level of individual voxels makes polyjet multi-material 3D printing highly suitable for the emulation of natural soft-hard interfaces [27–29].

Many types of architectures could be used as a basis for the design of biomimetic interfaces, particularly those that involve complex 3D architectures. However, most of the designs available in the literature are 2D and, at best, 2.5D [14]. This limitation leaves much of the potential of geometrical designs unexploited. Here, we selected a few types of architectures to study the effects of architecture types and design parameters on the mechanical performance of the resulting soft-hard interfaces. Triply periodic minimal surfaces (TPMS) [30–32] were one of the selected architectures because they offer large surface area to volume ratios and high genus values, both of which are highly beneficial for an enhanced interlocking of the interfacing phases. A high genus value means that there are multiple surface-connected yet volume-separated compartments available in the architecture of the material. Each of those compartments could be occupied by one of the interfacing phases. In this way, the phases interlock volumetrically across the vast surface area of the unit cells. A higher contact area between the material phases can also reduce strain concentrations. Architectures based on collagen-like helices [33,34] were also considered because they facilitate the creation of functional gradients while offering open cells and high surface areas. The design matrix was complemented by including randomly distributed particles, which are known to generate smooth functional gradients and arrest propagating cracks [35]. Moreover, the random distribution of particles can be integrated into multi-hierarchical arrangements [36] to prevent failure within the interface region.

In this study, we used both experiments and computational models to compare the various design options mentioned above and to elucidate the mechanisms determining the relative performance of different architectures. The experiments, which included uniaxial tensile and quad-lap shear tests as well as their associated full-field strain measurements using digital image correlation (DIC), allowed for a comprehensive and multi-faceted evaluation of the mechanical performance of soft-hard interfaces. At the same time, our computational models enabled a thorough analysis of the mechanistic aspects driving the performance of such interfaces, including the role of the incorporated 3D geometrical design features. In particular, we studied the relation between the internal geometry, the type of the transition function, and the contact surface on the one hand and the mechanical characteristics of the soft-hard interfaces, and the ensuing strain concentrations [37] on the other. This novel approach provides us with a pathway towards a better understanding of the mechanisms at play in the design of soft-hard interfaces and enables us to devise some design guidelines for improving the mechanical performance of bioinspired soft-hard interfaces, with potential applications in tissue engineering, soft robotics, and architected materials.

4.2. Materials and methods

4.2.1. 3D printing setup

We used a poly-jet multi-material 3D printer (ObjetJ735 Connex3, Stratasys® Ltd., USA) with voxel-level control to manufacture our biomimetic soft-hard interfaces. The commercially available photopolymers VeroCyan™ (RGD841, Stratasys® Ltd., USA) and Agilus30™ Clear (FLX935, Stratasys® Ltd., USA) were used for the hard and soft phases, respectively. Stacks of binary images detailing the type of the deposited material at each voxel were provided as input to the printer. In this approach, every image represents a layer of the 3D design. The maximum printing resolution was 300×600×900 dpi. We used the minimum edge size to print cube-shaped voxels with an edge length of 85 μm.

4.2.2. Design and manufacturing of tensile test interfaces

Due to the lack of standards available for the analysis of the complex 3D geometries required to analyze soft-hard interfaces, we considered the narrow section of a standard tensile test specimen shape (type IV) described in ASTM D638-14 [38] to constrain the dimensions of our designs (Figure 1a). These dimensions allowed for a design region of

384×96×48 voxels (32.51×8.1×4.0 mm^3). Within these regions, we kept the length of the soft region constant ($W_S = 8.128$ mm) and varied two interface parameters, namely the width (W_G) and geometrical design of the functional gradient (Figure 1b). We selected three different values of W_G (*i.e.,* 4.064, 8.128, 12.192 mm, equivalent to 48, 96, and 144 voxels), wherein we linearly varied the volume fraction of the hard phase (ρ) from 0 to 100%. We discretized these functions using cubic-shaped unit cells with five different geometries, including three TPMS-based architectures (*i.e.,* Octo (OC), Diamond (DI), and Gyroid (GY)), biomimetic collagen-like triple helices (CO), and randomly distributed particles (PA) (Figure 1b). Section S4.1 of the supporting information provides the details of the equations used for the generation of each design. It is important to note that the selected discretization strategy results in a significant discontinuity in the hard phase for the long OC design (*i.e.,* W_G = 12mm). We, nevertheless, included this design in the experimental groups to investigate the effects of such discontinuities on the mechanical performance of soft-hard interfaces. We included a control group without gradient transitions ($W_G = 0$ mm) (Figure S4.1a of the supporting information). Furthermore, to measure the morphological features of each interface, we calculated the percentage of soft-hard normal contact area (A_c) across the gradient lengths (Figure S4.1b of the supporting information). Finally, we projected each design into the narrow-gauge region of the tensile test specimens. Three specimens from each design were 3D printed, resulting in a total of 48 specimens.

4.2.3. Mechanical testing and post-processing

After manufacturing, we performed quasi-static uniaxial tensile tests with a mechanical testing bench (LLOYD instrument LR5K, load cell = 100 N) at a rate of 2 mm/min until failure. The device measured the displacements (u), forces (f), and time (t) at a sampling rate of 100 Hz. For all the tensile test specimens, we obtained full-field strain maps (the equivalent von Mises strains) at a frequency of 1 Hz using a 3D digital image correlation (DIC) system (Q-400, two cameras each with 12 MPixel, LIMESS GmbH, Krefeld, Germany) and its associated software (Instra 4D v4.6, Danted Dynamics A/S, Skovunde, Denmark). We, therefore, painted all the specimens white, followed by the application of a black dot speckle pattern.
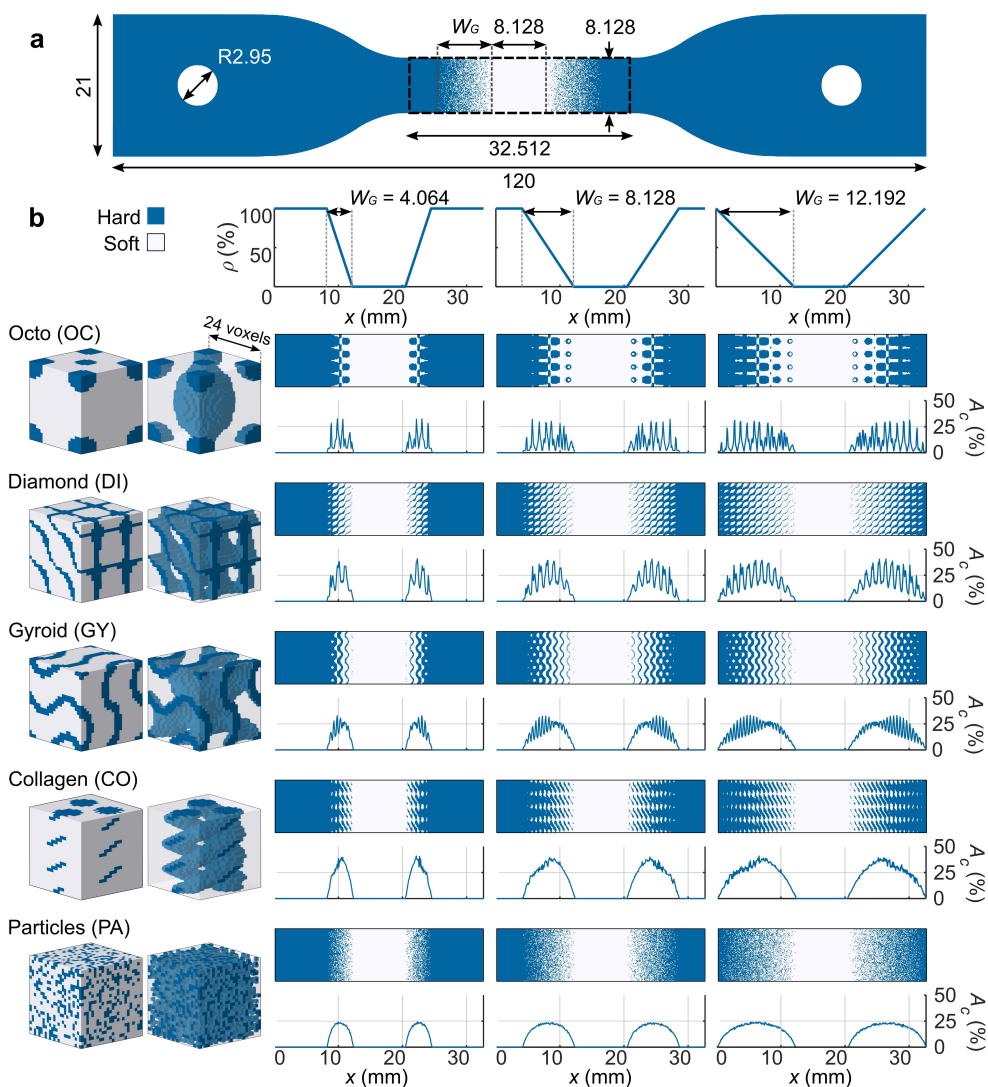
Figure 4.1. The soft-hard interface designs tested under tensile conditions. a) The standard tensile test specimens furnished with a functional gradient connecting the hard and soft polymer phases (out-of-plane thickness = 4 mm). These designs were 3D printed using a polyjet multi-material 3D printer. b) All the initial designs and their calculated percentage of the soft-hard normal contact area (A_c). We combined three different values of the gradient length (W_G) with five different unit cell geometries (i.e., Octo, Diamonds, Gyroids, collagen-like helices, and randomly distributed particles).

To generate the stress-strain curves, we defined virtual extensometers at the center of the soft section of every specimen using the DIC software and extracted the vectors of true

(logarithmic) strains (ϵ). We then post-processed these vectors and their respective forces (f) in MATLAB R2018b (Mathworks, USA) to generate their true stress vectors ($\sigma = (f/A_o)\exp(\epsilon), A_o = 32.512 \text{ mm}^2$). From the resulting curves, we calculated the elastic modulus, E, as the slope of the linear region of the stress-strain curves measured between 0 and 20% strain, the ultimate tensile strength, σ_{max}, as the maximum recorded stress, and the strain energy density, U_d, as the area under the stress-strain curve, also known as toughness.

4.2.4. Finite element analysis of the interface designs

We created quasi-static finite element method (FEM) models of our designs using a commercially available software suite (nonlinear solver, Abaqus Standard v.6.13, Dassault Systèmes Simulia, France). Since the designs were symmetric across their length, we considered one longitudinal half of each design (Figure S4.2a of the supporting information). Additionally, we only included one cross-sectional unit cell of every design, yielding a perpendicular area of 24×24 elements. This simplification was possible because a preliminary study comparing the results of the single unit cell models with those obtained using models incorporating a full quadrant indicated that while the absolute values may be somewhat different between both types of models, the primary observations and trends remain unchanged regardless of the selected model type (Section S4.2 and Figure S4.3 of the supporting information). Given the fact that single unit cell models are much more computationally efficient, we used them for the remainder of the study to compare a large number of design alternatives. These simplifications led to discretized models with 110,592 hexagonal hybrid elements (C3D8H, enhanced hourglass control), where each voxel was represented as a single element. The hard phase was modeled as a linear elastic material with an elastic modulus E of 2651 MPa and a Poisson's ratio, ν, of 0.4, while the soft phase was modeled as an Ogden hyperelastic material with the following material parameters: $N = 1$, $\mu_1 = 0.266$ MPa, $\alpha_1 = 3.006, D_1 = 0.113$. Finally, we applied a surface traction of $\sigma_{FEM} = 0.186$ MPa to the hard end-surface and symmetric boundary conditions (*i.e.,* $U_x = R_y = R_z = 0$) to the soft end-surface of the mesh. The computationally predicted distributions of the von Mises strains, obtained from each of the 8 integration points of every element, were used for validation and analysis. To corroborate the computational results, we compared the strain fields pertaining to the first transverse layer in the FEM models with those measured using DIC and obtained the ordinary coefficients of determination (R^2) for each design. The

agreement between the surface strains obtained computationally and experimentally (Figure S4.4 of the supporting information) confirmed the validity of the computational models and motivated the use of the full 3D strain distributions resulting from FEM simulations for a more complete analysis of each soft-hard interface.

4.2.5. Determination of maximum equivalent strains and strain concentration parameters

We used the true von Mises strains obtained from the DIC measurements and FEM simulations to study how the strains concentrated at the interfaces. To this end, we extracted the curves of the maximum equivalent strains $\epsilon_{eq,m}(x)$ from every cross-section layer across the length of the specimens. Additionally, we extracted the maximum strain value from these plots ($\epsilon_{\max}$) and divided it over the average equivalent strain at the center of the specimen (ϵ_N) to define the single-valued strain concentration parameter ($\epsilon_c = \epsilon_{\max}/\epsilon_N$) (Figure 2a), which we obtained from the DIC measurements and FEM estimations. We used the strain values corresponding to a stress magnitude of $\sigma = 0.186\ \text{MPa}$. To validate our simulations, we compared the DIC-measured $\epsilon_{eq,m}(x)$ and ϵ_c values with those calculated within the first (*i.e.,* surface) layer of the FEM models. The good agreement between the computational and experimental results at the surface of the specimens encouraged us to use $\epsilon_{eq,m}(x)$ and ϵ_c within the entire 3D geometry of the computational models for further analyses. Overall, these strain concentration parameters and the FEM-predicted strain distributions were used to study how the local geometry affected the performance of the functional gradients within the elastic loading regime.

4.2.6. Determination of the elastic modulus functions

We used the results from our computational models to study the elastic behavior exhibited by various designs. Towards this goal, we idealized the interfaces as linear systems of springs, where the elastic modulus function ($E(x) = \sigma_{\text{FEM}}/\epsilon_{\text{avg}}(x)$) is equivalent to the applied surface traction on the system, σ_{FEM}, over the average strain, $\epsilon_{\text{avg}}(x)$, of every transversal layer over each interface point (Figure S4.2b of the supporting information). We used these estimated functions to study how different factors, including the elastic modulus and overall rigidity, affect the performance of the interfaces.

4.2.7. Quad-lap shear designs, testing, post-processing, and finite element analysis

We extended our analyses to study the shear response of the designed architectures using quad-lap shear test specimens. We chose the designs that performed the best in the tensile tests (*i.e.,* GY, CO, and PA, $W_G = 4.572$ mm) and compared them to the control design (*i.e.,* without a gradient). Developing a geometry that enables the testing of functional gradients under shear loading was required because, to the best of our knowledge, no such standards currently exist. To obtain the appropriate dimensions of the specimens, we generated multiple geometries with the FEM software and simulated them. We used the dimensions of the specimen that yielded the elastic properties of the soft material ($E_{\text{soft}} = 1$ MPa, $\nu_{soft} = 0.49$) using only the forces and displacements of the virtual crosshead. After assigning the designs to the gradient regions, we printed these specimens (three per experimental group) and tested them under the same conditions as described above for the tensile tests. We calculated the true shear stresses ($\tau = f/(2tW), t = 3$ mm, $W = 33.528$ mm) and strains ($\gamma = d/(2H_S), H_S = 3.048$ mm) with the force and displacement vectors extracted from the mechanical testing machine. We then calculated the shear modulus (G, the initial slope of the stress-strain curves measured between 5% and 35% shear strain), maximum shear strength, τ_{max}, and shear strain energy density, U_d, as the area under the shear stress-strain curve of each test. Furthermore, we performed FEM simulations of each design under similar conditions as described above for the modeling of quasi-static tensile tests. In this case, the unit cell used in the gradient region had a perpendicular area of 36×36 elements and a length of 144 elements (with no symmetry assumed), resulting in 186,624 hexagonal hybrid elements (C3D8H) per simulation. We assigned linear elastic (*i.e.,* $E = 2651$ MPa, $\nu = 0.4$) and hyperelastic (*i.e.,* Ogden, $N = 1$, $\mu_1 = 0.266$ Mpa, $\alpha_1 = 3.006, D_1 = 0.113$) properties to the hard and soft elements, respectively. Furthermore, we applied a shear deformation to one of the end-surfaces of the mesh *(i.e., $U_x = 0.4257$ mm, $R_x = R_y = R_z = 0$)* while constraining all the displacements of the other. The results of the computational analysis were then used to calculate the strain concentration parameters of each design and for comparison with the experiments.

4.2.8. Design of a hybrid design based on our final findings

We further extended our analyses to exploit the full bioinspired potential of soft-hard interfaces. To do so, we combined multi-scale hierarchical organization, crack deflection

mechanisms, functional gradients, and smooth contact areas to generate a hybrid design. We selected and combined the best-performing designs from the initial analysis, defining a PA structure in which the particles were randomly scattered within a GY architecture, resulting in the GP group. To create a less stiff elastic modulus function, we decreased the densities of the hard phase, ρ, by 50%. We then 3D printed, tested, and computationally analyzed these designs under the same conditions as described above for the quasi-static tensile tests.
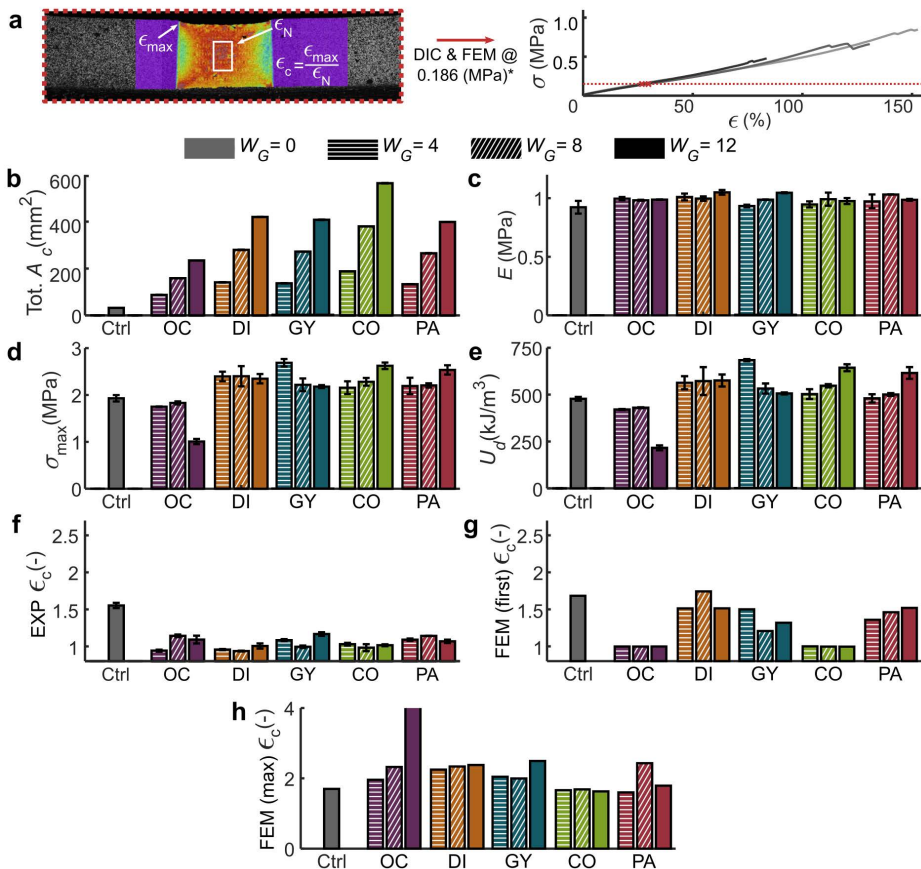

Figure 4.2. a) A representative example of a DIC measurement showing the regions from which the strain concentration parameters (ϵ_c) were calculated (obtained at the point where the equivalent stresses were 0.1866 MPa). The bar plots represent the morphological and mechanical properties of the studied designs (mean ± SD). These include b) the total soft-hard normal contact area, c) measured elastic modulus, d) maximum strength, e) strain energy density, f) experimentally measured ϵ_c, and the FEM-predicted ϵ_c results obtained from the top (*i.e.,* first) layer of the meshes(g) and the maximum value within from the entire (max) 3D structure (h).
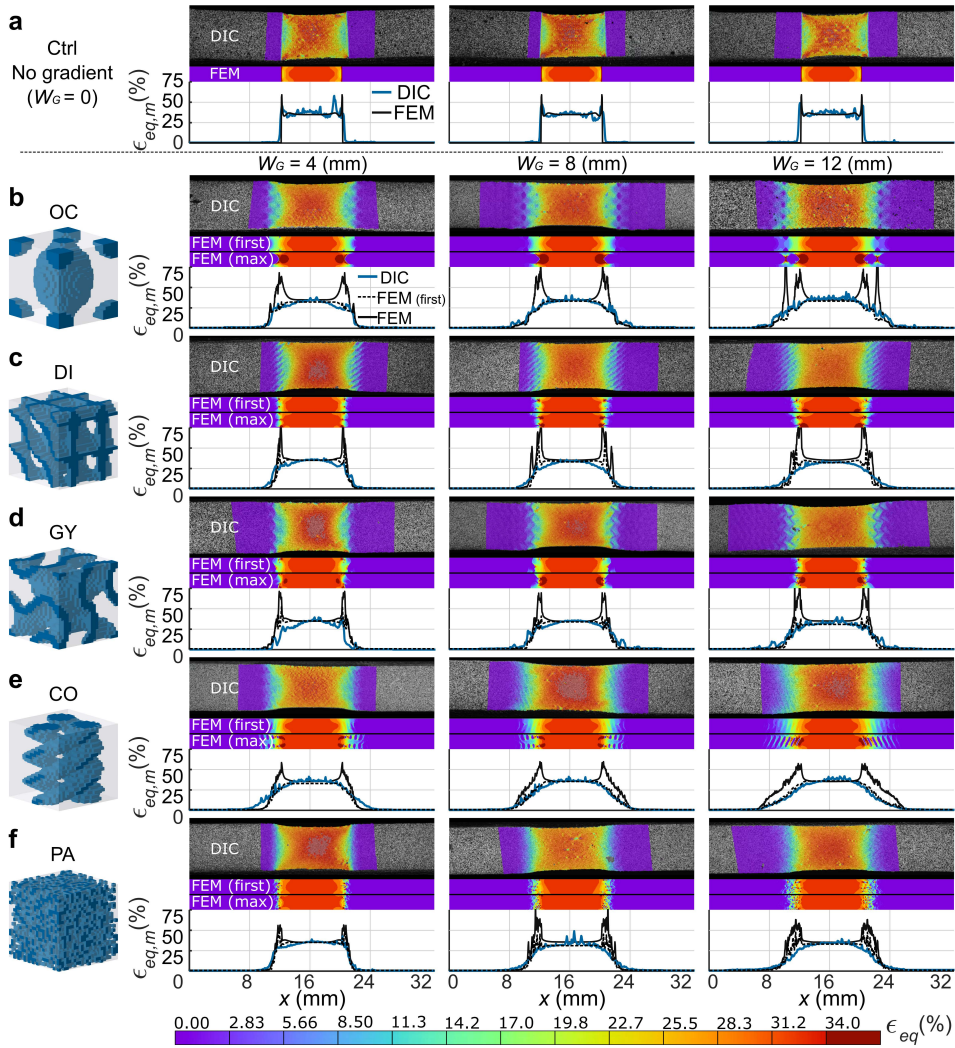
Figure 4.3. Representative strain distributions measured using DIC and predicted using the FEM models as well as the maximum equivalent strain ($\epsilon_{eq,m}$) plots for every design. The study groups include the a) control group, b) octo, c) diamond, d) gyroid, e) collagen-like helices, and f) randomly distributed particles. The FEM strain distributions are presented for the first layer and at the location where the maximum strains were predicted, for validation and analysis purposes, respectively.

4.3. Results and discussion

The integration of the different architectures into the soft-hard interfaces led to distinct patterns of A_c (Figure 1b) and resulted in different total values of the contact surface area

(**Tot.** A_c) (Figure 2b). None of these differences had a considerable effect on the initial elastic moduli (Figure 2c) calculated using the obtained stress-strain curves (Figure S4.5 of the supporting information). Nevertheless, the varying geometries and gradient lengths did affect the strength and toughness of the interfaces (Figure 2d-e). The best-performing designs were GY ($W_G = 4$ mm), CO ($W_G = 12$ mm), and PA ($W_G = 12$ mm). They all exhibited similar strengths and failure modes (*i.e.,* failure within the soft region), suggesting that the upper strength boundary of these interfaces was reached [39]. The control group under-performed all but the OC designs, confirming the importance of the implemented design strategies in improving the mechanical performance of soft-hard interfaces.

We found some evidence of the mechanism responsible for the failure of the control group specimens when assessing their DIC-measured **EXP** ϵ_c values (Figure 2f) and strain distributions (Figure 3a). According to this data, the shear strains at the edges of the interface were the primary culprits. This observation as well as the absence of high values of the von Mises strains at the center of the cross-section cut of the interface (Figure S4.6a of the supporting information) are consistent with the literature [4,40,41]. These superficial strain concentrations were not present in the DIC results of any functionally graded design. Moreover, the **EXP** ϵ_c values of the other groups were all much lower than those measured in the control group. This lack of shear strains explains the improved performance of most of the presented designs, because a proper interfacing of soft and hard materials requires a smooth transition from one phase to another so that the stress concentration in the softer material can be decreased [42]. The difference between the FEM-predicted ϵ_c values pertaining to the first layer of the models and those of the entire 3D structure (Figure 2g-f) indicate that the strain concentrations occurring within the 3D structure of the constructs may not always be fully visible on the surface. Therefore, a closer inspection to the results of the FEM simulations was necessary to elucidate the effects of the gradient morphology on the mechanical performance.

Comparing the DIC-measured strain distributions with the FEM results extracted from the first layer of the meshes allowed us to validate our computational models (Figure 3b-f). In general, the predicted and measured strain distributions followed the same patterns and were strongly correlated ($R^2 > 92.1$ %) (Figure S4.4 of the supporting information). For example, all the GY designs showed curved-like strain patterns in both the experiments and

simulations. In contrast, the strain distribution patterns of the DI and CO designs presented distinct diagonal lines. Similarly, the trends observed in the FEM $\epsilon_{eq,m}$ plots (of the first layer) resembled the DIC measurements. The simulations, however, showed higher peak strain values as compared to the experiments (*e.g.,* see the peaks at the edges of the DI designs or between individual voxels in the PA gradients). The absence of these peaks was likely caused by the limited DIC resolution (*i.e.,* between 22×10^3 and 27×10^3 facets per experiment), which was approximately six times lower than the resolution of the 3D-printed specimens (*i.e.,* 147×10^3 voxels). Furthermore, blending between the photopolymers prior to curing might have significantly reduced the magnitudes of the strain peaks [43,44]. The FEM predictions were, therefore, more discerning when trying to understand the effects of geometrical design on the mechanical performance of soft-hard interfaces. An additional set of simulations was, however, necessary to assess if simulating only a single unit cell instead of the entire interface was representative of the complete interfaces (Section S4.2 of the supporting information). This comparative study demonstrated that, while some differences are present in terms of the absolute strain values, the overall mechanical behavior, the deformation trends, and the elastic modulus functions remain consistent between the single unit cell models and models incorporating the actual full-size geometry of the specimens. This was a welcome outcome because it enabled us to use the single unit cell models in the remainder of the study to evaluate the performance of a large number of design alternatives. This corroboration of the computational results allowed us to analyze the different designs individually in a quest to unravel the mechanisms underlying their mechanical performance.

Although generally better than the control group, most OC and DI specimens failed at the edge of the interface (only one DI specimen ($W_G = 8$ mm) failed at the center of the soft region). An analysis of the FEM-predicted strain distributions of these groups showed the prevalence of severe strain concentrations at their interface edges (Figure 3b-c, supplementary videos 4.1 and 4.2), whose intensity was correlated to W_G. Upon closer inspection (Figure S4.6b-c of the supporting information), the sharp-edged tips of the hard material at the edge of the interface seemed to have induced these strain concentrations. These shapes are particularly problematic since the interfacial geometry cannot arrest the propagation of initial cracks. Comparing the A_c and $\epsilon_{eq,m}$ plots (Figure S4.7a-b of the supporting information) of both designs indicated that these strain concentrations are

associated with highly erratic A_c patterns. A smooth material transition may, thus, alleviate such effects. It is, therefore, necessary to change the density of the hard phase, ρ, as smoothly as possible by using a geometry for which the change in A_c is less abrupt, and ensure that there are no sharp ends in the selected geometrical design.

In the case of the long OC design (*i.e.,* $W_G = 12$ mm), the hard material discontinuity at the middle of the interface resulted in extreme strain concentrations (**FEM (max)** $\epsilon_c =$ **4.53**) and was the region where critical cracks initiated. This lack of connectivity, which is visible in the discontinuous A_c pattern of this design and in the supplementary video 4.1, led to extremely low values of interfacial strength and toughness (*i.e.,* approximately half the strength and toughness of the control group, Table S4.1 of the supporting information). Therefore, although TPMS structures can yield closed-cell structures, verifying their connectivity by assessing their surface contact area and making the necessary corrections to ρ is of great importance.

The GY results were particularly interesting because long gradients from this design ($W_G = 12$ mm) barely overperformed the control group, while the shorter version of the same design ($W_G = 4$ mm) outperformed all the other groups (Figure 2d-e). The short GY gradients presented failure modes where cracks initiated close to the interface but propagated through the soft region of the tensile specimens (supplementary video 4.3). In contrast, the other GY interfaces failed at the end of the interface. This performance difference can be due to several reasons. First, the GY specimens had A_c patterns that were not as torturous as the OC and DI designs (Figure S4.7c of the supporting information), explaining why their predicted **FEM** ϵ_c values were the lowest between the TPMS structures. More importantly, the strains of the short GY gradients mainly concentrated around the concave hard material shapes before the end of the gradient and at the edges of the interface, with the maximum strain values appearing close to the sheet-based Gyroid geometry (Figure S4.6d of the supporting information). This concave geometry, in turn, encased the regions with maximum strain concentrations, arresting the critical propagation of cracks. In comparison, the longer GY gradients mostly showed tip-edged strain concentrations at the soft ends of the interface, similar to those found in the OC and DI designs. Although the smooth A_c pattern appears to have contributed to the high performance of short GY designs, comparison with the other designs indicates that the ability to contain the strain

concentrations may have played a more important role in this regard, particularly given the fact that the short GY design was the only studied TPMS with this feature.

An important parameter affecting the performance of the soft-hard interface is the length over which the transition takes place (*i.e.,* W_G). The performance of a soft-hard interface is generally expected to improve as the length of the gradient increases, given that longer transitions lead to smoother changes in the elastic modulus, decreasing stress concentrations [42]. Indeed, the plots of the elastic modulus of the TPMS designs (Figure S4.7a-c of the supporting information) were increasingly smoother as W_G increased. The performance of the TPMS designs was, however, inversely related to W_G, as the strength values were higher for the specimens with shorter gradients while the **FEM** ϵ_c values were higher for the longer specimens. The local geometrical features at the end of a functional gradient are, therefore, more important in determining the mechanical performance of the interface than the overall smoothness of the function describing the transition of the elastic modulus. Consequently, it is important to utilize geometries that reduce the strain concentrations as W_G increases or include features that help in arresting cracks.

In contrast with the TPMS structures, the mechanical performance of the CO and PA designs was enhanced as W_G increased. In fact, the CO and PA designs with long gradients ($W_G = 12 \text{ mm}$) were some of the toughest designs within this study (supplementary videos 4.4 and 4.5). Moreover, most specimens of these two groups failed at the center of the soft region and not at the interface. When analyzing the FEM-predicted strain distributions of the CO designs (Figure 3d, Figure S4.6e of the supporting information), we observed that the deformations were primarily concentrated in the soft material regions between each coil of the functional gradient, with the cross-sectional strains showing circular patterns of strain that were reminiscent of helices. These patterns resulted in smooth $\epsilon_{eq,m}$ plots (Figure S4.7d of the supporting information) and the lowest FEM ϵ_c values of this study. Such a proper distribution of strains may be attributed to the high $tot. A_c$ values and smooth A_c patterns of these designs, which are similar to what is reported in the literature [40]. Furthermore, their elastic modulus functions were the most compliant, explaining the presence of strains across the longer sections of the gradient region (unlike in the TPMS results, where the strains were concentrated at the edges). Particularly for the long CO design, the smooth and well-

distributed strains across the entire gradient region indicated an increased strain energy storage capacity, leading to the high toughness values.

For the PA designs, the predicted **FEM** ϵ_c values were not proportional to W_G and the strain distributions exhibited irregular patterns that resembled the random nature of the designs (Figure 3f). The locations of these strain concentrations were not necessarily at the end of the interface, but in the single voxels of the soft material surrounded by the hard material across the entire gradient (Figure S4.6f of the supporting information). If a crack initiates around those stress concentration points, the nearby voxels could deflect it or arrest its progress, similar to what other studies have observed [45]. Furthermore, the comparatively higher magnitudes of strains across the gradient length produced more compliant elastic modulus functions in these designs, similar to the CO specimens (Figure S4.7e of the supporting information). These high strains mean more strain energy is stored in such specimens, resulting in higher toughness values, particularly for the long PA gradients. Overall, both CO and PA achieved their high toughness because they could store more energy in their gradient region and because of the crack-arresting features of their internal morphology.

We have so far only considered tension because this loading mode is typical in soft-hard interfaces (*e.g.,* cables, tendons, muscles). Soft-hard interfaces may, however, also fail under shear deformations, motivating the study of the presented designs under this loading regime. Since no standards are available for the geometrical design of functionally graded quad-lap specimens, a custom-made design was used (Figure 4a), enabling us to manufacture the specimens and perform mechanical testing (Figure 4b, supplementary videos 4.6 to 4.8). After post-processing, all the hyperelastic $\tau - \gamma$ curves had similar initial values of the shear modulus ($G_{\mathrm{avg}} = 0.308\ \mathrm{MPa}$, Figure 4c), confirming the proper design of the specimens and the satisfactory distribution of materials in the presented designs. In terms of the shear strength and toughness, however, the PA designs outperformed all other groups (Figure 4d). Moreover, the performance of the specimens was inversely related to their predicted FEM ϵ_c, suggesting that the internal morphology of these interfaces was responsible for this outcome. Based on these observations, we concluded that using PA reinforcement in the design of soft-hard interfaces can enhance their performance under shear deformations.
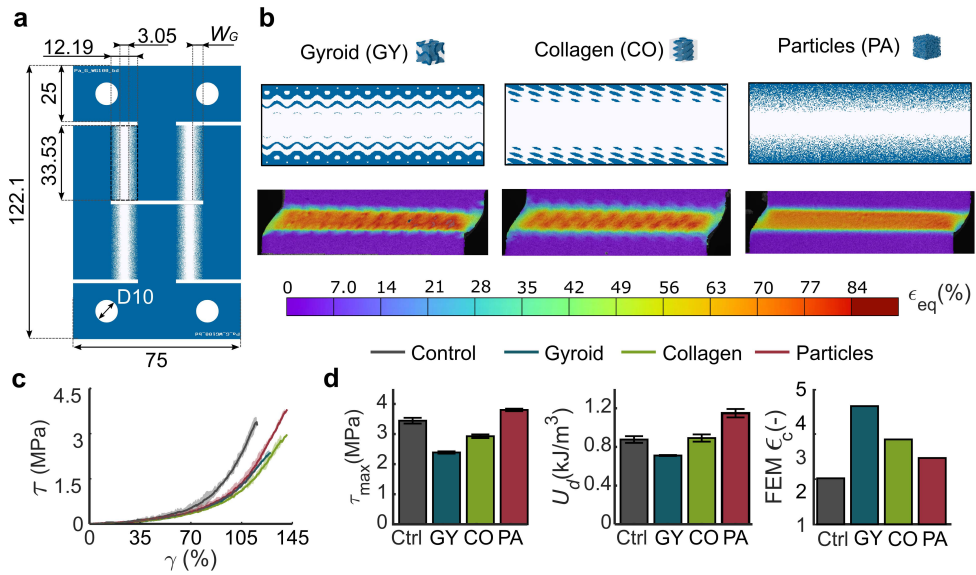
Figure 4.4. The specimens used in the shear tests and their corresponding results. a) The parametrized geometry of the quad-lap shear test specimens, with an out-of-plane thickness of **3 mm** and $W_G =$ **3.048 mm**. b) The selected geometries (e.g., GY, CO, and PA), chosen due to their high tensile performance. The presented DIC measurements of the equivalent shear strains correspond to a shear stress of **0.523 MPa**. c) The average (with shaded areas representing ± SD) shear stress vs. shear strain (τ vs. γ) curves for every design. d) The bar plots represent the measured shear modulus (G), strain energy density (U_d), and estimated FEM ϵ_c for each design (mean ± SD).

In summary, the data and analysis presented above indicate that there are several morphological and mechanical principles that can lead to a tough soft-hard interface. First, the A_c must be smooth to prevent any sudden changes in $\epsilon_{eq,m}$ across the functional gradient. Second, the corresponding **tot.** A_c values should be as high as possible to decrease the overall magnitude of strain concentrations. Furthermore, it is important for the functional gradients to be increasingly more compliant, particularly at the edges of the interface. This compliance will lead to increased average deformations across the entire interface length. Higher amounts of strain energy can, therefore, be stored in the gradient region, leading to diffused stress concentrations and tougher soft-hard interfaces. Finally, the design of the structures should be such that any initiated cracks can be arrested, particularly at the end of the gradient region. It is, therefore, essential to include analyses of the entire 3D geometry of the interface across every cross-section. Examples of such geometries include concave designs

implemented around strain concentration regions and randomly distributed particles. The selected geometries should also not include sharp tips of the hard phase at the edges of the interface because they create strain concentrations. Since most of the studied designs failed to implement all the aforementioned morphological features, we decided to extend our analysis by creating a design that combines the best performing TPMS (*i.e.,* the GY) with PA (Figure 5a-b). We hypothesized that adding particles to a Gyroid design (GY + PA = GP) will hinder the propagation of critical cracks while producing a smooth A_c pattern. Additionally, we decreased the ratio of the hard material, ρ, to 50% of its original value so that higher magnitudes of strain energy can be accommodated by the interface.
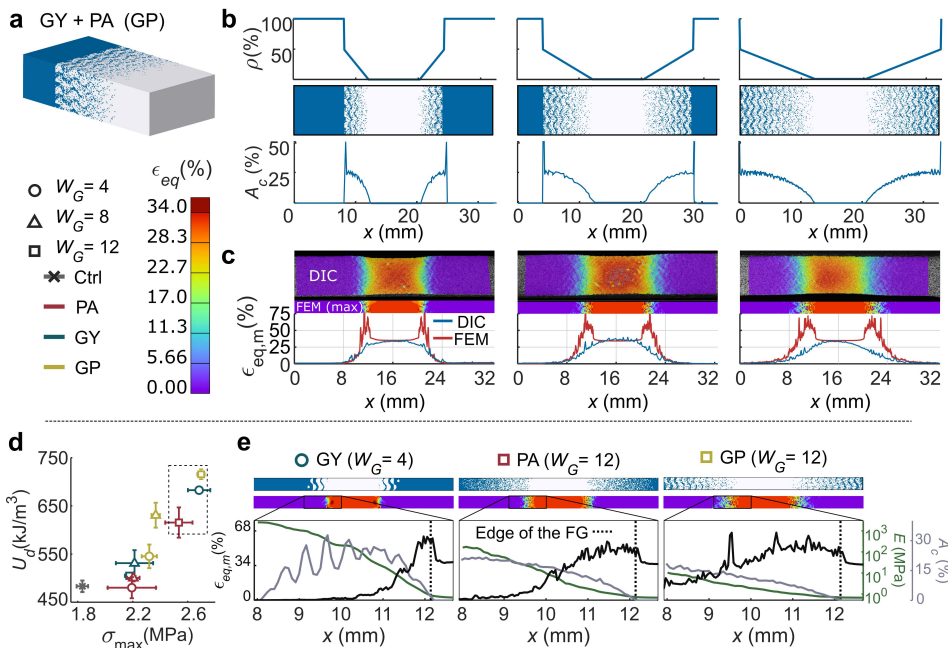

Figure 4.5. Hybrid designs combining gyroid geometries with randomly distributed particles (GP) through a multi-scale approach. b) The magnitude of the ρ functions were decreased to produce more compliant functional gradients while maintaining smooth A_c patterns. c) Representative strain distributions measured using DIC and predicted using computational models as well as $\epsilon_{eq,m}$ plots for these designs. d) A scatterplot comparing the σ_{max} vs. U_d results for the GY, PA, and GP designs. The GP specimens were among the best-performing ones. e) A detailed comparison of the mechanistic features of the best-performing GY, PA, and GP designs.

Our experiments confirmed that the GP specimens, indeed, exhibit many of the characteristics of high-performing soft-hard interfaces. The DIC-measured strain distributions of the GP specimens (Figure 5c, supplementary video 4.9) shared certain features with both the GY and PA designs while lacking any significant superficial strain concentrations. Overall, the 3D FEM models showed higher strain magnitudes and relatively higher levels of strain concentrations across the length of the functional gradient (Figure S4.6g of the supporting information). All in all, the GP designs yielded the smoothest modulus functions in this study, enabling more strain energy to be stored within the FG. Furthermore, their $\epsilon_{eq,m}$ plots showed that the strain concentrations vanish before the end of the gradient region (Figure S4.7f of the supporting information). Similar to the short GY and long PA designs, the presence of hard material around the locations of peak strains indicates that the interface can arrest initial cracks (Figure 5e). The performance of the GP specimens increased with W_G (Figure 5d). In fact, the long ($W_G = 12$ mm) GP specimens presented the highest toughness values in this study (*i.e.,* 1.48 times tougher than the control specimens). Moreover, additional ductile failure simulations showed that the failure modes and the mechanistic principles behind the performance of the GP and other geometries remained consistent with the aforementioned interface design guidelines (Section S4.3 and Figure S4.8 of the supporting information). These results confirm that the implementation of multi-scale features into a highly interdigitated and compliant functionally graded design further enhances the performance of soft-hard interfaces.

The results obtained here are not necessarily limited to the applied multi-material Polyjet printing technique and the specific materials used here. Indeed, the focus of the current study has been on identifying the guiding principles for the (geometrical) design of soft-hard interfaces at the individual voxel level. Currently, Polyjet multi-printing is the only widely available technique that can be controlled at the individual voxel level and can process multiple material phases with vastly different mechanical properties at a sub-50 micrometer scale. That is why we used this technique in the current study. However, the guiding design principles and their action mechanisms are primarily geometrical in nature and are formulated in reference to the patterns of the arrangement of both material phases. That is why we expect these mechanisms to be valid for other types of material combinations and (additive) manufacturing techniques. Indeed, additional computational analyses performed

using our models showed that the main guiding principles remain valid regardless of the ratio of the elastic properties of both phases (Section S4.4 and Figure S4.9 of the supporting information). Moreover, an analysis of the effects of photopolymer blending (Section S4.5 and Figure S4.10 of the supporting information) showed that even though material mixing can improve the performance of photopolymer composites, the general observations regarding the effects of various geometrical design alternatives on the performance of the interfaces remain unchanged [43,44]. Experimental studies of such effects are currently not possible outside multi-material Polyjet printing due to technological limitations. However, it is expected that the future developments of additive manufacturing techniques and materials will enable multi-material voxel-by-voxel printing also for other types of material connections, such as metal-metal (*e.g.,* Mg-NiTi), hydrogel-metal, and for other polymer-polymer connections processed using other additive manufacturing techniques (*e.g.,* FDM polymers). At its roots, this study concerns the mechanical behaviors observed at the interface of two interpenetrated phases, similar to the ones found in the interdigitated functional gradients of natural tissues. Histological studies in different organisms show similar general principles at work in multiple species, various material combinations, and anatomical sites [18,46]. This further supports the idea that the main guiding principles are valid regardless of the specific material combinations or mechanical functionalities.

4.4. Conclusions

We studied how the design of soft-hard interfaces influences their mechanical performance. Our results clearly show the role of increased contact area, elastic modulus functions, and design features that attenuate or constrain strain concentrations in the rational design of high-performing soft-hard interfaces. The application of the abovementioned design features yielded soft-hard interfaces whose strength approached the upper boundary of the possible strengths and whose toughness increased by $\approx 50\%$ as compared to that of the control specimens. Future work should employ these guidelines with computational methods to design optimized soft-hard interfaces. The presented results ultimately contribute to the development of the next generation of designer materials with applications in, among other areas, medical devices, tissue engineering, soft robotics, and the design of architected flexural mechanisms.

References

[1]   V.L. Hein, F. Erdogan, Stress singularities in a two-material wedge, Undefined. 7 (1971) 317–330. https://doi.org/10.1007/BF00184307.

[2]   R. Desmorat, F.A. Leckie, Singularities in bi-materials: parametric study of an isotropic/anisotropic joint, Eur. J. Mech. - A/Solids. 17 (1998) 33–52. https://doi.org/10.1016/S0997-7538(98)80062-4.

[3]   Z. Wu, Stress concentration analyses of bi-material bonded joints without in-plane stress singularities, Int. J. Mech. Sci. 50 (2008) 641–648. https://doi.org/10.1016/J.IJMECSCI.2008.01.004.

[4]   R.D. Adams, J. Coppendale, N.A. Peppiatt, Stress analysis of axisymmetric butt joints loaded in torsion and tension:, Http://Dx.Doi.Org/10.1243/03093247V131001. 13 (1978) 1–10. https://doi.org/10.1243/03093247V131001.

[5]   R. Balokhonov, V. Romanova, ON THE PROBLEM OF STRAIN LOCALIZATION AND FRACTURE SITE PREDICTION IN MATERIALS WITH IRREGULAR GEOMETRY OF INTERFACES, Facta Univ. Ser. Mech. Eng. 17 (2019) 169–180. https://doi.org/10.22190/FUME190312023B.

[6]   M.N. Saleh, M. Saeedifar, D. Zarouchas, S.T. De Freitas, Stress analysis of double-lap bi-material joints bonded with thick adhesive, Int. J. Adhes. Adhes. 97 (2020) 102480. https://doi.org/10.1016/J.IJADHADH.2019.102480.

[7]   R. Lopes Fernandes, S. Teixeira de Freitas, M.K. Budzik, J.A. Poulis, R. Benedictus, Role of adherend material on the fracture of bi-material composite bonded joints, Compos. Struct. 252 (2020) 112643. https://doi.org/10.1016/J.COMPSTRUCT.2020.112643.

[8]   Z. Wu, A method for eliminating the effect of 3-D bi-material interface corner geometries on stress singularity, Eng. Fract. Mech. 73 (2006) 953–962. https://doi.org/10.1016/J.ENGFRACMECH.2005.10.010.

[9]   U.G.K.K. Wegst, H. Bai, E. Saiz, A.P. Tomsia, R.O. Ritchie, Bioinspired structural materials, 14 (n.d.) 23–36. https://doi.org/10.1038/nmat4089.

[10]   F. Libonati, M.J. Buehler, Advanced Structural Materials by Bioinspiration , Adv. Eng. Mater. 19 (2017) 1600787. https://doi.org/10.1002/adem.201600787.

[11]   J.W.C. Dunlop, P. Fratzl, Biological Composites, Annu. Rev. Mater. Res. 40 (2010) 1–24. https://doi.org/10.1146/annurev-matsci-070909-104421.

[12]   A. Tits, D. Ruffoni, Joining soft tissues to bone: Insights from modeling and simulations, Bone Reports. 14 (2021) 100742. https://doi.org/10.1016/j.bonr.2020.100742.

[13]   L. Rossetti, L.A. Kuntz, E. Kunold, J. Schock, K.W. Müller, H. Grabmayr, J. Stolberg-Stolberg, F. Pfeiffer, S.A. Sieber, R. Burgkart, A.R. Bausch, The microstructure and micromechanics of the tendon–bone insertion, Nat. Mater. 2017 166. 16 (2017) 664–670. https://doi.org/10.1038/nmat4863.

[14]   C. Pitta Kruize, S. Panahkhahi, N.E. Putra, P. Diaz-Payno, G. Van Osch, A.A. Zadpoor, M.J. Mirzaali, Biomimetic Approaches for the Design and Fabrication of Bone-to-Soft Tissue Interfaces, ACS Biomater. Sci. Eng. (2021). https://doi.org/10.1021/ACSBIOMATERIALS.1C00620.

[15]   S.P. Ho, S.J. Marshall, M.I. Ryder, G.W. Marshall, The tooth attachment mechanism defined by structure, chemical composition and mechanical properties of collagen fibers in the periodontium, Biomaterials. 28 (2007) 5238–5245. https://doi.org/10.1016/J.BIOMATERIALS.2007.08.031.

[16]   A. Tits, E. Plougonven, S. Blouin, M.A. Hartmann, J.F. Kaux, P. Drion, J. Fernandez, G.H. van Lenthe, D. Ruffoni, Local anisotropy in mineralized fibrocartilage and subchondral bone beneath the tendon-bone interface, Sci. Reports 2021 111. 11 (2021) 1–17. https://doi.org/10.1038/s41598-021-95917-4.

[17]   A.R. Studart, Biological and Bioinspired Composites with Spatially Tunable Heterogeneous Architectures, Adv. Funct. Mater. 23 (2013) 4423–4436. https://doi.org/10.1002/adfm.201300340.

[18]   Z. Liu, M.A. Meyers, Z. Zhang, R.O. Ritchie, Functional gradients and heterogeneities in biological materials: Design principles, functions, and bioinspired applications, Elsevier Ltd, 2017. https://doi.org/10.1016/j.pmatsci.2017.04.013.

[19]   A. Miserez, T. Schneberk, C. Sun, F.W. Zok, J.H. Waite, The Transition from Stiff to Compliant Materials in Squid Beaks, Science (80-.). 319 (2008) 1816–1819. https://doi.org/10.1126/SCIENCE.1154117.

[20]   M.E. Launey, M.J. Buehler, R.O. Ritchie, On the Mechanistic Origins of Toughness in Bone, Http://Dx.Doi.Org/10.1146/Annurev-Matsci-070909-104427. 40 (2010) 25–53. https://doi.org/10.1146/ANNUREV-MATSCI-070909-104427.

[21]   H. Chai, J.J.-W. Lee, P.J. Constantino, P.W. Lucas, B.R. Lawn, Remarkable resilience of teeth, Proc. Natl. Acad. Sci. 106 (2009) 7289–7293. https://doi.org/10.1073/PNAS.0902466106.

[22]   A.S. Dalaq, D.W. Abueidda, R.K. Abu Al-Rub, Mechanical properties of 3D printed interpenetrating phase composites with novel architectured 3D solid-sheet reinforcements, Compos. Part A Appl. Sci. Manuf. 84 (2016) 266–280. https://doi.org/10.1016/J.COMPOSITESA.2016.02.009.

[23]   T. Li, Y. Chen, L. Wang, Enhanced fracture toughness in architected interpenetrating phase composites by 3D printing, Compos. Sci. Technol. 167 (2018) 251–259. https://doi.org/10.1016/J.COMPSCITECH.2018.08.009.

[24]   Z. Jia, Y. Yu, S. Hou, L. Wang, Biomimetic architected materials with improved dynamic performance, J. Mech. Phys. Solids. 125 (2019) 178–197. https://doi.org/10.1016/j.jmps.2018.12.015.

[25]   M. Zhang, Q. Yu, Z. Liu, J. Zhang, G. Tan, D. Jiao, W. Zhu, S. Li, Z. Zhang, R. Yang, R.O. Ritchie, 3D printed Mg-NiTi interpenetrating-phase composites with high strength, damping capacity, and energy absorption efficiency, Sci. Adv. 6 (2020) 5581–5589. https://doi.org/10.1126/SCIADV.ABA5581/SUPPL_FILE/ABA5581_SM.PDF.

[26]   O. Al-Ketan, R.K.A. Al-Rub, R. Rowshan, Mechanical Properties of a New Type of Architected Interpenetrating Phase Composite Materials, Adv. Mater. Technol. 2 (2017) 1600235. https://doi.org/10.1002/ADMT.201600235.

[27]   E.L. Doubrovski, E.Y. Tsai, D. Dikovsky, J.M.P. Geraedts, H. Herr, N. Oxman, Voxel-based fabrication through material property mapping: A design method for bitmap printing, CAD Comput. Aided Des. 60 (2015) 3–13. https://doi.org/10.1016/j.cad.2014.05.010.

[28]   C. Bader, D. Kolb, J.C. Weaver, S. Sharma, A. Hosny, J. Costa, N. Oxman, Making data matter: Voxel printing for the digital fabrication of data across scales and domains, Sci. Adv. 4 (2018). https://doi.org/10.1126/sciadv.aas8652.

[29]   S. Hasanov, A. Gupta, A. Nasirov, I. Fidan, Mechanical characterization of functionally graded materials produced by the fused filament fabrication process, J. Manuf. Process. 58 (2020) 923–935. https://doi.org/10.1016/J.JMAPRO.2020.09.011.

[30]   I. Maskery, L. Sturm, A.O. Aremu, A. Panesar, C.B. Williams, C.J. Tuck, R.D. Wildman, I.A. Ashcroft, R.J.M. Hague, Insights into the mechanical properties of several triply periodic minimal surface lattice structures made by polymer additive manufacturing, Polymer (Guildf). 152 (2018) 62–71. https://doi.org/10.1016/j.polymer.2017.11.049.

[31]   O. Al-Ketan, R. Rezgui, R. Rowshan, H. Du, N.X. Fang, R.K.A. Al-Rub, Microarchitected Stretching-Dominated Mechanical Metamaterials with Minimal Surface Topologies, Adv. Eng. Mater. 20 (2018) 1800029. https://doi.org/10.1002/ADEM.201800029.

[32]   O. Al-Ketan, R. Rowshan, R.K. Abu Al-Rub, Topology-mechanical property relationship of 3D printed strut, skeletal, and sheet based periodic metallic cellular materials, Addit. Manuf. 19 (2018) 167–183. https://doi.org/10.1016/J.ADDMA.2017.12.006.

[33]   C.T. Thorpe, C. Klemt, G.P. Riley, H.L. Birch, P.D. Clegg, H.R.C. Screen, Helical sub-structures in energy-storing tendons provide a possible mechanism for efficient energy storage and return, Acta Biomater. 9 (2013) 7948–7956. https://doi.org/10.1016/J.ACTBIO.2013.05.004.

[34]   X. Hu, P. Cebe, A.S. Weiss, F. Omenetto, D.L. Kaplan, Protein-based composite materials, Mater. Today. 15 (2012) 208–215. https://doi.org/10.1016/S1369-7021(12)70091-3.

[35]   M.J. Mirzaali, A. Herranz de la Nava, D. Gunashekar, M. Nouri-Goushki, R.P.E. Veeger, Q. Grossman, L. Angeloni, M.K. Ghatkesar, L.E. Fratila-Apachitei, D. Ruffoni, E.L. Doubrovski, A.A. Zadpoor, Mechanics of bioinspired functionally graded soft-hard composites made by multi-material 3D printing, Compos. Struct. 237 (2020) 111867. https://doi.org/10.1016/J.COMPSTRUCT.2020.111867.

[36]   M.J. Mirzaali, M. Cruz Saldívar, A. Herranz de la Nava, D. Gunashekar, M. Nouri-Goushki, E.L. Doubrovski, A.A. Zadpoor, Multi-Material 3D Printing of Functionally Graded Hierarchical Soft–Hard Composites, Adv. Eng. Mater. 22 (2020) 1901142. https://doi.org/10.1002/adem.201901142.

[37]   W.D. Pilkey, D.F. Pilkey, Z. Bi, Peterson's Stress Concentration Factors, 4th Editio, John Wiley & Sons, 2020. https://doi.org/10.1002/9781119532552.

[38]   ASTM D638, ASTM D638 - 14 Standard Test Method for Tensile Properties of Plastics, ASTM Stand. (2004). https://www.astm.org/Standards/D638 (accessed September 28, 2021).

[39]   T. Kuipers, R. Su, J. Wu, C.C.L. Wang, ITIL: Interlaced Topologically Interlocking Lattice for continuous dual-material extrusion, Addit. Manuf. 50 (2022) 102495. https://doi.org/10.1016/J.ADDMA.2021.102495.

[40]   T.S. Lumpe, J. Mueller, K. Shea, Tensile properties of multi-material interfaces in 3D printed parts, Mater. Des. 162 (2019) 1–9. https://doi.org/10.1016/J.MATDES.2018.11.024.

[41]   F. Liu, T. Li, X. Jiang, Z. Jia, Z. Xu, L. Wang, The effect of material mixing on interfacial stiffness and strength of multi-material additive manufacturing, Addit. Manuf. 36 (2020) 101502. https://doi.org/10.1016/J.ADDMA.2020.101502.

[42]   J.H. Waite, H.C. Lichtenegger, G.D. Stucky, P. Hansma, Exploring Molecular and Mechanical Gradients in Structural Bioscaffolds†, Biochemistry. 43 (2004) 7653–7662. https://doi.org/10.1021/BI049380H.

[43]   L. Zorzetto, L. Andena, F. Briatico-Vangosa, L. De Noni, J.M. Thomassin, C. Jérôme, Q. Grossman, A. Mertens, R. Weinkamer, M. Rink, D. Ruffoni, Properties and role of interfaces in multimaterial 3D printed composites, Sci. Reports 2020 101. 10 (2020) 1–17. https://doi.org/10.1038/s41598-020-79230-0.

[44]   L. De Noni, L. Zorzetto, F. Briatico-Vangosa, M. Rink, D. Ruffoni, L. Andena, Modelling the interphase of 3D printed photo-cured polymers, Compos. Part B Eng. 234 (2022) 109737. https://doi.org/10.1016/J.COMPOSITESB.2022.109737.

[45]   M.J. Mirzaali, M.E. Edens, A.H. de la Nava, S. Janbaz, P. Vena, E.L. Doubrovski, A.A. Zadpoor, Length-scale dependency of biomimetic hard-soft composites, Sci. Rep. 8 (2018) 12052. https://doi.org/10.1038/s41598-018-30012-9.

[46]   A.R. Studart, R. Libanori, R.M. Erb, Functional Gradients in Biological Composites, in: Bio-Bioinspired Nanomater., Wiley-VCH Verlag GmbH & Co. KGaA, Weinheim, Germany, 2014: pp. 335–368. https://doi.org/10.1002/9783527675821.ch13.

4.5 Supporting information

S4.1. Definition of the individual designs and 3D image generation

Overall, to obtain the geometries for each of our triply periodic minimal surfaces (TPMS) designs, we used the isosurface equations (U) of Gyroids, Diamonds, and Octo in their sheet form [1]. These equations across the cartesian system (x, y, z) are:

Gyroid $\qquad U_{\text{GY}} = \cos(x)\sin(y) + \cos(y)\sin(z) + coz(z)\sin(x) = 0 \qquad$ …(S1)

Diamond $\qquad \begin{aligned} U_{DI} = \sin(x)\sin(y)\sin(z) &+ \sin(x)\cos(y)\cos(z) \\ &+ \cos(x)\sin(y)\cos(z) \\ &+ \cos(x)\cos(y)\cos(z) = 0 \end{aligned}$ …(S2)

Octo $\qquad \begin{aligned} U_{\text{OC}} = 4(\cos(x)\cos(y) &+ \cos(y)\cos(z) + \cos(z)\cos(x)) \\ &- 3(\cos(x) + \cos(y) + \cos(z)) = 0 \end{aligned}$ …(S3)

For each of these designs, we defined the isosurfaces with the help of discrete 3D mesh vectors on MATLAB R2018b (Mathworks, USA), where each of the individual elements had the size of a voxel and the total edge of each cubic unit-cell was $2.032\ mm$ (or $24\ voxels$). We then discretized the equations based on the required hard material volume fraction ($\rho(x)$) function across the horizontal direction (x), yielding the desired 3D TPMS interface designs.

At the same time, we used simple parametric equations of a helix function for the Collagen designs [2]. We defined these equations in the cartesian system as:

$$x = ct; \quad y = r\sin(t + \phi); \quad z = r\cos(t + \phi) \qquad \text{…(S4)}$$

Where $t \in [0, 2\pi)$ defines the unit-cell discretization, $c = \frac{2.032}{2\pi}$ mm is a constant that provides the separation of the helix, $r = 0.508\ mm$ is the radius of the helix, and $\phi = \left[0, \frac{1}{3}, \frac{2}{3}\right]\pi$ is the phase angle that defines the rotation for each of the three helices in the design. After repeating each of these cubic $2.032\ mm$ edged unit-cells across the total dimensions of the interface, we used the $\rho(x)$ function to define the thickness of the helical beams, defining the proper material discretization.

S4.2. A comparative study between the full-quadrant and single unit-cell FEM models

We processed an additional set of simulations to study the effects of the number of modeled unit cells on the simulation results. In particular, we tried to establish whether the

models in which only a single unit cell was included could capture the behavior of the actual experimental tensile tests. To this end, we prepared simulations of 3 different designs. These were the non-graded control (W_G = 0 mm), the long OC (W_G = 12 mm), and the long PA (W_G = 12 mm) (Figure S3). We selected these designs because they are quadrant-symmetric, allowing us to simulate only 2 unit cells of the interface (*i.e.,* 1 along their thickness and 2 across their width). These simulations were prepared under the same conditions as described in the main article. However, symmetric boundary conditions were additionally applied on the $y = 0$ (*i.e., $U_y = 0, R_x = 0, R_z = 0$*) and $z = 0$ planes (*i.e., $U_z = 0, R_y = 0, R_z = 0$*).

The estimations made by the quadrant symmetric (Quad) model of the control group were remarkably similar to those of the single unit cell (UC) models and DIC-measured strain distributions (Figure S3a). In both types of simulations, the deformations were highly concentrated at the interface, with the Quad and UC estimations showing ϵ_c values of 2.28 and 1.7, respectively. Although the absolute strain values differed between both types of models, they occurred at the corners of the specimens regardless of the model type. The corners of the specimens are the locations where high values of shear deformation tended to be present. These peak strain values also appeared in the DIC measurements, where, as expected, the ϵ_c value was lower than those predicted computationally. This is due to the averaging effects caused by the lower resolution of the DIC measurements as compared to the computational models and the potential photopolymer mixing prior to curing. Finally, both UC and Quad simulations showed diminished values of the von Mises strains at the center of the cross-sections of the specimens, which is expected because, in this region, only volumetric strains occur.

In the case of the long OC geometries, the strain patterns of the first layer of the Quad and UC simulations were almost identical to those of the DIC measurements (Figure S3b). Similarly, the patterns of the $\epsilon_{eq,m}(x)$ distribution within the first layer of the specimens presented the same transitions as observed in the experimental results, indicating that both types of models capture the essential features of the experimental observations. Consistent patterns of strain were also present within the layers with the maximum strain value, regardless of the type of the FEM model. The FEM-predicted ϵ_c values were 6.36 and 4.53 for the Quad and UC simulations, respectively. Although the magnitude of these strain peaks

differed, the shapes of the maximum $\epsilon_{eq,m}(x)$ plots followed the same trends, with the strain peaks occurring in the regions with a hard discontinuous transition from the hard to the soft material. Similarly, the $E(x)$ functions estimated by both UC and Quad models were similar both in values and trends, indicating that the number of the modeled unit cells does not alter the essence of the predicted mechanical behavior.

Considering the long PA simulations, both Quad and UC models estimated somewhat higher peak strain values within the top layer of the interface than those measured through DIC (Figure S4c). As discussed in the main text of the article, the absence of these peaks in the DIC images was likely due to its lower resolution and the potential material mixing between single droplets of the photopolymers. Despite these differences, the $\epsilon_{eq,m}(x)$ values and their localizations were remarkably similar in both the Quad and UC models. Similar to both other designs, the strain values predicted by the Quad models were higher than those resulting from the UC simulations (**FEM (max)** ϵ_c = 1.84 and 1.79 for the Quad and UC models, respectively). In both cases, such strains were localized within the middle region of the interfaces and along the edges of the specimens. As described in the main text, the strain peaks observed within the regions made from mostly hard material are of relatively minor importance for the PA designs because any cracks initiated in these regions are likely to be arrested. Moreover, the plots of $\epsilon_{eq,m}(x)$ were remarkably similar in the regions closest to the soft material, indicating that the maximum strains estimated by the UC model are representative of the full specimens at regions where failure is most likely to occur. As in the case of the long OC specimens, little to no differences were present between the trends seen in the plots corresponding to the UC and Quad $E(x)$ models, further corroborating the claim that UC models can successfully capture the main mechanisms behind the observed differential mechanical behaviors of the various considered groups.

Overall, the main differences observed between the UC and Quad models were the **FEM (max)** ϵ_c values which were somewhat higher for the quadrant symmetric simulations. The localization of these peaks was, however, highly consistent between both types of models. Moreover, the differences in the peak strain values tended to disappear in the regions closest to the soft material, which are the most critical places (because failure due to a sub-optimal interface is likely to occur within those regions). Finally, the similarity between the elastic modulus functions predicted by both types of models allowed us to conclude that UC FEM

models are representative of the full-size models, allowing for the application of such computationally efficient simulations for the analysis of the remaining designs.

S4.3. A comparative study between the ductile failure mode within FEM simulations

We performed additional simulations to determine the failure modes that can occur within various soft-hard interface designs. These simulations were performed for the control (*i.e.,* non-graded), short (*i.e., W_G* = 4 mm) GY, long (*i.e., W_G* = 12 mm) CO, PA, and GP designs with the same meshes as the ones used for the initial hyperelastic simulations. In this case, however, we introduced plasticity and ductile damage with element deletion into the material models used for the soft material, allowing us to study the failure route of each design. Due to software (*i.e.,* Abaqus) limitations, such models required changing the elastic material properties of the soft material from hyperelastic to linear elastic (*i.e.,* elastic modulus E_{soft} = 1.3 MPa and ν_{soft} = 0.48) and the type of analysis from quasi-static to dynamic explicit. The yield stress point of the soft material was set to 1.2 MPa under a von Mises yield criterion, followed by a linear strain hardening modulus of 0.58 MPa, where element deletion was set for a plastic strain of 5%. These values are based on the existing coarse-graining models for these materials [3]. Regarding the boundary conditions, we applied a displacement to the hard edge of the specimens until mesh separation while applying symmetric boundary conditions to the soft edge of the mesh.

Following the post-processing stage (Supplementary videos 4.10 to 4.14), we found that the stress *vs.* strain curves of all the designs show similar increases in the stress followed by failure due to element deletion (Figure S8a). The long GP design showed the highest values of the strain energy density, while the short GY design underperformed when compared to the other designs (Figure S8b). Regarding the plastic energy dissipation prior to failure, the non-graded design showed hardly any capacity for energy dissipation (Figure S8c), instead featuring high strain concentrations at the edges of the interface, which caused its sudden failure (Figure S8d). Similarly, in the short GY models, the sharp-ended features at the edges of the specimens introduced strain concentrations that caused the separation of the mesh (Figure S8e), confirming the design guideline presented in the main text that recommends avoiding such features. It is, however, important to emphasize that the short GY designs showed the lowest strain concentration values among all the TPMS designs in the initial

hyperelastic FEM simulations. Indeed, potential photopolymer blending effects within the 3D-printed specimens may have ameliorated the negative effects of these features, explaining their improved performance in the initial experiments. The long CO and GP designs showed comparatively high strains along their interfaces with regions of relatively low values of strain concentrations that resulted in multiple regions of plastic deformations, confirming how relatively compliant transitions can help in accommodating strains through plastic energy dissipation and can prevent the catastrophic failure of more periodic interfaces. Moreover, both the PA and GP designs showed multiple regions of soft material separation along their interface prior to failure, where cracks were arrested by neighboring hard material voxels. These observations confirm how particle-based designs provide the additional toughening mechanism of crack deflection. However, it is important to mention that for such a mechanism to be applicable, the distribution of the randomly positioned particles must be periodic [4], unlike in these simulations where particles were present only in a very small cross-section area. All in all, this comparative study allowed us to study how the presented design guidelines that suggest avoiding sharp-ended geometries and including compliant transitions and crack-arresting features have the potential to positively affect the performance of soft-hard interfaces.

S4.4. A comparative study of the effects of varying the elastic modulus of the hard material

We included additional quasi-static hyperelastic computational simulations to analyze the effects that the elastic modulus of the hard material has on the strain concentrations of the interfaces. These simulations were performed for three different interface designs (*i.e.,* GY $W_G = 4$, CO $W_G = 12$, and PA $W_G = 12$) under the same conditions as presented in Section 2.4 of the main text. Four values of the elastic modulus were tested (*i.e.,* $E_{\mathrm{Hard}} = [250, 1000, 2651, \text{and } 10000]$ MPa).

After post-processing, we found that, as the E_{Hard} values are varied, there are only limited changes in the overall ϵ_c peak values corresponding to each design (Figure S9). For the CO design, the changes in the properties of the hard material only affected the magnitude of the ϵ_c transition function along the gradient, which increased when decreasing E_{Hard}. The general patterns of strain distribution, however, remained consistent. The location of the ϵ_c peaks remained in the concave and sharp regions of the short GY specimens, within the soft

regions of each helix in the CO specimens, and in the single soft material particles located along the interface of the PA specimens. These results indicate that even though the properties of the hard material influence the interface behavior to some extent, the overall performance of the interfaces is primarily dependent on the geometrical aspects of the functional gradients.

S4.5. Analysis of the effects of photopolymer blending

Additional ductile fracture analyses were performed to unravel the potential effects of photopolymer blending on the performance of soft-hard interfaces. Towards this end, we introduced an algorithm that allowed us to create an intermediate phase between the soft and hard phases throughout the entire geometry of the specimens in our computational models (Figure S10a). For this intermediate phase, we first changed the element-to-voxel ratio from 1 to 27 (3×3×3). To consider the potential blending at the edges of each voxel [5], we updated the value of the ratio of the hard material ρ'_{ijk} of each element across the ijk directions ($i.e.,$ initially $\rho' = 0$ for pure soft and $\rho' = 1$ for pure hard material) by averaging it with its adjacent elements. This averaging was performed using the following equation:

$$\boldsymbol{\rho'_{i,j,k}} = \frac{1}{27} \sum_{m=-1}^{1} \sum_{n=-1}^{1} \sum_{o=-1}^{1} \rho'_{i+m,j+n,k+o} \qquad \text{...(S5)}$$

The resulting ρ' values of each element were then used as input for obtaining the elastoplastic properties of each element, where coarse-graining models for large deformations similar to those existing in the literature were used as the constitutive models [3]. We applied this process for the non-graded control design and the long PA ones and compared their resulting mechanical response with those of their non-blend variants. Since increasing the element to voxel representation by 27 would make computational models infeasible, we restricted the meshes to interfaces of 12×12 voxels in the surface area and 96 voxels in length, yielding 373248 C3D8 elements per mesh. The resulting four simulations were processed under the same conditions as described in the Section S4.3 of this document.

After post-processing the results (Supplementary videos 4.15-4.18), the blended version of both the control and the PA gradients showed improvements in their ultimate stress and strain energy density (Figure S10 b-c). For the non-graded design, the strength increased from 0.382 MPa to 0.399 MPa, while the strain energy density increased from 20.04 kJ/m^3 to

22.37 kJ/m^3. As for the PA, the strength increased from 0.41 to 0.45 MPa, whereas the strain energy density improved from 35.96 to 44.6 kJ/m^3. The relatively larger improvements observed in the particle-based design can be partially attributed to the increased contact surface area between the polymer phases. It is important to acknowledge, however, that the separation of the blend phases highly depends on the selected coarse-graining model. In this case, we assumed that the ultimate strain before the separation of the intermediate phase is given by the rule of mixtures between the hard and soft material phases. This assumption was necessary because no experimental data exist regarding the ultimate strain of the sub-voxel blended phase. That being said, the overall strain distribution of the blended simulations and the failure modes of both designs were remarkably similar regardless of whether blending was implemented in the models (Figures S10e). In the case of the PA designs, multiple non-critical cracks were present prior to failure for both simulations, indicating that the crack deflection capacity of this design remains present regardless of whether blending is implemented in the models.

In short, these analyses showed that while photopolymer mixing plays a potential toughening role by reducing interfacial strain concentrations, the overall behavior and the toughening mechanisms achieved by varying the geometry of the interface remain consistent between the models incorporating such a blending effect and those neglecting it. To properly account for the additional toughening mechanisms resulting from blending, one would need to perform additional experimental characterizations of the effects of photopolymer blending on the complex particle-based composites, building up on the existing analyses of soft-hard slab connections [5,6].

List of supporting tables

Table S4.1. The quasi-static tensile test results corresponding to the various types of functional gradient (mean ± standard deviation).

Geometry	Gradient Width W_G (mm)	Elastic modulus E (MPa)	Ultimate tensile strength $\sigma_{\max}$ (MPa)	Strain energy density U_d (kJ/m³)	DIC-measured ϵ_c (-)	FEM-estimated ϵ_c (-)
Control	0.000	0. 9727±0.006	1.8336±0.084	483.112±23.90	1.5529±0.071	1.699
Gyroid (GY)	4.064	0.9313±0.022	2.6824±0.162	682.564±11.01	1.0805±0.029	2.0450
	8.128	0.9854±0.004	2.2128±0.270	531.134±53.90	0.9916±0.032	1.9967
	12.192	1.0444±0.008	2.1747±0.063	504.993±10.53	1.1638±0.048	2.4933
Diamond (DI)	4.064	1.0105±0.058	2.3957±0.203	563.165±69.80	0.9566±0.015	2.2475
	8.128	0.9963±0.037	2.399±0.431	571.999±148.84	0.9365±0.011	2.3372
	12.192	1.0497±0.040	2.3479±0.199	575.331±64.10	1.0050±0.070	2.3804
Octo (OC)	4.064	0.9959±0.028	1.7508±0.011	420.576±4.73	0.9423±0.026	1.9600
	8.128	0.9822±0.008	1.8308±0.067	430.172±4.29	1.1428±0.035	2.3228
	12.192	0.9879±0.003	1.007±0.111	216.064±25.97	1.0922±0.105	4.5312
Collagen (CO)	4.064	0.9468±0.052	2.1563±0.272	502.658±52.28	1.0295±0.035	1.6625
	8.128	0.9913±0.112	2.2817±0.164	547.302±17.12	0.9824±0.094	1.6852
	12.192	0.9755±0.051	2.6234±0.139	643.332±37.12	1.0153±0.026	1.6295
Particles (PA)	4.064	0.9730±0.117	2.1931±0.351	480.182±43.88	1.0903±0.031	1.6000
	8.128	1.0314±0.001	2.2043±0.090	500.503±14.64	1.1414±0.002	2.4305
	12.192	0.9860±0.015	2.5354±0.198	615.399±62.65	1.0682±0.044	1.7915
GY+PA (GP)	4.064	1.0154±0.053	2.3202±0.110	545.249±48.94	1.0910±0.017	2.7173
	8.128	0.9335±0.012	2.3669±0.060	630.617±51.79	1.0182±0.075	2.2441
	12.192	0.9693±0.090	2.6975±0.036	715.459±18.32	1.0421±0.025	2.0593

Table S4.2. The quasi-static shear test results corresponding to the various types of functional gradients (mean ± standard deviation).

Geometry	Gradient Width W_G (mm)	Shear modulus G (MPa)	Ultimate shear strength τ_{max} (MPa)	Strain energy density U_d (kJ/m³)	FEM-estimated ϵ_c (-)
Control	0.000	0.3673±0.0102	3.4158±0.0960	0.8766±0.0504	2.3490
Gyroid (GY)	4.572	0.2815±0.0142	2.3868±0.0379	0.7114±0.0663	4.4659
Collagen (CO)	4.572	0.2817±0.0110	2.9269±0.0606	0.8921±0.0103	3.4884
Particles (PA)	4.572	0.3023±0.0495	3.8016±0.0415	1.1489±0.0871	2.9438

List of supporting figures
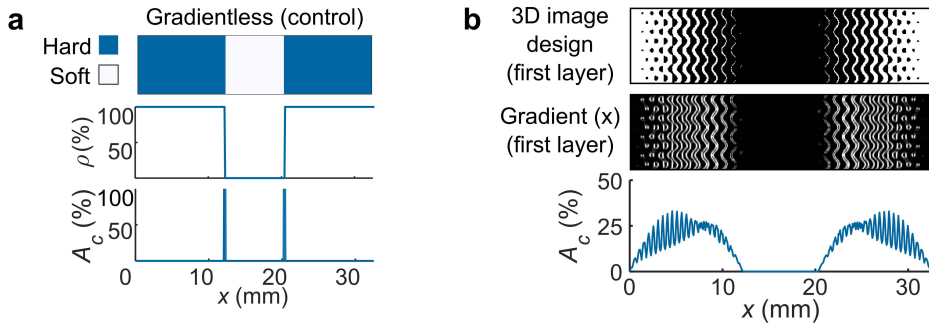
Figure S4.1. a) The design of the control group and its material distribution, where no gradient was considered between both phases. b) The schematic representation of the process to calculate the percentage of hard-soft normal contact area (A_c) for every design. To calculate A_c, we used the 3D image gradient in the x-direction, which was calculated via the Sobel method and normalized the total surface area of each cross-sectional layer for every design.
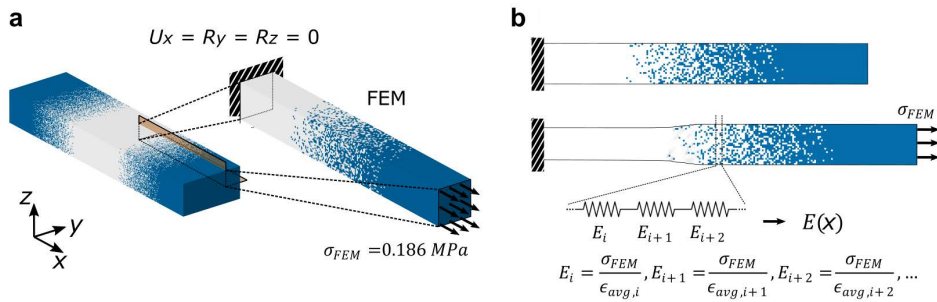
Figure S4.2. a) We considered one cross-sectional unit-cell (24×24 voxels) and one-half of the symmetric interface to generate the meshes of every computational simulation, where we prescribed symmetric boundary conditions ($U_x = R_y = R_z = 0$) on its soft (white) edge and surface traction on its hard (blue) end. b) The schematic representation for calculating the elastic modulus function ($E(x)$) of every design, where we idealized each cross-sectional layer of the FGs into linear springs, from which we obtained their average deformations ($\epsilon_{avg,i}$) and elastic moduli (E_i).
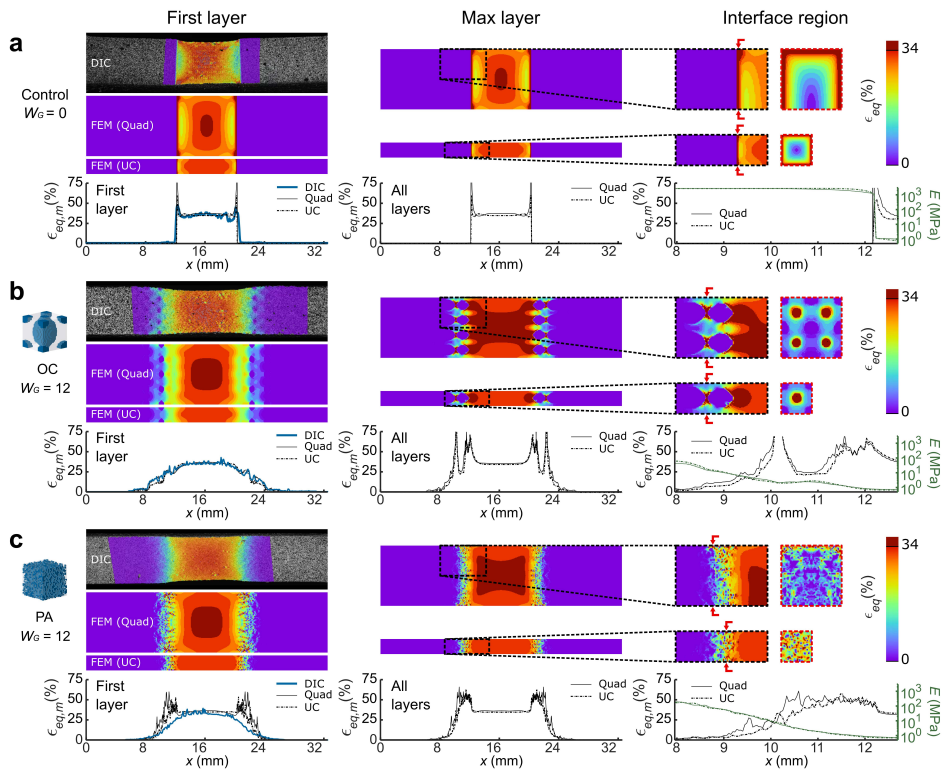
Figure S4.3 A comparison between the results of the symmetric quadrant (Quad) and single unit cell (UC) FEM models. We performed detailed comparisons between the results of both types of simulations on the one hand and the DIC measurements on the other. In particular, we compared the maximum equivalent strains and the plots corresponding to the elastic modulus transitions between these simulations and the DIC-based measurements. The selected designs were the non-graded control group (a), the long OC designs (b), and the long PA (c).
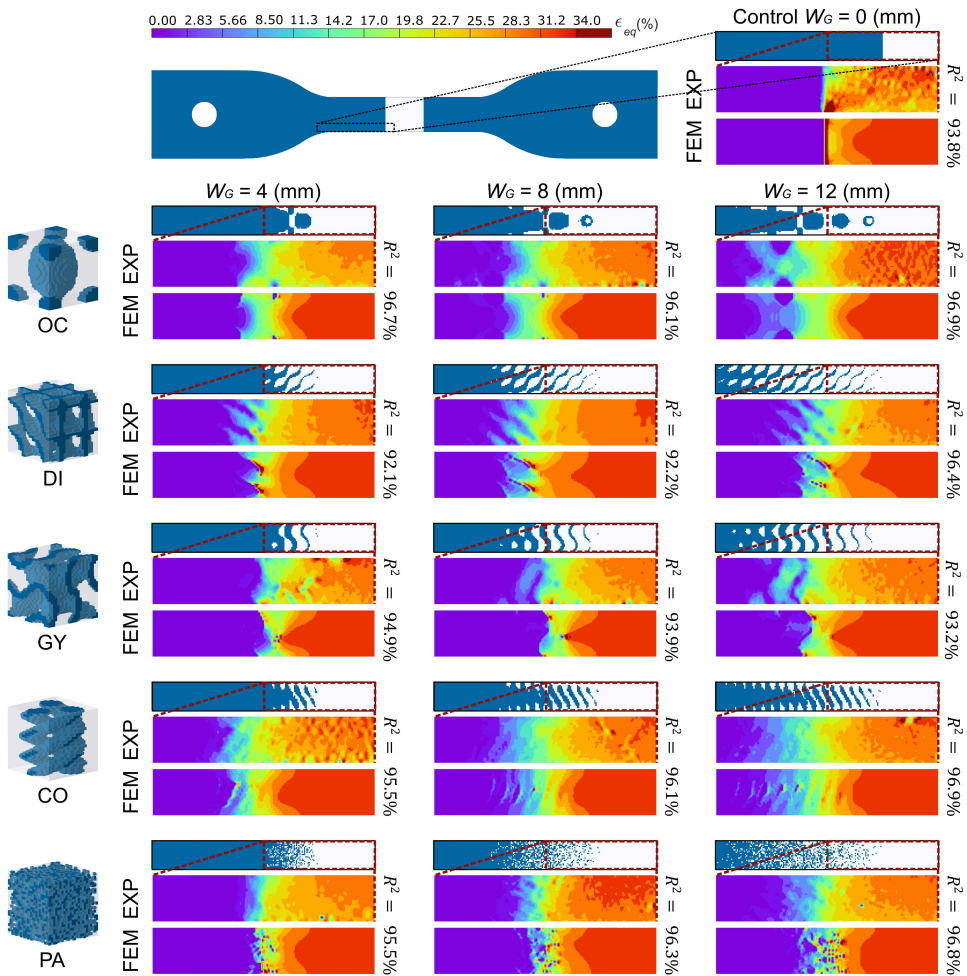
Figure S4.4. A comparison between the surface strains of the experimental DIC measurements and strain of the top surface of the FEM simulations. The R^2 values represent the ordinary coefficients of determination when comparing all the strains between the images.
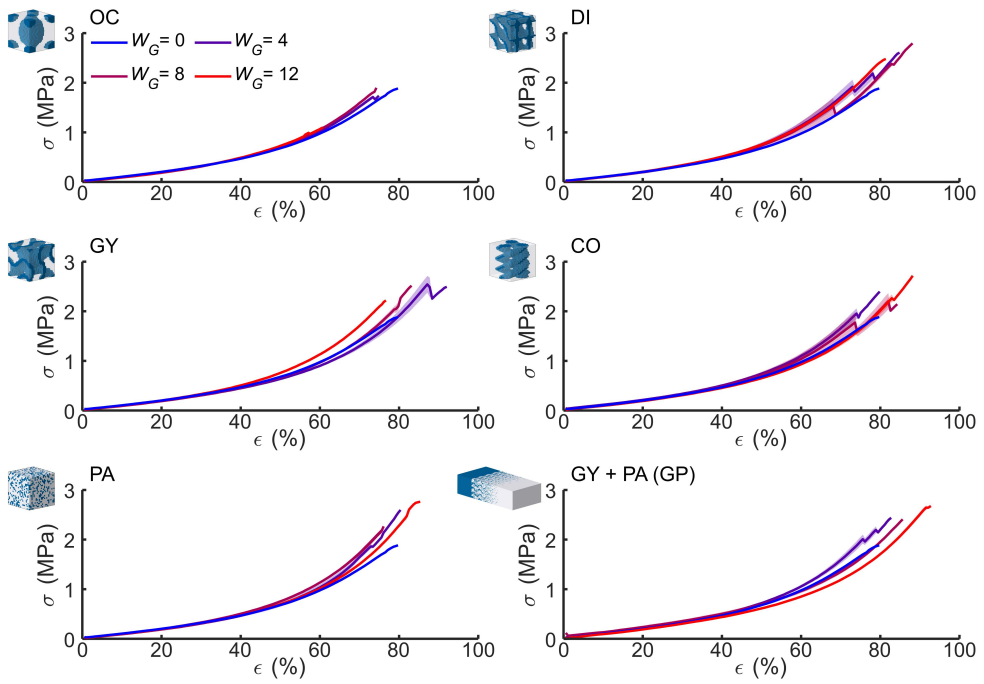
Figure S4.5. The quasi-static tensile test results. The true stress *vs.* strain (σ *vs.* ϵ) show the mean (and shaded $\pm SD$) hyperelastic behavior of the tested interfaces, where each color represents a different gradient length (W_G).
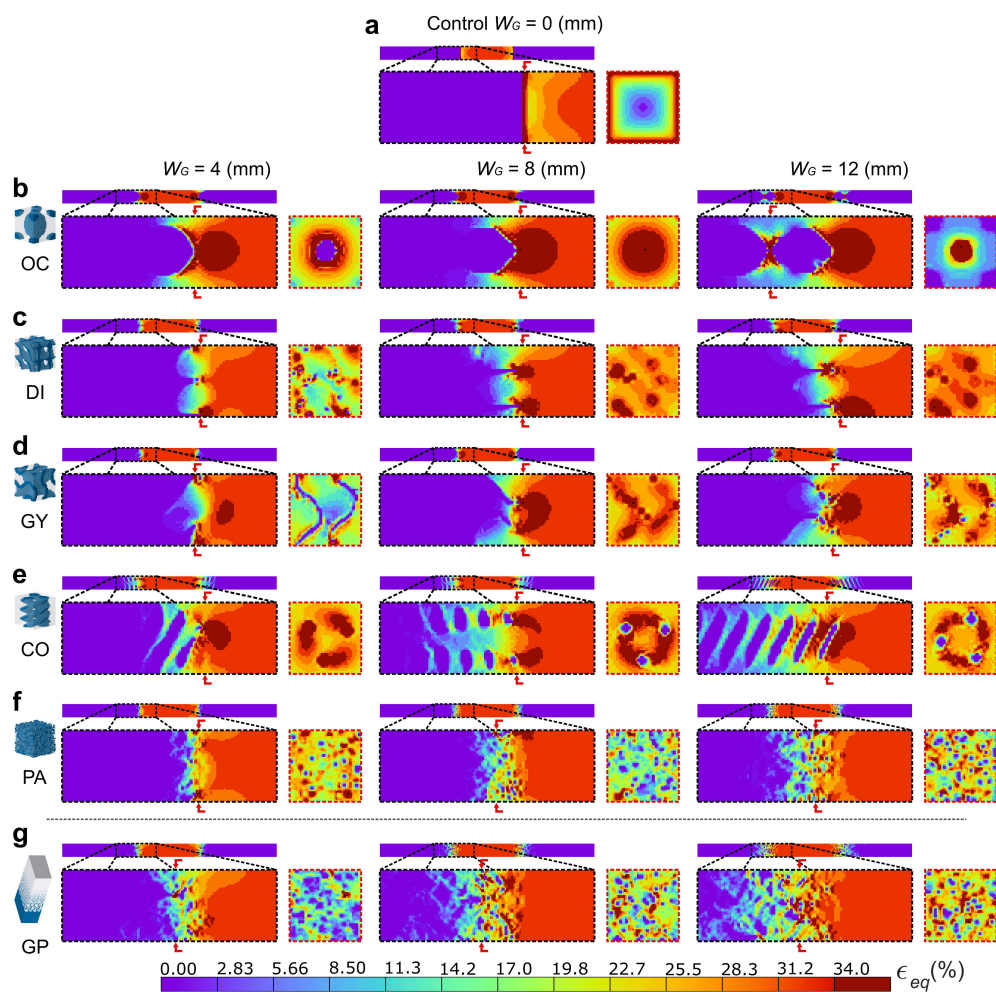
Figure S4.6. The FEM-predicted distributions of the true equivalent strain of every studied interface under tensile conditions obtained from the transversal and cross-sectional layers that presented the peak strain values. The strains of every figure were obtained from the layer that presented the peak values of strain for every design. The designs were the Octo (a), Diamond (b), Gyroid (c), collagen (d), randomly-reinforced particles (e), and Gyroid + particles interface (f).

Figure S4.7. Detailed plots comparing the A_c pattern and estimated elastic modulus $E(x)$ with the estimated maximum equivalent strain, $\epsilon_{eq,m}(x)$, for every interface at the final 4 mm of every studied FG. The designs were the octo (a), diamond (b), gyroid (c), collagen (d), randomly-reinforced particles (e), and gyroid + particles interface (f).
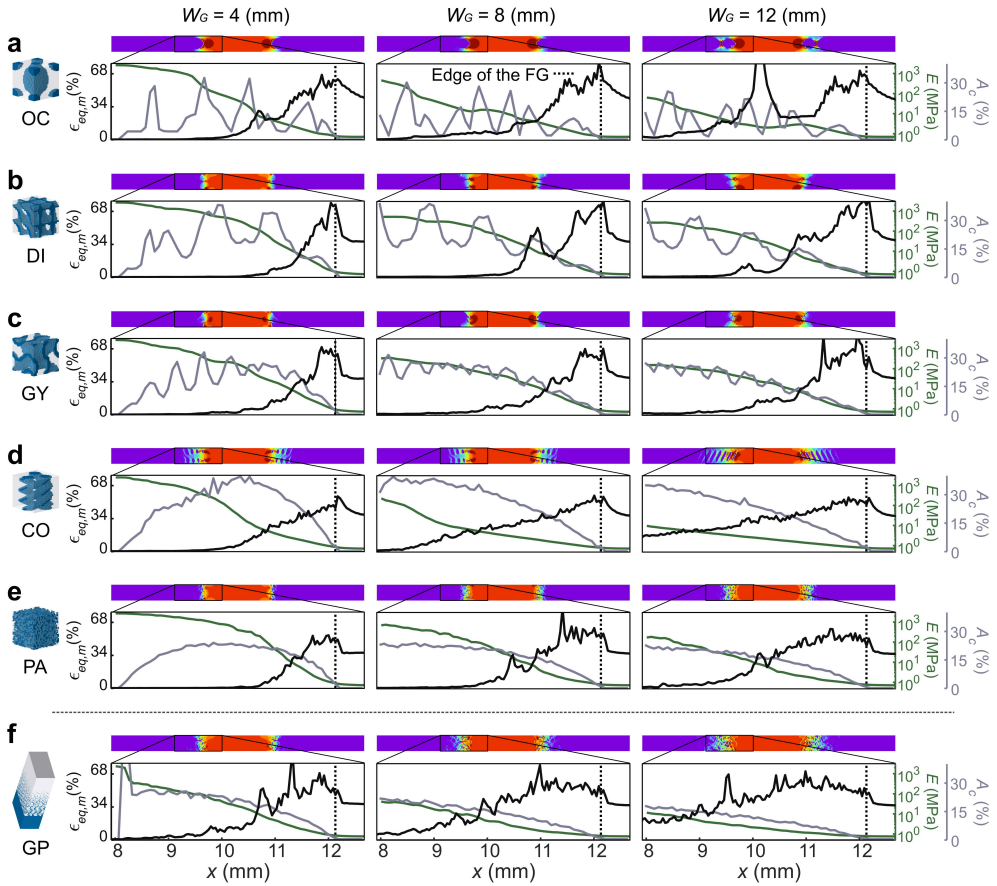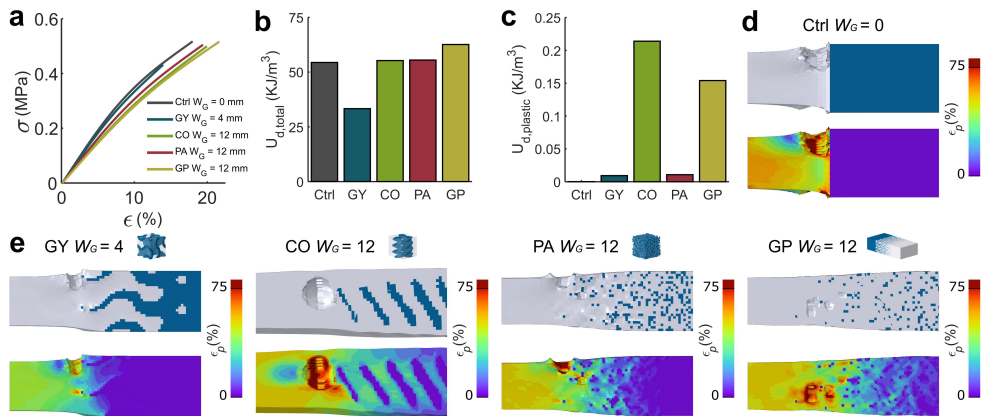
Figure S8. The results of the ductile failure analysis applied to a selected number of designs. a) Stress vs. strain curves of all considered designs. The values of the total (b) and plastic (c) strain energy densities. d) and e) the distribution of the first principal strain in the simulations and the failure modes prior to critical failure.
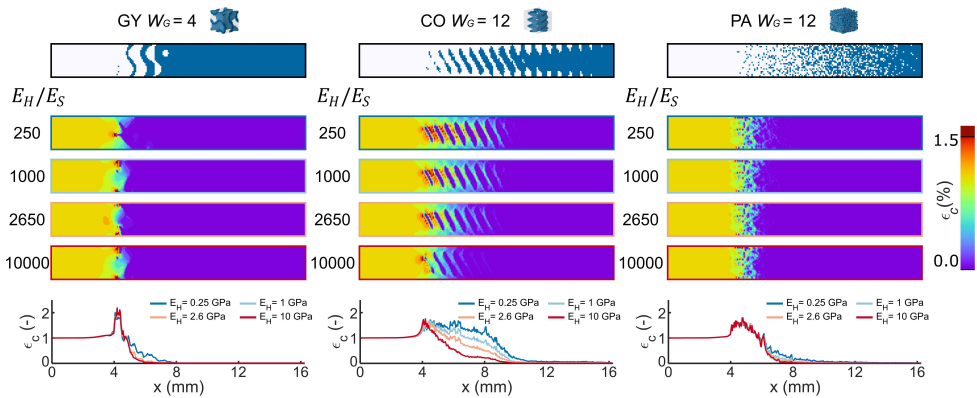

Figure S9: The strain concentrations resulting from the different ratios of the elastic modulus of the hard material to that of the soft material. These results confirm that the maximum values of ϵ_c remain relatively similar, and the patterns of the ϵ_c transition along the interface remain consistent with the gradient geometries.
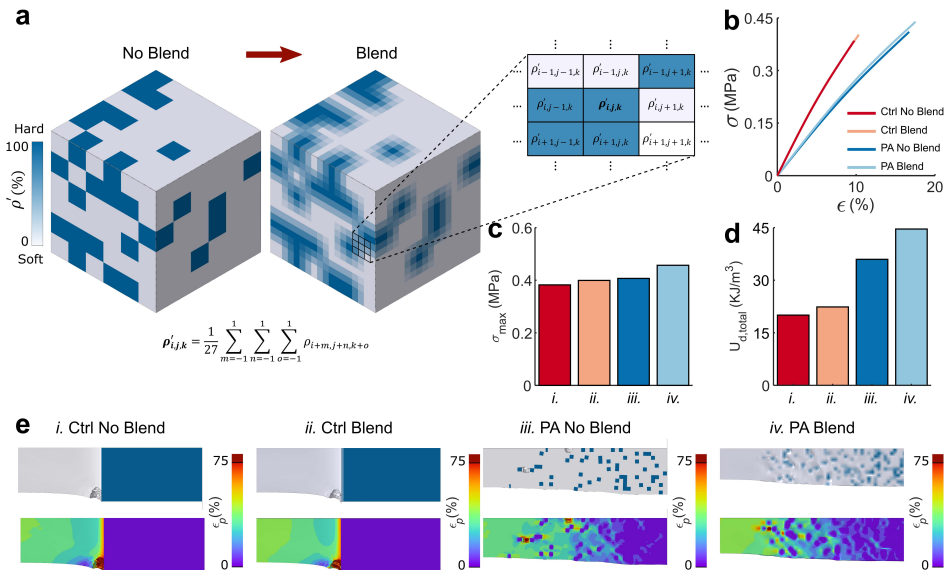
Figure S4.10: The effects of photopolymer blending on the outcome of explicit ductile failure FEM simulations. a) The hard material ratio (ρ') of a blended photopolymer composite is obtained by averaging the initial value of each element with those of its adjacent elements. b) the stress *vs.* strain curves, c) the ultimate stress, and d) the ultimate strain of the resulting simulations. e) the distributions of the first principal true strain of each design just before its critical failure.

Supporting references

[1]   S.C. Kapfer, S.T. Hyde, K. Mecke, C.H. Arns, G.E. Schröder-Turk, Minimal surface scaffold designs for tissue engineering, Biomaterials. 32 (2011) 6875–6882. https://doi.org/10.1016/J.BIOMATERIALS.2011.06.012.

[2]   E.W. Weisstein, Helix, MathWorld--A Wolfram Web Resour. (n.d.). https://mathworld.wolfram.com/Helix.html.

[3]   M.C. Saldívar, E.L. Doubrovski, M.J. Mirzaali, A.A. Zadpoor, Nonlinear coarse-graining models for 3D printed multi-material biomimetic composites, Addit. Manuf. 58 (2022) 103062. https://doi.org/10.1016/J.ADDMA.2022.103062.

[4]   M.J. Mirzaali, M.E. Edens, A.H. de la Nava, S. Janbaz, P. Vena, E.L. Doubrovski, A.A. Zadpoor, Length-scale dependency of biomimetic hard-soft composites, Sci. Rep. 8 (2018) 12052. https://doi.org/10.1038/s41598-018-30012-9.

[5]   L. Zorzetto, L. Andena, F. Briatico-Vangosa, L. De Noni, J.M. Thomassin, C. Jérôme, Q. Grossman, A. Mertens, R. Weinkamer, M. Rink, D. Ruffoni, Properties and role of interfaces in multimaterial 3D printed composites, Sci. Reports 2020 101. 10 (2020) 1–17. https://doi.org/10.1038/s41598-020-79230-0.

[6]   L. De Noni, L. Zorzetto, F. Briatico-Vangosa, M. Rink, D. Ruffoni, L. Andena, Modelling the interphase of 3D printed photo-cured polymers, Compos. Part B Eng. 234 (2022) 109737. https://doi.org/10.1016/J.COMPOSITESB.2022.109737.
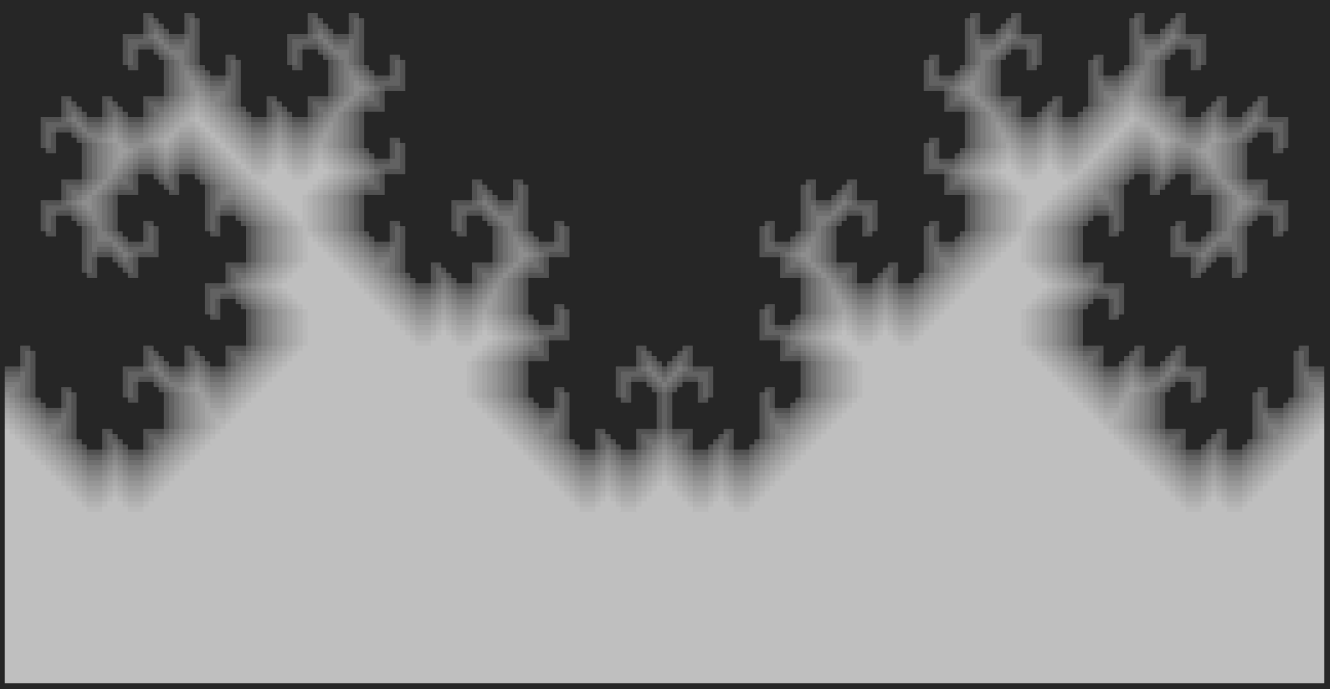
5

Multi-Material 3D Printing of Functionally Graded Hierarchical Soft–Hard Composites

5. Multi-Material 3D Printing of Functionally Graded Hierarchical Soft–Hard Composites

Abstract

Hard biological tissues (e.g., nacre and bone) have evolved for millions of years, enabling them to overcome the conflict between different mechanical properties. The key to their success lies in the combination of limited material ingredients (i.e., hard and soft constituents) and mechanistic ingredients (e.g., functional gradients and building block hierarchical organization). However, the contribution of each material and mechanistic ingredient is still unknown, hindering the development of efficient synthetic composites. Quantitative and systematic studies of hard–soft composites are required to unravel every factor's role in properties outcome. Herein, a voxel-by-voxel multi-material 3D printing technique is used to design and additively manufacture different groups of hard–soft composites. Several combinations of gradients, multilevel hierarchies, and brick-and-mortar arrangements are created. Single-edge notched fracture specimens are mechanically tested and computationally simulated using extended finite element method (XFEM). It is found that functional gradients alone are not sufficient to improve fracture properties. However, up to twice the fracture energy of the hard face is observed when combining functional gradients with hierarchical designs, significantly increasing composite properties. Microscopic analysis, digital image correlation, and strain distributions predicted with XFEM are used to discuss the mechanisms responsible for the observed behaviors.

5.1. Introduction

Hard biological tissues, of which bone and nacre are prime examples, are staggeringly efficient structural materials. Through millions of years of evolutionary refinement, nature has found ways to overcome the conflict between different mechanical properties. [1,2] The structural performances of nearly all conventional engineering materials pale in comparison with that high level of multifaceted mechanical efficiency. A particularly tall order that engineering materials usually fall short of is combining high levels of stiffness with toughness and strength. Engineers, therefore, have to choose one property over another, often resulting in toughness being prioritized over strength for the reasons of safety, [3,4] thereby rendering engineering structures highly inefficient. [1]

It is unclear how exactly hard biological tissues achieve such remarkable degrees of structural performance. Intensive research, particularly during the last decade, has

successfully identified the *ingredients* of this success story. On the one hand, the *material ingredients* are usually a relatively soft organic phase, which is based on natural polymers such as proteins and polysaccharides, and an inorganic hard phase, which is made from ceramics such as calcium salts or silica.[2,5–7] On the other hand, the main design strategies or the *mechanistic ingredients* are the application of functional gradients,[8,9] and intricate placement of hard–soft structures (*e.g.,* in a brick-and-mortar fashion) as well as the use of hierarchical structures.[10–13] However, identifying such material and mechanistic ingredients has not enabled us to achieve a similar level of efficiency in our man-made materials, as it is unclear how these mechanistic and material ingredients interact with each other at different spatial and time scales, how important the contribution of each mechanism is, and how one mechanism modulates the effects of the others. In a way, the major mysteries in the design of hard tissues remain largely unsolved.

One approach used by many researchers to unravel the mystery of hard tissues is detailed histological studies aimed at better understanding the nature and role of different material ingredients [14–17] as well as detailed mechanical characterization at different scales [18–22] combined with computational models that could reveal the role of different mechanistic ingredients. [23–26] A major challenge in such approaches is the high degrees of interspecies [27–29] and intraspecies [30,31] variability as well as location dependency of the measured properties [32–34] that make it extremely challenging to perform quantitative and systematic analyses aimed at answering the aforementioned questions and unraveling the mystery of the human bone.

Here, we propose an alternative "voxel-by-voxel" approach, which is analogous to the "atom-by-atom" design paradigm often cited in material science [35–37] and aims to unravel the underlying mechanisms of bone through multiscale design of bone-like hard–soft composites. The different "mechanistic ingredients" can then be systematically incorporated in the design of such bone-like composites to study their effects quantitatively and with a minimum degree of variability. Such an approach was impossible to apply until a few years ago because its success is dependent on the availability of *multi-material* additive manufacturing (AM = 3D printing) techniques that allow for the fabrication of hard–soft composites at multiple length scales. However, recent advances in multi-material AM techniques, including voxel-based polyjet 3D printing, [38–40]

5.2. Methods

To separate the effects of different mechanisms from each other, we designed five different experimental groups including 1) a group of specimens with functional gradients (GRAD), 2) a group of specimens with a single-level brick-and-mortar design but without functional gradients (BM-SL), 3) a group of specimens with both a single-level brick-and-mortar design and functional gradients (BM-GRAD-SL), 4) a group of specimens with a two-level hierarchical brick-and-mortar design but without functional gradients (BM-2L), and 5) a group of specimen incorporating both a two-level hierarchical brick-and-mortar design and functional gradients (BM-GRAD-2L) (Figure 5.1). The specimens used in all five groups were single-edge notched fracture specimens.

We used a multi-material AM technique working on the basis of jetting multiple streams of UV-curable photopolymers (Objet350 Connex3, polyjet multi-material 3D printer, Stratasys Ltd., USA) [38] for the fabrication of our specimens. The minimum resolution of the printer was 600 dpi along the x-axis, 300 dpi along the y-axis, and 847 dpi along the z-axis, resulting in a cuboid voxel with the following dimensions: $42{\times}84{\times}30 \ \mu m^3$. This cuboid was, therefore, the minimum achievable building block used in our designs. We used commercially available materials VeroCyanTM (RGD841) and Agilus30TM Black (FLX985) for the deposition of the hard and soft phases, respectively. The specimens were designed so as to have similar average local hard volume fractions ($\rho = \frac{\sum Vox_{hard}}{\sum Vox_{all}}$) in front of their crack tips (*i.e.,* $\bar{\rho}_c \approx 38\%$) (Figure 5.1d-h, bottom row, and Table S5.2 of the supporting information). The target overall hard volume fraction ($\bar{\rho}_o$) of the specimens was 71% (Table S5.2 of the supporting information).

The designs were defined through binary images files which acted as the input files for the 3D printer and had values of either 1 or 0 assigned to the hard or soft phases, respectively. To process the designs, we introduced a linear gradient pattern in the specimens with functional gradients and defined it in a gray-scale image. These gray-scale images were later converted into binary images using halftoning algorithms [41] (*i.e.,* GRAD, BM-GRAD-SL, BM-GRAD-2L groups) (Figure 5.1d, f, h). The specimens without functional gradients (*i.e.,* BM-SL, BM-2L groups) had only brick-and-mortar patterns in their structures, which were directly designed as binary images (Figure 5.1e, and g). The BM-2L specimens had similar

brick-and-mortar subunits in their first level of hierarchy similar to those of BM-SL (Figure 5.1b). Incorporating those subunits as the building blocks of another brick-and-mortar arrangement created a second level of hierarchy for the BM-2L specimens (Figure 5.1c). The image analysis steps were performed in Matlab (R2017b, Mathworks, US). As there are no standards available to follow for the design of these functionally graded composites, we designed our fracture specimens based on the recommendations provided in the literature for the fracture tests of ductile and brittle composites [42,43]. The geometrical parameters of the specimens are presented in Figure 5.1. The initial crack was placed in the middle of the specimens, spanned 20% of their widths, and was placed at the weakest point with lowest hard volume fraction. In order to attach the specimens to the grippers of the mechanical testing machine, the lower and upper sides of the specimens were extended. The extended parts were made from the same hard material as the hard phase of the composites and were printed together with the specimens.

To perform the fracture tests, the specimens were subjected to a quasi-static uniaxial tensile load (stroke rate = 2 mm/min). Unless otherwise stated, a Lloyd machine (LR5K, load cell = 5 kN) was used for the mechanical tests. The specimens were attached to the machine by a custom-made aluminum gripping system and were fixed using aluminum pins. A pre-load equal to 1 N was applied at the beginning of the tests. The time (T), force (F), and deformation (u) were recorded by the testing equipment.

The normal stress (σ) was calculated as the applied load (F) divided by the initial effective cross-section area: $A_0 = t \times (W - a_0)$, where t is the thickness, W is the width, and a_0 is the length of the initial crack. The strain (ε) was defined as the relative displacement (u) with respect to the initial length of the specimen (L). The stiffness (E) was defined as the stiffest slope of the elastic region of the stress-strain curves. To calculate the stiffness, a moving regression algorithm with a bounding box of 0.2% was used to find the greatest value of the slope. The fracture stress (σ_{max}) was defined as the maximum stress registered during the tests. The fracture energy (U) was defined as the energy required to break the specimen and was calculated by numerically integrating the area below the stress-strain curves.

5. Multi-Material 3D Printing of Functionally Graded Hierarchical Soft−Hard Composites
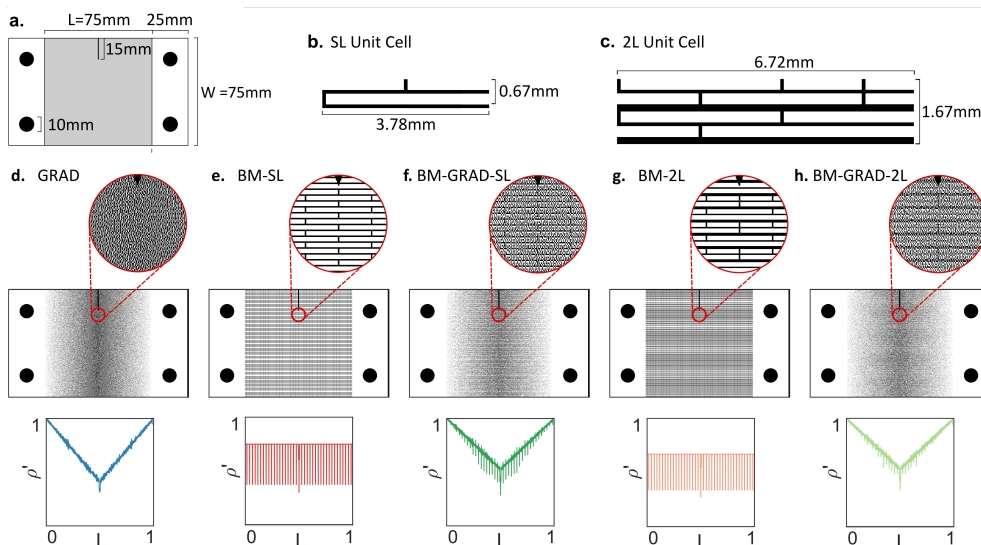

Figure 5.1 A schematic drawing of a single-edge notched fracture specimen a) with the corresponding dimensions used in the current study. We used brick-and-mortar unit cells to create structures with b) one and c) two levels of hierarchy. Binary images were used to 3D print specimens with graded designs, nongraded designs, and a combination of both. d) The specimens with a gradient (GRAD) had 100% hard volume fraction at the regions far from the crack line, which was linearly and symmetrically reduced to 40% in the middle of the specimens along with the initial crack position. e) We used a brick-and-mortar subunit to create our nongraded architected structures (BM-SL). f) The superposition of the graded and non-graded specimens created a new group (BM-GRAD-SL). g) The second level of hierarchy was also defined by combining several subunit cells (BM-2L). h) The superstition of the GRAD and BM-2L designs resulted in the design of the double-level brick-and-mortar specimens with a gradient (BM-GRAD-2L).

We also measured the full-field strain maps using the digital image correlation (DIC) technique. The DIC tests were carried out on a Zwick Roell machine (Zwick GmbH & Co. KG, load cell = 20 kN). The surface of the specimen was first cleaned and then speckled by black dot patterns. In order to enhance the contrast with the black speckles, the specimens were illuminated using a profilux LED during the experiments. Two high-resolution digital cameras (4 MP with CMOS chip) recorded the movements of the speckle patterns during our experiments. The full-field strain maps were then determined using the associated commercial software (Vic-3D 8, Correlated Solutions, SC, USA).

We analyzed the characteristics of the fracture surfaces of our specimens using a digital microscope (Keyence® vhx-5000) at 200x magnifications (zoom lens = VH-Z20T) followed by scanning electron microscopy (JSM-IT100, JEOL, Tokyo, Japan, electron beam energy = 10 kV, magnification = 30,000x).

We also performed computational simulations of the crack propagation tests using the extended finite element method (XFEM) implemented in a commercially available nonlinear code (Abaqus v.6.14, Dassault Systèmes Simulia, US). Plane strain quadratic elements (CPE8) were used for the discretization of the specimen geometries defined by the bitmap images, which were also used for the 3D printing of the specimens. Ideally, the geometry of the finite element models has to be discretized up to the size of the voxel size of the 3D printed structures (*i.e.,* 42 μm), as this would allow for matching the manufacturing resolution. However, that would have resulted in a formidably large number of elements for the XFEM simulations. To decrease the number of elements in our computational models, we coarse-grained the bitmap images and assigned an average value of the hard volume fraction to each coarse-grained element. Each element within the XFEM models, therefore, represented a number of neighboring voxels from the original binary image (Figure 5.2). The density of each element was, then, calculated using an averaged greyscale value of all the original voxels it represented. Therefore, the total density of each voxel dictates the final material properties of that element. The new density of each element with the resolution of n bits per edge was calculated as $\rho' = \rho_{vox} = \frac{\sum bits_{hard}}{n^2}$. This density was used to calculate the individual element's elastic modulus $E(\rho')$, separation strain $\epsilon_{sep}(\rho')$ for the crack separation analysis. From our experimental data, we obtained polynomial expressions correlating the mechanical properties and the hard volume fraction of the new element (Table S5.1 of the supporting information). The crack propagation criteria were set based on the maximum strain separation, which means two elements were separated only if their strain values exceeded the maximum strain separation value. These models and their parameters are presented in Figure 5.2 and Table S5.1 of the supporting information.

The monolithic experimental data was used to obtain the individual hard and soft material properties (Figure 5.2d-e), and was also used to obtain polynomial expressions. We applied displacement control at the top of the model, while fully bounding the lower end. The

displacement value increased until full separation was achieved. Strain fields and reaction forces were recorded throughout the computational simulations.
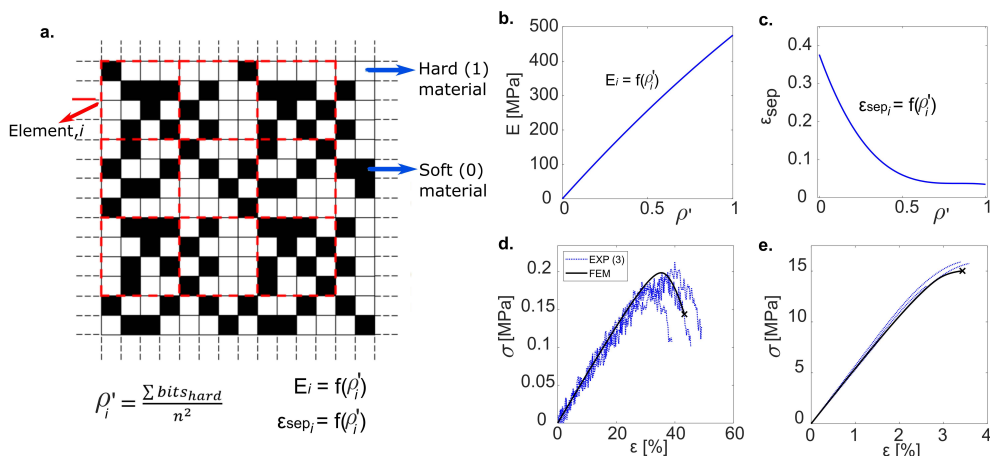

Figure 5.2 a) A schematic drawing of the averaging method used for coarse-graining and for assigning the mechanical properties of the coarse-grained elements in our computational models. A graphical representation of the polynomial relationship of the b) stiffness and c) separation strain as a function of the hard volume fraction (ρ'). The parameters of the models are shown in Table S5.1, supporting information. A comparison of the stress–strain curves predicted by our computational models (XFEM) and experimental observations for monolithically d) soft and e) hard materials.

5.3. Results and discussion

The stress–strain curves of the specimens in different groups showed a similar trend in which the reaction force (or stress) linearly increased. This trend continued until the ductile fracture phase started (Figure 5.3a). After reaching their maximum values, all groups exhibited nonlinearly decreasing forces and, thus, softening behaviors. The specimens without gradients (BM-SL and BM-2L) presented the least ductile fracture, as their ultimate strains were the lowest among the different designs (Figure 5.3a). Contrary to those, the specimens from the GRAD group showed the highest ultimate strain but the lowest maximal stress (Figure 5.3a,b). Interestingly, the specimens with a combination of brick-and-mortar structures and gradients (*i.e.,* BM-GRAD-SL, BM-GRAD-2L) showed a mixture of the behaviors of both graded and nongraded designs (Figure 5.3b).
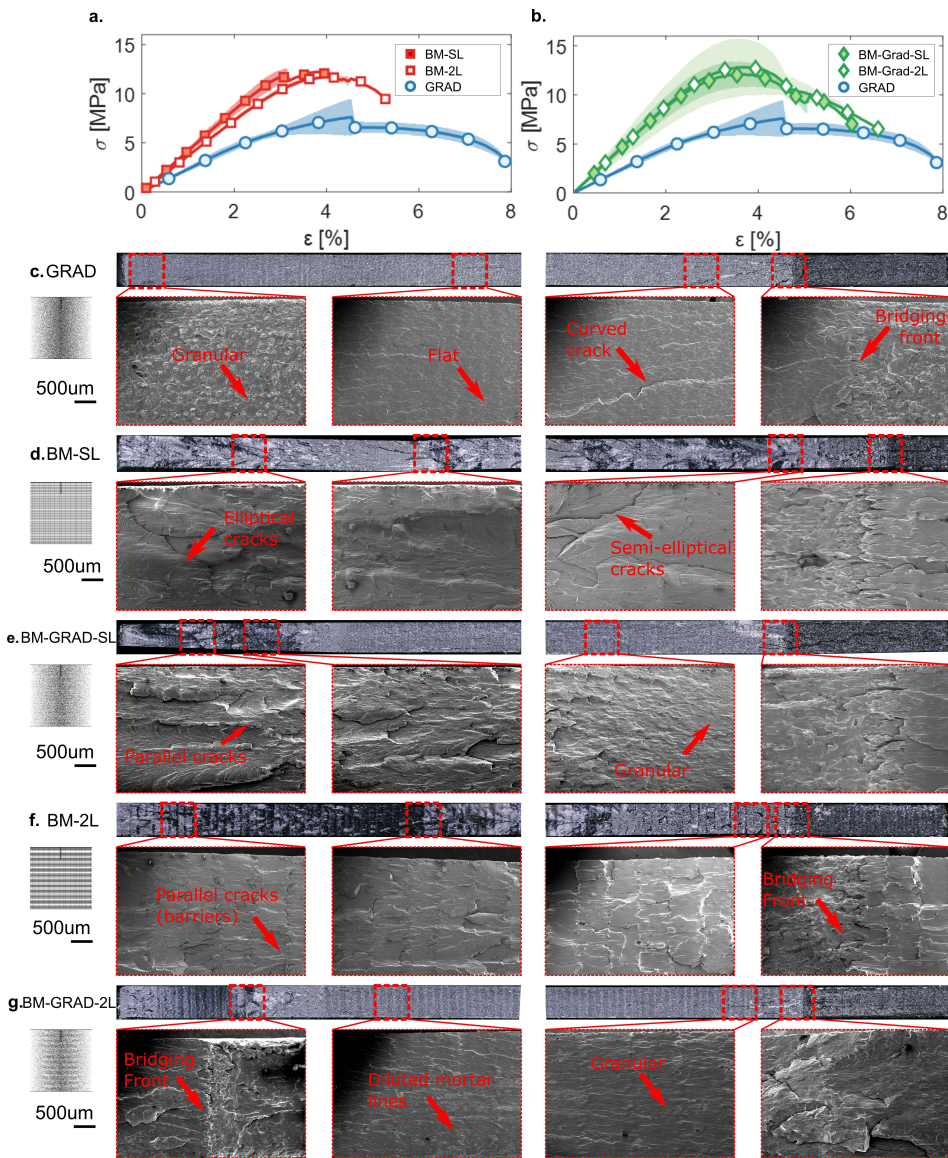
Figure 5.3 a,b) The experimental stress–strain curves of the specimens tested in the current study, with GRAD data presented in both as reference. The optical microscopy and SEM images corresponding to the highlighted regions (in red) from the fracture surfaces of the c) GRAD, d) BM-SL, e) BM-GRAD-SL, f) BM-2L, and g) BM-GRAD-2L groups.

The initial crack propagated in a straight line for the specimens with gradients, while crack-bridging was observed for the nongraded specimens (Figure 5.3c,d,f). The fracture

surface of the GRAD specimens showed a high concentration of microcracks in front of the initial crack (Figure 5.3c). As the initial crack propagated in the specimen, these microcracks coalesced and formed curved cracks that deflected to the free surface of the specimens (Figure 5.3c). However, when the initial crack had almost moved to the middle of the specimen, the majority of the macrocracks were parallel to the fracture surface, exhibiting a flat surface with granular-like profile (Figure 5.3c).

The fracture surface of the BM-SL specimens showed very different characteristics than those of the GRAD specimens (Figure 5.3d). Several semielliptical and elliptical macrocracks were observed on the fracture surface of the BM-SL specimens (Figure 5.3d, SEM subfigures), which could be due to the crack bridging occurred as the specimens ruptured (Figure 5.3d). During testing, these specimens failed more swiftly than the others, which correlates with the fact that they were also the most brittle. In addition, the overall surface of these specimens was less flat than those of the GRAD group (Figure 5.3c,d). Introducing a gradient in the BM-SL specimens resulted in the formation of microcracks that were in parallel with the width of the specimens (Figure 5.3e). This formation continued as the initial crack propagated in the specimens until it reached the last third of the specimen after which the crack was deflected (Figure 5.3e). Overall, a considerably more granular profile was observed for the BM-GRAD-SL specimens (Figure 5.3e), but this profile was not more than the fully gradient designs. These observations suggest that the failure mechanisms of the BM-GRAD-SL group are a combination of both of those mechanisms that were previously discussed for the GRAD and BM-SL specimens.

The mortars in the second level of the BM-2L specimens acted as crack barriers preventing further microcrack propagation (Figure 5.3f, SEM subfigures). Unlike the BM-SL specimens, most of the microcracks that were formed on the fracture surface of the BM-2L specimens were parallel to the crack front (Figure 5.3f), and their orientation did not change as the crack propagated. Introducing gradients in these specimens (BM-GRAD-2L), smoothened and diluted the mortar lines observed in the BM-2L specimens (Figure 5.3g). Therefore, the size of the microcracks in the BM-GRAD-2L specimens was notably smaller than those of the BM-2L group. The microcracks in the BM-GRAD-2L group were mostly distributed in parallel with their widths (Figure 5.3g). All the failure mechanisms observed in previous designs were also present in the latter group. This synergy of mechanisms may be

responsible for the overall higher BM-GRAD-2L performance as compared with those of other design groups.

The mechanical properties of the monolithic and composite materials are compared in Table S5.3, Supporting Information. When compared with the structured patterns, GRAD specimens were found to have lower stiffness and maximal stress, but higher fracture strains (Figure 5.4a–c). However, having an ordered architecture (*i.e.,* brick-and-mortar) in the BM-SL and BM-2L groups could activate other toughening mechanisms in those structures, thereby resulting in higher stiffness and fracture stress values.

Comparing the properties of the groups BM-SL and BM-2L showed that the specimens with a single level of brick-and-mortar hierarchy had slightly higher stiffnesses and fracture stresses than those with two-level hierarchies (Figure 5.4c). However, the fracture energies of the BM-2L specimens were up to 1.5 and 1.3 times higher than those of the BM-SL and monolithically hard specimens, respectively (Figure 5.4a,b). This can be due to the activation of the crack-dissipation mechanisms caused by the presence of a thicker mortar line at the second hierarchical level in the BM-2L specimens. In addition, the structured organization of hard/soft materials at the second hierarchical level could be paralleled as an "impurity placement" in the composite, preventing crack propagation.

Implementing the gradient in the BM-GRAD-SL and BM-GRAD-2L specimens did not influence the stiffness values and fracture stresses as compared with those without gradients (Figure 5.4a–c). The fracture energies of the groups with both single-level and two-level hierarchies, however, increased after introducing the gradients (Figure 5.4a,b). This can be explained by the fact that the brick-and-mortars in the BM-GRAD-SL and BM-GRAD-2L groups did not have purely hard fibers (or soft matrices) in their microstructures. The random distribution of the particles inside the bricks and mortars can create more obstacles along the crack path, which can make it more difficult for the crack to propagate through the specimen. Therefore, more energy was required to break the specimen apart. Interestingly, comparing our results with those of purely hard specimens showed that the fracture energy of the BM-GRAD-2L specimens reached higher values (almost 2 times) than those of the monolithically hard ones (Figure 5.4a,b).

145
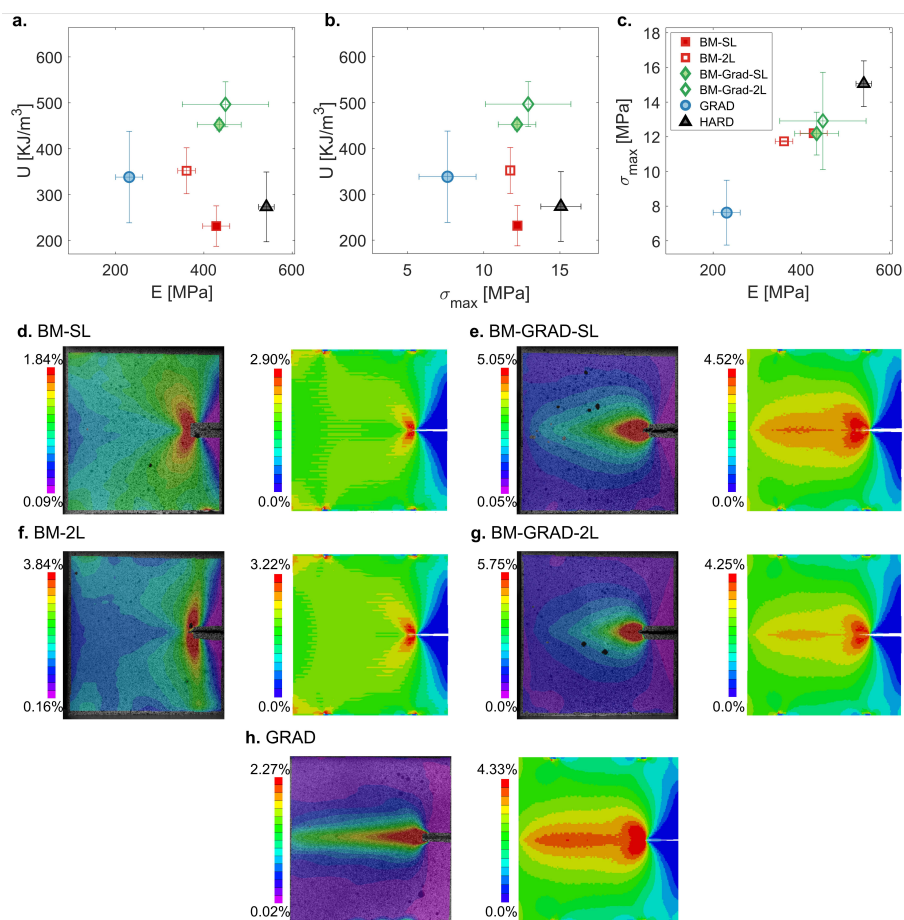
Figure 5.4 The Ashby plots of the experimental results showing the duos of the a) fracture energy versus stiffness, b) fracture energy versus fracture stress, and c) fracture stress versus elastic stiffness. A comparison of the patterns of the strain distribution obtained from our DIC experiments and computational models for the specimens from the groups d) BM-SL, e) BM-GRAD-SL, f) BM-2L, g) BM-GRAD-2L, and h) GRAD.

We also adjusted the mechanical properties of each specimen with respect to their target overall hard volume fraction, $\bar{\rho}_o$, and the target hard volume fraction in front of the crack tip, $\bar{\rho}_c$ (Figure S5.1, supporting information). As the difference between the actual and target hard volume fractions were relatively small (*i.e.,* ~3.5%, Table S5.2 of the supporting information), we assumed a linear correlation between the mechanical properties and the hard volume fractions. This adjustment did not change the order of the mechanical properties, and graded

structures with two-level hierarchies showed higher fracture energies among all cases (Figure S5.1).

We validated the accuracy of our computational models by performing a one-to-one comparison with the average experimental data for every design for different mechanical properties (Figure S5.2, supporting information). The group rankings between experiments and computational models were consistent for every property regardless of the type of mechanical properties. Our computational models could also predict the values of stiffness and fracture stress with high levels of accuracy. In our computational models, the fracture energies were calculated up to the point that they reached the maximum stress value. Slight deviations from the one-to-one correspondence line (Figure S5.2c, supporting information) for the fracture energies calculated using our computational models as compared with the experimental values was likely caused by the assumptions we made in our models. Those assumptions involved using 2D-plane strain elements and the coarse-graining of our elements. In addition, we assumed a strain separation value for the propagation of the cracks. Choosing an energy-based criterion for the element separation may, therefore, mitigate some of those deviations.

The strain patterns resulting from the DIC measurements and computational models were very similar (Figure 5.4d–h). In all groups with and without gradients, a high strain concentration was seen in front of the crack tip (Figure 5.4d–h). This strain localization in the BM-SL and BM-2L groups formed a butterfly-shaped region in the crack tip, characteristic of mode I crack propagation experiments (Figure 5.4d,f). The existence of the brick-and-mortar patterns in these specimens did not substantially affect the strain distribution.

The strain distributions for the specimens with a gradient (*i.e.,* the BM-GRAD-SL, BM-GRAD-2L and GRAD groups) showed a more substantial zone of strain localization as well as higher values of the von-Mises strain (Figure 5.4e,h). The strain distribution for the graded specimens was distributed across the entire crack path. The length of this strain distribution was larger for the graded specimens (*i.e.,* the GRAD group) (Figure 5.4h). The overall patterns of strain distribution obtained from our computational models were consistent with our experimental observations (Figure 5.4d–h). These strain distributions confirm that

introducing gradients can significantly change the strain distribution in front of the crack tip and directly affect the energy required for crack propagation.

The biomimetic design approaches proposed in this study can have several applications in the field of biomedical engineering such as in the fabrication of functionally graded dental [44,45] and orthopaedic implants [46] as well as engineering complex tissues [47] or interfaces. [48–50] The combination of hierarchical designs and functionally graded paradigms can also be used together with optimization approaches to find optimal designs required for better tissue (bone) remodeling. [32,51]

We have so far discussed various toughening mechanisms, including granular-like reinforcement (for the graded specimens), multiscale hierarchical arrangements, crack-bridging, and crack barriers. There are also other potential geometry-based toughening mechanisms that were not considered in the current study. For example, introducing certain arrangements of short fibers instead of granular-like reinforcements may add additional toughening mechanisms to the composites. Moreover, different orientations or organizations of bricks-and-mortars unit cells can also be explored in combination with the presented mechanisms. This includes geometries such as chiral, helix, or diamond-like unit cell arrangements. Optimizing the arrangements of such unit cells can result in highly improved properties of advanced architected materials. Finally, in addition to the role of geometry, printing at even finer resolutions (*e.g.,* nanoscale resolutions) using other AM techniques such as direct laser writing (DLW) [52,53] can potentially activate other fracture mechanisms similar to those seen in bone.

5.4. Conclusion

In summary, our results suggest that gradients, as a standalone tool, cannot affect the fracture properties of functionally graded hard−soft composites. However, functional gradients with hierarchical designs enable hard−soft brick-and-mortar composites to achieve higher fracture energies as compared with the composites that only benefit from hierarchical designs. These combinations can reach up to 2 times higher fracture energies than the hard phase itself. The results presented here can open up new frontiers in understanding how nature combines mechanistic tools to achieve extremely efficient structural materials and

assist in the development of designer materials [54–57] that have numerous potential applications in high-tech industries.

References

[1]   R.O. Ritchie, The conflicts between strength and toughness, Nat. Mater. 10 (2011) 817–822. https://doi.org/10.1038/nmat3115.

[2]   U.G.K. Wegst, H. Bai, E. Saiz, A.P. Tomsia, R.O. Ritchie, Bioinspired structural materials, Nat. Mater. 14 (2015) 23–36. https://doi.org/10.1038/nmat4089.

[3]   F. Libonati, M.J. Buehler, Advanced Structural Materials by Bioinspiration , Adv. Eng. Mater. 19 (2017) 1600787. https://doi.org/10.1002/adem.201600787.

[4]   A.R. Studart, Biological and Bioinspired Composites with Spatially Tunable Heterogeneous Architectures, Adv. Funct. Mater. 23 (2013) 4423–4436. https://doi.org/10.1002/adfm.201300340.

[5]   J.W.C. Dunlop, P. Fratzl, Biological Composites, Annu. Rev. Mater. Res. 40 (2010) 1–24. https://doi.org/10.1146/annurev-matsci-070909-104421.

[6]   H.D. Espinosa, J.E. Rim, F. Barthelat, M.J. Buehler, Merger of structure and material in nacre and bone - Perspectives on de novo biomimetic materials, Prog. Mater. Sci. 54 (2009) 1059–1100. https://doi.org/10.1016/j.pmatsci.2009.05.001.

[7]   S. Weiner, L. Addadi, Design strategies in mineralized biological materials, J. Mater. Chem. 7 (1997) 689–702. https://doi.org/10.1039/a604512j.

[8]   Z. Liu, M.A. Meyers, Z. Zhang, R.O. Ritchie, Functional gradients and heterogeneities in biological materials: Design principles, functions, and bioinspired applications, Elsevier Ltd, 2017. https://doi.org/10.1016/j.pmatsci.2017.04.013.

[9]   A.R. Studart, R. Libanori, R.M. Erb, Functional Gradients in Biological Composites, in: Bio-Bioinspired Nanomater., Wiley-VCH Verlag GmbH & Co. KGaA, Weinheim, Germany, 2014: pp. 335–368. https://doi.org/10.1002/9783527675821.ch13.

[10]   F. Barthelat, H. Tang, P.D. Zavattieri, C.M. Li, H.D. Espinosa, On the mechanics of mother-of-pearl: A key feature in the material hierarchical structure, J. Mech. Phys. Solids. 55 (2007) 306–337. https://doi.org/10.1016/j.jmps.2006.07.007.

[11]   P. Fratzl, M.M.G. Guille, Hierarchy in Natural Materials, Hierarchically Struct. Porous Mater. From Nanosci. to Catal. Sep. Opt. Energy, Life Sci. (2011) 29–39. https://doi.org/10.1002/9783527639588.CH2.

[12]   L.J. Gibson, The hierarchical structure and mechanics of plant materials, J. R. Soc. Interface. 9 (2012) 2749–2766. https://doi.org/10.1098/rsif.2012.0341.

[13]   N. Reznikov, R. Shahar, S. Weiner, Bone hierarchical structure in three dimensions, in: Acta Biomater., Elsevier Ltd, 2014: pp. 3815–3826. https://doi.org/10.1016/j.actbio.2014.05.024.

[14]   I. Fernández-Tresguerres Hernández-Gil, M. Angel Alobera Gracia, M. del Canto Pingarrón, L. Blanco Jerez, J. Carlos, P. Titular, Physiological bases of bone regeneration I. Histology and physiology of bone tissue, Med Oral Patol Oral Cir Bucal. (2006).

[15]   K. Inoue, H. Ohgushi, T. Yoshikawa, M. Okumura, T. Sempuku, S. Tamai, Y. Dohi, The Effect of Aging on Bone Formation in Porous Hydroxyapatite: Biochemical and Histological Analysis, J. Bone Miner. Res. 12 (1997) 989–994. https://doi.org/10.1359/jbmr.1997.12.6.989.

[16]   U.T. Iwaniec, T.J. Wronski, R.T. Turner, Histological analysis of bone, Methods Mol. Biol. 447 (2008) 325–341. https://doi.org/10.1007/978-1-59745-242-7_21.

[17]   R. Müller, H. Van Campenhout, B. Van Damme, G. Van Der Perre, J. Dequeker, T. Hildebrand, P. Rüegsegger, Morphometric analysis of human bone biopsies: A quantitative structural comparison of histological sections and micro-computed tomography, Bone. 23 (1998) 59–66. https://doi.org/10.1016/S8756-3282(98)00068-4.

[18]   T. Hoc, L. Henry, M. Verdier, D. Aubry, L. Sedel, A. Meunier, Effect of microstructure on the mechanical properties of Haversian cortical bone, Bone. 38 (2006) 466–474. https://doi.org/10.1016/j.bone.2005.09.017.

[19]   G. Lewis, J.S. Nyman, The use of nanoindentation for characterizing the properties of mineralized hard tissues: State-of-the art review, J. Biomed. Mater. Res. - Part B Appl. Biomater. 87 (2008) 286–301. https://doi.org/10.1002/jbm.b.31092.

[20]   M.J. Mirzaali, J.J. Schwiedrzik, S. Thaiwichai, J.P. Best, J. Michler, P.K. Zysset, U. Wolfram, Mechanical properties of cortical bone and their relationships with age, gender, composition and microindentation properties in the elderly, Bone. 93 (2016) 196–211. https://doi.org/10.1016/j.bone.2015.11.018.

[21]   M.J. Mirzaali, F. Libonati, D. Ferrario, L. Rinaudo, C. Messina, F.M. Ulivieri, B.M. Cesana, M. Strano, L. Vergani, Determinants of bone damage: An ex-vivo study on porcine vertebrae, PLoS One. 13 (2018) e0202210. https://doi.org/10.1371/journal.pone.0202210.

[22]   J.Y. Rho, L. Kuhn-Spearing, P. Zioupos, Mechanical properties and the hierarchical structure of bone, Med. Eng. Phys. 20 (1998) 92–102. https://doi.org/10.1016/S1350-4533(98)00007-1.

[23]   M.J. Buehler, S. Keten, T. Ackbarow, Theoretical and computational hierarchical nanomechanics of protein materials: Deformation and fracture, Prog. Mater. Sci. 53 (2008) 1101–1241. https://doi.org/10.1016/j.pmatsci.2008.06.002.

[24]   M.J. Mirzaali, V. Mussi, P. Vena, F. Libonati, L. Vergani, M. Strano, Mimicking the loading adaptation of bone microstructure with aluminum foams, Mater. Des. 126 (2017) 207–218. https://doi.org/10.1016/j.matdes.2017.04.039.

[25]   G.A. Holzapfel, R.W. Ogden, Mechanics of Biological Tissue, Springer Berlin Heidelberg, 2006. https://doi.org/10.1007/3-540-31184-X.

[26]   M. Tawhai, J. Bischoff, D. Einstein, A. Erdemir, T. Guess, J. Reinbolt, Multiscale modeling in computational biomechanics, IEEE Eng. Med. Biol. Mag. 28 (2009) 41–49. https://doi.org/10.1109/MEMB.2009.932489.

[27]   J. Aerssens, S. Boonen, G. Lowet, J. Dequeker, Interspecies Differences in Bone Composition, Density, and Quality: Potential Implications for in Vivo Bone Research, Endocrinology. 139 (1998) 663–670. https://doi.org/10.1210/ENDO.139.2.5751.

[28]   M. Fini, R. Giardino, In Vitro and in VIVO Tests for the Biological Evaluation of Candidate Orthopedic Materials: Benefits and Limits, Https://Doi.Org/10.1177/228080000300100301. (2003). https://doi.org/10.1177/228080000300100301.

[29]   X. Wang, A.S. Shanbhag, H.E. Rubash, C.M. Agrawal, Short-term effects of bisphosphonates on the biomechanical properties of canine bone, (1999). https://doi.org/10.1002/(SICI)1097-4636(19990315)44:4.

[30]   S.Z.M. Brianza, P. D'Amelio, N. Pugno, E. Zini, A. Zatelli, F. Pluviano, K. Cabiale, M. Galloni, G.C. Isaia, Microdamage accumulation changes according to animal mass: An intraspecies

investigation, Calcif. Tissue Int. 88 (2011) 409–415. https://doi.org/10.1007/S00223-011-9470-8/FIGURES/1.

[31] H.W. Courtland, P. Nasser, A.B. Goldstone, L. Spevak, A.L. Boskey, K.J. Jepsen, Fourier transform infrared imaging microspectroscopy and tissue-level mechanical testing reveal intraspecies variation in mouse bone mineral and matrix composition, Calcif. Tissue Int. 83 (2008) 342–353. https://doi.org/10.1007/S00223-008-9176-8/FIGURES/8.

[32] D. Lin, Q. Li, W. Li, S. Zhou, M. V. Swain, Design optimization of functionally graded dental implant for bone remodeling, Compos. Part B Eng. 40 (2009) 668–675. https://doi.org/10.1016/j.compositesb.2009.04.015.

[33] T. Sugiyama, L.B. Meakin, W.J. Browne, G.L. Galea, J.S. Price, L.E. Lanyon, Bones' adaptive response to mechanical loading is essentially linear between the low strains associated with disuse and the high strains associated with the lamellar/woven bone transition, J. Bone Miner. Res. 27 (2012) 1784–1793. https://doi.org/10.1002/JBMR.1599.

[34] Y.N. Yeni, C.U. Brown, Z. Wang, T.L. Norman, The influence of bone morphology on fracture toughness of the human femur and tibia, Bone. 21 (1997) 453–459. https://doi.org/10.1016/S8756-3282(97)00173-7.

[35] A.S. Edelstein, J.S. Murday, B.B. Rath, Challenges in nanomaterials design, Prog. Mater. Sci. 42 (1997) 5–21. https://doi.org/10.1016/S0079-6425(97)00005-4.

[36] J.K. Nørskov, T. Bligaard, J. Rossmeisl, C.H. Christensen, Towards the computational design of solid catalysts, Nat. Chem. 2009 11. 1 (2009) 37–46. https://doi.org/10.1038/nchem.121.

[37] M.D. Porter, Combinatorial Materials Science, John Wiley & Sons, Hoboken, NJ, USA, 2007. https://books.google.nl/books?hl=en&lr=&id=tRdvxlL7mL0C&oi=fnd&pg=PR5&ots=kFqxUmCPUn &sig=aNxkwK3oyK394LPOySUogE1CFRU&redir_esc=y#v=onepage&q&f=false (accessed January 23, 2023).

[38] E.L. Doubrovski, E.Y. Tsai, D. Dikovsky, J.M.P. Geraedts, H. Herr, N. Oxman, Voxel-based fabrication through material property mapping: A design method for bitmap printing, CAD Comput. Aided Des. 60 (2015) 3–13. https://doi.org/10.1016/j.cad.2014.05.010.

[39] M.J. Mirzaali, M.E. Edens, A.H. de la Nava, S. Janbaz, P. Vena, E.L. Doubrovski, A.A. Zadpoor, Length-scale dependency of biomimetic hard-soft composites, Sci. Rep. 8 (2018) 12052. https://doi.org/10.1038/s41598-018-30012-9.

[40] Mirzaali, Nava, Gunashekar, Nouri-Goushki, Doubrovski, Zadpoor, Fracture Behavior of Bio-Inspired Functionally Graded Soft–Hard Composites Made by Multi-Material 3D Printing: The Case of Colinear Cracks, Materials (Basel). 12 (2019) 2735. https://doi.org/10.3390/ma12172735.

[41] A. Cheddad, J. Condell, K. Curran, P. Mc Kevitt, Digital image steganography: Survey and analysis of current methods, Signal Processing. 90 (2010) 727–752. https://doi.org/10.1016/J.SIGPRO.2009.08.010.

[42] R. Long, C.Y. Hui, Fracture toughness of hydrogels: measurement and interpretation, Soft Matter. 12 (2016) 8069–8086. https://doi.org/10.1039/C6SM01694D.

[43] M.G.J. Jonathan A. Salem, George D. Quinn, Fracture Resistance Testing of Monolithic and Composite Brittle Materials, Vol. 1409, ASTM International, West Conshohocken, PA, USA, 2002. https://books.google.nl/books?hl=en&lr=&id=UflLL0t5b0sC&oi=fnd&pg=PP7&ots=LrM-

MU_EQV&sig=hrKxMx-u8aX9LLWaO-hU1zhZ-Xw&redir_esc=y#v=onepage&q&f=false (accessed January 23, 2023).

[44]   F. Watari, A. Yokoyama, M. Omori, T. Hirai, H. Kondo, M. Uo, T. Kawasaki, Biocompatibility of materials and development to functionally graded implant for bio-medical application, Compos. Sci. Technol. 64 (2004) 893–908. https://doi.org/10.1016/j.compscitech.2003.09.005.

[45]   W. Pompe, H. Worch, M. Epple, W. Friess, M. Gelinsky, P. Greil, U. Hempel, D. Scharnweber, K. Schulte, Functionally graded materials for biomedical applications, Mater. Sci. Eng. A. 362 (2003) 40–60. https://doi.org/10.1016/S0921-5093(03)00580-X.

[46]   M. Thieme, K.P. Wieters, F. Bergner, D. Scharnweber, H. Worch, J. Ndop, T.J. Kim, W. Grill, Titanium powder sintering for preparation of a porous functionally graded material destined for orthopaedic implants, J. Mater. Sci. Mater. Med. 12 (2001) 225–231. https://doi.org/10.1023/A:1008958914818/METRICS.

[47]   A.G. Mikos, S.W. Herring, P. Ochareon, J. Elisseeff, H.H. Lu, R. Kandel, F.J. Schoen, M. Toner, D. Mooney, A. Atala, M.E. Van Dyke, D. Kaplan, G. Vunjak-Novakovic, Engineering Complex Tissues, Https://Home.Liebertpub.Com/Ten. 12 (2006) 3307–3339. https://doi.org/10.1089/TEN.2006.12.3307.

[48]   N. Lee, J. Robinson, H. Lu, Biomimetic strategies for engineering composite tissues, Curr. Opin. Biotechnol. 40 (2016) 64–74. https://doi.org/10.1016/J.COPBIO.2016.03.006.

[49]   P.J. Yang, J.S. Temenoff, Engineering orthopedic tissue interfaces, Tissue Eng. - Part B Rev. 15 (2009) 127–141. https://doi.org/10.1089/TEN.TEB.2008.0371/ASSET/IMAGES/LARGE/FIG-1.JPEG.

[50]   A. Seidi, M. Ramalingam, I. Elloumi-Hannachi, S. Ostrovidov, A. Khademhosseini, Gradient biomaterials for soft-to-hard interface tissue engineering, Acta Biomater. 7 (2011) 1441–1451. https://doi.org/10.1016/j.actbio.2011.01.011.

[51]   S. Arabnejad Khanoki, D. Pasini, Multiscale design and multiobjective optimization of orthopedic hip implants with functionally graded cellular material, J. Biomech. Eng. 134 (2012). https://doi.org/10.1115/1.4006115.

[52]   M. Röhrig, M. Thiel, M. Worgull, H. Hölscher, 3D Direct Laser Writing of Nano- and Microstructured Hierarchical Gecko-Mimicking Surfaces, Small. 8 (2012) 3009–3015. https://doi.org/10.1002/SMLL.201200308.

[53]   I.A. Paun, R.C. Popescu, C.C. Mustaciosu, M. Zamfirescu, B.S. Calin, M. Mihailescu, M. Dinescu, A. Popescu, D. Chioibasu, M. Soproniy, C.R. Luculescu, Laser-direct writing by two-photon polymerization of 3D honeycomb-like structures for bone regeneration, Biofabrication. 10 (2018) 025009. https://doi.org/10.1088/1758-5090/AAA718.

[54]   R. Hedayati, M.J. Mirzaali, L. Vergani, A.A. Zadpoor, Action-at-a-distance metamaterials: Distributed local actuation through far-field global forces, APL Mater. 6 (2018) 036101. https://doi.org/10.1063/1.5019782.

[55]   M.J. Mirzaali, A. Caracciolo, H. Pahlavani, S. Janbaz, L. Vergani, A.A. Zadpoor, Multi-material 3D printed mechanical metamaterials: Rational design of elastic properties through spatial distribution of hard and soft phases, Appl. Phys. Lett. 113 (2018) 241903. https://doi.org/10.1063/1.5064864.

[56]   M.J. Mirzaali, S. Janbaz, M. Strano, L. Vergani, A.A. Zadpoor, Shape-matching soft mechanical metamaterials, Sci. Rep. 8 (2018) 965. https://doi.org/10.1038/s41598-018-19381-3.

[57]   P.M. Reis, H.M. Jaeger, M. van Hecke, Designer Matter: A perspective, Extrem. Mech. Lett. 5 (2015) 25–29. https://doi.org/10.1016/j.eml.2015.09.004.

5.5 Supporting information

List of supporting tables

Table S5.1. The polynomial expressions that were fitted to the mechanical properties during our experiments and the overall hard volume fractions.

Mechanical properties	Coefficients			
	a_3	a_2	a_1	a_0
$E(\rho) = a_2\rho'^2 + a_1\rho' + a_0$	0	-75.81	551.41	-0.09
$\epsilon_{sep}(\rho) = a_3\rho'^3 + a_2\rho'^2 + a_1\rho' + a_0$	-0.58	1.45	-1.21	0.38

Table S5.2. The difference between the target and actual values of the hard volume fractions in front of the crack tips, $\bar{\rho}_c = 38\%$, and the entire specimens, $\bar{\rho}_o = 71\%$.

Specimen designs	$\rho_{c,i} - \bar{\rho}_c\,[\%]$	$\rho_{o,i} - \bar{\rho}_o\ [\%]$
GRAD	3.64	-0.60
SL-BM	-0.32	2.25
SL-GRAD-BM	3.78	5.08
2L-BM	-4.43	-5.98
2L-GRAD-BM	3.78	5.08

Table S5.3. The mean ± standard deviation of the mechanical properties of the experimental groups used in this study as well as those of monolithically hard and soft materials.

Specimen designs	E [MPa]	σ_{max} [MPa]	U [KJ/m3]
GRAD	230.73 ± 30.60	7.63 ± 1.87	338.28 ± 99.64
SL-BM	427.96 ± 30.65	12.21 ± 0.13	231.56 ± 43.99
SL-GRAD-BM	432.72 ± 49.73	12.18 ± 1.24	452.33 ± 11.81
2L-BM	360.75 ± 19.94	11.74 ± 0.04	352.62 ± 50.04
2L-GRAD-BM	448.87 ± 97.82	12.91 ± 2.80	496.73 ± 49.02
Hard	541.57 ± 17.61	15.06 ± 1.32	273.36 ± 73.96
Soft	0.65 ± 0.08	0.20 ± 0.01	51.40 ± 8.66

List of supporting figures
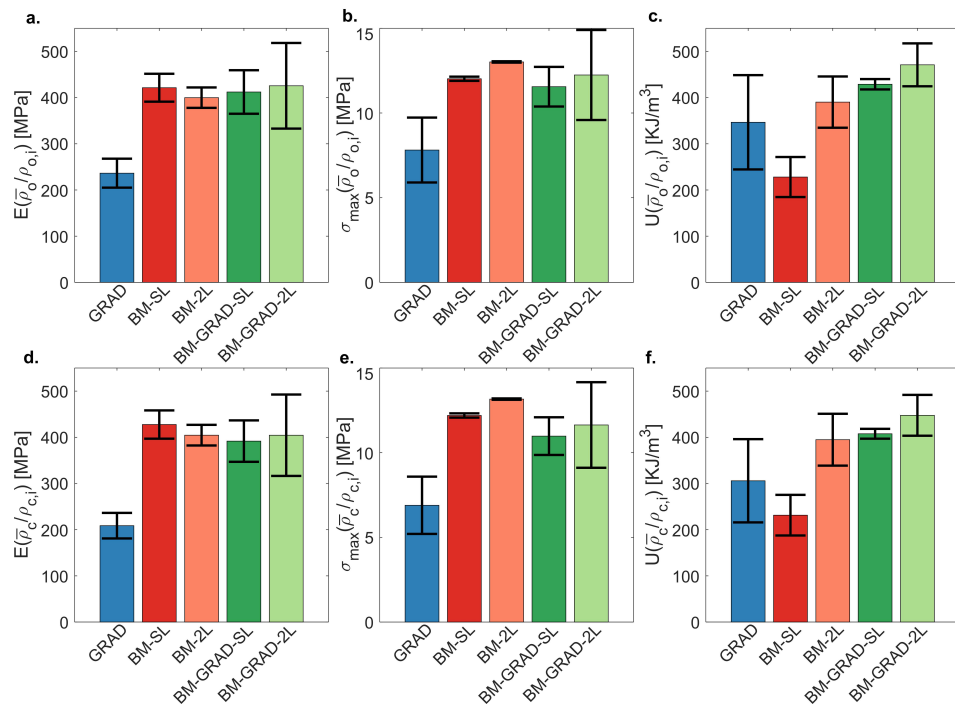
Figure S5.1. The mechanical properties (*i.e.,* stiffness (a), maximum fracture stress (b), and fracture energy (c)) adjusted with respect to the target hard volume fraction of all the designs, $\bar{\rho}_o$, and the overall hard volume fraction of individual specimens, $\rho_{o,i}$. The mechanical properties (*i.e.,* stiffness (d), maximum fracture stress (e), and fracture energy (f)) were also adjusted with respect to the target hard volume fraction in front of the crack tip, $\bar{\rho}_c$, and the individual hard volume fraction in front of the crack tip $\rho_{c,i}$, for each design.
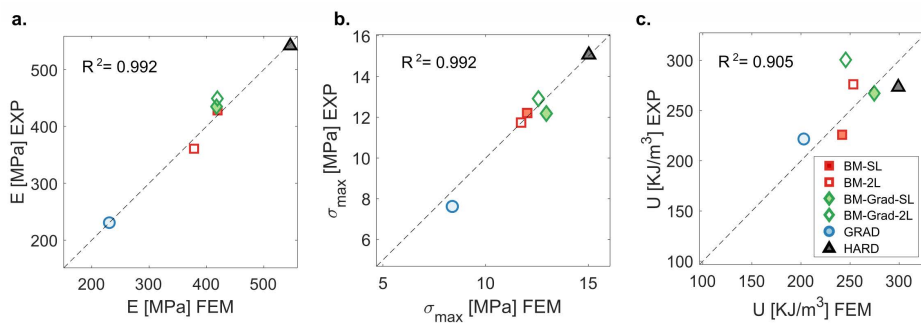
Figure S5.2. Correspondence (one-to-one) between the experimental and computational results for the stiffness (a), fracture stress (b), and fracture energy (c).

6

Mimicking living bones to optimize hierarchical, multi-material 3D printed auxetic metamaterials

6. Mimicking living bones to optimize hierarchical, multi-material 3D printed auxetic metamaterials

Abstract

Recent developments in the design and (additive) manufacturing of cellular materials have ushered in a new age of architected metamaterials. Despite the unmatched and exotic mechanical properties that these metamaterials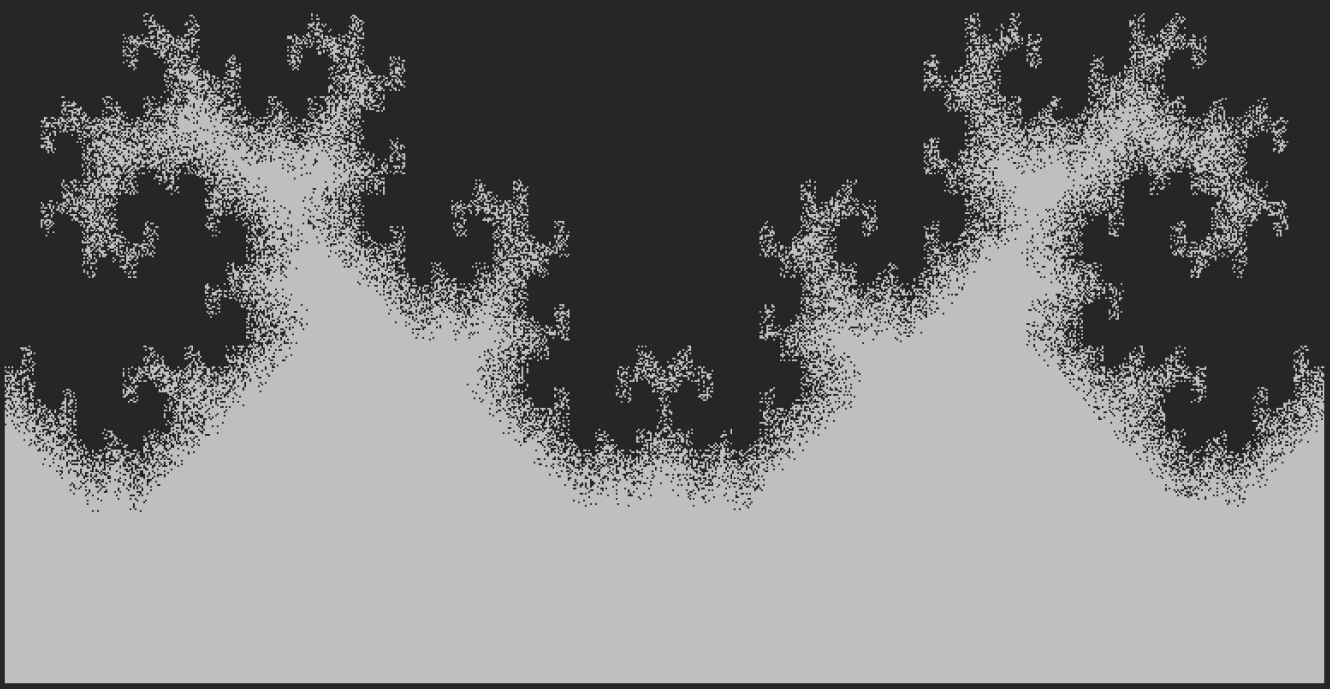 exhibit, their internal structures are rife with sub-optimal performance. For example, the onset of stress concentration regions in classic unit cell designs results in early structural failure. Furthermore, the elastic properties of transversely isotropic monophasic metamaterials (i.e., duos of elastic modulus and Poisson's ratio) are dependent on their unit cell geometry, limiting their achievable design space. Living cellular materials, such as bone tissue, have been facing similar challenges regarding their mechanical performance. Equipped with millions of years of evolution, such living materials have found ingenious ways to optimize their mechanical performance. Here, we mimic living bones to optimize the mechanical performance of auxetic metamaterials. Our mimicry involves the introduction of a hierarchical design approach with multiple length scales and the rational positioning of a soft and a hard phase at the individual voxel level using a multi-material voxel-based 3D printer. More importantly, we use a bone tissue adaptation algorithm that maintains a homeostatic strain energy density condition to distribute the soft and hard voxels in the body of each re-entrant unit cell, thereby introducing an additional length scale of features. Applying this process to unit cells with different ratios of the hard to the soft material resulted in 1. a significant expansion of the envelope of the achievable elastic properties, 2. more homogeneous distributions of the strain energy density within the architecture of the metamaterials, and 3. up to 78% stronger metamaterials as compared to the initial designs. We demonstrate that the applied bone-mimicking design approach leads to the emergence of an intermediate length scale between both original length scales (i.e., unit cell and voxel scales), which is responsible for the abovementioned improvements in the mechanical performance of auxetic metamaterials. Taken together, our results show the utility of mimicking living bone for the rational design of stress-worthy multiscale mechanical metamaterials that combine unusual elastic properties with high mechanical performance.

6.1. Introduction

In recent years, there has been a paradigm shift in the materials design community towards creating structures with unusual properties (*e.g.,* negative Poisson's ratio, ultra-stiffness or flexibility, and shape morphing) [1–4]. These properties, such as elastic stiffness and Poisson's ratio, can even go beyond their mutually exclusive theoretical limits [5–9]. Although various methods have been proposed to decouple these properties (*e.g.,* introducing degrees of non-affinity and multi-material metamaterials) [10,11], such metamaterial design techniques have several limitations. For example, the junctions of the structural elements constituting the microarchitectures of many such designs effectively function as hinges, thereby causing non-homogenous strain distributions and considerable degrees of stress concentration [12–14]. These strain concentrations promote early crack initiation and growth, leading to diminished mechanical performance and premature failure. Addressing such design issues while also maintaining and preferably expanding the envelope of possible elastic properties is an open challenge.

Living organisms have been facing similar challenges in their load-bearing tissues where combining lightweight, high mechanical performance, and exotic properties (*e.g.,* negative or zero values of the Poisson's ratio [15,16]) has been instrumental in maximizing their 'fitness' for survival. Through millions of years of evolution, living organisms have developed ingenious strategies to satisfy these seemingly incompatible design requirements. Two of these strategies include the hierarchical arrangement of microarchitectural features and combining soft (*e.g.,* collagen) and hard (*e.g.,* hydroxyapatite) phases [17–20]. This seamless integration of hierarchy and multiple phases within the fabric of load-bearing tissues is rooted in the evolutionary processes that can circumvent the infamous material property trade-off (*e.g.,* the incompatibility between high strength and high toughness in engineering materials) [21,22]. An important example of such living materials is bone, which through a remodeling process optimizes its mechanical response to the mechanical loads it experiences [23,24].

Here, we mimic living bone to address the open challenge regarding the design of stress-worthy mechanical metamaterials with unusual elastic properties. While bone tissue adaptation has been linked to the optimal mechanical performance in trabecular bone [25,26], direct applications of this approach to the design of mechanical metamaterials are

yet to be reported [27]. Our biomimetic design approach involves the introduction of a microarchitecture hierarchy with multiple length scales and the rational positioning of a soft and a hard phase at the individual voxel level using a multi-material voxel-based additive manufacturing technique [28–31]. We used a modified theoretical model of the bone tissue process working on the basis of homeostatic strain energy density to optimize the distribution of the hard and soft voxels within the fabric of each re-entrant or honeycomb unit cell of an auxetic and a conventional metamaterial, thereby introducing two hierarchical length scales (*i.e.*, unit cell and voxel). We then evaluated the elastic properties and stress-worthiness of the developed auxetic metamaterials using both computational models and experiments. The elastic properties and mechanical performance of the designed mechanical metamaterials were then benchmarked against control groups consisting of single-scale, monolithic specimens.

6.2. Materials and methods

6.2.1. Initial unit cell design

We designed two generic unit cells for our analysis, a re-entrant (auxetic) and regular (non-auxetic) honeycomb with entrant angles, θ, of -20º and 20º, respectively (Figure 6.1A). We utilized an in-house MATLAB script (R2018b, MathWorks, USA) to generate one-quarter representations of these designs in a voxel form with dimensions of 80, 40, and 4 voxels in height (H_{uc}), width (W_{uc}), and out-of-plane thickness (L_{uc}), respectively. The thickness of each strut consisted of 12 voxels, equivalent to 30% of W_{uc}. The dimension of each voxel was 42×84×27 µm^3. For both angles, we used a 3D Stucki dithering technique [32] to obtain several unit cells with varying ratios of the volume of the hard phase to that of the total volume (ρ = 17, 33, 50, 67, or 83%) (Figure S6.1 of the supporting information). We completed the unit cells by mirroring the quarter designs.

6.2.2. Numerical simulations

An in-house Python (v2.7.3) script allowed for the integration of the designs into a commercial nonlinear FEM package (Abaqus Standard v.6.14, Dassault Systèmes Simulia, France) to generate quasi-static finite element method (FEM) models (Figure 6.1B). This script converted the voxel designs into hexahedral element (C3D8) meshes and assigned the material properties of each voxel. After performing a mesh convergence study (Section S6.1

of the supporting information), we selected a 1:1 ratio of elements to voxel for simulating the bone tissue adaptation process. To validate the experimental results, we performed additional simulations with a 64:1 ratio (*i.e.*, 64 elements per voxel). We modeled the hard phase using a linear elastic constitutive equation (elastic modulus E = 2651 MPa, Poisson's ratio v = 0.4) while a hyperelastic constitutive model was used for the soft one (Odgen, N = 1, shear modulus μ_1 = 0.266 MPa, constants α_1 = 3.006 and D_1 = 0.113) [33]. After assigning periodic boundary conditions to the unit cells, we simulated two displacement-controlled uniaxial tensile tests per design (*i.e.,* along directions 1 and 2), each with an equivalent strain of ϵ = 0.25%. From these simulations, we extracted the reaction forces (f_1 and f_2) and displacements (u_{11}, u_{12}, u_{22}, and u_{21}) of each unit cell based on which we calculated the respective elastic properties (*i.e.,* $E_{11} = (f_1/(L_{uc}u_{11})$, $E_{22} = f_2/(L_{uc}u_{22})$, $v_{12} = -u_{12}/u_{11}$, and $v_{21} = -u_{12}/u_{22}$). Finally, we extracted the vectors containing the strain energy density (SED) of each voxel of the entire lattice (*i.e.,* $\mathbf{U_1}$ and $\mathbf{U_2}$).

6.2.3. Bone-mimicking computational model for rational distribution of soft and hard voxels

We defined our bone-mimicking optimization routine as an iterative procedure where the voxels within the unit cells were continuously committed or converted to a specific material based on their relative strain energy density (**SED**) (Figure 6.1C). For every iteration, after running the simulations with loading in both directions, the algorithm extracted the SED of each voxel (**SED$_1$ and SED$_2$ for directions 1 and 2, respectively**). Then, to remove the anisotropic effects of the unit cell, it performed min-max feature scaling on these vectors ($\mathbf{U} = (\mathbf{SED} - \min(\mathbf{SED}))/(\max(\mathbf{SED}) - \min(\mathbf{SED}))$ for directions 1 and 2), from which it calculated the effective SED vector **S** as:

$$\mathbf{S} = \lambda\mathbf{U_1} + (1 - \lambda)\mathbf{U_2} \tag{1}$$

where λ is a weighting parameter. Four operations were then concurrently performed using this ranked vector. First, the soft voxels with the highest effective SED (*i.e.,* 0.5% of all the voxels within the unit cell) were converted into hard voxels. Conversely, the same number of hard voxels with the lowest effective SED values were converted to soft voxels to maintain a consistent ρ during the whole process. After converting to any material, the voxels were committed to remain as such to prevent them from continuously oscillating between hard

and soft voxels. For the third operation, the soft elements with the lowest effective SED (*i.e.,* 0.5% of all the voxels) were assumed to show a sufficient capacity for energy absorption and were committed to the soft phase for the future iterations. In the last operation, the same number of hard voxels with the highest effective SED values were committed to the hard phase. This process is repeated in each iteration until all the voxels have committed to either the hard or the soft phase. Since the values within the ranked vector **S** drive the remodeling of the unit cell, the parameter λ determines the anisotropic bias of the remodeling process, where $\lambda = 0$ and $\lambda = 1$ fully bias the remodeling process towards direction 1 or direction 2, respectively, while $\lambda = 0.5$ does not prioritize either one of the directions. We performed a detailed analysis of the SED redistribution achieved by the algorithm for a single representative design (*i.e., θ* = -20º, *ρ* = 50%). Towards this end, we calculated the normalized **SED** vectors of the unit cells (*i.e.,* the SED value of each voxel divided by the total SED within the unit cell) throughout the remodeling process for all the evaluated λ values.

6.2.4. Voxel-by-voxel multi-material 3D printing

A PolyJet multi-material 3D printer (ObjetJ735 Connex3, Stratasys® Ltd., USA) with voxel-level control enabled (voxel resolution of 300×600 dpi with layers of 27 mm) was used to manufacture the validation specimens. For the hard and soft phases, we used the VeroCyan™ (RGD841, Stratasys® Ltd., USA) and Agilus30™ Clear (FLX935, Stratasys® Ltd., USA) UV-curable photopolymers, respectively. We defined two lattice configurations for testing along either direction 1 or 2 (Figure 6.1D) and based their dimensions on the existing literature [29]. After a comparative study of multiple lattice sizes (Section S6.2 of the supporting information), we determined that 4×4 unit cells per specimen with a voxel size of 127×254×84 µm³ minimized unwanted PolyJet material mixing while still reflecting the periodicity of the designed lattices. We selected eight different designs for manufacturing (Table 6.1), from which we generated the required stacks of binary images as input for the 3D printer. In those binary images, each bit specified whether or not each phase is deposited at the position of the corresponding voxel. Three specimens were printed from each design.
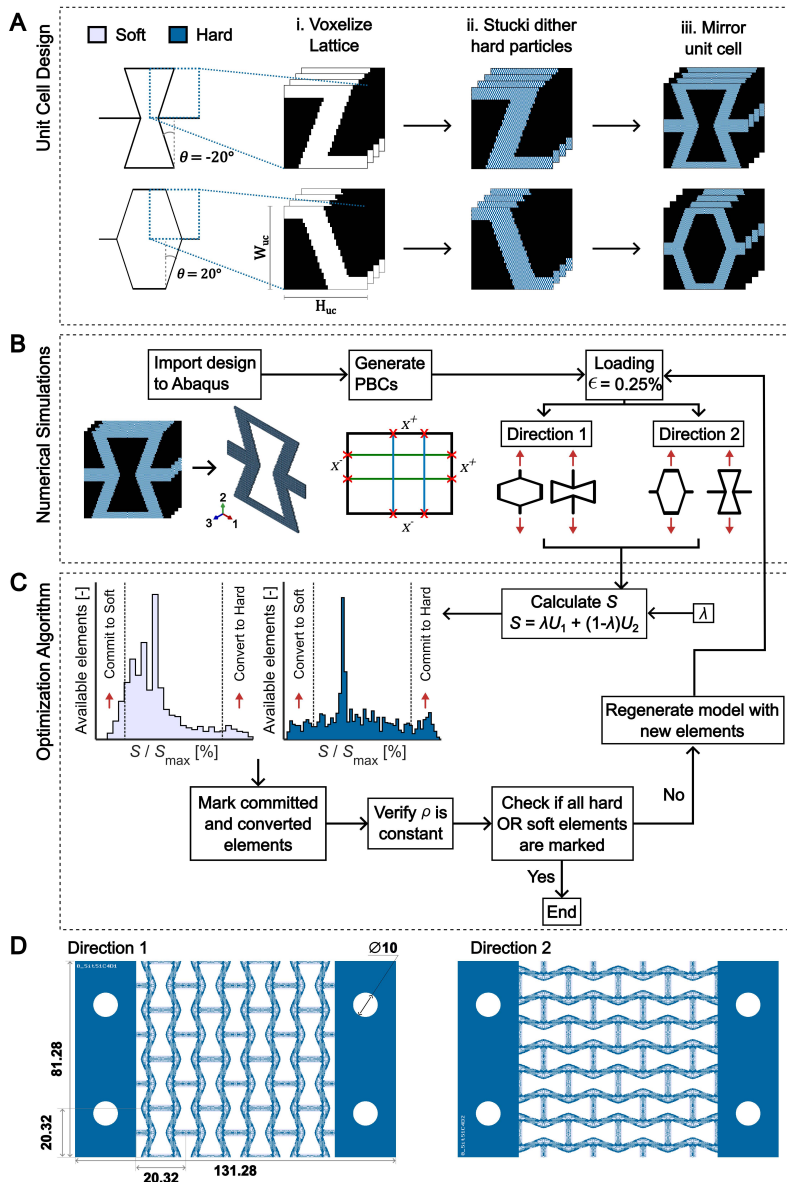
Figure 6.1. Schematic drawings illustrating the entire design and optimization process. A) The process used for the generation of the initial unit cell designs where a quarter of the unit cell geometries are converted into 4 stacks of 40×80 voxels (i.) and hard and soft voxels are distributed within the struts (ii.) prior to mirroring them into a complete unit cell (iii.). B) The generated designs are then imported into a FEM software suite where periodic boundary conditions (PBCs) are assigned, and two quasi-static tensile tests are simulated along both orthogonal directions. C) The SED of each voxel is then used to commit or convert the voxels to a material type (*i.e.,* hard or soft) while maintaining a constant number of hard voxels. The process of simulation and remodeling continues until all the voxels have been committed to a specific material type. D) The representative design of the additively manufactured 4×4 unit cell lattices for experimental validation (off-plane thickness = 3 mm).

6. Mimicking living bones to optimize hierarchical, multi-material 3D printed auxetic metamaterials

Table 6.1. The designs selected for fabrication and mechanical testing. *These designs were used for control and were made of only the hard material.

Name	$\theta[°]$	ρ [%]	λ	Iteration	Direction
$Hard_1$*	-20	100	-	-	1
$Hard_2$*	-20	100	-	-	2
$E_{1,initial}$	-20	50	-	0	1
$E_{2,initial}$	-20	50	-	0	2
$E_{1,max}, \lambda_{0.75}$	-20	50	0.75	22	1
$E_{1,max}, \lambda_{0.50}$	-20	50	0.50	50	1
$E_{2,max}, \lambda_{0.50}$	-20	50	0.50	50	2
$E_{2,max}, \lambda_{0.25}$	-20	50	0.25	50	2

6.2.5. Mechanical testing and full-field strain measurements

We performed quasi-static tensile tests on the 3D printed specimens to validate our computational analyses and evaluate the performance of the optimized designs. We used a mechanical test bench (Instron ElcetroPuls E10000, load cell = 10 kN) to apply a deformation of 2 mm/min until failure. We registered the time (t) and force (f) signals at a frequency of 100 Hz. Prior to testing, the specimens were coated with a white paint followed by a black speckle pattern. We then measured the local deformations using a digital image correlation (DIC) system (Q-400 2x 12MPixel LIMESS GmbH, Krefeld, Germany) with a frequency of 1 Hz. The associated DIC software (Instra 4D v4.6, Dantec Dynamics A/S, Skovunde, Denmark) was then employed to construct the full-field maps of the principal strains in the centermost unit cell of each specimen. We also utilized digital extensometers to measure the longitudinal (ϵ_L) and transverse (ϵ_T) strains of these unit cells throughout the tests. Subsequently, we used a MATLAB script to calculate the true stresses ($\sigma = f/A_o \exp(\epsilon_L)$, $A_o = 325.12$ mm²), Poisson's ratios ($\upsilon = -\epsilon_T/\epsilon_L$, measured at 0.25% longitudinal strain), elastic moduli (E, the slope of a line fitted between 0.1% and 0.25% strain of the $\sigma - \epsilon_L$ curve), and the ultimate tensile strength (σ_{UTS}, the maximum recorded stress) of all the specimens. Finally, we obtained the coefficients of determination (R^2) between the experimental and computational results to quantify the correlation between both types of results.
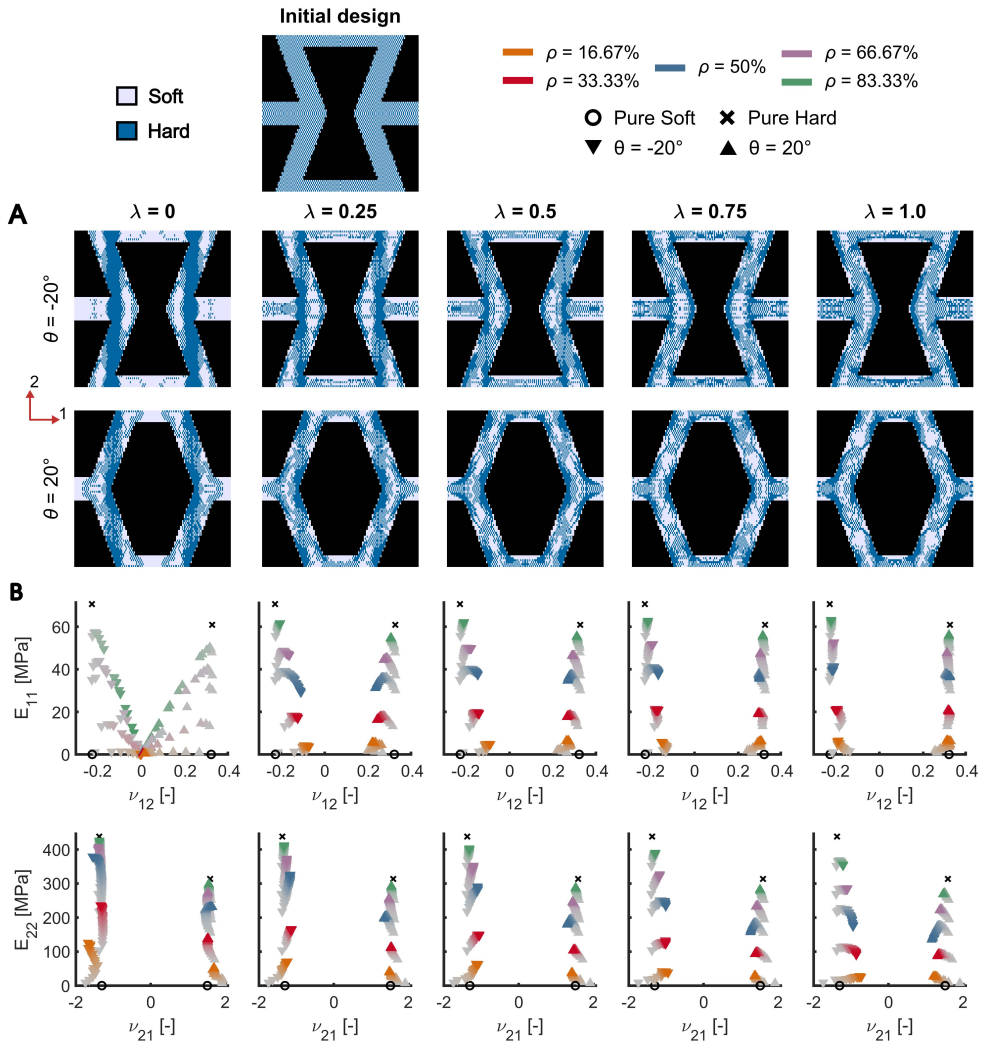
Figure 6.2. A) The hierarchical features with an intermediate length scale, which emerged from the application of the remodeling algorithm for the specimens with 50% hard voxels. B) These features resulted in the expansion of the envelope of the achievable elastic properties. The parameter λ determines the bias of the remodeling algorithm towards loading along direction 1 (*i.e.*, $\lambda = 1$) or direction 2 (*i.e.*, $\lambda = 0$). The grey-to-colored scale represents the initial to final remodeling iterations, respectively.

6.3. Results and discussion

6.3.1 Performance of the remodeling process

Subjecting the initial unit cell designs to the adaptations of the remodeling process led to the emergence of a myriad of unit cells and provided a more extensive design space than the initial quasi-random designs (Figure 6.2 and Figure S6.3 of the supporting information). For every ρ, λ, and θ combination, each remodeling iteration resulted in a unique arrangement of hard and soft voxels. These unique arrangements gave rise to emergent geometrical features with an intermediate length scale between those of the unit cells and voxels. The type of the emergent feature reflected the bias towards either one of the loading directions as specified by λ (Figure 6.2A). For example, selecting $\lambda = 0$ led to hard material distributions in the shape of parallel fibers along direction 2 for both auxetic and non-auxetic structures. The emergence of such features is expected because **S** solely depends on the loading along direction 2, leading to a highly anisotropic unit cell (Figure 6.2B). Conversely, $\lambda = 1$ resulted in concentrations of the hard material around the lattice corners with acute angles and along the edges of their opposing ends. These types of emergent 'lattice-within-lattice' arrangements were responsible for increasing the flexural rigidity of the struts, thereby enhancing the structural stiffness along direction 1. A combination of these two remarkable design features emerged for intermediate λ values. Moreover, the emergence of these design features took place regardless of ρ (Figure S6.3A of the supporting information), indicating the consistency of the obtained computational results and supporting the conclusion that such design features can be used for the adjustment of the anisotropic properties of (hierarchical) lattice structures.

The wide range of the emergent features also meant that the envelope of the achievable elastic properties was considerably expanded (Figure 6.2B, Figure S6.3B of the supporting information). More specifically, the properties varied anisotropically and corresponded to λ. After remodeling, the models processed with a λ value of 1 increased E_{11} *(e.g.,* by 12.4% and 22% for $\rho = 50\%$, $\theta = -20°$ and 20°, respectively) while reducing E_{22}. For $\lambda = 0$, E_{22} increased regardless of the ρ value (*e.g.,* by 73.9% and 48.6% for $\rho = 50\%$, $\theta = -20°$ and 20°, respectively), while E_{11} dropped to near-zero values. Moreover, for these extreme scenarios, the process minimally affected the Poisson's ratio along the preferred remodeling direction (*i.e.,* ν_{12} and

v_{21} for $\lambda = 1$ and $\lambda = 0$, respectively) while these converged to zero in the orthogonal direction. A mixture of these property enhancements or reductions existed for the intermediate values of λ. As expected, the most isotropic changes of elastic behavior were achieved when $\lambda = 0.5$.
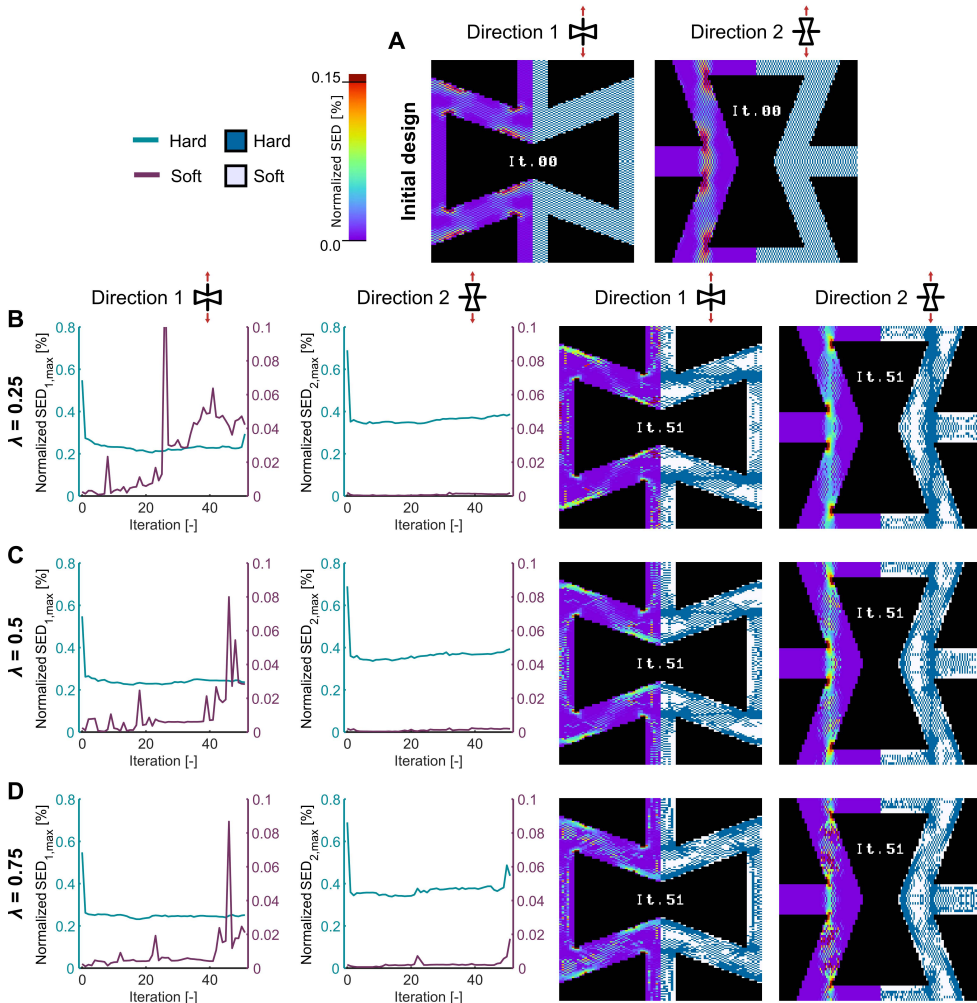
Figure 6.3. A) The normalized SED values of the initial quasi-random bitmap designs when loaded in tension along both orthogonal directions. As the remodeling process progressed, an intermediate length scale emerged while the peaks and distributions of normalized SED adjusted: B) $\lambda = 0.25$, C) $\lambda = 0.5$, and D) $\lambda = 0.75$.

We then examined the effects of applying the bone-mimicking optimization process on the redistribution of SED to study whether the applied design methodology attenuates the

stress concentrations present in the re-entrant and honeycomb unit cells. Before remodeling, the representative auxetic design (*i.e.,* $\lambda = 0.5$, $\rho = 50\%$) presented high degrees of strain energy concentration in the areas close to the strut corners for both types of loading directions (Figure 6.3A). These peaks were within the hard voxels and, regardless of λ, were attenuated within the initial iterations (Figure 6.3B-D). Although the soft voxels generally showed increasing energy peaks as the remodeling process progressed (particularly when loaded along direction 1), the magnitudes of these peaks were lower than those of the hard voxels by one order of magnitude. After remodeling, substantial energy peaks were only present when the highly anisotropic designs were loaded orthogonal to their intended loading direction (*i.e.,* direction 1 for $\lambda = 0$ and direction 2 for $\lambda = 1$) (Figure S6.4B-C of the supporting information). For the remaining cases, the features introduced by the optimizations resulted in more homogeneous energy distributions (Supplementary videos 6.1-5, Figure S6.4D of the supporting information). Moreover, the total SED plots (Figure S6.4E of the supporting information) indicated that, as the remodeling progressed, an increasing amount of energy accumulated within the unit cells along their preferred remodeling direction, explaining their general stiffening. These phenomena indicate that the remodeling algorithm promotes a synergistic arrangement of the hard and soft voxels to improve the mechanical response of the unit cells, which we further validated with experiments.

6.3.2 Experimental validation

The auxetic monolithically hard lattices, which were designed as controls, exhibited a linear elastic behavior followed by brittle failure (Figure 6.4A). In contrast, all the quasi-random initial bitmap designs had a nonlinear response and presented a stress-softening behavior, indicating that plastic deformations were present. The designs that resulted from remodeling showed a similar response. However, their response was stiffer, and their ultimate tensile stress (σ_{UTS}) was higher for all the considered cases (Table S6.1 of the supporting information). In fact, for the tested designs, σ_{UTS} was up to 1.78 times higher along direction 1 (*i.e.,* $E_{1,max}, \lambda_{0.75}$) and up to 1.77 times stronger along direction 2 (*i.e.,* $E_{2,max}, \lambda_{0.25}$). Similarly, the elastic modulus was up to 1.8 (*i.e.,* $E_{1,max}, \lambda_{0.75}$) and 3.67 (*i.e.,* $E_{1,max}, \lambda_{0.75}$) times higher along directions 1 and 2, respectively. These drastic improvements in the

mechanical behavior of the specimens demonstrate that the remodeling algorithm can substantially enhance the properties of the initial sub-optimal designs.
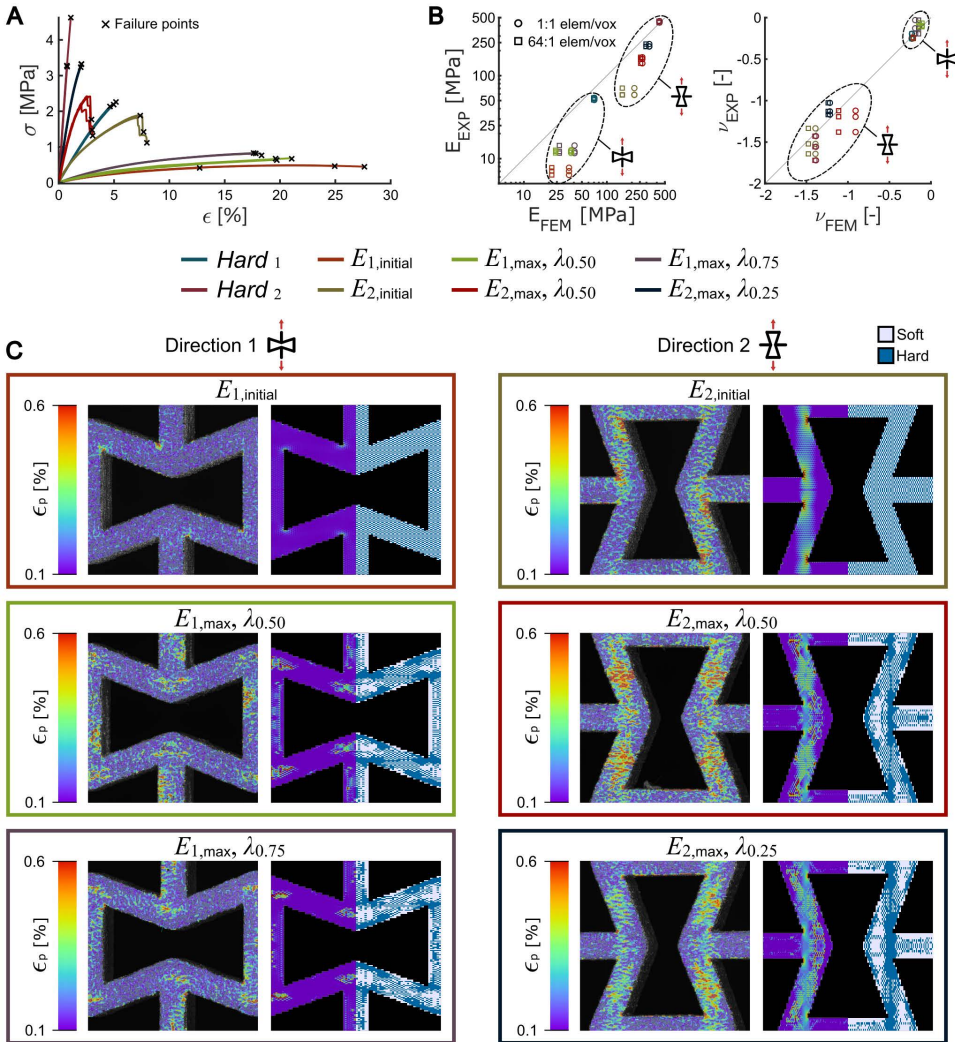
Figure 6.4. A) The stress-strain curves corresponding to the validation tests performed on a selected number of designs with 50% hard voxels. B) The experimental *vs.* simulation results for the elastic modulus (E) and Poisson's ratio (ν) for two different numbers of elements per voxel (*i.e.,* 1:1 and 64:1). C) The distribution of the first true principal strain (ϵ_p) as measured by DIC and as predicted by our FEM models (tensile strain = 0.25%).

A one-to-one comparison analysis between the measured and the FEM-predicted mechanical properties indicated that the FEM models can accurately predict the mechanical

properties of the specimens (*i.e.,* $R^2_{E,1:1}$ = 86.3% for the elastic moduli, $R^2_{v,1:1}$ = 94.31% for the Poisson's ratios, Figure 6.4B), where R values refer to the Pearson's correlation coefficients that were calculated to quantify the correlation between the experimental and computational data. The elastic moduli of the control group (*i.e.,* monolithically hard lattices) were predicted most accurately, while those of the bitmap designs were overestimated. These discrepancies were due to the alternating nature of the material properties within the bitmap unit cells, which are known to result in stiffness overestimations [28,33]. We, therefore, increased the element-to-voxel ratio of the FEM models from 1:1 to 64:1, which improved the accuracy of the validation simulations, particularly for the elastic modulus (*i.e.,* $R^2_{E,64:1}$ = 91.85%, $R^2_{v,64:1}$ = 96.5%). However, this improved accuracy came with four orders of magnitude increase in the CPU time (Figure S6.2B of the supporting information), which rendered performing the iterative remodeling analysis at such representations infeasible. The improvements in the mechanical properties remained consistent and, in fact, even improved upon using higher element-to-voxel ratios. The emergent design features were also consistent between both levels of discretization. Moreover, the Poisson's ratios were captured highly accurately even when the smaller number of elements per voxel (*i.e.,* 1:1) was used. We, therefore, concluded that a 1:1 element-to-voxel ratio was sufficient for running the bone-mimicking design optimization routine. Once the optimal design is found, one can use a higher element-to-voxel ratio to capture the elastic properties of the resulting designs more accurately. Another option would be to run a few additional steps of design optimization starting from the design resulting from the lower ratio simulations. When we used this latter strategy, the resulting distributions of the soft and hard phases were highly consistent with each other, regardless of the number of elements used per voxel (Figure S6.2C of the supporting information).

When comparing the FEM-predicted strain distribution with the full-field strain measurements performed using DIC, we found that the simulations captured the most important features of the experimentally observed deformation patterns (Figure 6.4C). For the initial quasi-random designs, we observed peaks of strains at the hinge locations of the specimens and a relatively homogeneous distribution of lower strain values throughout the unit cell. These distributions explain the lower maximum stress and elastic moduli of the initial designs. The strain distributions of the remodeled designs were generally more homogeneous in both the simulations and experiments. Both of the designs that resulted

from the application of the optimization algorithm to loading along direction 1 (*i.e.,* $E_{1,max}, \lambda_{0.50}$ and $E_{1max}, \lambda_{0.75}$) concentrated the strains around the strut intersections and along the struts parallel to the loading direction, which is similar to the FEM predictions. Similarly, the designs that were optimized for loading along direction 2 (*i.e.,* $E_{2,max}, \lambda_{0.50}$ and $E_{2,max}, \lambda_{0.25}$) led to increased strains within the diagonal struts with relatively higher strains present in the experiments than in the simulations. These more homogeneous strain distributions confirm the success of the proposed bone-mimicking design algorithm in improving the utilization of the available hard and soft voxels through the emergence of geometrical features at an intermediate length scale between the unit cell and voxel dimensions. This proposed design approach can, therefore, be applied to the rational design of metamaterials with enhanced load-bearing capabilities and longer service lives. The combination of unusual elastic properties and stress-worthiness offered by such designs would allow for the development of metamaterial-based devices, such as implantable medical devices [34], soft robots [35], and soft digital logic mechanisms for control and actuation [36,37].

6.4. Conclusions

We mimicked living bones through the introduction of a remodeling-inspired algorithm that rationally distributes hard and soft voxels within the unit cells of mechanical metamaterials. There are, therefore, two length scales that are introduced to the algorithm (*i.e.,* the length scales corresponding to the unit cell dimensions and voxel size). A third, intermediate length scale then emerges from the application of the proposed algorithm. This leads to the formation of design features that eventually result in the expansion of the envelope of the achievable elastic properties, attenuation of the stress peaks responsible for crack initiation and growth, as well as improved failure properties and, thus, improved stress-worthiness of mechanical metamaterials. The parameters of the remodeling algorithm, including the one determining the bias towards a specific loading direction, determine the isotropic or anisotropic nature of the obtained mechanical properties. One could, therefore, bias the algorithm towards a specific loading direction while limiting the available material budget (*e.g.,* by limiting the number of (hard) voxels) to create highly efficient structures that can carry the intended loads with the minimum weight. The experimental validations demonstrate the accuracy of the computational models while also revealing improvements in

the ultimate tensile strength. Further work should, therefore, seek to augment our computational models to investigate the generated designs more efficiently. Both the proposed approach and the emergent design features could be applied to the design of multiple types of devices in various high-added-value industries, including medicine, soft robotics, and beyond.

References

[1]   D. Chen, X. Zheng, Multi-material Additive Manufacturing of Metamaterials with Giant, Tailorable Negative Poisson's Ratios, Sci. Rep. 8 (2018) 9139. https://doi.org/10.1038/s41598-018-26980-7.

[2]   M.J. Mirzaali, S. Janbaz, M. Strano, L. Vergani, A.A. Zadpoor, Shape-matching soft mechanical metamaterials, Sci. Rep. 8 (2018) 965. https://doi.org/10.1038/s41598-018-19381-3.

[3]   X. Zheng, H. Lee, T.H. Weisgraber, M. Shusteff, J. DeOtte, E.B. Duoss, J.D. Kuntz, M.M. Biener, Q. Ge, J.A. Jackson, S.O. Kucheyev, N.X. Fang, C.M. Spadaccini, Ultralight, ultrastiff mechanical metamaterials, Science (80-.). 344 (2014) 1373–1377. https://doi.org/10.1126/SCIENCE.1252291/SUPPL_FILE/ZHENG.SM.PDF.

[4]   K. Bertoldi, V. Vitelli, J. Christensen, M. Van Hecke, Flexible mechanical metamaterials, Nat. Rev. Mater. 2017 211. 2 (2017) 1–11. https://doi.org/10.1038/natrevmats.2017.66.

[5]   A.A. Zadpoor, Mechanical meta-materials, Mater. Horizons. 3 (2016) 371–381. https://doi.org/10.1039/C6MH00065G.

[6]   H.M.A. Kolken, A.A. Zadpoor, Auxetic mechanical metamaterials, RSC Adv. 7 (2017) 5111–5129. https://doi.org/10.1039/c6ra27333e.

[7]   J.U. Surjadi, L. Gao, H. Du, X. Li, X. Xiong, N.X. Fang, Y. Lu, Mechanical Metamaterials and Their Engineering Applications, Adv. Eng. Mater. 21 (2019) 1800864. https://doi.org/10.1002/ADEM.201800864.

[8]   X. Ren, R. Das, P. Tran, T.D. Ngo, Y.M. Xie, Auxetic metamaterials and structures: a review, Smart Mater. Struct. 27 (2018) 023001. https://doi.org/10.1088/1361-665X/AAA61C.

[9]   M.N. Andersen, F. Wang, O. Sigmund, On the competition for ultimately stiff and strong architected materials, Mater. Des. 198 (2021) 109356. https://doi.org/10.1016/J.MATDES.2020.109356.

[10]   M.J. Mirzaali, R. Hedayati, P. Vena, L. Vergani, M. Strano, A.A. Zadpoor, Rational design of soft mechanical metamaterials: Independent tailoring of elastic properties with randomness, Appl. Phys. Lett. 111 (2017) 051903. https://doi.org/10.1063/1.4989441.

[11]   M.J. Mirzaali, H. Pahlavani, E. Yarali, A.A. Zadpoor, Non-affinity in multi-material mechanical metamaterials, Sci. Reports 2020 101. 10 (2020) 1–10. https://doi.org/10.1038/s41598-020-67984-6.

[12]   O. Eren, H.K. Sezer, N. Yalçın, Effect of lattice design on mechanical response of PolyJet additively manufactured cellular structures, J. Manuf. Process. 75 (2022) 1175–1188. https://doi.org/10.1016/J.JMAPRO.2022.01.063.

[13]   V.S. Deshpande, M.F. Ashby, N.A. Fleck, Foam topology: bending versus stretching dominated architectures, Acta Mater. 49 (2001) 1035–1040. https://doi.org/10.1016/S1359-6454(00)00379-7.

[14]   C. Zhan, M. Li, R. McCoy, L. Zhao, W. Lu, 3D printed hierarchical re-entrant honeycombs: Enhanced mechanical properties and the underlying deformation mechanisms, Compos. Struct. 290 (2022) 115550. https://doi.org/10.1016/J.COMPSTRUCT.2022.115550.

[15]   R. Gatt, M. Vella Wood, A. Gatt, F. Zarb, C. Formosa, K.M. Azzopardi, A. Casha, T.P. Agius, P. Schembri-Wismayer, L. Attard, N. Chockalingam, J.N. Grima, Negative Poisson's ratios in tendons:

6. Mimicking living bones to optimize hierarchical, multi-material 3D printed auxetic metamaterials

An unexpected mechanical response, Acta Biomater. 24 (2015) 201–208. https://doi.org/10.1016/J.ACTBIO.2015.06.018.

[16]   C. Lees, J.F.V. Vincent, J.E. Hillerton, Poisson's Ratio in Skin, Biomed. Mater. Eng. 1 (1991) 19–23. https://doi.org/10.3233/BME-1991-1104.

[17]   U.G.K. Wegst, H. Bai, E. Saiz, A.P. Tomsia, R.O. Ritchie, Bioinspired structural materials, Nat. Mater. 2014 141. 14 (2014) 23–36. https://doi.org/10.1038/nmat4089.

[18]   W. Huang, D. Restrepo, J.Y. Jung, F.Y. Su, Z. Liu, R.O. Ritchie, J. McKittrick, P. Zavattieri, D. Kisailus, Multiscale Toughening Mechanisms in Biological Materials and Bioinspired Designs, Adv. Mater. 31 (2019) 1901561. https://doi.org/10.1002/ADMA.201901561.

[19]   M. Grossman, D. Pivovarov, F. Bouville, C. Dransfeld, K. Masania, A.R. Studart, Hierarchical Toughening of Nacre-Like Composites, Adv. Funct. Mater. 29 (2019) 1806800. https://doi.org/10.1002/ADFM.201806800.

[20]   S.E. Naleway, M.M. Porter, J. McKittrick, M.A. Meyers, Structural Design Elements in Biological Materials: Application to Bioinspiration, Adv. Mater. 27 (2015) 5455–5476. https://doi.org/10.1002/adma.201502403.

[21]   J.W.C. Dunlop, P. Fratzl, Biological Composites, Annu. Rev. Mater. Res. 40 (2010) 1–24. https://doi.org/10.1146/annurev-matsci-070909-104421.

[22]   D. Sen, M.J. Buehler, Structural hierarchies define toughness and defect-tolerance despite simple and mechanically inferior brittle building blocks, Sci. Rep. 1 (2011) 1–9. https://doi.org/10.1038/srep00035.

[23]   R. Huiskes, R. Rulmerman, G.H. Van Lenthe, J.D. Janssen, Effects of mechanical forces on maintenance and adaptation of form in trabecular bone, Nat. 2000 4056787. 405 (2000) 704–706. https://doi.org/10.1038/35015116.

[24]   R. Huiskes, H. Weinans, H.J. Grootenboer, M. Dalstra, B. Fudala, T.J. Slooff, Adaptive bone-remodeling theory applied to prosthetic-design analysis, J. Biomech. 20 (1987) 1135–1150. https://doi.org/10.1016/0021-9290(87)90030-3.

[25]   H. Weinans, R. Huiskes, H.J. Grootenboer, The behavior of adaptive bone-remodeling simulation models, J. Biomech. 25 (1992) 1425–1441. https://doi.org/10.1016/0021-9290(92)90056-7.

[26]   K.I. Tsubota, T. Adachi, Y. Tomita, Functional adaptation of cancellous bone in human proximal femur predicted by trabecular surface remodeling simulation toward uniform stress state, J. Biomech. 35 (2002) 1541–1551. https://doi.org/10.1016/S0021-9290(02)00173-2.

[27]   I. Giorgio, M. Spagnuolo, U. Andreaus, D. Scerrato, A.M. Bersani, In-depth gaze at the astonishing mechanical behavior of bone: A review for designing bio-inspired hierarchical metamaterials, Math. Mech. Solids. 26 (2021) 1074–1103. https://doi.org/10.1177/1081286520978516/ASSET/IMAGES/LARGE/10.1177_1081286520978516-FIG2.JPEG.

[28]   M.C. Saldívar, E.L. Doubrovski, M.J. Mirzaali, A.A. Zadpoor, Nonlinear coarse-graining models for 3D printed multi-material biomimetic composites, Addit. Manuf. 58 (2022) 103062. https://doi.org/10.1016/J.ADDMA.2022.103062.

[29]   M.J. Mirzaali, M. Cruz Saldívar, A. Herranz de la Nava, D. Gunashekar, M. Nouri-Goushki, E.L. Doubrovski, A.A. Zadpoor, Multi-Material 3D Printing of Functionally Graded Hierarchical Soft–Hard Composites, Adv. Eng. Mater. 22 (2020) 1901142. https://doi.org/10.1002/adem.201901142.

[30]   G.X. Gu, C.T. Chen, D.J. Richmond, M.J. Buehler, Bioinspired hierarchical composite design using machine learning: Simulation, additive manufacturing, and experiment, Mater. Horizons. 5 (2018) 939–945. https://doi.org/10.1039/c8mh00653a.

[31]   S. Hasanov, A. Gupta, A. Nasirov, I. Fidan, Mechanical characterization of functionally graded materials produced by the fused filament fabrication process, J. Manuf. Process. 58 (2020) 923–935. https://doi.org/10.1016/J.JMAPRO.2020.09.011.

[32]   M.J. Mirzaali, M.E. Edens, A.H. de la Nava, S. Janbaz, P. Vena, E.L. Doubrovski, A.A. Zadpoor, Length-scale dependency of biomimetic hard-soft composites, Sci. Rep. 8 (2018) 12052. https://doi.org/10.1038/s41598-018-30012-9.

[33]   M.C. Saldivar, E.T.W. Shen, E.L. Doubrovski, M.J. Mirzaali, A.A. Zadpoor, Bioinspired rational design of multi-material 3D printed soft-hard interfaces, (2022). https://doi.org/10.48550/arxiv.2206.13615.

[34]   H.M.A. Kolken, S. Janbaz, S.M.A. Leeflang, K. Lietaert, H.H. Weinans, A.A. Zadpoor, Rationally designed meta-implants: a combination of auxetic and conventional meta-biomaterials, Mater. Horizons. 5 (2018) 28–35. https://doi.org/10.1039/C7MH00699C.

[35]   A.G. Mark, S. Palagi, T. Qiu, P. Fischer, Auxetic metamaterial simplifies soft robot design, Proc. - IEEE Int. Conf. Robot. Autom. 2016-June (2016) 4951–4956. https://doi.org/10.1109/ICRA.2016.7487701.

[36]   A. Pal, V. Restrepo, D. Goswami, R. V. Martinez, Exploiting Mechanical Instabilities in Soft Robotics: Control, Sensing, and Actuation, Adv. Mater. 33 (2021) 2006939. https://doi.org/10.1002/ADMA.202006939.

[37]   F. Vanneste, O. Goury, J. Martinez, S. Lefebvre, H. Delingette, C. Duriez, Anisotropic soft robots based on 3d printed meso-structured materials: Design, modeling by homogenization and simulation, IEEE Robot. Autom. Lett. 5 (2020) 2380–2386. https://doi.org/10.1109/LRA.2020.2969926.

6.5 Supporting information

S6.1. FEM mesh convergence study

We performed a mesh convergence study to determine how many FEM elements per voxel were necessary to obtain accurate simulation results (Figure S6.2A-B). Towards this end, we selected three auxetic designs: the Hard$_2$, $E_{2,\text{Initial}}$ (ρ = 50%), and the $E_{2,\text{max}}$, $\lambda_{0.25}$ (ρ = 50%). We prepared multiple FEM discretizations of these designs, where we varied the number of FEM elements that represented each hard or soft voxel. The discretizations were 1:1, 4:1, 27:1, and 64:1 elements per voxel. Furthermore, we performed additional optimization processes at different discretization levels to evaluate the consistency of the emerging features obtained from the tissue adaptation process. These optimizations were performed with λ = 0.25 and 0.75 (ρ = 50%), with discretizations of 1:1, 4:1, and 27:1 elements per voxel. We included an additional process where the final designs of the 1:1 optimizations were used as input for an optimization process with a discretization of 27:1 elements per voxel. This last process was performed for ten iterations to showcase how the features obtained from a low-resolution model can be refined without using extensive computational resources.

After performing the simulations, there was virtually no variation between the results of the Hard$_2$ models (Figure S6.2A). The other two designs converged to lower values of elastic modulus when increasing the elements per voxel, indicating that a higher number of elements per voxel yields more accurate results when assuming lattice periodicity and no material mixing. However, the rapid increase in the computational time (Intel® Xeon® W-2133 CPU @ 3.6 GHz, 128 Gb RAM) renders the application of a large number of elements per voxel infeasible in the case of iterative processes such as in remodeling analyses (Figure S6.2B). Furthermore, when comparing the emerging features from optimization processes at different levels of discretization (*i.e.,* 1:1, 8:1, 27:1, and 1:1 followed by 27:1), the regions of hard material concentration and feature shapes were consistent, with only increased feature connectivity observed for finer meshes (Figure S6.2C). We, therefore, proceeded with the 1:1 discretizations for the remodeling analyses. Additionally, we performed simulations at 64:1 elements per voxel to obtain more accurate estimations of the final designs used in the validations and compare them to the experimental test results.

S6.2. Experimental lattice size comparison test

We performed a preliminary mechanical test to determine how many unit cells per lattice yielded mechanical properties that reflect the lattice periodicity and minimize material mixing between the voxels (Figure S6.2D-E). For this purpose, we selected two designs, one with a homogeneous material distribution (*i.e.,* Hard$_2$) and a composite design (*i.e., E*$_{2,max}$, $\lambda_{0.25}$), and 3D printed them in three different lattice configurations. These were lattices with 4×4, 6×6, and 12×12 unit cells per specimen, where the size of the voxel was scaled accordingly to maintain a total specimen size of 81.28×131.28 mm^2 (Figure 6.1D). After testing these specimens, the elastic moduli from the Hard$_2$ specimens closely followed the estimations from the 64:1 elements per voxel simulations. This result indicates that all the lattices sufficiently followed periodicity conditions as prescribed in the FEM simulations. The results of the *E*$_{2,max}$, $\lambda_{0.25}$, however, demonstrated higher variations between the different configurations, with the 4×4 lattice result being the closest to the 64:1 model. Since material mixing mainly occurs between the hard and soft surfaces at the scale of the native printer resolution (*i.e.,* 300×600×900 dpi), and after considering that larger voxel sizes have higher volume-to-surface area ratio, we attributed the better performance of the 4×4 lattices to a minimized material mixing. Therefore, we used this configuration to perform the experimental validations.

6. Mimicking living bones to optimize hierarchical, multi-material 3D printed auxetic metamaterials

List of supporting tables

Table S6.1. The experimental *vs.* predicted result for every validation quasi-static test.

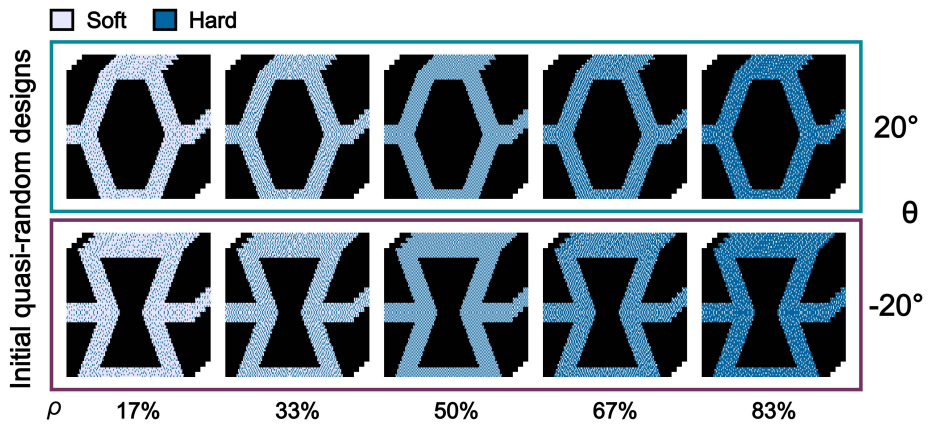|	Elastic modulus E_{exp} (MPa)	Poisson's ratio v_{exp}	Ultimate tensile strength σ_{max} (MPa)	FEM Elastic modulus E_{FEM} 1:1 (MPa)	FEM Poisso's ratio v_{FEM} 1:1	FEM Elastic modulus E_{FEM} 64:1 (MPa)	FEM Poisso's ratio v_{FEM} 64:1
Hard$_1$	53.0304	-0.1939	2.2607				
	54.0782	-0.2538	2.1340	70.6387	-0.2290	69.3570	-0.2301
	50.8746	-0.2464	2.1866				
Hard$_2$	435.7944	-1.4283	3.2498				
	452.9566	-1.5567	4.6245	431.2253	-1.3850	425.1875	-1.3981
	454.3087	-1.7197	3.2799				
$E_{1,initial}$	7.0629	-0.2391	0.4131				
	6.3464	-0.2479	0.4860	35.0015	-0.2292	21.6996	-0.2113
	7.7675	-0.2508	0.4827				
$E_{2,initial}$	58.5560	-1.6420	1.8781				
	70.7080	-1.3347	1.8909	214.4616	-1.3910	153.4000	-1.4769
	58.7387	-1.5218	1.8135				
$E_{1,max}, \lambda_{0.75}$	14.3780	-0.0295	0.8194				
	12.1836	-0.1953	0.8294	40.7963	-0.1897	26.7446	-0.1484
	11.6359	-0.1280	0.8168				
$E_{1,max}, \lambda_{0.50}$	12.1809	-0.0659	0.6733				
	11.6889	-0.0983	0.6324	37.0652	-0.1424	24.1569	-0.1066
	12.6183	-0.1095	0.6694				
$E_{2,max}, \lambda_{0.50}$	166.5172	-1.1948	2.4134				
	158.6566	-1.3795	2.2227	267.8261	-0.9078	255.2822	-1.1118
	140.8315	-1.1218	2.4200				
$E_{2,max}, \lambda_{0.25}$	225.3115	-1.0272	3.2354				
	223.9685	-1.1300	3.3260	324.4782	-1.2168	296.2970	-1.2381
	240.5084	-1.1688	3.3180				

List of supporting figures

Figure S6.1. Representative bitmap images of the four layers defined for the initial quasi-random designs used for remodeling involving five different values of hard material volume fraction ρ and two values of lattice (re)entrant angle (θ).

6. Mimicking living bones to optimize hierarchical, multi-material 3D printed auxetic metamaterials
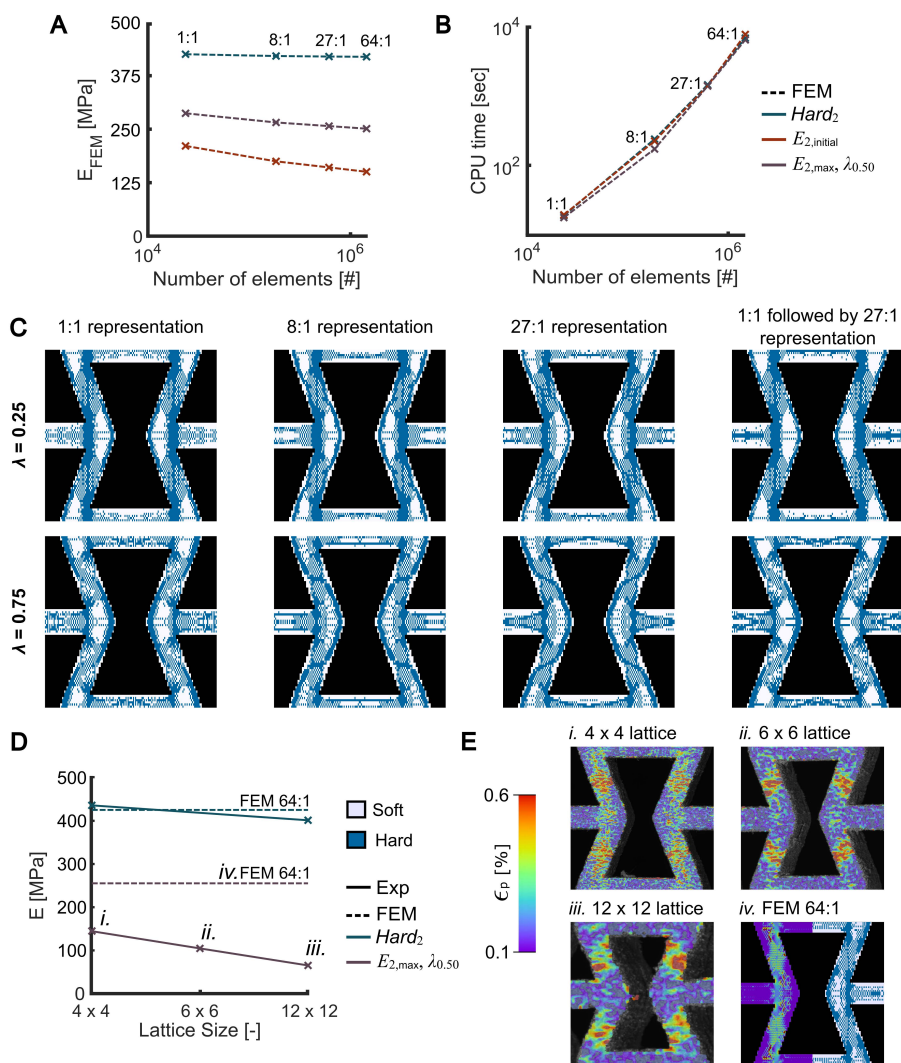
Figure S6.2. A) The results of the mesh convergence study performed to study the effects of the number of elements per voxel on the results of the FEM simulations. B) The CPU time required to run a single increment of quasi-static tension under linear elastic conditions for the different meshes. C) The emergent features obtained after performing two optimization processes (*i.e., ρ = 50%, λ = 0.25 and 0.75*) at different levels of discretization (*i.e.,* 1:1, 8:1, 27:1, and 1:1 followed by 27:1 elements per voxel). D) A comparison between the test results corresponding to different lattice sizes. We loaded lattices with different sizes in tension to analyze the effects of lattice periodicity and material mixing within the specimens. E) The distribution of the first principal true strain within the centermost unit cell of the different tested configurations, where the 4×4 lattices presented a more refined response that was the most similar to the high-fidelity simulations performed using a large number of elements per voxel (64:1).
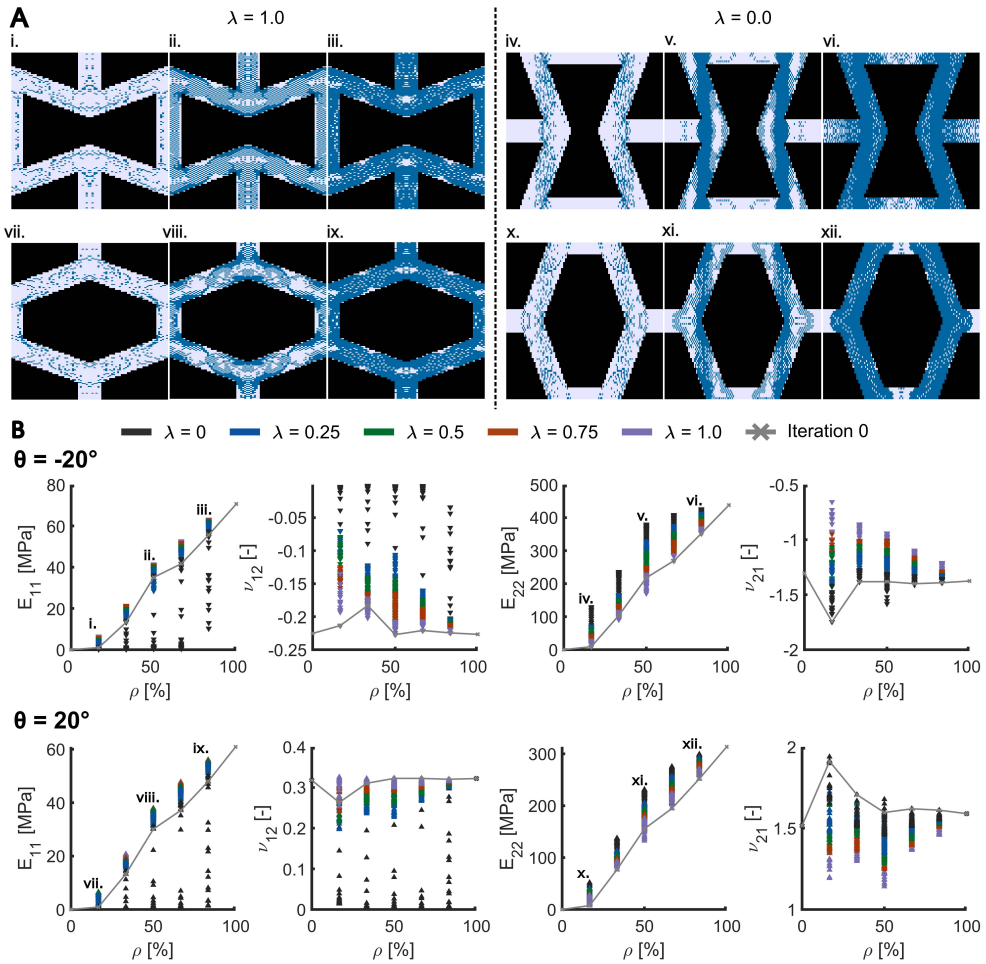
Figure S6.3. A) The representative images of the stiffest unit cells (*i.e.,* in directions 1 and 2) showcasing the hierarchical features introduced by the remodeling algorithm for varying values of hard material volume fraction ρ. B) The anisotropic mechanical properties achievable after performing remodeling for various ρ values and different (re)entrant angles (θ), where the λ parameter indicates remodeling bias towards direction 1 (*i.e.,* $\lambda = 1$) or direction 2 (*i.e.,* $\lambda = 0$), respectively.
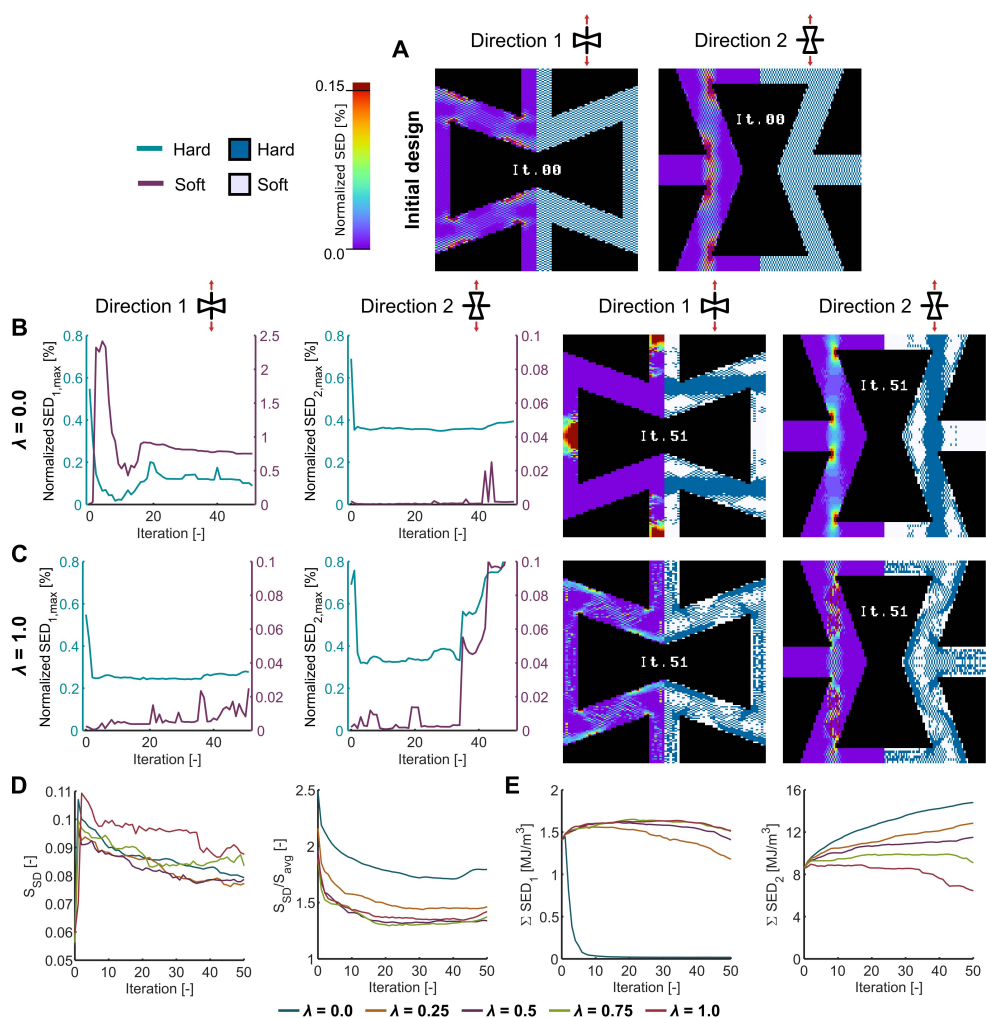
Figure S6.4. A) The normalized strain energy density (SED) (the SED of each voxel divided by the total SED in the system) distributions of the initial quasi-random bitmap designs when loaded in tension for both directions. Throughout remodeling, the peaks and distributions of normalized SED are readjusted due to the developing intermediate hierarchical features enabled by B) λ = 0.0 and C) λ = 1.0 values of the anisotropic weighting parameter. D) The overall standard deviation (S_{SD}) and standard deviation divided by the mean (S_{SD}/S_{avg}) of the effective SED (S) within the lattices throughout the optimization process, showcasing that the tissue adaptation model results in more homogeneous energy distributions. E) The total SED within the auxetic (θ = -20º) unit cells throughout the remodeling process for varying values of λ.

7

Concluding Remarks

"Every part contained a memory of the other parts it was directly attached to."

— Stanisław Lem, The Invincible
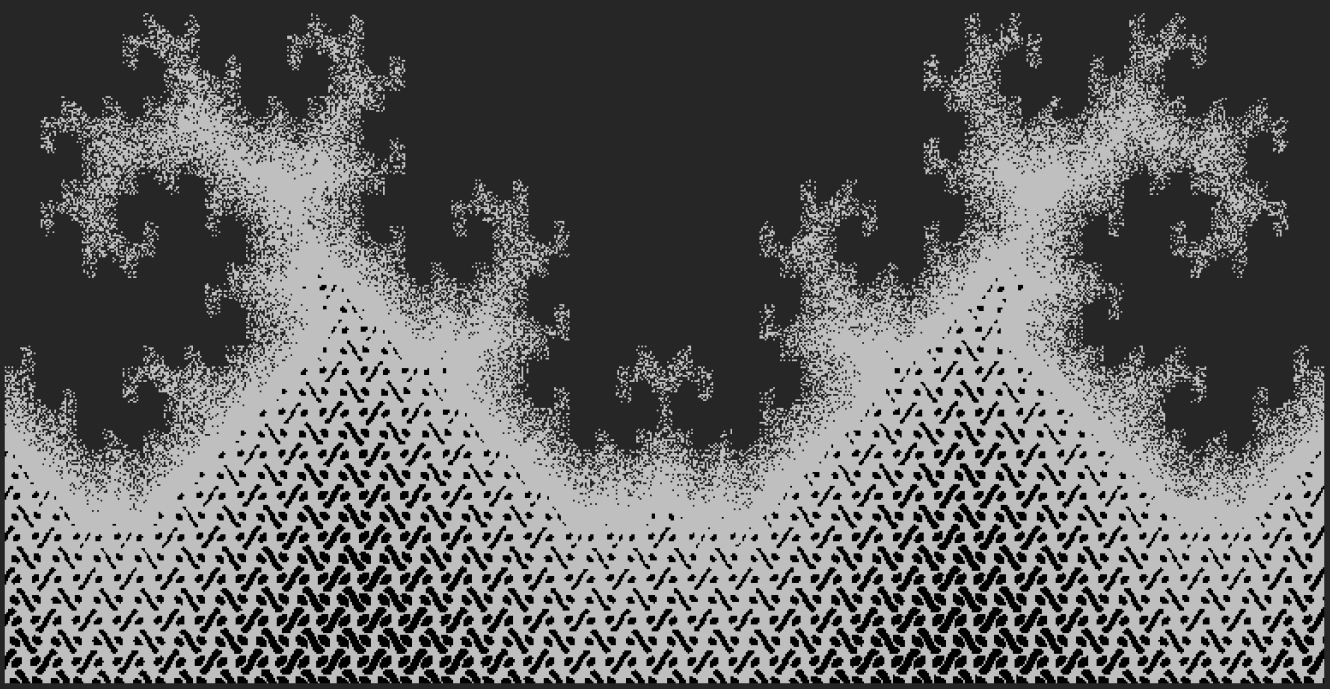
7.1 Main findings

In a quest to unlock the secrets of the brilliant designs of living tissues, this thesis sought *to study the effects of multiple bioinspired design principles and their synergy in the development of high-performing bioinspired bitmap composites*. Our approach was to incorporate a range of bioinspired design concepts, including functional gradients and multiscale hierarchical organization, into the structure of soft-hard composites using voxel-based additive manufacturing methods. The result was the production of highly intricate structures that mimic the design principles found in living tissues, such as bone, tendon, and the enthesis. The versatility and efficiency of such principles allowed for tuning the effective behavior of synthetic materials, all the while enhancing their mechanical properties, such as strength and toughness. In this section, we summarize the main findings of this thesis in accordance with the sub-objectives presented in **Chapter 1**.

On the interactions between soft and hard voxels

In **Chapters 2 and 3**, we delved into various methodologies to determine the mechanical behavior resulting from variations in the local arrangement of soft-hard composites. Three different experimental strategies at multiple length scales (*i.e.,* micro-, meso-, and macroscales) allowed us to accomplish such a task. These included nanoindentation experiments (**Chapter 2**) and two variations of quasi-static tension (**Chapters 2 and 3**). These techniques allowed for mapping the elastoplastic design space of these composites, which we modeled after introducing several mathematical expressions. In this respect, we showed that simple modifications of classic co-continuous models of particle-reinforced composites are sufficient to model the elastic behavior of randomly distributed voxels at low strain levels. However, the more complex nonlinear elastoplastic behavior was better estimated with constitutive models for large deformations. Two types of finite element method (FEM) simulations were introduced to evaluate the performance of these models: heterogeneous and coarse-grained ones. The latter provided computationally efficient simulations by representing large voxel systems as downscaled equivalents. The former, limited to hard and soft voxels, enabled comprehensive analyses of the effects of individual microscale features, such as strain concentration and energy redistribution. The results and tools generated in this part were critical for seamlessly integrating bioinspired features into voxel-based materials.

On functionally graded soft-hard interfaces

Understanding the interactions between soft and hard materials led to the generation of functional gradients with elastic modulus functions that mimic those found in natural tissues (*e.g.,* sigmoid, power-law) (**Chapter 2**). The integration of these gradients in the design of bone-ligament connections and intervertebral disks using additive manufacturing techniques resulted in significant improvements to the overall strength and toughness of the constructs when compared to their non-graded counterparts. We discussed how these remarkable improvements were due to the smoothening of stress concentration regions and the elimination of shear deformations.

A more extensive study of functional gradients for soft-hard interfacing (**Chapter 4**) demonstrated that efficient interpenetrating geometries constrain and attenuate strain concentration regions caused by property mismatches. This was achieved by increasing the contact area between the phases, smoothing their elastic modulus transition function, and eliminating sharp-ended features at the interface. Following such design guidelines enabled the rational design of soft-hard interfaces with a mechanical performance close to the maximal theoretical strength limits of the soft material, as well as up to 1.5 times higher toughness than non-graded interfaces. Not limited to soft-hard interfaces, **Chapter 5** demonstrated that incorporating similar gradients within composite designs highly increases the ductility of the specimens that are loaded under mode I fracture conditions. These improvements were achieved by dissipating stresses along the crack path and promoting crack deflection through the random distribution of particles within the lattice.

On the synergy of multiscale hierarchical organization

Similar to what is observed in natural materials, the results of **Chapters 3, 5, and 6** indicated that multiscale hierarchical features are an effective tool for the incorporation of multiple toughening mechanisms and fine-tuning the response of bitmap composites. In **Chapter 5**, we showcased how multiscale brick-and-mortar features increasingly improve the strength of fracture specimens by promoting crack bridging around mortar lines parallel to the initial cracks of mode I fracture specimens. When hierarchically combining these features with the aforementioned highly ductile gradients, the resulting composite showcased the toughening benefits of both structures, resulting in the toughest and strongest composite designs of the study.

Utilizing tissue adaptation algorithms led to the incorporation of hierarchical features that enabled the optimization of the strain energy distributions within biomimetic constructs and fine-tuning of their effective mechanical behavior. In **Chapter 3**, the inverse coarse-graining approach combined with a bone remodeling process incorporated multiscale soft-hard features that highly resembled those in femoral bones. These features redistributed the internal strain energy within the geometry, resulting in 4.5 times higher elastic energy than the initial homogeneous material distribution without increasing the required volume of the hard material. A similar algorithm presented in **Chapter 6** led to the emergence of an intermediate hierarchical level of features between a voxel microarchitecture and an auxetic lattice macroarchitecture. These features expanded the envelope of the achievable properties of these scaffolds and allowed for controlling their anisotropic response. Moreover, the rearrangement of voxels attenuated the high energy concentrations at the hinges of the scaffold, resulting in 1.8 times stronger lattices.

7.2. General Discussion

The main findings of this work contributed towards a better understanding of the interactions of the soft and hard voxels as well as towards the development of design guidelines and tools for incorporating features similar to those found in natural materials. This section analyzes the various design methodologies, their practical applications, and their significance in the larger context of the existing literature. Furthermore, we acknowledge the remaining challenges and unresolved questions encountered during this research endeavor.

On the mechanical behavior of voxelized composites

Within **Chapter 2**, a combination of experiments at multiple length scales, including existing nanoindentation [1,2] and the introduction of quasi-static uniaxial test protocols, allowed for the evaluation of the entire design space of voxel-based materials with just a few experiments and provided extensive datasets for modeling their behavior. Regardless of the applied protocol, the resulting highly nonlinear relationships between voxel morphology and effective mechanical behavior were akin to the one reported for similar materials with a more limited number of data points [3]. However, using existing particle-reinforced composite models led to high residual plots, which were primarily attributed to the random arrangement of materials and the high ratio of the elastic modulus of the hard phase to that

of the soft phase. The modifications introduced to co-continuous models proved the most successful at overcoming this problem and provided an accurate estimation of their elastic behavior for small deformations.

The design space for large deformations, which is fundamental for understanding the failure mechanics of voxelized composites, was mapped in **Chapter 3** using tensile test specimens with different distributions of material while recording their deformations using digital image correlation. The data from these tests allowed us to define the parameters of foam-based constitutive models [4], which were highly effective at modeling the complex behavior transition between the mostly hyperelastic soft material to the elastoplastic hard material. Nevertheless, the accuracy of both the co-continuous and constitutive models for large deformation depended on the random discretization of cubic-shaped voxels. Therefore, adjustments must be made if different variations of the voxel aspect ratio and joint probability function (*i.e.,* the connectivity of the voxels [5]) are to be implemented. Moreover, the accuracy of our models may be further enhanced by incorporating the effects of drop-on-drop photopolymer blending between the materials, which are known to affect the effective mechanical behavior of these composites [6].

The results of both tensile and nanoindentation experiments of **Chapter 2** were evaluated through the development of heterogeneous computational simulations. However, it is crucial to consider that their accuracy highly depends on the number of elements used to represent every voxel, which cubically increases the computational requirements. Although this problem was not present in the case of the coarse-grained models of **Chapter 3**, the accuracy of these models when estimating the ultimate strains of our designs was relatively lower. Moreover, excessive coarse-graining can remove important features within large voxel designs. These effects can be (somewhat) overcome by improving the resolution of the measurement equipment or utilizing more complex constitutive models [7,8].

Overall, the models developed to describe the interactions between soft and hard voxels are essential for designing composites in terms of their effective mechanical properties instead of solely material morphology, as seen in the existing literature [9]. Moreover, these models set the groundwork for the further incorporation of complex biomimetic design features into voxel-based materials [10].

7. Concluding Remarks

On soft-hard interfacing

In addition to analyzing the interactions between hard and soft materials, we also implemented and studied the performance of functional gradients to interface soft and hard materials. In **Chapter 1**, simplifying voxel-based architectures as systems of linear or parallel springs enabled the direct design of interfaces in terms of their effective mechanical properties. This concept and its validation process resulted in the introduction of a standard for the discretization of functional gradients, which can be adapted in the future to create other gradients in terms of multiple mechanical phenomena, such as those seen in the enthesis (*e.g.,* anisotropy and viscoelasticity). Regarding the studied transition shapes, our experiments on biomimetic constructs (*i.e.,* knee ligaments and intervertebral disks) showed that sigmoids and sinusoidal functions ameliorated the interfacial strains the most. These **results suggest that continuous** 'S'-shaped functions are excellent candidates as a parting point for future gradient optimization studies. Similar shapes could be applied in devices where limiting the length of the interface is fundamental (*e.g.,* soft robotics and medical instruments).

In **Chapter 4**, we performed an extended analysis of functional gradient specimens under uniaxial tension and shear loading conditions. Although the standard for tensile testing was similar to the one introduced in **Chapters 1 and 2**, a standard for pure shear testing is lacking in the literature [11]. Although the quad-lap shear specimen design introduced in this work provided sufficient information about the shear behavior of these composites, other designs, such as one-lap shear tests, could provide additional information on the multi-modal behavior of functional gradient designs.

Regardless of the deformation mode, the analysis of various functional gradient designs based on interpenetrating soft and hard phases led to the definition of several design cues that aid in minimizing strain concentrations caused by the mismatch in the mechanical properties of interfacing materials [12]. We showed how fundamental it is to discretize the soft and hard voxels such that the ensuing strain concentrations are reduced (or at least constrained by the surrounding hard material) by controlling multiple parameters. Mainly, concave-shaped interface features, such as those seen in short gyroid and collagen designs, showed lower strain concentrations than those of sharp features. Similarly, smooth contact surface area profiles and compliant transitions of elastic modulus trended to diminish strain

concentrations, as seen in particle and collagen designs. All these concepts for an appropriate definition of soft-hard interfacing were applied to generate an additional design, which yielded the strongest and toughest specimens within this study. However, it is essential to consider that soft-hard voxels under any configuration always present some degree of strain concentration. This intrinsic effect calls for more extensive analyses, perhaps through brute-force approaches [13,14], to find specific voxel configurations that ensure the minimization or constraining of strain concentrations in the soft phase. Overall, these functional gradient analyses provided a much-needed set of standards for testing interfaces in multiple loading conditions and design guidelines that enable the creation of high-performing devices relevant to many applications (*e.g.,* reconstructive surgery, soft robotics, medical instruments).

On the hierarchical organization of soft-hard voxels

The analyses of multiple brick-and-mortar and graded designs performed in **Chapter 5** allowed for elucidating the contribution of multiple design paradigms to strengthen and toughen composites. On the one hand, graded features around regions where failure may be expected can delocalize stress singularities and introduce micro-cracks around that dissipate energy from critical cracks. Although these mechanistic effects led to highly ductile behavior, the strength of the composites was compromised. On the other hand, the stronger brick-and-mortar designs, similar to those seen in nacre-inspired studies [15], attenuated the stress peaks through mortar lines surrounding the crack tip and showed signs of crack bridging, particularly when two hierarchy levels of features were present. Similar to what has been observed in the bone, these two toughening principles coexisted when combining the different features hierarchically, resulting in composites that were both tough and strong while keeping the volume of the hard material constant. These results demonstrated the remarkable versatility of voxel-based techniques for manufacturing biomimetic devices with multiple bioinspired features. These results call for new algorithms that incorporate these hybrid brick-and-mortar features within the regions of heterogeneous constructs where the hard phase is prevalent (*e.g.,* the cortical bone region of the femur presented in **Chapter 3**) [16,17].

In **Chapter 6**, the simple addition of hard and soft voxels within the struts of (re)entrant metamaterials highly extended the design space of these lattices. Although this positive outcome allowed for the tuning of their elastic behavior without changing the lattice

morphology, it did not reduce the concentrations of strain energy density at the hinge areas of these lattices, which are known to hinder their mechanical performance [18]. Therefore, an optimization algorithm inspired by bone tissue adaptation [19] was used to optimally distribute the hard and soft voxels, which lead to the emergence of an intermediate hierarchical level. Utilizing the heterogeneous FEM models, this algorithm allowed for re-assigning the voxels within the lattices according to their values of strain energy density. The shape of these features was mainly determined by the λ parameter, which controls the anisotropic remodeling preference of the algorithm. However, their connectivity improved by increasing the number of mesh elements representing each voxel, which came at a much higher computational cost.

Regardless of the element-to-voxel ratio used in the computational models, these features further extended the elastic design space of the lattices, all while decoupling their elastic modulus and Poisson's ratio, similar to what has been proposed with other methods [20]. Moreover, the remodeling process resulted in more homogeneous strain distributions within the metamaterial unit cells. However, to fully corroborate that this response was present in the experimental tests, we scaled up the lattice designs by a factor of three. This scaling was relevant because mixing between both material phases was blurring the remodeled features at the maximum voxel resolutions. This indicated that considering the effects of interface material mixing is particularly important when the performance of a structure depends on the arrangement of just a few voxels, as seen in the lattices presented in this chapter. Moreover, the more homogeneous strain distributions in the remodeled designs resulted in an improved elastic response and up to 1.8 times stronger lattices. These outcomes call for implementing similar evolution-based algorithms [21,22] to optimize and further extend the performance of other metamaterial designs.

7.3. Recommendations for future research

Based on the findings and questions left open in this thesis, a few research lines that could be followed are suggested to implement even more bioinspired design principles for the generation of tough and strong synthetic composites.

First, a better understanding of the interface properties between the hard and the soft voxels due to photopolymer blending is essential for improving the accuracy of

computational simulations. Similar to the existing soft-hard slab models [23], considering an 'interphase' on adjacent hard or soft voxels would be an ideal method to account for the presence of material mixing. Such an interface can be introduced during the voxel to FEM mesh subdivision process within the heterogeneous simulations. However, such a study does not guarantee that the limitations regarding the computing time of the heterogeneous simulations are solved.

In terms of voxel morphology, our work mainly focused on studying cubic-shaped voxels and their random discretization. Including different voxel shapes and aspect ratios, however, is still open to investigation. For example, analyzing voxel aspect ratios that span from plate-like to fiber-like arrangements can lead to the direct design of constructs with exotic anisotropic properties, further extending the design space of voxelized materials.

Moreover, several other aspects of material behavior need to be studied within the context of soft-hard voxelized materials. Perhaps the most relevant phenomenon is viscoelasticity, particularly in the presence of a third fluid phase [24,25]. Such a characterization, together with anisotropic arrangements, could yield complex biomimetic constructs that mimic the impact resistance properties of human cartilage and can still be connected to other hard constructs [26].

Regarding the remaining bioinspired design paradigms that were not included in this work, recent studies have demonstrated the great potential of adopting lamellar and osteon-like structures to toughen composites [27,28]. A natural follow-up for implementing these structures within synthetic materials is the application of voxel-based techniques to discretize and manufacture these features within complex geometries. For example, osteon-like structures could be discretized by using anisotropic voxel arrangements within the microarchitecture of femur-like shaft constructs to improve their bending and torsion responses.

All in all, the principles of voxelized technology and morphogenetic/mechanically guided bioinspired design principles can be applied to optimize the design of devices within a multitude of fields. Examples include, but are not limited to, multistable deployable implants [29–31], prosthetic assemblies [32,33], flexible medical instruments [34,35], and soft robotics [36]. Above all else, these principles could underlie the design guidelines for the next generation of skeletally-relevant implants, such as maxillofacial replacements [37] and

optimized tissue engineering scaffolds with multiple functionalities and decoupled mass properties [38]. Nevertheless, it is crucial to ensure that the biocompatibility of these materials is sufficient before the implementation of these concepts. Voxel-based manufacturing techniques, therefore, need to be further developed to enable the processing of alternative biocompatible materials (*e.g.,* hydrogel-metal infusion [39]). Limitations notwithstanding, the essential principles presented here underpin the necessity for future engineers and designers to be cognizant of not only material choice and macro-scale design, but also micro-scale material arrangement. Simply put, this work emphasizes that there is only one way to synthetically replicate the functionality of natural tissues: one bit at a time.

References

[1]   M.J. Mirzaali, A. Herranz de la Nava, D. Gunashekar, M. Nouri-Goushki, R.P.E. Veeger, Q. Grossman, L. Angeloni, M.K. Ghatkesar, L.E. Fratila-Apachitei, D. Ruffoni, E.L. Doubrovski, A.A. Zadpoor, Mechanics of bioinspired functionally graded soft-hard composites made by multi-material 3D printing, Compos. Struct. 237 (2020) 111867. https://doi.org/10.1016/J.COMPSTRUCT.2020.111867.

[2]   A. Tits, E. Plougonven, S. Blouin, M.A. Hartmann, J.F. Kaux, P. Drion, J. Fernandez, G.H. van Lenthe, D. Ruffoni, Local anisotropy in mineralized fibrocartilage and subchondral bone beneath the tendon-bone interface, Sci. Reports 2021 111. 11 (2021) 1–17. https://doi.org/10.1038/s41598-021-95917-4.

[3]   L. Zorzetto, L. Andena, F. Briatico-Vangosa, L. De Noni, J.M. Thomassin, C. Jérôme, Q. Grossman, A. Mertens, R. Weinkamer, M. Rink, D. Ruffoni, Properties and role of interfaces in multimaterial 3D printed composites, Sci. Reports 2020 101. 10 (2020) 1–17. https://doi.org/10.1038/s41598-020-79230-0.

[4]   Q. Liu, G. Subhash, A phenomenological constitutive model for foams under large deformations, Polym. Eng. Sci. 44 (2004) 463–473. https://doi.org/10.1002/PEN.20041.

[5]   N.A. Meisel, D.A. Dillard, C.B. Williams, Impact of material concentration and distribution on composite parts manufactured via multi-material jetting, Rapid Prototyp. J. 24 (2018) 872–879. https://doi.org/10.1108/RPJ-01-2017-0005/FULL/PDF.

[6]   F. Liu, T. Li, X. Jiang, Z. Jia, Z. Xu, L. Wang, The effect of material mixing on interfacial stiffness and strength of multi-material additive manufacturing, Addit. Manuf. 36 (2020) 101502. https://doi.org/10.1016/J.ADDMA.2020.101502.

[7]   T. Beda, An approach for hyperelastic model-building and parameters estimation a review of constitutive models, Eur. Polym. J. 50 (2014) 97–108. https://doi.org/10.1016/J.EURPOLYMJ.2013.10.006.

[8]   H. Fallahi, F. Taheri-Behrooz, A. Asadi, Nonlinear Mechanical Response of Polymer Matrix Composites: A Review, Https://Doi.Org/10.1080/15583724.2019.1656236. 60 (2019) 42–85. https://doi.org/10.1080/15583724.2019.1656236.

[9]   Mirzaali, Nava, Gunashekar, Nouri-Goushki, Doubrovski, Zadpoor, Fracture Behavior of Bio-Inspired Functionally Graded Soft–Hard Composites Made by Multi-Material 3D Printing: The Case of Colinear Cracks, Materials (Basel). 12 (2019) 2735. https://doi.org/10.3390/ma12172735.

[10]   A.R. Studart, Biological and Bioinspired Composites with Spatially Tunable Heterogeneous Architectures, Adv. Funct. Mater. 23 (2013) 4423–4436. https://doi.org/10.1002/adfm.201300340.

[11]   I. Vu, L. Bass, N. Meisel, B. Orler, C.B. Williams, D.A. Dillard, Characterization of Multi-Material Interfaces in PolyJet Additive Manufacturing, (2015). https://repositories.lib.utexas.edu/handle/2152/89393 (accessed February 10, 2023).

[12]   A.R. Studart, R. Libanori, R.M. Erb, Functional Gradients in Biological Composites, in: Bio-Bioinspired Nanomater., Wiley-VCH Verlag GmbH & Co. KGaA, Weinheim, Germany, 2014: pp. 335–368. https://doi.org/10.1002/9783527675821.ch13.

[13]   S.E. Naleway, M.M. Porter, J. McKittrick, M.A. Meyers, Structural Design Elements in Biological Materials: Application to Bioinspiration, Adv. Mater. 27 (2015) 5455–5476. https://doi.org/10.1002/adma.201502403.

[14]   Z. Jin, Z. Zhang, K. Demir, G.X. Gu, Machine Learning for Advanced Additive Manufacturing, Matter. 3 (2020) 1541–1556. https://doi.org/10.1016/j.matt.2020.08.023.

[15]   G.X. Gu, F. Libonati, S.D. Wettermark, M.J. Buehler, Printing nature: Unraveling the role of nacre's mineral bridges, J. Mech. Behav. Biomed. Mater. 76 (2017) 135–144. https://doi.org/10.1016/j.jmbbm.2017.05.007.

[16]   J. Deering, K.I. Dowling, L.A. DiCecco, G.D. McLean, B. Yu, K. Grandfield, Selective Voronoi tessellation as a method to design anisotropic and biomimetic implants, J. Mech. Behav. Biomed. Mater. 116 (2021) 104361. https://doi.org/10.1016/j.jmbbm.2021.104361.

[17]   A. Ghazlan, T.D. Ngo, P. Tran, Three-dimensional Voronoi model of a nacre-mimetic composite structure under impulsive loading, Compos. Struct. 153 (2016) 278–296. https://doi.org/10.1016/j.compstruct.2016.06.020.

[18]   C. Zhan, M. Li, R. McCoy, L. Zhao, W. Lu, 3D printed hierarchical re-entrant honeycombs: Enhanced mechanical properties and the underlying deformation mechanisms, Compos. Struct. 290 (2022) 115550. https://doi.org/10.1016/J.COMPSTRUCT.2022.115550.

[19]   R. Huiskes, R. Rulmerman, G.H. Van Lenthe, J.D. Janssen, Effects of mechanical forces on maintenance and adaptation of form in trabecular bone, Nat. 2000 4056787. 405 (2000) 704–706. https://doi.org/10.1038/35015116.

[20]   M.J. Mirzaali, H. Pahlavani, E. Yarali, A.A. Zadpoor, Non-affinity in multi-material mechanical metamaterials, Sci. Reports 2020 101. 10 (2020) 1–10. https://doi.org/10.1038/s41598-020-67984-6.

[21]   M. Milazzo, F. Libonati, S. Zhou, K. Guo, M.J. Buehler, Biomimicry for natural and synthetic composites and use of machine learning in hierarchical design, Biomimicry Mater. Des. Habitats Innov. Appl. (2022) 141–182. https://doi.org/10.1016/B978-0-12-821053-6.00002-3.

[22]   M. Maurizi, C. Gao, F. Berto, Interlocking mechanism design based on deep-learning methods, Appl. Eng. Sci. 7 (2021) 100056. https://doi.org/10.1016/J.APPLES.2021.100056.

[23]   L. De Noni, L. Zorzetto, F. Briatico-Vangosa, M. Rink, D. Ruffoni, L. Andena, Modelling the interphase of 3D printed photo-cured polymers, Compos. Part B Eng. 234 (2022) 109737. https://doi.org/10.1016/J.COMPOSITESB.2022.109737.

[24]   F.F. Abayazid, M. Ghajari, Material characterisation of additively manufactured elastomers at different strain rates and build orientations, Addit. Manuf. 33 (2020) 101160. https://doi.org/10.1016/J.ADDMA.2020.101160.

[25]   L.B. Bezek, M.P. Cauchi, R. De Vita, J.R. Foerst, C.B. Williams, 3D printing tissue-mimicking materials for realistic transseptal puncture models, J. Mech. Behav. Biomed. Mater. 110 (2020) 103971. https://doi.org/10.1016/J.JMBBM.2020.103971.

[26]   J. Eschweiler, N. Horn, B. Rath, M. Betsch, A. Baroncini, M. Tingart, F. Migliorini, The Biomechanics of Cartilage—An Overview, Life. 11 (2021). https://doi.org/10.3390/LIFE11040302.

[27]   G. Grezzana, H.-C. Loh, Z. Qin, M.J. Buehler, A. Masic, F. Libonati, Probing the Role of Bone Lamellar Patterns through Collagen Microarchitecture Mapping, Numerical Modeling, and 3D-Printing, Adv. Eng. Mater. 22 (2020) 2000387. https://doi.org/10.1002/adem.202000387.

[28]   F. Libonati, A.E. Vellwock, F. Ielmini, D. Abliz, G. Ziegmann, L. Vergani, Bone-inspired enhanced fracture toughness of de novo fiber reinforced composites, Sci. Reports 2019 91. 9 (2019) 1–12. https://doi.org/10.1038/s41598-019-39030-7.

[29]   Y. Yang, M.A. Dias, D.P. Holmes, Multistable kirigami for tunable architected materials, Phys. Rev. Mater. 2 (2018) 110601. https://doi.org/10.1103/PhysRevMaterials.2.110601.

[30]   K.R. Ryan, M.P. Down, C.E. Banks, Future of additive manufacturing: Overview of 4D and 3D printed smart and advanced materials and their applications, Chem. Eng. J. 403 (2021) 126162. https://doi.org/10.1016/J.CEJ.2020.126162.

[31]   M.A. Leeflang, F.S.L. Bobbert, A.A. Zadpoor, Additive manufacturing of non-assembly deployable mechanisms for the treatment of large bony defects, Addit. Manuf. 46 (2021) 102194. https://doi.org/10.1016/J.ADDMA.2021.102194.

[32]   D. Kokkinis, F. Bouville, A.R. Studart, 3D Printing of Materials with Tunable Failure via Bioinspired Mechanical Gradients, Adv. Mater. 30 (2018) 1705808. https://doi.org/10.1002/ADMA.201705808.

[33]   J.S. Cuellar, G. Smit, A.A. Zadpoor, P. Breedveld, Ten guidelines for the design of non-assembly mechanisms: The case of 3D-printed prosthetic hands, Proc. Inst. Mech. Eng. Part H J. Eng. Med. 232 (2018) 962–971. https://doi.org/10.1177/0954411918794734/ASSET/IMAGES/LARGE/10.1177_0954411918794734-FIG2.JPEG.

[34]   K. Lussenburg, M. Scali, A. Sakes, P. Breedveld, Additive Manufacturing of a Miniature Functional Trocar for Eye Surgery, Front. Med. Technol. 4 (2022) 7. https://doi.org/10.3389/FMEDT.2022.842958.

[35]   C. Culmone, G. Smit, P. Breedveld, Additive manufacturing of medical instruments: A state-of-the-art review, Addit. Manuf. 27 (2019) 461–473. https://doi.org/10.1016/J.ADDMA.2019.03.015.

[36]   E. Sachyani Keneth, A. Kamyshny, M. Totaro, L. Beccai, S. Magdassi, E. Sachyani Keneth, A. Kamyshny, S. Magdassi, M. Totaro, L. Beccai, 3D Printing Materials for Soft Robotics, Adv. Mater. 33 (2021) 2003387. https://doi.org/10.1002/ADMA.202003387.

[37]   A. van Kootwijk, V. Moosabeiki, M.C. Saldivar, H. Pahlavani, M.A. Leeflang, S. Kazemivand Niar, P. Pellikaan, B.P. Jonker, S.M. Ahmadi, E.B. Wolvius, N. Tümer, M.J. Mirzaali, J. Zhou, A.A. Zadpoor, Semi-automated digital workflow to design and evaluate patient-specific mandibular reconstruction implants, J. Mech. Behav. Biomed. Mater. 132 (2022) 105291. https://doi.org/10.1016/J.JMBBM.2022.105291.

[38]   F.S.L. Bobbert, K. Lietaert, A.A. Eftekhari, B. Pouran, S.M. Ahmadi, H. Weinans, A.A. Zadpoor, Additively manufactured metallic porous biomaterials based on minimal surfaces: A unique combination of topological, mechanical, and mass transport properties, Acta Biomater. 53 (2017) 572–584. https://doi.org/10.1016/J.ACTBIO.2017.02.024.

[39]   M.A. Saccone, R.A. Gallivan, K. Narita, D.W. Yee, J.R. Greer, Additive manufacturing of micro-architected metals via hydrogel infusion, Nat. 2022 6127941. 612 (2022) 685–690. https://doi.org/10.1038/s41586-022-05433-2.

7. Concluding Remarks

Acknowledgments

On March 2016, I woke up at 4:00 am to check my email. Although the Master's acceptance letter from TU Delft made me feel jolly and gay, my family and neighbors were not as amused. It turned out that those early morning celebrations were not as pleasant when out of context. Two months later, when receiving the scholarship acceptance message from CONACYT, the uproar became collective since this happened at 7:30 in the afternoon, and I was surrounded by some of my trustworthy friends from **Formula SAE UNAM** (I miss you too much, **Melvin**, you were one of the best human beings I have ever met), with whom I am grateful for all the enriching experiences we shared. Also, I am incredibly grateful to **CONACYT** for the M.Sc. opportunity and the following Ph.D. scholarship extension since these allowed me to pursue my dreams of jumping into the healthcare sector and experience living in the Netherlands again, the country with whom I fell in love after my BSc exchange.

I am very thankful to my promotor **Amir Zadpoor**, who inspired many of the master's program students and me to pursue the track of biomaterials and tissue biomechanics. I am also highly thankful for extending your hand and allowing me to join the tissue biomechanics section as a Ph.D. candidate. Your knowledge, guidance, advice, and attention to detail have been invaluable for me during these long and hard years. I would also like to express my sincere gratitude to my co-promotor **Mohammad Mirzaali** for introducing me to the fascinating topics of bioinspired and bitmap composites and for taking me under his arm throughout the Ph.D. process. Your consistent support, suggestions, feedback, challenges, insightful comments, extremely hard-working nature, and encouragement have been fundamental to completing this work. Most importantly, I want to express my appreciation for all your help and assistance in writing the idea generator grant, which not only allowed us to acquire the necessary equipment for the project but allowed balancing my financial situation during these tough years.

I would like to express my sincere appreciation to the professors and staff members who contributed to this work. To **Zjenja Doubrovski and Davide Ruffoni,** I highly appreciate your help and collaboration on our projects as well as your expertise and knowledge during the development of this project. To **Lidy Fratila-Apachitei, Gerjo van Osch, Michele Fenu,**

197

and Silvia Lopa, I am deeply thankful for all your knowledge and support on cell behavior and biocompatibility. I also would like to thank **Sander Leeflang and Joris van Dam**, whose extraordinary help and experimental and manufacturing knowledge helped keep the projects moving forward. I also extend my gratitude to M.Sc. students **Robin, Carlos, Paul, and Edwin** for their contributions to this thesis. Particularly, I want to thank **Edwin** for his highly disciplined attitude and hard work. I cannot finish counting all the added value you have provided to this project. Let's just hope that we have learned not to underestimate how much time we need to finish a project (although our projects seem to highly dislike being finished). I also want to thank **Shima Salehi** for withstanding all the experiments and analysis of cell behavior and demonstrating that sharing the frustration of a project makes them more bearable.

Well, as some bald person loves repeating, "It's about family", and I think that one of the significant advantages of living an ex-pat life is that you get to have around as many families as existential crises (you have to be careful on how you count or you will end up discovering you also have multiple *karasses*). It is quite hard to keep an order on how to acknowledge each of them, so I will go by chronological order and by how far away they are at the moment of writing this dissertation.

First, I want to express my gratitude to my good old friends from Mexico, particularly those who have been there since my late teens. **Vite, Pimi, Pipe, Daniel, Baez, Dario, Javier, Bernie, and Hiroki**, all of you have a special place in my heart. You have been there withstanding my annoying personality for many years, and somehow you still think that talking to me is a great idea. You have been islands of joy and fun and support throughout the best and the worst times, and I don't know what would have been of me without you. And talking about existential crises, I cannot leave this section without acknowledging my dear friend **Mony**, with whom for more than a decade I have shared many adventures and conversations about purpose and the meaning of life and how far away we are supposed to go to find the correct questions to the ultimate answers. I just want to say that I am extremely proud of your bravery and spirit; please don't stop being you.

Continuing with the Bellybutton people, I want to thank those with whom I've managed to mingle and relate over what is the Mexican-to-the-Netherlands experience, particularly those who were the leftovers from the M.Sc. scholarship program. To you, **Guillermo,**

Leonel, Max, and Christian, I am very thankful for sharing the experience of living abroad and still finding that we are not lonely in pursuing an improved life away from our original homes. Believe it or not, you have been an incredible example of how to go on in life when you realize that there is no way to go back.

To the Marcushof people, particularly to **Almira, Ceri, Alice, Tess, Sami, Pepe, Miguel, Anton** (I'm holding that cigar for after the defense)**, Alasdair, and Yuya**, I only have to say that you were some of the most fun and insane people I have ever had the chance to meet in my life, and sharing those early ex-pat times with you engraved the incredible memories I have from Delft within me. I hope your lives are merry, long, and full of joy.

No modern acknowledgment section can go along without mentioning those who were around when surviving the pandemic (and beyond), and for that, I cannot stare at no other than those coming and going members of Markt 65. To all of you, **Caro, Amal, Su, Monica, Joey, Sam, Alicia, Anya, Miri, and Eirini**. Every single one of you little phenomenal individuals has been an important member of the experience of living within both extremely restricted spaces and fundamentally warm and jovial minds. It has been an incredible honor to share days, evenings, games, drinks, experiences, and the washing machine with all of you. I don't know anyone else who deserves a garden and BBQs and peaceful lives more than you. **Miri** your designer skills might have saved the printing of this thesis.

On a closer note, it would be impossible not to acknowledge the incredible humans I met during my Ph.D. experience. Although most of them have moved on, **Francoise, Eline, Sebastien, Costanza, Teunis, Khashayar, and Ingmar**, have been exceptionally inspiring over the academic potential of a Ph.D. candidate and have been an example throughout my journey. At the same time, it would be a crime not to recognize that the Fishtank community, **Pier, Chun-Feng, Jon, Judith, Edwin, Katerina, Rick, Zhen, Lars, Pavlo, Teddy, and George**, were just the most exceptional, kind, and brotherly people one could wish to have close by, both within and outside the office space. Your companionship, friendship, lightheartedness, absurd humor, and coffee addiction were fundamental for overcoming all the challenges of the last years with a long smile on my face, and I am thrilled to say that our friendship and fame have gone far beyond our office space for forgotten people. Do not forget my friends; *Everything not forbidden is compulsory*, and having fun is not forbidden. A great advantage of the biomedical field is that people have not only brilliant minds but also very

social hearts. To my other colleagues and friends, **Niko, Kirsten, Monika, Fabian, Ebrahim, Helda, Merle, Lorenzo, Suzanne, Dirk, Jiahui, Marit, Jette, Maria, Cristoph, Ludovica, Sara, and Federica**, sharing all the department leisure time with you was a privilege. I hope you continue illuminating the day of every future colleague you have for the rest of your days as much as you have done to mine. Just don't forget to remind **Niko** that he has to behave. Also, I also want to acknowledge **Peggy** and **Hugo** for being the book definition of real personalities. Thank you for your wonderful cookies and self-made brews.

Talking about *karasses*, I find that all these years living in this country would have been less exemplary of a good life without having all my close baerritos. It is very hard to imagine how I would have gone through the last lustrum without my extended family members **Tim, Alba, Timba, Maria, Nacho, Macho, Su, Hakki, Sukki, Andres, Isa, Anisa, Albert, Conchita, Godorras, Jack, Regina, and Yuun**. We have shared amazing times, experiences, and adventures, celebrating our latest achievements and life progress. You are the perfect examples of kind and real human beings, and I am honored to call you my friends. I cannot wish for anything, but for your lives to continue on the incredible path they are all going through. *May your roads go ever on and on, and may the hair on your toes never fall off.*

Well, it is quite hard to write anything about my *ripe-for-bokononism* soul brothers without adding anything peculiar. The problem is, that is exactly what **Andres, Jack, and Albert** are: the weirdest yet best friends one would ever wish to have. There is little I wish more than more adventures and autistic times with you, where our activities range from doing absolutely nothing to everything all at once. Whether it's listening to Torime on a night road trip countless times, performing pagan ritual dances in the tomb of Agamemnon, going on long runs in the land of rabbits with **Andres** and being told that *"Everything the light touches is Las Encinas"*, embracing defeat in every game ever invented with **Albert** (even when it's everyone against him), or sharing countless dinners followed by evening rants with **Jack,** I just hope we continue this level of insanity until our 111th birthday parties. *May your shadows never grow less, and may your beards never grow thin.*

There is this little story my **Mom** loves telling everyone about how I, as a toddler, hated going to school and would often say, "But yeah, Mom, after finishing kindergarten, it's over". She solved this issue by taking me to a very humble man's home who lived in quite troubled conditions and told me that he stopped studying after kindergarten. Welly well, it seems that

she was a master of inception long before Leonardo DiCaprio was. It even feels short-handed to say that I am eternally grateful for all the love you have given and all the sacrifices you have made for both Gabriel and me. From the gestation period, when I was but a little fetus engineer, through my childhood, when I'd cry about everything, along the puberty times of "it's not a phase Mom, this is who I really am! ", and the later stages of "you will do your job better if you stop complaining about it", you have been an unwavering pillar of support and care and the best example I have about overcoming hardship with shear willpower and a clear head. I hold immense love for you, and I aspire to embody even a fraction of the exemplary role model that you have been for someone else. To my older brother **Gabriel**, I want you to know that I sincerely appreciate sharing growing up with you and going through so many hard and good times together. You consistently demonstrated the greater responsibility, relevance, friendliness, artistry, and creativity between the two of us, serving as an exceptional role model in my life.

I must finish this section by truthfully thanking the **graduate school of TU Delft**, not only because of all the unintentional laughs it caused, but because it introduced me to whom would become my girlfriend, **Suellen**. There is yet to be a more transcendental moment than having met you that February day of 2019, and there is nothing that I cherish more than the times we have had together ever since. From the initial times when getting to know each other, to the fantastic escape trips we had to obscure places, to surviving and even enjoying the pandemic by being next to each other, and now, while overcoming the final challenges of our Ph.D. journeys together, I am extremely happy that I have met you. My life would not be even remotely as good as it is now without you, and I cannot imagine life without every single one of the beautiful parts that define your being. Your magnificent brain, affectionate heart, unique and eccentric personality, highly-resilient spirit, and ability to craft the most exotic potions have become my ultimate inspiration and reason to smile in life. Whether I am looking towards the past, enjoying the present, or envisioning the future, your company guarantees that I will happily continue saying: *"If this isn't nice, I don't know what is".* You deserve all the flowers of the airport.

Mauricio Saldivar.

Delft.

So it goes.

List of publications

A. Publications

- M. J. Mirzaali*, **M. C. Saldívar***, A. Herranz de la Nava, D. Gunashekar, M. Nouri-Goushki, E. L. Doubrovski, A. A. Zadpoor, Multi-Material 3D Printing of Functionally Graded Hierarchical Soft-Hard Composites (2020), Advanced Engineering Materials, 22, 1901142. *Both authors contributed equally.

- J. C. Wei, B. Blaauw, G. G. M. van der Pol, **M. C. Saldívar**, C. Lai, J. Dankelman, T. Horeman, Design of an Affordable, Modular Implant Device for Soft Tissue Tension Assessment and Range of Motion Tracking During Total Hip Arthroplasty (2022), IEEE Journal of Translational Engineering in Health and Medicine, 10, 2500310.

- H. Pahlavani, M. Amani, **M. C. Saldívar**, J. Zhou, M. J. Mirzaali, A. A. Zadpoor, Deep learning for the rare-event rational design of 3D printed multi-material mechanical metamaterials (2022), Communications materials, 3:46.

- **M. C. Saldívar***, E. Tay*, E. L. Doubrovski, M. J. Mirzaali, A. A. Zadpoor, Bioinspired rational design of multi-material 3D printed soft-hard interfaces (2022), under review, preprint available on arXiv. *Both authors contributed equally.

- T. van Manen, V. Moosabeiki, **M. C. Saldívar**, M. J. Mirzaali, A. A. Zadpoor, Theoretical stiffness limits of 4D printed self-folding metamaterials (2022), Communications materials, 3, 43.

- A. van Kootwijk, V. Moosabeiki, **M. C. Saldívar**, H. Pahlavani, M.A. Leeflang, S. Kazemivand Niar, P. Pellikaan, B.P. Jonker, S.M. Ahmadi, E.B. Wolvius, N. Tümer, M. J. Mirzaali, J. Zhou, A. A. Zadpoor, Semi-automated digital workflow to design and evaluate patient-specific mandibular reconstruction implants (2022), Journal of the Mechanical Behavior of Biomedical Materials (2022), 132, 105291.

- **M. C. Saldívar**, E. L. Doubrovski, M. J. Mirzaali, A. A. Zadpoor, Nonlinear Coarse-graining Models for 3D Printed Multi-material Biomimetic Composites (2022), Additive Manufacturing, 58, 103062.

- Y. Kubo, J. Herrera, R. Beckmann, M. Weiler, H. Pahlavani, **M. C. Saldívar**, K. Szymanski, S. Rosenhain, A. Fragoulis, S. Leeflang, A. Slowik, F. Gremse, M. Wolf, M. J. Mirzaali, A. A. Zadpoor, C. Jan Wruck, T. Pufe, M. Tohidnezhad, H. Jahr, Nuclear factor erythroid 2-related factor 2 (Nrf2) deficiency causes age-dependent progression of female osteoporosis (2022), BMC Musculoskeletal Disorders, 23,1015.

- **M. C. Saldivar**, S. Salehi, R. Veeger, M. Fenu, A. Cantamessa, M. Klimopoulou, G. Talò, M. Moretti, S. Lopa, D. Ruffoni, G.J.V.M. van Osch, L. E. Fratila-Apachitei, E. L. Doubrovski, M. J. Mirzaali, A. A. Zadpoor, Rational positioning of 3D printed micro-bricks to realize high-fidelity, multi-functional soft-hard interfaces (2023), under review, preprint available on bioRxiv.
- **M. C. Saldivar***, E. Tay*, E. L. Doubrovski, M. J. Mirzaali, A. A. Zadpoor, Mimicking Living Bones to Optimize Hierarchical, Multi-Material 3D Printed Auxetic Metamaterials (2023), under review, preprint available on CellPress. *Both authors contributed equally.

B. Conference presentations

- **M. C. Saldivar**, M. J. Mirzaali, E. L. Doubrovski, A. A. Zadpoor, Computational Modeling of Bioinspired Composites Fabricated by Multi-material Voxel-based 3D Printing, TERMIS, Maastricht, the Netherlands (2021, oral presentation).
- **M. C. Saldivar**, E. L. Doubrovski, M. J. Mirzaali, A. A. Zadpoor, Computational Modeling and Crack Analysis of Bioinspired Voxel-based Multi-material Composites, European Society of Biomechanics, Milan, Italy (2021, oral presentation).
- **M. C. Saldivar,** E. Tay, E. L. Doubrovski, M. J. Mirzaali, A. A. Zadpoor, Triply Periodic Minimal Surface for Bioinspired Dissimilar Material Interfacing, European Society of Biomechanics, Porto, Portugal (2022, oral presentation).
- **M. C. Saldivar**, E. L. Doubrovski, M. J. Mirzaali, A. A. Zadpoor, Multi-scale Non-linear Modeling of Biomimetic Composites using a Coarse-graining Approach, World Congress on Computational Mechanics, Yokohama, Japan (2022, oral presentation).
- **M. C. Saldivar**, R. Veeger, Q. Grossman, A. Cantamessa, D. Ruffoni, E. L. Doubrovski, M. J. Mirzaali1, A. A. Zadpoor, Characterization and Modeling of Functional Gradients for Enabling Tough Biomimetic Devices, European Society of Biomaterials, Bordeaux, France (2022, poster presentation).
- M. J. Mirzaali, **M. C. Saldivar**, E. Tay, E. L. Doubrovski, A. A. Zadpoor, Biomimetic 3D Printed Interfaces, European Society of Biomechanics, Maastricht, the Netherlands (2023, oral presentation).

C. Awarded Grants

- **M. C. Saldivar**. Micro-architecture property-space and optimum functional conditions mapping of bioinspired multi-material 3D printable composites with the use of finite element method in conjunction with machine learning algorithms, Idea Generator project, round 2019-2, NWO, the Netherlands.

Curriculum Vitae

Mauricio C. Saldivar was born in Mexico City, Mexico, on July 24th, 1992. He received his B.Sc. degree in Mechatronics Engineering (cum laude) from the National Autonomous University of Mexico in 2015 and was an engineer in the automotive sector between 2015 and 2016 in Ford, Mexico. He received his M.Sc. degree in Biomedical Engineering (cum laude) from Delft University of Technology, The Netherlands, in 2018. During his master's study, he worked on the computational simulation of knee implant micromotions and bone collapse models in the Orthopedic Research Lab in Nijmegen, the Netherlands. Late in 2018, he started his Ph.D. in the Biomechanical Engineering department at the Faculty of Mechanical, Maritime, and Materials Engineering of Delft University of Technology, The Netherlands. In it, he worked on the design and optimization of voxel-based composites and devices through the applications of bioinspired design principles under the supervision of Prof. Amir A. Zadpoor and Dr. Mohammad J. Mirzaali.